SCUOLA DI DOTTORATO
UNIVERSITÀ DEGLI STUDI DI MILANO-BICOCCA

Department of Physics G. Occhialini

PhD program in: Physics and Astronomy Cycle: 34°

Curriculum in: Astrophysics

New insights into the physics of Gamma-Ray Burst prompt emission

Ravasio Maria Edvige

Registration number 748103

Tutor: Dr. Ghirlanda Giancarlo

Co-tutor: Dr. Lara Nava, Prof. Gabriele Ghisellini

Coordinator: Marta Calvi

ACADEMIC YEAR 2021/2022

UNIVERSITÀ DEGLI STUDI DI MILANO-BICOCCA

DOCTORAL THESIS

New insights into the physics of Gamma-Ray Burst prompt emission

Author:
Maria Edvige Ravasio

Supervisor:
Dr. Giancarlo Ghirlanda
Dr. Lara Nava
Prof. Gabriele Ghisellini

Thesis submitted in fulfillment of the requirements for the degree of Doctor of Philosophy

October 28, 2021

Declaration of Authorship

This thesis is a summary of the main research projects performed during my PhD course. Most of the work presented here is an elaboration, though not comprehensive, of ideas and results reported on articles previously published in peer-reviewed journals.

Here I report the complete list of my publications as of October 28, 2021:

- *Consistency with synchrotron emission in the bright GRB 160625B observed by Fermi*
  Ravasio M.E., Oganesyan G., Ghirlanda G., Nava L., Ghisellini G., Pescalli A., Celotti A., (2018), A&A
  https://doi.org/10.1051/0004-6361/201732245

- *THESEUS and Gamma-Ray Bursts: a valuable contribution to the understanding of prompt emission*
  Nava L., Oganesyan G., Ravasio M.E., Amati L., Ghirlanda G., O'Brien P., Osborne Julian P., Willingale R., (2018), Proceedings of the THESEUS Workshop 2017, Journal of the Italian Astronomical Society
  https://arxiv.org/abs/1802.01683

- *Evidence of two spectral breaks in the prompt emission of Gamma-Ray Bursts*
  Ravasio M.E., Ghirlanda G., Nava L., Ghisellini G., (2019), A&A
  https://doi.org/10.1051/0004-6361/201834987

- *GRB 190114C: from prompt to afterglow?*
  Ravasio M.E., Oganesyan G., Salafia O. S., Ghirlanda G., Ghisellini G., Branchesi M., Campana S., Covino S., Salvaterra R., (2019), A&A
  https://doi.org/10.1051/0004-6361/201935214

- *Probing the extragalactic fast transient sky at minute timescales with DECam*
  Andreoni I., Cooke J., Webb S., Rest A., Pritchard T.A., Caleb M., Chang S., Farah W., Lien A., Möller A., Ravasio M.E., Abbott M. C., Bhandari S., Cucchiara A., Flynn C.M., Jankowski F., Keane E.F., Moriya T.J., Onken C., Parthasarathy A., Price D.C., Petroff E., Ryder S., Wolf C., (2020), MNRAS
  https://doi.org/10.1093/mnras/stz3381

- *The rise and fall of the high-energy afterglow emission of GRB 180720B*
  Ronchi M., Fumagalli F., Ravasio M. E., Oganesyan G., Toffano M., Salafia O. S., Nava L., Ascenzi S., Ghirlanda G., Ghisellini G., (2020), A&A,
  https://doi.org/10.1051/0004-6361/201936765

- *Proton-synchrotron as the radiation mechanism of the prompt emission of GRBs?*
  Ghisellini G., Ghirlanda G., Oganesyan G., Ascenzi S., Nava L., Celotti A., Salafia O. S., Ravasio M. E., Ronchi M., (2020), A&A
  https://doi.org/10.1051/0004-6361/201937244

- *GRB Prompt Emission Spectra: The Synchrotron Revenge*
  Ravasio M.E., (2020), Proceeding of the Yamada Conference LXXI: Gamma-ray Bursts in the Gravitational Wave Era 2019
  https://arxiv.org/pdf/2003.10447.pdf

- *Spectral index-flux relation for investigating the origins of steep decay in γ-ray bursts*
  Ronchini S., Oganesyan G., Branchesi M., Ascenzi S., Bernardini M.G., Brighenti F., Dall'Osso S., D'Avanzo P., Ghirlanda G., Ghisellini G., Ravasio, M. E., Salafia O.S., (2020), Nature Communications
  https://doi.org/10.1038/s41467-021-24246-x

- *Gamma-Ray Burst studies with THESEUS*
  Ghirlanda, G., Salvaterra, R., Toffano, M., Ronchini, S., Guidorzi, C., Oganesyan, G., Ascenzi, S., Bernardini, M. G., Camisasca, A. E., Mereghetti, S., Nava, L., Ravasio, M. E., Branchesi, M., Castro-Tirado, A., Amati, L., Blain, A., Bozzo, E., O'Brien, P., Götz, D., Le Floch, E. Osborne, J. P., Rosati, P., Stratta, G., Tanvir, N., Bogomazov, A. I., D'Avanzo, P., Hafizi, M., Mandhai, S., Melandri, A., Peer, A., Topinka, M., Vergani, S. D., Zane, S., (2021), Experimental Astronomy
  https://doi.org/10.1007/s10686-021-09763-3

- *The slope of the low-energy spectrum of prompt gamma-ray burst emission*
  Toffano, M., Ghirlanda, G., Nava, L., Ghisellini, G., Ravasio, M. E., Oganesyan, G., (2021), A&A
  https://doi.org/10.1051/0004-6361/202141032

- *Multi-wavelength view of the close-by GRB 190829A sheds light on gamma-ray burst physics*
  Salafia, O. S.*, Ravasio, M. E.*, Yang, J., An, T.*, Orienti, M., Ghirlanda, G., Nava, L., Giroletti, M., Mohan, P., Spinelli, R., Zhang, Y., Marcote, B., Cimò, G., Wu, X., Li, Z., (2021), Submitted to Nature Astronomy (*corresponding authors)
  https://arxiv.org/abs/2106.07169

- *GRB 201015A: VLBI observations of the shortest Gamma-Ray Burst ever detected at Very High Energy*
  Giarratana, S., Rhodes, L., Marcote, B., Fender, R., Ghirlanda, G., Giroletti, M., Nava, L., Paredes, J. M., Ravasio, M. E., Ribó, M., (2021), in preparation

- *The high-energy extension of prompt emission spectra of bright Fermi GRBs*
  Ravasio M.E., et al., (2021), in preparation

Abstract

Gamma-ray bursts (GRBs) are powerful flashes of γ-ray (keV–MeV range) photons, occurring at cosmological distances (observed up to z =9.2) and lasting from a few seconds up to several hundreds of seconds, during which a huge isotropic equivalent energy (up to a few 10^{54} erg) is emitted. According to the duration of the γ-ray emission, GRBs are classified as long (with duration >2 s) and as short GRBs (with duration <2 s). This intense and highly variable γ-ray emission, called prompt, is followed by a long-lasting ($\sim$up to several months) emission, called afterglow, which extends from the radio band up to γ-rays. Tens of years of data collection and theoretical studies paved the way for the elaboration of a widely accepted standard model, that links these powerful sources to the accretion of matter on a newborn stellar-mass black hole or neutron star. According to the standard model, the extraction of rotational energy from the central engine powers two opposite relativistic jets: the prompt emission is produced by the conversion of a small fraction (10-20%) of the jet kinetic energy into radiation, while the afterglow is produced when the jet is decelerated by the circum-burst medium.

After more than 50 years from their discovery, there are still many open and highly debated questions in the GRB standard model. Among others, it is poorly understood what is the process that accelerates the relativistic jet, which is the composition of such a jet and how its energy reservoir is internally dissipated and converted to produce the powerful emission we observe. The nature of the radiative processes responsible for the observed prompt radiation is still unestablished, preventing us from constraining the physical properties of these sources. The prompt emission spectrum is typically fitted with a function consisting of two power–laws with slopes α and β smoothly connected at a peak energy $E_{\rm peak}$. The non-thermal spectral shape of the observed spectrum and the strong magnetic fields ($B' \sim 10^4 - 10^6$ G) expected in the emitting region call for synchrotron radiation from fast cooling electrons. However, the observed spectral slope α of several GRBs is harder than synchrotron predictions. Only recently, a substantial revision of the characterization of the prompt emission spectra down to the soft X-rays allowed to discover the presence of an additional spectral break, which has been identified as the synchrotron cooling frequency (Oganesyan et al., 2017).

Motivated by these results, I searched for the presence of a spectral break at higher energies, using *Fermi*/GBM data. Adopting a more flexible empirical function with two spectral breaks, the time-resolved spectral analysis of GRB 160625B first, and then of an extended sample of 10 bright long GRBs, allowed to find an additional spectral break $E_{\rm break}$, located between $\sim$ 20 keV and 500 keV, in the majority ($\sim$ 70%) of the spectra analyzed. These results confirm the presence of a break below the νF_ν peak in long GRBs spectra, and prove that the break energies can assume values as large as a few hundreds of keV. The photon indices of the two power–laws below and above $E_{\rm break}$ are $\langle\alpha_1\rangle = -0.58 \pm 0.16$ and $\langle\alpha_2\rangle = -1.52 \pm 0.20$, respectively. These are remarkably consistent with the predicted values for synchrotron emission in marginally fast cooling regime. When fitting with the standard empirical function, the distribution of the low-energy photon index is peaked at $\langle\alpha\rangle$= -1.02$\pm$0.19, lying in the middle of the two distributions of α_1 and α_2. This suggests that the value $\alpha \sim -1$, commonly found in previous studies, can be regarded as a weighted mean of two slopes, -2/3 and -3/2, which characterize the spectrum below and above the spectral break. Spectral simulations suggest that the separation of $E_{\rm break}$ from $E_{\rm peak}$ and the photon statistics of the spectrum can hamper the identification of the break with the currently available instruments. This might explain

why this fundamental feature has not been identified before. The consistency with synchrotron emission has been tested also by adopting a physical synchrotron model, which has been fitted to the spectral data of the long GRB 180720B. The fit highlighted the presence of two different break energies in the prompt spectra, confirming the marginally fast cooling regime, in agreement with the results obtained with an empirical function. In addition, I investigated, for the first time, the possible presence of the break in 10 short GRBs: contrary to long ones, short GRBs do not show the break, but the low-energy photon index is consistent with -2/3, suggesting that in these sources $E_{\rm break} \sim E_{\rm peak}$.

The results presented in this thesis support the marginally fast cooling synchrotron scenario, whose identification in the prompt spectrum has fundamental implications for the understanding of the physical parameters of the emitting region. The relative small ratio (closer to unity for short GRBs) of the characteristic synchrotron frequencies directly implies that the emitting particles do not cool completely. In turn this requires a magnetic field strength $B' \lesssim 10$ G, orders of magnitude smaller than the expectations for an emitting region located at $R \sim 10^{13-14}$ cm from the central engine. Assuming larger radii ($R \sim 10^{16}$ cm) would avoid a strong inverse Compton component, which indeed is not observed at $\sim$GeV energies, but it would be incompatible with the typical $\sim$ms variability timescale of the lightcurve and with the deceleration radius. Therefore, the set of physical parameters implied by these results represents a serious challenge for the GRB standard model. A possible solution may come from the proton-synchrotron scenario. Ascribing the emission to protons, which hold a much longer cooling timescale than electrons, the observed cooling frequency can be explained assuming standard values both for the magnetic field and for the radius of the emitting region. While the proton-synchrotron scenario seems to be a viable solution, further investigations on its capability to explain all the observational constraints are required.

I expanded my study of the prompt emission spectrum by including its characterization at higher energies. The extension of the accessible range up to GeV energies, thanks to the inclusion of LAT data in the spectral analysis, revealed in 10 out of 22 bursts the presence of a spectral cutoff at high energies. Interpreted as due to pair-production opacity, the exponential cutoffs provide the estimates of the bulk Lorentz factor Γ of the jet, which are consistent with the values of Γ inferred from the afterglow onset in a constant medium density. The extension at high energies allowed me also to better determine the high-energy power-law slope β, which is a key parameter to constrain the corresponding slopes p of the underlying energy distribution of non-thermal accelerated particles. Assuming the emission as due to synchrotron, I found a quite broad distribution of p, centered around a median value of $p = 2.86$ extending with a tail up to $p \sim$5–7. Given the theoretical uncertainties on the energy distribution of accelerated particles in mildly-relativistic shocks, these results provide useful observational benchmarks for the development of the theory of particle acceleration applied to the prompt emission case.

My PhD project also included the study of the first three GRBs detected at VHE, namely GRB 180720B, GRB 190114C and GRB 190829A, for what concerns their emission at frequencies lower than the VHE range. In both GRB 180720B and GRB 190114C, the study of the temporal and spectral evolution of the solely high-energy emission allowed me to sample the smooth transition from the prompt to the afterglow phase. This led to pinpoint the peak of the afterglow lightcurve (in *Fermi*/LAT data for GRB 180720B and in *Fermi*/GBM data for GRB 190114C), and to derive the bulk Lorentz factor Γ of the jet for both bursts. In the case of GRB 190829A, the broadband modeling of the multi–wavelength data, including high-resolution VLBI observations of its radio counterpart and VHE data detected by the H.E.S.S. telescopes, allowed to infer interesting constraints on the GRB physical parameters (e.g. a relatively small fraction of electrons accelerated by the forward shock and a small efficiency of the prompt emission in converting the jet

total energy into radiation).

The results presented in this thesis provide meaningful constraints on the physical parameters of the GRB prompt emission and, coupled with future observations of GRBs at VHE, they can offer new perspectives for a deeper understanding of the physics behind these powerful sources.

Thesis overview

In this thesis, I mainly focus on the characterization and interpretation of prompt emission spectra of GRBs, both at low and high energies. After a brief introduction to the GRB phenomenon and the issues related to the prompt emission phase (Chapter 1 and 2), I present the search for the presence of a low energy break with an empirical function and the consistency with a physical synchrotron model in Chapter 3, together with the investigation on the possible observational biases hiding the presence of the break. In Chapter 4 I describe the results of the extension of the analysis of the prompt emission spectra at higher energies, including LAT data. The discussion of the physical interpretation of the results obtained in the two previous Chapters is reported in Chapter 5. In addition, I present the study of the first three GRBs detected at $\sim$ TeV energies, from the perspective of their emission at lower frequencies, in Chapter 6. I briefly discuss and summarize the main results obtained in this thesis in Chapter 7.

Contents

Chapter 1

Introduction

This introduction is meant to provide a brief overview of the Gamma-Ray Burst (GRB) phenomenon, starting from the serendipitous discovery, passing through the main observational properties of prompt and afterglow emission, which are the building blocks of the so–called *GRB standard model*, to conclude with the current understanding of GRB progenitors and their connections with multi-messenger astronomy. Far from being exhaustive, my treatment will be focused on those observations and concepts which are fundamental for the arguments dealt with in my thesis.

1.1 History of a serendipitous discovery

The nuclear test ban treaty of 1963, crucial in the de-escalation of the Cold War, was aimed at controlling the proliferation of nuclear weapons, banning their tests both in the atmosphere and in space. In October 1963 the US Air Force launched the first in a series of military satellites, called "Vela" (from the Spanish verb *velar*= to watch), for the monitoring of the bright and fast gamma-ray outburst expected to be produced from the detonation during potential illicit tests. While it is unclear if these satellites detected an illicit nuclear test during their activity, they brought to the world the discovery of a new class of cosmic transient: Gamma-Ray Bursts. The first GRB was detected on July 2, 1967 by Vela 3 and 4 satellites as a bright flash of gamma-rays, as shown in Fig. 1.1. Despite the limited localization capabilities of the Vela constellation, which exploited the time delays between the detection of bursts in different satellites and Earth blocking, the origin was suspected to be cosmic. It was clear early on that these events did not meet the expectations of nuclear tests, in terms of duration, spectrum and variability. The announcement of this and other 15 events to the scientific community was made only in 1973 by R. W. Klebesadel (Klebesadel, Strong, and Olson, 1973), due to complicated data analysis process and to the need of more data to confirm the cosmic origin of such events. Such flares were completely unexpected and immediately triggered the astronomical community.

In the first 20 years from the announcement, despite hundreds of theoretical models and several satellites tried to investigate it, the nature of GRBs remained a complete mystery. These sources were detected only at γ-ray energies and for a few tens of seconds. Moreover, the lack of information about distances and the small number of known objects prevented the estimate of the energetic involved in these events and their spatial distribution, leading to a debate on their galactic or extragalactic origin.

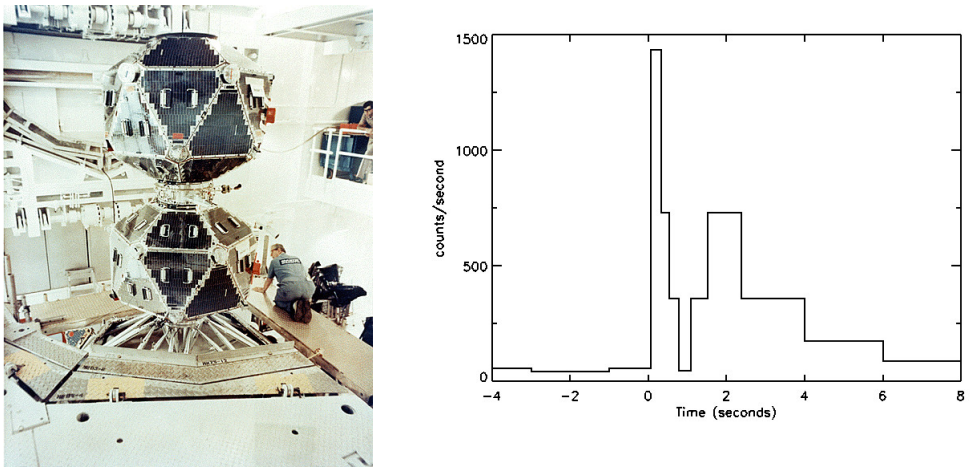

FIGURE 1.1: Left: two of the Vela Satellites series (Vela–5A/B), which discovered the first GRB, in the Clean Room. Right: lightcurve of the first ever observed GRB, on July 2, 1967. From: https://heasarc.gsfc.nasa.gov/docs/vela5b/vela5b_images.html.

A significant step forward on the study of the nature of GRBs was done by the Compton Gamma-Ray Observatory (CGRO), launched in 1991, with its instruments Burst And TranSient Experiment (BATSE) and Energetic Gamma-Ray Experiment Telescope (EGRET). These instruments allowed the collection of over 2700 GRBs with a broad band coverage of the γ–ray emission (i.e. spectra from 10 keV to few GeV), and they showed that these events are isotropically distributed across the sky (see Fig. 1.2) and their cumulative fluence distribution deviates from the power–law slope of $-3/2$ expected for a uniformly distributed population of sources. These observational evidences gave a significant support to the extragalactic origin interpretation of GRBs.

If GRBs were extragalactic, the rapid variability and the huge energy involved would imply the presence of a slowly fading emission (called afterglow, see Section 1.3) at longer wavelengths (from X-ray down to the radio band), following the main γ–ray event (Paczynski and Rhoads, 1993). However, no follow-up detections at other wavelenghts were reported at that time, since the error-boxes on the GRBs' positions provided by BATSE contained a large number of possible counterparts.

The search for such emission did not produce results until 1997, thanks to the Italian-Dutch satellite BeppoSAX, launched in 1996. This satellite was able to produce small error boxes of GRBs' positions in the sky (of the order of arcmin) that were immediately communicated to the scientific community by the Gamma-ray Coordinates Network (GCN). This strategy led to the discovery of the first X-ray afterglow following the burst GRB 970228. Soon later the afterglow of another event, GRB 970508, was observed and led to the first redshift measurement (Reichart, 1998) of a GRB: $z = 0.835$. This discovery showed, for the first time, that GRBs are extragalactic and are among the most powerful sources of electromagnetic radiation known in the Universe.

In the nearly half a century since the announcement of their discovery, the interest in GRBs had continuously grown. Over the years, several X–ray and γ–ray satellites have been launched to study the striking features of these cosmic sources, such as KONUS/WIND in 1994, the High Energy Transient Explorer (HETE-2) in 2000, the INTErnational Gamma-Ray Astrophysics Laboratory (INTEGRAL) in 2002, the Neil Gehrels Swift Observatory (Swift) in 2004 and the Astro-Rivelatore Gamma a Immagini Leggero (AGILE) in 2007. The last satellite, launched in 2008, was the Fermi Gamma-ray Space Telescope (see Section 2.4), on whose data is based most of the results presented

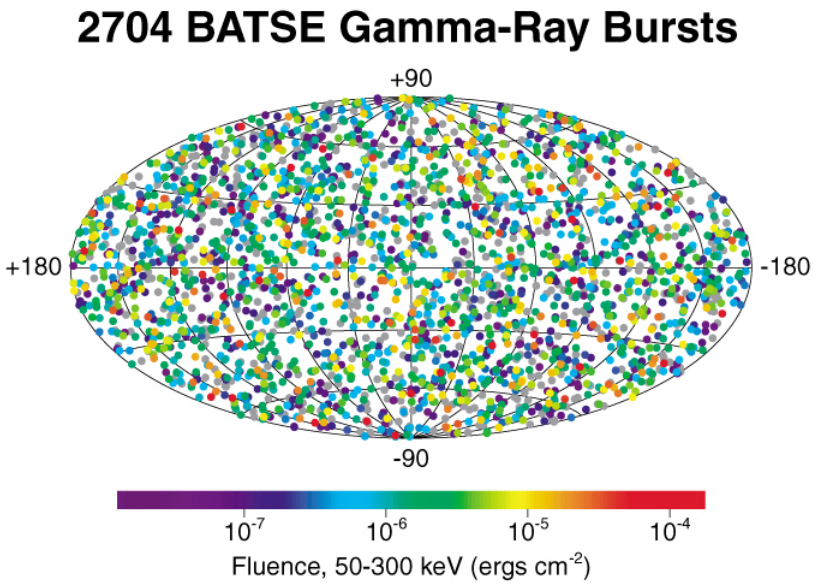

FIGURE 1.2: Distribution on the sky of 2704 GRBs detected by BATSE in 9 years, color coded by the measured fluence (i.e. flux integrated over the individual event duration) of the burst. The bursts are distributed isotropically and this is true for all different fluence levels. Image obtained from https://heasarc.gsfc.nasa.gov/docs/cgro/batse/

in this thesis. At present days GRBs are also routinely followed-up with telescopes on the ground, and they are one of very few classes of sources to be identified from the low-frequency radio band up to the very high energy γ-rays, as recently demonstrated by the $\sim$TeV detections of MAGIC and H.E.S.S. telescopes (MAGIC Collaboration et al., 2019b; de Naurois and H. E. S. S. Collaboration, 2019; HESS collaboration, Abdalla, et al., 2021). The extreme luminosity of GRBs allows us to detect them at high redshift, up to z$\sim$9 (Cucchiara et al., 2011). Acting as the farthest cosmic lighthouse currently known, they illuminate the close–by host environment and the intergalactic medium providing us with a mean to study the chemical evolution of the Universe and the population of first stars. Finally, GRBs became also subject of study as counterpart of gravitational wave signals and neutrinos, establishing their key role in the multi-messenger astronomy (that combines information from electromagnetic, gravitational wave and potentially neutrino signals, see Section 1.6).

1.2 The prompt emission

To distinguish it from the afterglow emission, the initial, highly variable and brief gamma-ray emission, namely the GRB itself, is called *prompt emission*.

1.2.1 Temporal properties

The prompt emission light curves are known for their complexity and their lack of homogeneity. There is significant diversity from burst to burst, and few bursts look similar to others. Figure 1.3 shows some examples of the possible behaviors of the prompt emission light curves. They are usually characterized by a fast variability timescale, of the order of a few milliseconds (e.g. Golkhou and Butler 2014). The shape of a single pulse is typically asymmetric, with a sharp rising phase and a shallower decay, often modeled by

a "FRED" (fast-rise-exponential-decay) function. A fraction of GRBs ($\sim$ 10%) also shows precursors, i.e. emission pulses preceding the trigger, usually lower in flux and separated from the main event by a quiescent phase).

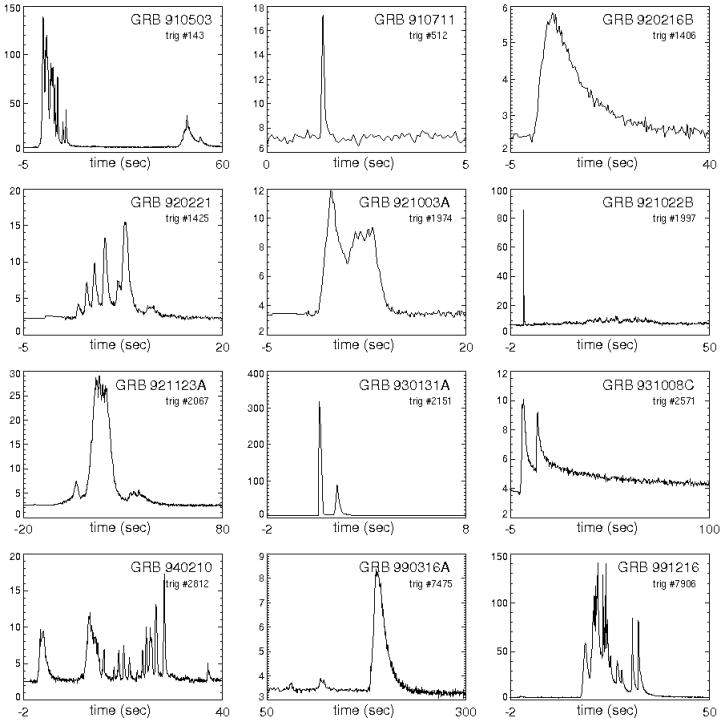

FIGURE 1.3: Light curves of 12 bright GRBs detected by BATSE, a NASA mission aboard the Compton Gamma-Ray Observatory. It is clearly shown the complexity and the complete lack of homogeneity associated with this phenomenon. From the public BATSE archive http://gammaray.msfc.nasa.gov/batse/grb/catalog/.

To measure the burst duration, it has been historically used the quantity T_{90}, which corresponds to the time interval in which the accumulated flux goes from 5% to 95% of the total measured flux with respect to the level of the background; that is, containing 90% of the total flux. Figure 1.4 shows the distribution of the T_{90} for all the bursts detected by BATSE. The distribution is clearly bimodal, showing one peak at 0.3 sec and the other at about 50 sec, with an overlap at approximately 2 sec. Based on this bimodal duration distribution, GRBs have been historically divided into two classes: bursts with duration less than 2 s are classified as *short* GRBs and those that last for more than 2 s are called *long* GRBs (Kouveliotou et al., 1993). This distinction is based on the observed durations, which depends on the sensitivity of the instrument, on the energy band and on the background model, and not on the intrinsic ones that are occurring in the rest frame of the central engine. However, the present increasing number of z measurements seems to confirm the bimodality of the duration distribution despite the exact threshold could be less sharp than typically adopted.

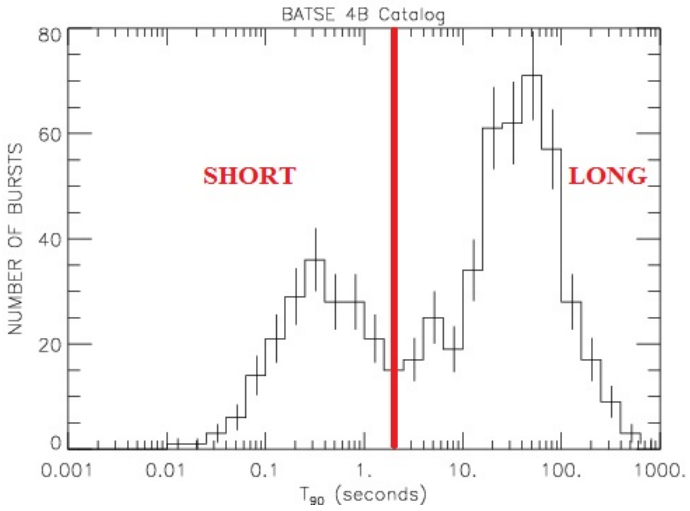

FIGURE 1.4: The distribution of T_{90} of all GRB in the BATSE 4B Catalog. From https://gammaray.nsstc.nasa.gov/batse/grb/duration/.

Even before any information about the distance or the physical origin of GRBs was known, the bimodal distribution of the duration suggested the existence of two physically distinct progenitors. A more detailed discussion on the progenitors of GRBs will be given in Section 1.5.

1.2.2 Spectral properties

The spectrum of the GRB prompt emission has a non-thermal shape and is typically characterized by two power-law segments smoothly connected at a break energy. When sufficient statistics is available, the typical prompt emission spectrum is usually fitted by an empirical function, known as the "Band" function (Band et al., 1993), made by two power–laws smoothly joined at one break energy. The photon number spectrum of the Band function is:

$$N(E) = A \begin{cases} \left(\frac{E}{100\,keV}\right)^{\alpha} exp[-\frac{E}{E_0}] & E < (\alpha-\beta)E_0 \\ \left(\frac{(\alpha-\beta)E_0}{100\,keV}\right)^{\alpha-\beta} exp(\beta-\alpha)\left(\frac{E}{100\,keV}\right)^{\beta} & E \geq (\alpha-\beta)E_0 \end{cases} \tag{1.1}$$

where $N(E)dE$ represents the photon flux (in units of photons cm^{-2} s^{-1} keV^{-1}) in the energy bin dE, A is the normalization factor at 100 keV (in units of photons cm^{-2} s^{-1} keV^{-1}), α is the low-energy power-law index, β is the high-energy power-law index, and E_0 is the break energy (in units of keV). The spectral energy distribution (SED) corresponds to E^2N(E) or νF_ν. In the νF_ν representation, the typical prompt emission spectrum is a peaked function. The energy where the νF_ν spectrum peaks is called $E_{\rm peak}$ and in the Band function defined in Eq. 1.2.2 is given by

$$E_{peak} = (2+\alpha)E_0 \ . \tag{1.2}$$

Figure 1.5 shows an example of the spectrum of GRB 990123, well fitted by the Band function (Briggs et al., 1999).

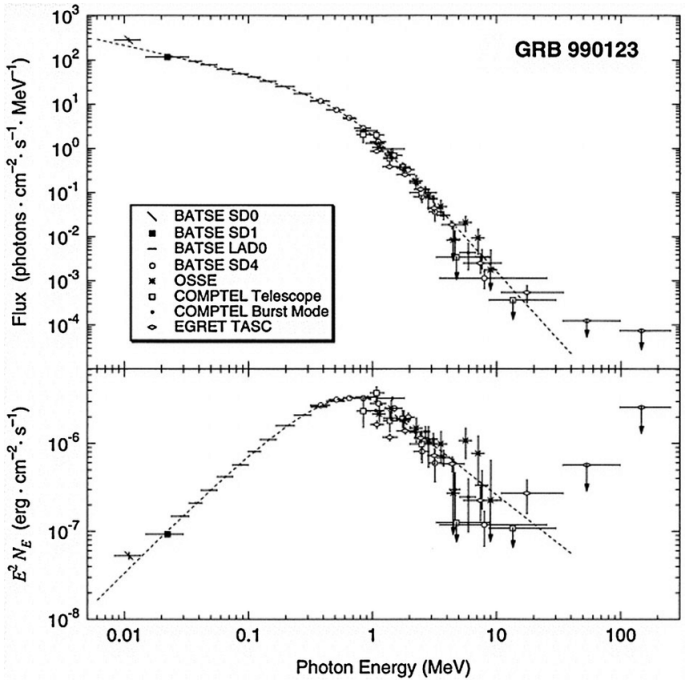

FIGURE 1.5: Typical time-integrated spectrum of the prompt emission of a GRB (in this case GRB 990123), fitted with the Band function defined in Eq.1.2.2. The spectrum is shown both in the photon flux N(E) (top panel) and in the νF_ν representation (bottom panel). Taken from Briggs et al. 1999

In those cases where the low statistics of the decaying spectrum coupled to the lower detector response at high energies prevents to properly constrain the high energy slope β, the spectrum is often well fit by a single power–law with an exponential cutoff, called CPL:

$$N(E) = A\left(\frac{E}{100\,keV}\right)^{\alpha} exp\left(-\frac{E}{E_0}\right) \tag{1.3}$$

Historically, GRB spectra have been fitted with empirical functions (i.e. Band or CPL) as representative of a large class of non-thermal models (however, in Chapter 2 these empirical functions will be changed and substituted by new ones). The approach, as will be further explained in the rest of the thesis, was to compare the empirical fit results with what expected from the theory of emission models. Several works found that the typical values of the peak energy is around a few hundreds of keV and the power-law slopes below and above the peak energy are characterized by the typical values of $\alpha \sim$ -1 and $\beta \sim$ -2.3 (e.g. Band et al. 1993; Ghirlanda, Celotti, and Ghisellini 2002; Kaneko et al. 2006; Nava et al. 2011a; Gruber et al. 2014). Theoretical arguments regarding the properties of the emission region (see Sec. 1.4.2 and Chap. 2) identifies the synchrotron process as the main radiative mechanism responsible for the γ–ray emission, but the above mentioned slopes of the observed spectra are inconsistent with the synchrotron predictions. A detailed description of the inconsistency between the observed GRBs prompt emission spectra and the predicted ones will be given in Chapter 2, as it is strongly connected to the work done in this thesis.

The typical flux of a prompt emission spectrum in the range 10 keV–40 MeV is distributed roughly in the range 10^{-7}–10^{-5} erg cm^{-2} s^{-1}. The typical energy fluence accumulated over the time interval of the prompt emission in the range 10 – 1000 keV is $\sim 10^{-5}$ erg cm^{-2} and its distribution extends from $\sim 10^{-7}$ up to $\sim 10^{-3}$ erg cm^{-2}, as

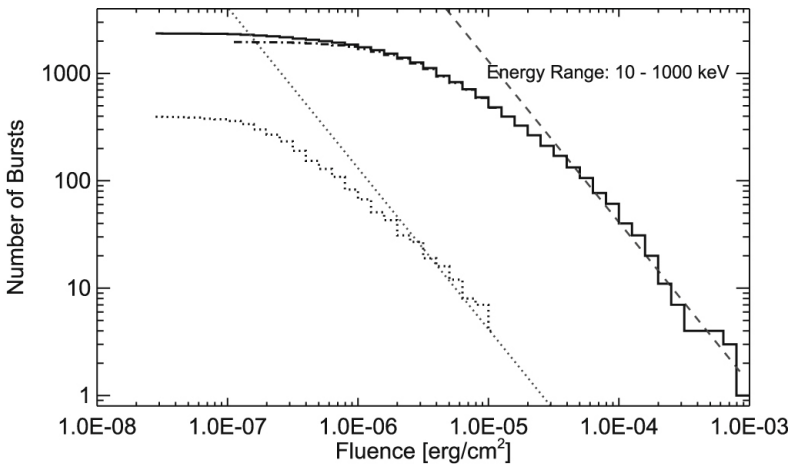

FIGURE 1.6: Cumulative distribution of fluence in the energy range 10 – 1000 keV for the 2356 GRB in the fourth Fermi/GBM Catalog. Distributions are shown for the total sample (solid histogram), short GRBs (dots), and long GRBs (dash–dots). A power law with a slope of -3/2 (dashed line) is drawn for reference. Taken from von Kienlin et al. 2020.

shown in Figure 1.6 (Gruber et al., 2014; von Kienlin et al., 2020). The implied distribution of isotropic equivalent energies $E_{\rm iso}$ of the prompt emission, which depends on the estimates of the redshift of the GRB, ranges between $\sim 10^{48}$ and a few times 10^{54} erg.

1.3 The afterglow emission

From the observational point of view, the afterglow is a slowly fading emission that usually begins after the prompt emission, and lasts from hours to months. Since its discovery in 1997 by the BeppoSAX satellite (Costa et al., 1997), the afterglow emission phase has been studied in details thanks to the follow-up observations of many GRBs with several telescopes on ground and in space. It is visible across all the electromagnetic spectrum, with its characteristic frequencies slowly rolling from X-ray, through Optical, down to Radio.

1.3.1 Temporal properties

Before the launch of the *Swift* satellite, the observations of the afterglow emission were made mainly in the optical range. The typical optical light curves, usually obtained at late times, showed a decaying power-law trend of the flux with time, as $F_\nu \propto t^{-\alpha}$ (with $\alpha \sim 1$). With respect to the prompt emission, the afterglow emission turns out to be characterized by a lower variability.

However, the observations performed by the X–Ray Telescope (XRT) on board of the *Swift* satellite ushered in a new era in this field, changing the common understanding of the GRB afterglow phase (Gehrels, Ramirez-Ruiz, and Fox, 2009). Thanks to the fast slewing of the satellite, the XRT instrument is able to point toward the GRB within ∼60 seconds from the trigger, refining the position of the GRB down to few arcsec scales and following its afterglow evolution up to late times (of the order of $\sim$ ks). This allowed to observe many GRBs X-ray counterparts in the 0.3-10 keV energy range and to unveil the complex behaviour of their light curves, revealing that it deviates from the simple power–law decaying trend previously observed (see e.g. Kann et al. 2010). The newly discovered features in the X-ray light curves are summarized in Figure 1.7 (Zhang et al., 2006). At

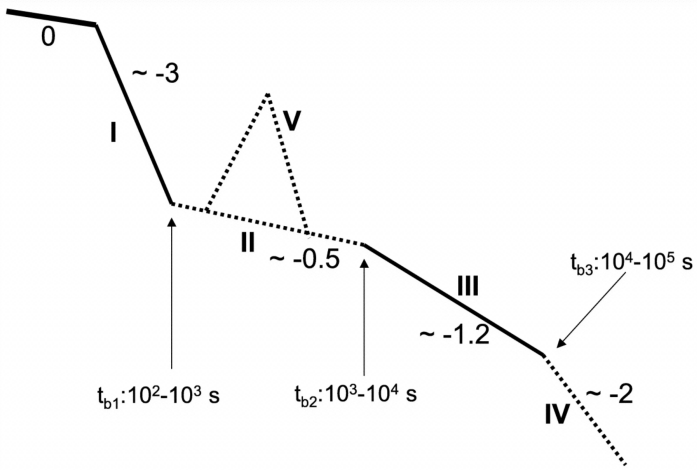

FIGURE 1.7: A sketch of the canonical X–ray afterglow light curve, which shows 5 distinct components, based on the observational data from *Swift*/XRT. Taken from Zhang et al. 2006

early times, the lightcurves observed by XRT show a steep decay, with a temporal index steeper than -2, that is often supposed to be related to the tail of prompt emission. Some X–ray afterglows also show a shallow plateau phase, where the temporal decay index is -0.5 or larger: over the plateau it is possible to observe superimposed features, like flares, whose origin is still debated. In most GRBs the early phase is then followed by the normal decay phase, with typical index $\sim$-1, namely the usual segment that was already observed in the optical bands. If the afterglow is sufficiently bright to be detected after a few days, it can show an achromatic steepening of the temporal decay index, which becomes $\sim$-2. This change in the flux decay at late time is called *jet break*, and, as it will be explained later in Sec. 1.4, it provides one of the most compelling evidence of the presence of a jet in GRBs.

1.3.2 Spectral properties

GRB afterglows have been followed-up in a very wide range of frequencies, from GeV energies down to the radio band. From simultaneous observations it has been possible to build and study several broadband afterglow SEDs, which feature one single emission component with a non-thermal shape. The afterglow SEDs reveal the presence of multiple power–law segments connected by spectral breaks, that evolves with time towards lower frequencies. The radiative process responsible for the afterglow emission is thought to be synchrotron. Indeed, synchrotron radiation typically provides a good fit to most of the multi-wavelength afterglow data for GRBs. As an example, in Fig. 1.8 are reported the observations and the synchrotron modeling of the afterglow spectra of GRB 130427A (the brightest burst ever observed by Fermi) spanning 18 orders of magnitude in frequency and 4 orders of magnitude in time (Perley et al., 2014).

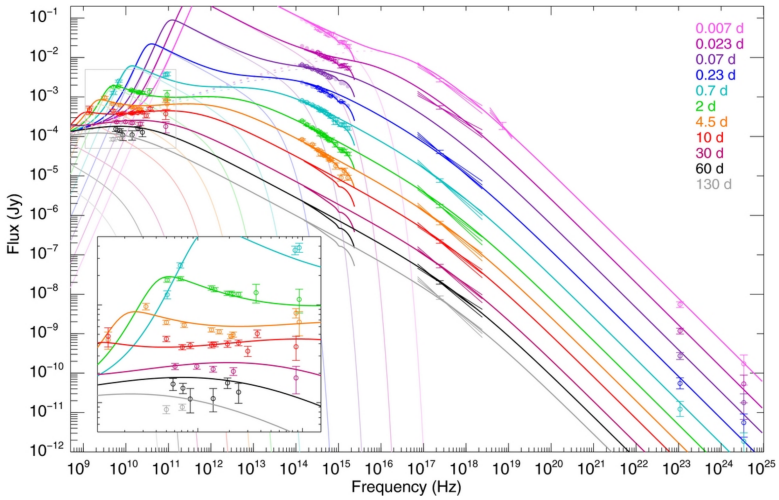

FIGURE 1.8: Example of a broadband GRB afterglow spectrum. The example refers to the observations of the afterglow of GRB 130427A spanning from the low-frequency radio to the 100 GeV LAT bands. Different colors corresponds to different observational epochs. The solid lines represent the prediction of the standard synchrotron afterglow theory (see Sec. 1.4), which provides an excellent description of the entire data set, a span of 18 orders of magnitude in frequency and 4 orders of magnitude in time. The inset at lower left shows a magnified version of the radio part of the SED for times t > 0.7 days. Taken from Perley et al. 2014.

Recently, a new window on the GRB afterglow spectrum has been opened. After decades of searches, a high significance detection of Very High Energy (VHE) emission has been finally reported by the Major Atmospheric Gamma Imaging Cherenkov Telescopes (MAGIC) for GRB 190114C (MAGIC Collaboration et al., 2019b). This first detection was welcomed with enthusiasm by the astrophysical community, as TeV photons from GRBs are expected to provide crucial new information on the physical mechanisms of energy dissipation, particle acceleration and radiation in these powerful objects. The detections of ∼TeV emission from GRBs are hampered by several factors, among which the Extragalactic Background Light (EBL) attenuation, which significantly reduce the detectable VHE emission for the typical distances involved in GRBs (e.g., the attenuation factor at 1 TeV being ∼250 for GRB 190114C located at z=0.42).

This observation revealed a new emission component in the afterglow of the GRB, as shown in Figure 1.9. In particular, coupled with an intensive multi-wavelength campaign, this VHE observation has suggested that the Synchrotron Self-Compton (SSC) mechanism is the main candidate for the ∼TeV emission (MAGIC Collaboration et al., 2019a), with a similar amount of energy released in the synchrotron and inverse Compton components.

After the first high–significance detection, other GRBs have been detected at VHE and to date, a total of 5 GRBs have been reported to have TeV emission: GRB 190114C, GRB 180720B, GRB 190829A, GRB 201015A, GRB 201216C (Abdalla et al., 2019; HESS collaboration, Abdalla, et al., 2021; Blanch et al., 2020a; Blanch et al., 2020c). All of them are related to the afterglow phase and all originate from long bursts. During my PhD, I have studied three of these five GRBs (GRB 190114C, GRB 180720B, GRB 190829A), analyzing their keV-MeV emission, and in this thesis I report the results of these studies in Chapter 6.

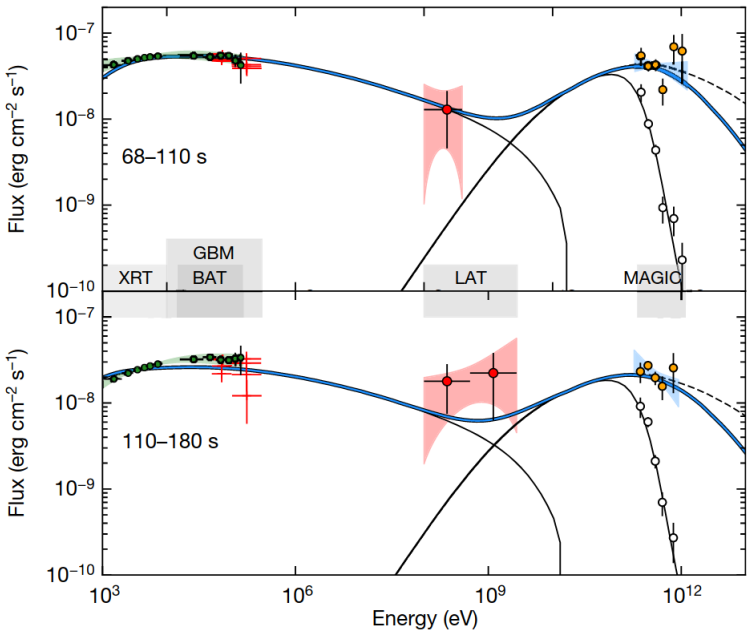

FIGURE 1.9: The first ever high-significance detection of VHE photons from the afterglow of a GRB, detected by the MAGIC Telescope, following the prompt emission of GRB 190114C. In particular, it is clearly shown the presence of the second peaked component, revealed by the VHE data, and corresponding to the SSC component. The thick blue curve represents the modelling of the broadband spectra in two time intervals (68–110 s and 110–180 s) with the synchrotron and SSC components, respectively represented by the thin solid lines, over 9 orders of magnitude. Empty circles show the observed MAGIC spectrum, uncorrected for the attenuation caused by the EBL. For further details, see MAGIC Collaboration et al. 2019a.

1.4 The general picture

Over the years, the growing number of multi-wavelength observations of GRBs have shaped the development of a basic *standard model* aimed at describing the whole GRB phenomenon. The most accepted scenario is the so-called *fireball model*, that assumes:

i) the presence of a compact object (typically a black hole or a millisecond magnetar) and an accretion disk, which together constitute the *central engine*, accreting the infalling matter and launching two relativistic jets, i.e. fireballs made of pairs, photons and some baryons;

ii) an *internal relativistic shock* between two or more fireballs, launched at different velocities by the central engine, that converts the kinetic energy of the outflow into thermal energy of the particles and produces the short–duration prompt emission observed in γ–rays;

iii) an *external relativistic shock*, due to the deceleration of the fireball that interacts with the circum–burst medium surrounding the progenitor, giving rise to the long–lasting afterglow emission, visible at longer wavelength (X–ray, optical and radio).

An artistic representation useful to understand the commonly accepted GRB standard model is shown in Figure 1.10. In the following, I describe more in details the theoretical arguments behind the GRB standard model and the mechanism producing the GRB phenomenon.

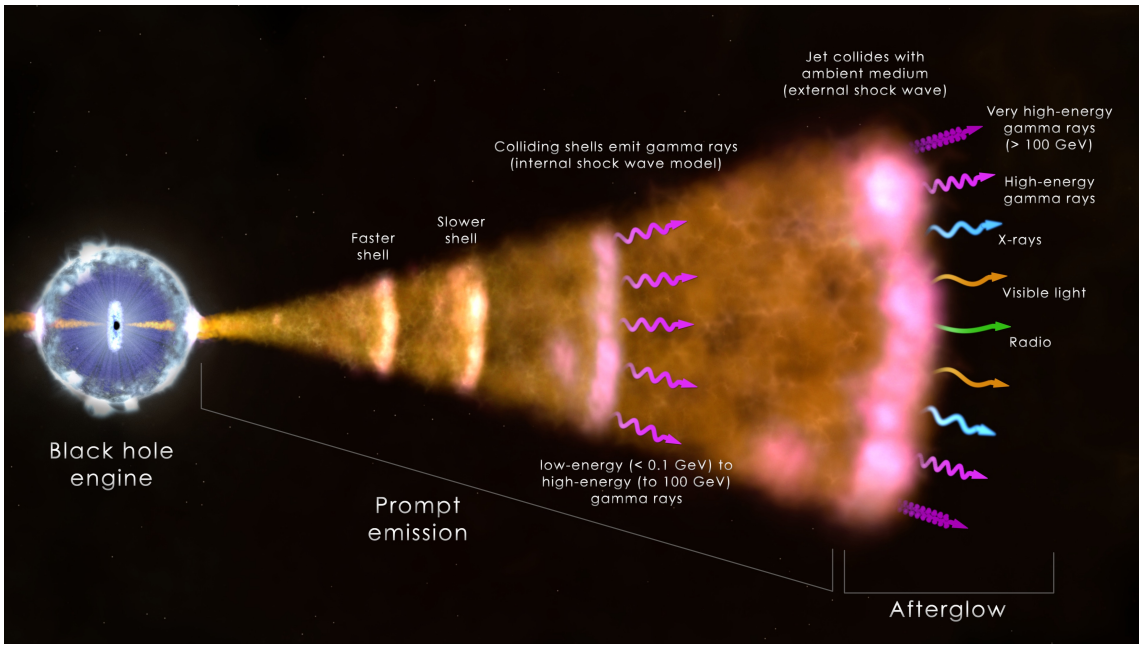

FIGURE 1.10: This artistic impression shows the representative scenario of the formation of the different emission components of a GRB. Credit: NASA/Goddard Space Flight Center/ICRAR

1.4.1 Compactness argument

The 'compactness problem' provided one of the first theoretical arguments supporting the relativistic nature of GRBs (Ruderman, 1975; Schmidt, 1978; Piran, 1995). This argument was used to solve an apparent paradox which I briefly summarize in the following.

Given the short variability timescale $t_{\rm var}$ of a few tens of milliseconds observed in the prompt emission (Bhat et al., 1992; Walker, Schaefer, and Fenimore, 2000; MacLachlan et al., 2013; Golkhou and Butler, 2014), the size of the emission region is approximately $R \sim$

$ct_{\rm var} \sim 3 \times 10^8\,(t_{\rm var}/10\,{\rm ms})$ cm. For a typical long GRB, a fluence of $F \sim 10^{-6}$ erg cm^{-2} and a redshift $z \sim 2$ imply an isotropic energy released in γ–rays $E_{\rm iso} = 4\pi d_L^2 F/(1+z) \sim 10^{52}$ erg (where d_L^2 is the luminosity distance of the burst). Such an extreme energy confined in a relatively small volume makes the emitting region opaque for the pair–production process ($\gamma\gamma \rightarrow e^+e^-$). Indeed, the observed spectrum (see Fig. 1.5) has a large fraction $f_{\rm th}$ of high–energy γ–ray photons above the pair–production threshold $2m_ec^2$. The optical depth for pair–production can be written as:

$$\tau_{\gamma\gamma} \sim f_{\rm th}\sigma_T 4\pi d_L^2 F/R^2 m_e c^2 \ . \tag{1.4}$$

For typical GRBs parameters, the resulting optical depth is very large, $\tau_{\gamma\gamma} \sim 10^{15}$ (Piran, 1995). This optical depth should prevent us from observing the typical non-thermal spectrum of the prompt emission.

The compactness problem can be solved if we consider the emitting matter as moving relativistically towards the observer. In fact, if we consider the relativistic effects and assume a relativistic bulk motion with a Lorentz factor Γ, the comoving–frame energy of the photons is lowered by a factor Γ, modifying the fraction $f_{\rm th}$ by a factor $\Gamma^{-2\beta}$, where β is the photon index of the observed spectrum. In addition, the timescale of the emission is longer by the same factor Γ, implying a larger emitting radius ($R \sim ct_{\rm var}\Gamma^2$) and therefore a smaller photon density. These combined relativistic effects help to lower the value of the optical depth, that becomes a function of Γ, namely $\tau_{\gamma\gamma} \propto \Gamma^{-2-2\beta}$. For the same typical GRB parameters used before, an optical depth of order unity is found for $\Gamma \gtrsim 100$. Therefore, the requirement that the emission region must be optically thin to the highest-energy observed photons implies that the GRB ejecta are relativistic.

So far, such compactness argument has been used in the literature to estimate Γ in a few GRBs (Lithwick and Sari, 2001; Vianello et al., 2018; Tang et al., 2015; Fermi Large Area Telescope Team et al., 2012), assuming an on-axis viewing angle. Recently, the theoretical computation of the optical depth for pair–production has been also extended to include the cases of off-axis GRBs (Matsumoto, Nakar, and Piran, 2019a; Matsumoto, Nakar, and Piran, 2019b).

I applied the compactness argument in this thesis to derive an estimate of the bulk Lorentz factor of GRBs which showed an exponential cutoff in their high–energy spectrum (see Chapter 4 and Section 5.2) and I have used the off-axis extension of this argument in the case of GRB 190829A to derive a limit on the viewing angle (see Section 6.3).

1.4.2 The prompt phase

According to the standard model, the most accepted picture for the prompt emission is the *internal shock* scenario (Rees and Meszaros, 1992). Discontinuous energy injection at the base of the jet (in the polar region of the compact object) produces what can be schematically thought of as *fireballs* of baryons and high energy photons. The extremely large internal pressure drives an accelerated expansion which converts the internal energy into kinetic energy of the expanding fireballs, which reach relativistic speeds (as required by the compactness argument explained above). During this relativistic accelerated expansion phase, $\Gamma \propto R$, where Γ is the Lorentz factor and R is the distance of the fireball from the black hole (Shemi and Piran, 1990; Piran, Shemi, and Narayan, 1993).

To provide a relativistic motion of the fireball ($\Gamma \sim 100$), the baryon load should be small, but present. Indeed, in the absence of baryons, a fireball of pure pairs would stop accelerating at a relatively small distance from the central engine and would reach a relatively small bulk velocity, which is inconsistent with the larger values derived from the

observations. Moreover, a pure radiation fireball would produce a black-body (BB) spectrum that is inconsistent with the non-thermal spectrum observed in the prompt emission phase. Instead, the presence of even a small amount of baryons (approximately $\sim 10^{-6}$ solar masses) makes the fireball opaque to Thomson scattering and pair–production: the photons remain trapped in the fireball and they continue to accelerate it until most of their initial energy has been converted into bulk motion.

After the acceleration phase, the fireball continues its relativistic motion with a constant Γ, entering the so-called coasting phase. As the fireball expands, the photon energy and number density drop, until it becomes transparent at the photospheric radius ($R_{\rm ph} \sim 10^{12-13}$ cm for typical parameters) and photons are able to escape: a thermal flash is the first electromagnetic emission that a single fireball can produce (Daigne and Mochkovitch, 2002).

In this phase, the dissipation of the fireball kinetic energy occurs through the development of the so-called *internal shocks*. If the central engine is not completely impulsive but works intermittently, it can produce many fireballs with slightly different Lorentz factors. The internal shocks develop when a fireball that travels slightly faster catches up the slower one preceding it. These shocks accelerate the charged particles and amplify the magnetic field, giving rise to the highly variable observed prompt emission. The observed light curve is thought to be the superposition of several shocks, which in the more realistic case can be the results of even more than a two–body encounter as schematically described above. The main difficulty of the internal shocks model is a rather low efficiency for the conversion of the kinetic energy into γ–rays, a few per cent only (Mochkovitch, Maitia, and Marques, 1995; Kobayashi, Piran, and Sari, 1997; Daigne and Mochkovitch, 1998), unless assuming extreme differences in the relative speed of the colliding fireballs. Most of the kinetic energy is then stored into the merged fireballs and will be eventually dissipated during the afterglow phase.

Another mechanism proposed for the internal dissipation of the jet energy is the magnetic reconnection (Thompson, 1994; Spruit, Daigne, and Drenkhahn, 2001; Drenkhahn and Spruit, 2002; Lyutikov and Blandford, 2003). In this case, the outflow dominated by the magnetic energy, in contrast to the hot matter–dominated outflow (fireball) scenario explained above. In both cases, a fraction of the internal energy of the outflow is given to accelerate electrons which, due to the presence of intense magnetic fields, are expected to emit through synchrotron and/or inverse–Compton process.

The identification of the radiative process shaping the prompt emission spectrum is crucial, because it allows to understand the nature of the outflow content and the dissipation processes. The detailed characterization of the prompt emission spectral properties over a wide energy range is the main goal of this thesis. A more detailed discussion on the prompt emission spectral characterization and the theoretical implications on the GRBs physics will be provided in Chapter 2.

1.4.3 The afterglow phase

After producing the prompt emission, the fireball still has a large part of the initial kinetic energy. The fireball proceeds with a constant Γ until it meets the interstellar medium (ISM) surrounding the GRB progenitor (see Fig. 1.10), so it starts to incorporate matter and begins to decelerate. As soon as the rest mass of the collected ISM becomes comparable to the kinetic energy of the ejecta, two shocks naturally develop and propagate in two directions: a forward shock, that sweeps up the surrounding medium, and a reverse shock, that propagates into the GRB ejecta (Mészáros and Rees, 1997; Sari and Piran, 1999; Kobayashi, 2000; Gao and Mészáros, 2015). While the forward shock gives rise

to the long–lasting broadband afterglow emission, the reverse shock can give rise to a short–term optical/IR flash and a radio flare. In both cases, at the shock the particles are accelerated by the Fermi process and are thought to radiate through synchrotron emission. Indeed, synchrotron radiation from the external shock provides a good fit to the multi-wavelength afterglow data for GRBs (e.g. Panaitescu and Kumar, 2002, see also Fig. 1.8). As long as the expansion is ultra–relativistic, the dynamics of the decelerating ejecta can be described by the self-similar spherical expansion given by Blandford and McKee 1976. When the ejecta becomes mildly relativistic (Lorentz factor $\Gamma \sim 3$) a slow transition to the Newtonian regime takes place, after which the system resembles a supernova remnant.

As the GRB ejecta is decelerated and the strength of the relativistic beaming diminishes, the edge of the jet becomes visible to the observer. In particular, when the inverse of the bulk Lorentz factor becomes comparable to the jet half-opening angle ($\Gamma^{-1} \sim \theta_{\rm jet}$), the afterglow light curves show an achromatic steepening of their decay, that is usually referred to as the *jet break*. This behaviour was predicted by Rhoads (1997) and it was indeed observed in the optical and radio light curves of several GRBs afterglows in the following years (e.g. Harrison et al. 1999; Price et al. 2001; Burrows et al. 2006; Cenko et al. 2010; Troja et al. 2016), leading to an average estimate of the jet half-opening angle $\theta_{\rm jet} \sim 2$–10°. The detection of a jet break is one of the most compelling evidences in favour of the presence of a collimated outflow in GRBs. If the ejecta are collimated, though, it is possible to derive the actual collimation-corrected kinetic energy released in these explosions (lowered by a factor $\sim \theta_{\rm jet}^2$), that is between 10^{48} and 10^{52} erg/s. The modeling of GRB afterglows indicates that the energy radiated in the prompt emission is only a fraction ($\sim 10 - 20\%$) of the total kinetic energy of the jet (Fan and Piran, 2006; Zhang et al., 2007; Wygoda et al., 2016; Beniamini, Nava, and Piran, 2016).

1.5 Progenitors

Before knowing anything about the possible association of GRBs to other cosmic sources, the bimodal distribution of the GRBs duration (see Fig. 1.4) already pointed towards the presence of two different progenitors. Moreover, a distinctive feature of GRBs is that they do not repeat, they are one-off events. This indicates that the system creating them could be destroyed, as also supported by the fact that a huge amount of energy (i.e. comparable to that observed in the prompt phase of up to 10^{54} erg) is released on a timescale of tens of seconds or less. The millisecond timescale variability of the prompt emission suggests, from causality arguments, that the emission should come from a small scale region with typical extension of few 10^7-10^8 cm. This supported the hypothesis that the progenitor of GRBs could be compact objects, either neutron stars (NS) or black holes (BH), which are also the favorite sites for the extraction of a huge amount of energy. These features led to the hypothesis that these powerful emissions of γ-rays are generated by the accretion of matter on a BH of stellar mass.

The association with a catastrophic event makes more difficult to identify the progenitor, since when we detect a GRB the progenitor is already disrupted. However, in some cases the follow-up observations of GRBs afterglows allowed to identify some of the features of the destroyed progenitor. These observations, coupled with the theoretical arguments described above, led to the commonly accepted scenario that associates long GRBs to the death of massive stars and short GRBs to the mergers of two compact objects in a binary system (see Fig. 1.11). Both cases naturally leads to the formation of a stellar BH surrounded by an accretion disk. This picture seems to be consistent also with the properties of the host galaxies of long and short GRBs. Long events tend to populate star

forming galaxies while short GRBs have been found in different hosts (from ellipticals to irregular, Berger 2014).

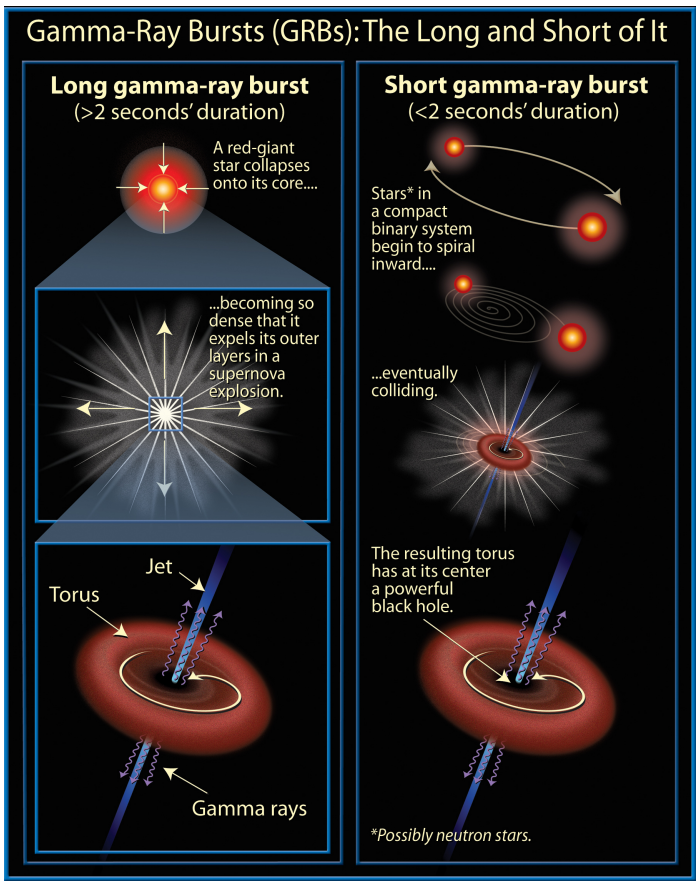

FIGURE 1.11: Schematic representation of the two favoured progenitor scenarios for the formation of long GRBs (left) and short GRBs (right). Credit: NASA and A. Feild. From: https://hubblesite.org/contents/media/images/2006/20/1916-Image.html

1.5.1 Long GRBs

The scenario of the collapse of the core of a massive star, later known as the *collapsar scenario*, has been suggested by Woosley (1993), who identified the Wolf–Rayet stars with masses greater than 10–15 solar masses as the promising GRB progenitor candidates. The first confirmation of this hypothesis came in 1998 with the direct association of the long close-by GRB 980425 with the supernova SN1998bw (Galama et al., 1998). Fig. 1.12 shows on the left an image of the host galaxy of GRB 980425 where the supernova event is evident as a bright spot, which is not present in the pre-discovery image shown on the right. In the following years, several other cases of observation of a supernova explosion following the emission of a GRB ($\sim$ 2-3 weeks after the GRB prompt emission) were made. The observational signature of a supernova in the associated GRB afterglow is a late-time bump in the optical lightcurve, as shown in Fig. 1.13, and broad line features in the optical spectra. Moreover, resolved host galaxies of long GRBs are typically irregular and star forming galaxies and the GRB is preferentially located in their brightest spots, i.e. in highly star forming regions where the massive stars are born (Fruchter et al., 2006).

The supernovae observations and the connection to the host galaxy active regions both confirm the hypothesis that long GRBs are a possible outcome of the collapses of

massive stars (Cano et al., 2017; D'Elia et al., 2015; Berger et al., 2011; Sparre et al., 2011; Sollerman et al., 2006; Mazzali et al., 2003; Kulkarni et al., 1998).

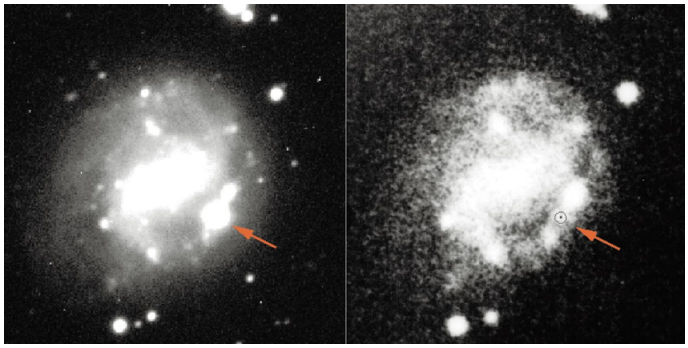

FIGURE 1.12: Two images showing the discovery of the supernova SN 1998bw, which followed the long GRB 980425. For comparison, beside the image of the discovery taken by the ESO's New Technology Telescope (NTT) on May 1 1998 (left), it is shown also the image taken with the UK Schmidt Telescope in 1976 (right). From Galama et al. 1998.

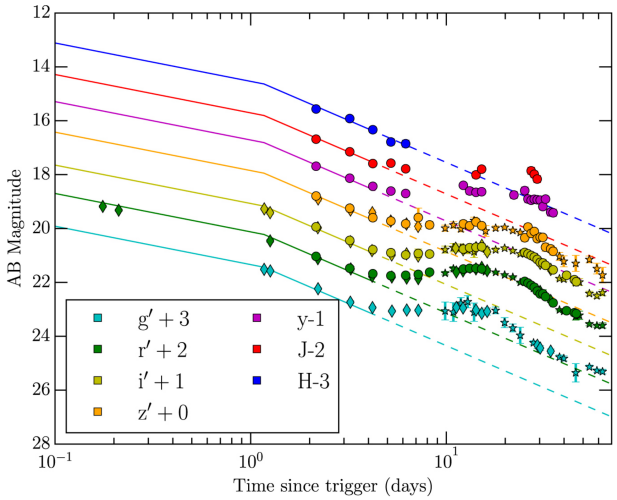

FIGURE 1.13: Example of the typical signature of supernova emission in the GRB optical lightcurve. In particular, data shows optical and NIR light curves of GRB 130702A, solid lines indicate power–law fits to the GRB afterglow lightcurve, while dashed lines mark the extrapolated power–law behaviour, over which the supernova bump is clearly visible. Taken from Toy et al. 2016.

1.5.2 Short GRBs

Regarding short GRBs, the catastrophic merger of two compact objects in binary systems, either made of two neutron stars (NS–NS) or of a neutron star and a black hole (NS–BH), has been considered a possible channel through which a short GRB is produced (Eichler et al., 1989). This hypothesis is supported by the fact that short GRB are typically found in host galaxies with relatively low star formation rate and the GRB position has a large offset from the host galaxy (Fong, Berger, and Fox, 2010). This is consistent with a population of NS–NS binaries, which end up merging due to the loss of rotational energy of the system through the emission of gravitational waves (GW).

The connection between the short GRBs and the merger of two compact objects has been recently probed with the detection of the short GRB 170817A almost 2 seconds after

the source of gravitational waves GW 170817, detected by the LIGO and VIRGO interferometers on the 17th of August 2017 (Abbott et al., 2017). The time-frequency map of GW 170817 together with the lightcurve of GRB 170817A are shown in Figure 1.14.

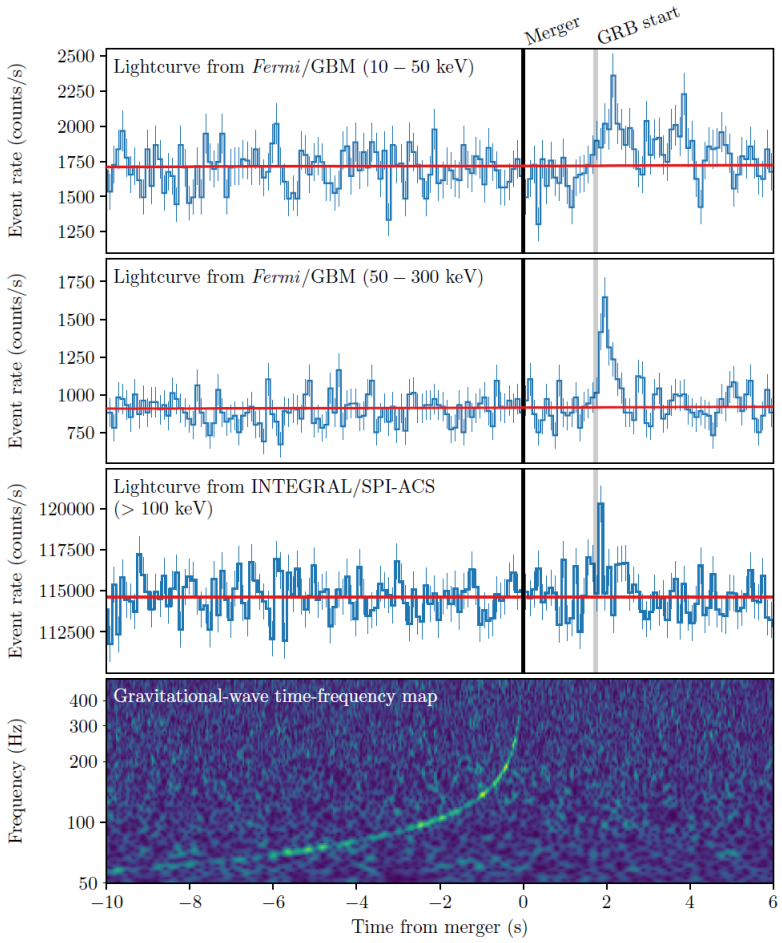

FIGURE 1.14: The joint detection of GW170817 and GRB 170817A. In the first and second panel is shown the Fermi/GBM lightcurve for GRB 170817A in the 10 – 50 keV and in the 50 – 300 keV energy ranges. In the third panel is shown the INTEGRAL SPI-ACS lightcurve at energies greater than 100 keV. The fourth panel displays the time-frequency map of GW170817, obtained by coherently combining LIGO-Hanford and LIGO-Livingston data. From https://www.ligo.org/science/Publication-GW170817GRB/

A few hours later, ground–based telescopes identified the host galaxy of the GW source, NGC 4993, by detecting the optical and Near-Infrared (NIR) counterpart, (e.g., Coulter et al. 2017; Pian et al. 2017; Drout et al. 2017; Shappee et al. 2017; Chornock et al. 2017). Few days later the source was observed also in the X–ray and radio bands, and the observations continued for years after the GW event (Troja et al., 2017; Haggard et al., 2017; Alexander et al., 2017b; Alexander et al., 2018; D'Avanzo et al., 2018; Mooley et al., 2018; Ghirlanda et al., 2019; Hajela et al., 2019; Troja et al., 2020).

The study of this unique event has provided us an unprecedented insight into the physics of short GRBs and binary neutron star (BNS) mergers. In addition to the fact that BNS mergers can be progenitors of short GRBs, from this joint detection we also learned that (i) the merger launched relatively massive ($\sim 0.03\ M_{\odot}$) fast ($v \sim 0.2\ c$) ejecta responsible for the first-ever detection of a bright thermal *kilonova* emission, powered by the radioactive decay of heavy elements (Pian et al., 2017; Smartt et al., 2017) and (ii) a

relativistic jet emerged from the BNS ejecta, it has a structure (i.e. angular dependence of energy and bulk velocity) and was oriented $\sim$20 $^\circ$ from the line of sight (Mooley et al., 2018; Ghirlanda et al., 2019). In fact, thanks to this off-axis orientation, it was possible to observe, for the first time in the GRB field, the evidence of superluminal motion of the ejecta, which is a clear signature of the presence of a relativistic jet.

1.6 Multi-messenger astronomy

The GW/GRB 170817 event, observed both through gravitational waves and with electromagnetic radiation, opened a new era for the multi–messenger astronomy, in which GRBs play a major role. Indeed, their extreme progenitor systems are the most natural sites for the production of other astrophysical messengers, which include gravitational waves, ultra high energy cosmic rays (UHECRs) and neutrinos.

1.6.1 Gravitational-waves

The detection of a GW signal associated to a GRB can help in investigating and potentially answering to many open questions on the physical processes involved in a compact binary merger and in the physics of GRBs. For example, it is a fundamental diagnostic for the identification of the GRB progenitor. In fact, different progenitors are expected to have distinct gravitational waves signatures (Bartos, Brady, and Márka, 2013; Flanagan and Hughes, 1998). In particular, compact star mergers have a characteristic *in-spiral chirp* signal, that would give definitive identification of the short GRB progenitor. The analysis of the GW signal could also reveal the different natures of the post merger product: a black hole engine would show a *ring-down* signal after the merger phase while a supramassive neutron star would give extended gravitational wave signals. Also long GRBs can have strong gravitational wave counterparts, which are of great interest for the astrophysical community as they represent a unique opportunity to probe the collapse dynamic, otherwise inaccessible to electromagnetic observations. However, the GW signal due to a massive star core collapse is subject to large uncertainties as it strongly depends on the rather unknown SN explosion mechanisms (Bethe, 1990; Logue et al., 2012; Powell et al., 2016; Andersson et al., 2013). Nevertheless, the next joint detections of a GW signal and GRBs can be very useful to investigate the physics of the progenitors of GRBs, either long or short.

The GW170817 event was only at 40 Mpc and this is the only joint GW-GRB detection so far. The upcoming observing run O4 (expected to start in mid 2022) of the LIGO, Virgo and KAGRA network will be able to extend the accessible horizon potentially up to $\sim$200 Mpc for BNS mergers, providing triggers to search for their electromagnetic counterparts. Among the awaited breakthrough, there is the discovery of the electromagnetic counterpart of BH–NS merger, a system potentially able to launch a jet and produce a GRB (e.g. Paschalidis, Ruiz, and Shapiro 2015; Ruiz, Shapiro, and Tsokaros 2018). The next GW signal will allow to clarify how common is the formation of a successful relativistic jet and what are the main differences between the NS–NS and BH–NS mergers.

Moreover, the scientific potential reward from a joint detection GW/GRB can extend to results of broader physical interests. For example, gravitational wave detections can be used as 'standard siren', namely to set a redshift-independent estimate of the source distance, especially with third-generation detectors such as the Einstein Telescope (Maggiore et al., 2020; Punturo et al., 2010). In this case, the association with a GRB is fundamental as it becomes one of the most powerful tools to constrain cosmological parameters. For example, the GW/GRB 170817 provided an independent measurement of the Hubble

constant H_0, crucial to cosmology as it represents the local expansion rate of the Universe (Abbott et al., 2017). Such measurement could help in alleviating the current tension between the two main measurements of the Hubble constant, obtained from Planck observations of the CMB and from the SNIa distance ladder, and in understanding if the discrepancy is due to possible systematics or is the sign of a cosmological crisis that requires new paradigms. Future observations of a GRB associated to a GW will enable the Hubble constant to be constrained to high precision.

1.6.2 UHECRs and neutrinos

GRBs compete with blazars and starburst galaxies as the most powerful cosmological particle accelerators. The possibility that GRBs can produce both PeV neutrinos and UHECRs has been proposed long ago (Waxman, 1997) and it requires the acceleration of more massive particles than electrons, i.e. protons or heavier nuclei. The particle acceleration mechanism that drives proton acceleration should also produce a shower of neutrinos, because accelerated protons will interact through the photomeson ($p\gamma$) process with the γ–rays emitted in the prompt phase. The observation of neutrinos from GRBs would provide evidence for proton acceleration in their jets, answering to the compelling question of whether GRBs can significantly contribute to the neutrino and UHECRs background flux. So far, no neutrino event has been detected in correlation with a GRB from large neutrino detectors, such as IceCube and ANTARES (Aartsen et al., 2016; Aartsen et al., 2017; Adrián-Martínez et al., 2013), indicating a limited neutrino production in the most powerful sources. For this reason, fainter GRB, the so–called low luminosity GRBs, or even chocked jets have been suggested as better candidates than bright, successful jets to account for the diffuse neutrino flux, although likely not dominant (Murase et al., 2006; Denton and Tamborra, 2018).

In the near future, the potential of the multi–messenger astronomy will be fully exploited thanks to the current and next generation GW interferometers network operating in synergy with innovative multi-wavelenght observatories, such as the Cherenkov Telescope Array (CTA) (Actis et al., 2011a; Acharya et al., 2013), the Vera Rubin Observatory (Ivezić et al., 2019), the European Extremely Large Telescope (E-ELT) (Gilmozzi and Spyromilio, 2007), the Square Kilometre Array (SKA) (Carilli and Rawlings, 2004), and the next generation neutrinos detector KM3NeT (Adrián-Martínez et al., 2016), to name a few. The multi–messenger observations provided by these facilities will greatly enrich our understanding of the physics of GRBs.

Chapter 2

Prompt emission

In this Chapter I provide a more detailed description of the issues related to the prompt emission spectra. I first discuss the observational properties of the prompt emission spectra as inferred by the observations obtained with different satellites, then I present the main radiation mechanism proposed to explain the observed spectra. I discuss the open issues on such physical interpretation of the prompt emission, and how they have been tackled over the years. This set the context of the main research project of my thesis, which is focused on the prompt emission characterization and interpretation. Finally, a brief description of the *Fermi* satellite instruments, providing most of the data analyzed in this thesis, is given at the end of this Chapter.

2.1 Observational spectral properties

The prompt emission spectra have been extensively analyzed over the years, focusing mostly in the keV-MeV energy range. The BATSE and *Fermi* Catalogs provide the largest number ($\sim$ a few thousands) of GRBs spectra known to date and with the widest energy range. As described in Sec. 1.2, GRB prompt emission spectra are characterized by a non-thermal shape. The spectral data are typically fitted with 4 different functions: power-law (PL), cut-off power-law (CPL), Band and Smoothly Broken Power Law (SBPL). When the statistics is high and the energy band is sufficiently wide, spectra are typically fitted by two power-laws (with photon index α and β respectively) smoothly jointed at a characteristic energy (e.g. see top panel in Fig. 2.1). In a νF_ν representation, if $\alpha > -2$ and $\beta < -2$ the spectrum peaks at such characteristic energy, called peak energy $E_{\rm peak}$ (e.g. bottom panel of Fig. 2.1). The observed peak energies are widely distributed from $\sim$ 20-30 keV up to a few MeV, with a typical value of $\sim$200 keV. As an example, Fig. 2.2 shows the distribution of the peak energy of the GRBs analyzed in the *Fermi*/GBM Catalog covering the first four years of the mission: the reported average value for the peak energy is $E_{\rm peak}$=196^{+336}_{-100} keV. The typical photon index β of the high–energy power–law is $\beta < -2$. As an example, the right plot of Fig. 2.3 shows the distribution of β for the GRBs spectra included in the *Fermi*/GBM Catalog, which is distributed around $\langle\beta\rangle = -2.14^{+0.27}_{-0.37}$.

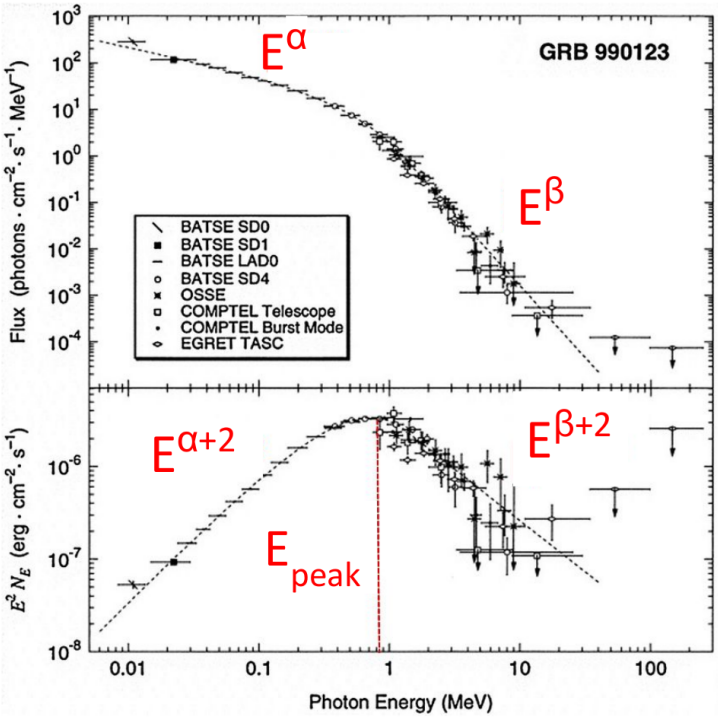

FIGURE 2.1: Example of a typical GRB spectrum, fitted with the Band function, shown both in the photon spectrum representation (top panel) and in the E^2N_E (or νF_ν) representation (bottom panel). The data belong to GRB 990123, one of the brightest bursts detected in the pre-*Swift* era by both the CGRO and BeppoSax satellite. The photon indices α and β of the decaying power–laws at low and high energies are labeled in red in the top panel and the corresponding values in the νF_ν representation in the bottom panel, where also the peak energy $E_{\rm peak}$ is shown. Adopted from Briggs et al., 1999.

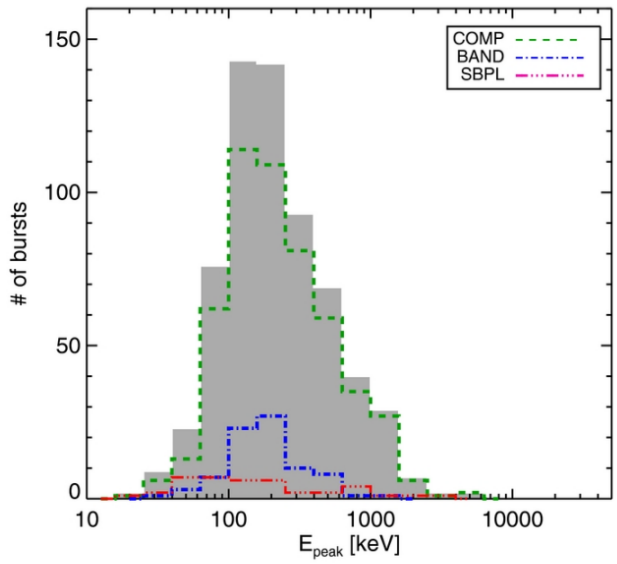

FIGURE 2.2: Distribution of the peak energy of the GRB spectra observed by *Fermi*/GBM in the first four years of activity. The grey filled histogram represents the overall distribution, while the colored empty histograms are the contributions of each best fitting spectral model. Taken from Gruber et al. 2014.

For the purposes of this chapter, I focus now on the low-energy part of the spectrum, as it is where the spectrum is inconsistent with the synchrotron predictions. The observed GRB prompt spectra are found to have, on average, a low-energy photon index $\langle\alpha\rangle \sim -1$ and this result is confirmed by observations performed with different instruments (Kaneko et al., 2006; Gruber et al., 2014; Nava et al., 2011b; Lien et al., 2016a; Goldstein et al., 2012; Preece et al., 2000). Kaneko et al. (2006) analyzed the 8459 time-resolved spectra extracted from 340 long GRBs observed by BATSE in the energy range ~ 20 keV - 2 MeV. They found that the average low-energy spectral index is $\alpha = -1.02^{+0.26}_{-0.28}$ for long GRBs. These results have been confirmed also by the analysis of the GRBs observed by *Fermi*/GBM. Fig. 2.3 shows the distribution of the low-energy photon index reported in Gruber et al. (2014), with the contribution of each best fitting model highlighted with colored lines. The overall distribution of the low-energy photon index is centered around $\alpha = -1.08^{+0.43}_{-0.44}$.

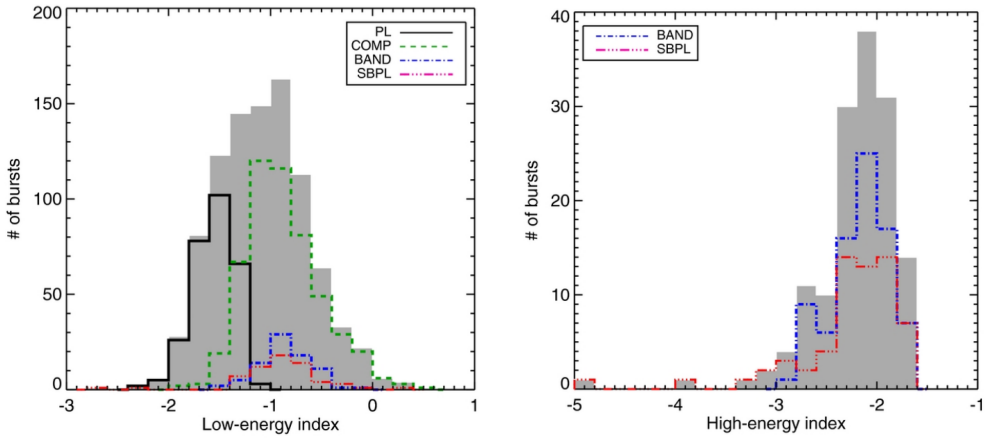

FIGURE 2.3: Distribution of the low-energy photon index α (left plot) and of the high-energy photon index β (right plot) of the GRB spectra observed by *Fermi*/GBM in the first four years of activity. The colored empty histograms indicate the best fitting spectral model, reported in the legend, contributing to the overall distribution of low-energy indices (grey filled histogram). For the β parameter, only the distributions related to the functions with a high-energy power–law (namely Band and SBPL) are reported. Taken from Gruber et al. (2014).

Short GRBs prompt emission appears instead harder with respect to long GRBs (Kouveliotou et al., 1993) based on the count ratios between the low-energy and high-energy bands (hardness ratio). Ghirlanda et al., 2009, analyzing 79 short and 79 long GRBs observed by BATSE, found that the low-energy spectral index of short bursts is harder than that of long ones, namely the average values are $\alpha_{\rm short} = -0.4 \pm 0.5$ and $\alpha_{\rm long} = -0.92 \pm 0.42$. The distributions of the α values found by Ghirlanda et al. (2009) are shown in Fig. 2.4. Similar results were found for short and long GRBs detected by *Fermi*/GBM. For example, Nava et al. 2011b published the results of spectral analysis on a sample of 438 *Fermi*/GBM bursts. As for the BATSE bursts, also short GRBs detected by *Fermi*/GBM display a harder low-energy photon index ($\alpha_{\rm short} = -0.50 \pm 0.40$) than the long ones ($\alpha_{\rm long} = -0.92 \pm 0.35$).

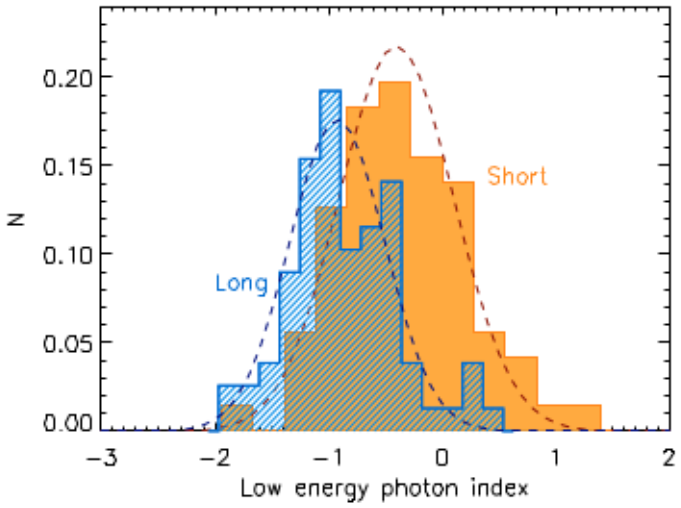

FIGURE 2.4: Normalized distribution of the low energy photon index α for 79 short (filled orange histogram) and 79 long (hatched blue histogram) GRBs observed by BATSE and analysed in Ghirlanda et al. (2009). Dashed lines are Gaussian distributions fitted to the histograms.

2.2 Theoretical predictions

One of the foremost unanswered questions about GRBs is the physical mechanism by which prompt γ-rays are produced. Despite thousands of GRBs have been detected by different satellites in the last fifty years, the radiative process responsible for the observed γ-ray emission has not been clearly identified yet. As shown in the previous Section, the low-energy slope of the spectrum is distributed around -1 and the high-energy part of the spectrum is characterized by a power–law, with a typical slope $\beta < -2$. These two properties indicate a non-thermal radiative process as responsible of the prompt emission. Independently from the details of mechanism responsible for the dissipation of the jet energy (internal shocks or magnetic reconnection events), the development of mildly relativistic shocks might lead to the presence of accelerated electrons. The presence of a strong magnetic fields in the emission region therefore, coupled with the shock-accelerated electrons, points to synchrotron emission as the most natural and efficient process (Rees and Meszaros, 1994a; Katz, 1994; Tavani, 1996; Sari, Narayan, and Piran, 1996; Sari, Piran, and Narayan, 1998a). In this section, I briefly summarize the basics of synchrotron radiation, and its application in the context of the GRB prompt emission physics. The detailed description of this radiative process can be found in Rybicki and Lightman (1986) and in Ghisellini (2013).

2.2.1 Synchrotron process

Synchrotron emission occurs when there are relativistic charged particles moving in a magnetic field. Consider a relativistic electron of charge e, of Lorentz factor γ_e and speed v_e moving into a region of constant magnetic field B[1]. The angle θ that the velocity vector makes with the magnetic field line is called *pitch angle*. The synchrotron power emitted

[1]The quantities expressed in this Section are related to the comoving frame, but for the sake of simplicity they are not expressed as primed quantities.

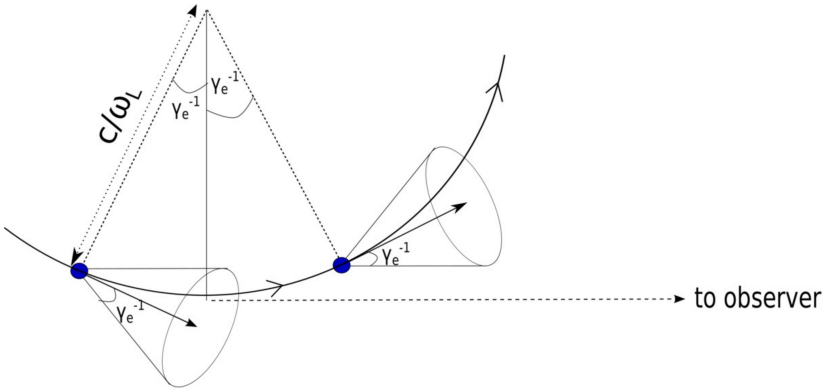

FIGURE 2.5: This figure shows a part of the orbit of an electron moving in a magnetic field. From the point of view of a distant observer, as due to the beaming of photons in the forward direction, the radiation from the electron is received only for a small segment of the orbit, in particular when the velocity vector of the electron lies within $1/\gamma_e$ of the observer line of sight. Taken from Kumar and Zhang 2015.

by a single electron of Lorentz factor γ_e and pitch angle θ in a magnetic field B is:

$$P_{\rm syn} = \frac{2e^4 B^2 \gamma_e^2 \beta_e^2 \sin^2(\theta)}{3m_e^2 c^3} = \sigma_T c B^2 \gamma_e^2 \beta_e^2 \sin^2\theta/4\pi \tag{2.1}$$

where $\sigma_T = 8\pi e^4/3m_e^2c^4 = 6.65 \cdot 10^{-25}$ cm^2 is the Thomson cross section. In the case of an isotropic distribution of pitch angles, we can average the term $\sin^2\theta$ over the solid angle, obtaining:

$$P_{\rm syn} = \frac{4}{3}\sigma_T c U_B \gamma_e^2 \beta_e^2 \tag{2.2}$$

where $U_{\rm B} = \frac{B^2}{8\pi}$ is the magnetic energy density.

The Larmor frequency of the electron is

$$\omega_L = \frac{eB}{\gamma_e m_e c}. \tag{2.3}$$

Due to relativistic beaming of photons, a distant observer receives radiation from the electron when the electron velocity vector lies within an angle γ_e^{-1} from the observer line of sight (see Fig. 2.5). The characteristic synchrotron frequency emitted by an electron of Lorentz factor γ_e is:

$$\nu_{\rm syn} \sim \frac{eB\gamma_e^2}{2\pi m_e c}. \tag{2.4}$$

For a single electron, the synchrotron spectrum is a function peaked at a specific frequency $\nu \sim 0.29\ \nu_{\rm c}$, where $\nu_c = 3/2\,\nu_{\rm syn}\sin(\theta)$. The spectrum S_ν below the peak is a power-law function $S_\nu \propto \nu^{1/3}$, while above the peak it is a power–law with an exponential cutoff $S_\nu \propto e^{-\nu/\nu_c}$.

It is useful now to extend the discussion to the synchrotron spectrum produced by a population of electrons. Let us assume a power-law distribution of electrons, namely $dN_{\rm e}/d\gamma_{\rm e} \propto \gamma_e^{-p}$, for $\gamma_{\rm min} < \gamma_e < \gamma_{\rm max}$, where $\gamma_{\rm min}$ and $\gamma_{\rm max}$ are the minimum and maximum Lorentz factor of the accelerated electrons. Using Eq. 2.4, it is possible to find the synchrotron spectrum F_ν by adding up contributions from all those electrons with

Lorentz factors with $\gamma_{\rm min} < \gamma_e < \gamma_{\rm max}$, namely:

$$S_\nu = \int_{\gamma_{min}}^{\gamma_{max}} d\gamma_e \frac{dN_e}{d\gamma_e} P_{\rm syn}(\nu) \propto \nu^{-(p-1)/2}. \tag{2.5}$$

This results is important as it demonstrates that for a power–law distribution of particles, the total synchrotron emission spectrum has also a power-law shape, and the two slopes are related to each other.

2.2.2 Expected synchrotron radiation in GRB prompt emission

The fast–cooling regime corresponds to a situation when the cooling timescale of electrons is much smaller than the dynamical time of the system. In the opposite situation, slow–cooling regime takes place. In order to determine which is the regime relevant in the prompt emission of GRBs, let us derive the characteristic timescale of cooling for synchrotron radiation and the dynamic timescale[2].

The cooling time can be calculated as the ratio between the initial electron energy and the electron power $P_{\rm syn}$ (see Eq. 2.2):

$$t'_{\rm cool} = \frac{E'}{P'_{\rm syn}} = \frac{\gamma'_e m_e c^2}{4/3 \sigma_T c U'_{\rm B} \gamma'^2_e \beta^2} \tag{2.6}$$

Considering $U'_{\rm B} = \frac{B'^2}{8\pi}$ and moving to the observer frame, one can obtain

$$t^{\rm obs}_{\rm cool} = t'_{\rm cool} \frac{1+z}{\Gamma} = \frac{6\pi m_e c}{\sigma_T \gamma'_e B'^2} \frac{1+z}{\Gamma} \tag{2.7}$$

Assuming the strong magnetic field usually thought to be present at the emitting region $B' \sim 10^6$ G [3] the synchrotron cooling time is very short, of the order of

$$t^{\rm obs}_{\rm cool} \sim 10^{-8} \Gamma_2^{-1/2} \nu^{\rm obs\ -1/2}_{200\,\rm keV} B'^{-3/2}_6 (1+z)^{1/2} \text{ s} \ . \tag{2.8}$$

In this formula the relation between the $\nu_{\rm syn}$ and the magnetic field B given from Eq. 2.4 and typical parameters, such as $\Gamma = 100$ and the observed peak energy of the spectrum $h\nu^{\rm obs}_{\rm peak}$ = 200 keV have been used.

It is useful to compare this cooling time with the dynamical one, necessary for the shells to cool via adiabatic process at the internal shock (IS) radius $R_{\rm IS} \sim 10^{13}$ cm:

$$t^{\rm obs}_{\rm ad} = \frac{R_{\rm IS}}{2c\Gamma^2}(1+z) \sim 1.6 \times 10^{-2} R_{13} \Gamma_2^{-2} (1+z) \text{ s} \ . \tag{2.9}$$

Note that the cooling timescale is much shorter than the dynamical one ($t^{\rm obs}_{\rm cool} \ll t^{\rm obs}_{\rm ad}$), resulting in an efficient radiative dissipation: in this situation adiabatic energy losses are therefore negligible. For the typical parameters assumed in the above calculations, it is clear that the cooling mechanism takes place under a fast cooling regime.

The characteristic synchrotron frequency associated with the cooling of electrons is $\nu'_{\rm cool}$. Combining the cooling timescale expressed in Eq. 2.6 with the synchrotron frequency in Eq. 2.4, it is possible to obtain the so-called *synchrotron cooling frequency*:

$$\nu'_{\rm cool} = \frac{3qB'\gamma'^2_{\rm cool}}{4\pi m_e c} \sim \frac{27\pi q m_e c}{\sigma_{\rm T}^2 B'^3 t'^2_{\rm cool}} \tag{2.10}$$

[2] In this Section the comoving quantities are expressed as primed quantities.

[3] The estimate of the cooling timescale will be further considered in Chapter 5, assuming a range of magnetic field $B' = 10^4 - 10^6$ G.

This is the frequency corresponding to the electron Lorentz factor $\gamma'_{\rm cool}$ and it represents the frequency above which the photons are produced by electrons that effectively cool. Due to energy losses, the electron energy distribution changes for $\gamma'_e > \gamma'_{\rm cool}$.

This can be seen from the continuity equation for electrons in the energy space, namely:

$$\frac{\partial}{\partial t}\frac{dN'_e}{d\gamma'_e} + \frac{\partial}{\partial \gamma'_e}\left[\dot{\gamma}'_e \frac{dN'_e}{d\gamma'_e}\right] = Q(\gamma'_e) \tag{2.11}$$

where $dN'_e/d\gamma'_e$ is the instantaneous electron spectrum of the system at the epoch t, and $Q(\gamma'_e)$ is the source function above a minimum injection Lorentz factor $\gamma'_{\rm min}$ of the electrons. For synchrotron radiation, the energy loss rate of the electron is

$$\dot{\gamma}'_e = \frac{\sigma_T B'^2 \gamma'^2_e}{6\pi m_e c} \propto B'^2 \gamma'^2_e \tag{2.12}$$

For fast cooling, electrons are cooled rapidly to the energy $\gamma'_{\rm cool} < \gamma'_{\rm min}$. In the regime $\gamma'_{\rm cool} < \gamma'_{\rm e} < \gamma'_{\rm min}$, the source function is $Q(\gamma'_{\rm e}) = 0$. The continuity equation has a steady state solution ($\partial/\partial t = 0$) for time-independent magnetic field B' which is:

$$\frac{dN'_e}{d\gamma'_e} \propto \dot{\gamma}_e'^{-1} \propto \gamma'^{-2}_e \tag{2.13}$$

thus the electron energy distribution has spectral index $p = 2$.

The corresponding synchrotron spectrum of this part of the electron energy distribution is $S_\nu \propto \nu^{-1/2}$. The photon spectral index, defined as $dN_\nu/dE_\nu \propto E_\nu^\alpha$, where E_ν is the photon energy and N_ν is the photon number flux, would then be $\alpha = -3/2$.

Therefore, the so called "fast cooling" regime of synchrotron emission provides a specific prediction about the shape of the emitted spectrum. Assuming that electrons acquire the power-law energy distribution assumed above, the emission spectrum consists of 3 power-laws smoothly connected by 2 breaks, corresponding respectively to the cooling frequency $\nu_{\rm cool}$ and to the minimum frequency $\nu_{\rm min}$ (the latter being related to the minimum energy $\gamma'_{\rm min}$ of the shock accelerated electrons). The fast cooling photon spectrum is:

$$N_\nu \propto \begin{cases} \nu^{-2/3} & for\ \nu < \nu_{\rm cool} \\ \nu^{-3/2} & for\ \nu_{\rm cool} < \nu < \nu_{\rm min} \\ \nu^{-p/2-1} & for\ \nu > \nu_{\rm min} \end{cases} \tag{2.14}$$

Note that, due to the fast cooling regime, electrons cool to a frequency $\nu_{\rm cool} < \nu_{\rm min}$ and this determines the characteristic ordering of the synchrotron frequencies.

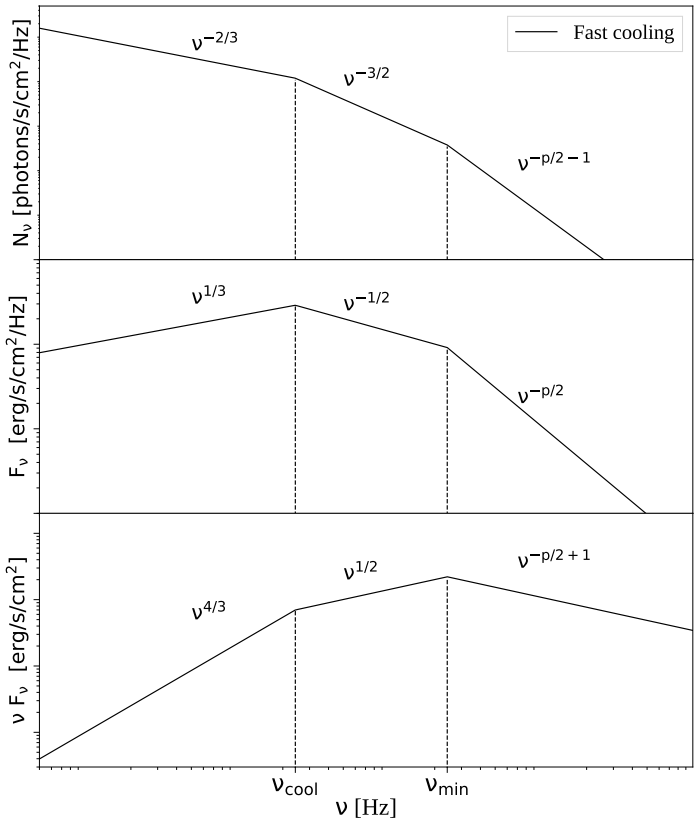

FIGURE 2.6: Schematic spectrum for the synchrotron emission in fast cooling regime. The three panels show the different representations of the spectrum that can be found in the literature. Top panel: photon flux spectrum (indicated with N_ν). Middle panel: energy flux spectrum (indicated as F_ν). Bottom panel: νF_ν representation.

As can be seen from Eq. 2.14 and in Fig. 2.6 (top panel), the predicted photon flux spectrum, between $\nu_{\rm cool}$ and $\nu_{\rm min}$, should be $N_\nu \propto \nu^{-3/2}$.

2.3 Open issues

The comparison between GRB low-energy spectral slopes α, shown in Fig. 2.4 and in Fig. 2.3, and the expected slope $-3/2$ of synchrotron emission in fast cooling regime, implies that a large fraction, i.e. > 70 %, of long GRBs and almost all short GRBs have spectra harder than the predicted value. Moreover, a small, but sizeable fraction, of long and short GRBs has spectral slope even harder than -2/3, the hardest slope expected for synchrotron emission, violating the so-called *synchrotron line-of-death* (Preece et al., 1998). This inconsistency between the predicted and the observed spectra represents a serious challenge against their interpretation as due to synchrotron radiation (Preece et al., 1998; Ghisellini, Celotti, and Lazzati, 2000; Frontera et al., 2000; Ghirlanda, Celotti, and Ghisellini, 2002; Ghirlanda, Celotti, and Ghisellini, 2003; Kaneko et al., 2006; Sakamoto et al., 2011a; Nava et al., 2011b; Goldstein et al., 2012; Gruber et al., 2014; Lien et al., 2016a). In my PhD thesis I focus on the issue of the inconsistency of the photon indices.

Another serious challenge for the synchrotron interpretation, which I will not treat in my thesis, is represented by the width of the spectrum. Several works claimed that the observed spectral width around the peak energy is narrower than the one predicted by synchrotron (Axelsson and Borgonovo, 2015; Yu et al., 2015b), even though the argument

is still debated in the literature. These studies adopt different empirical methods to measure the width of the spectrum. These measurements are then compared to the width of some idealized emission mechanisms spectra, e.g. blackbody and synchrotron, the latter derived from single-particle and from the broader Maxwellian and power-law distribution. These studies found that a large fraction (around ∼70–90%) of the GRB spectra analyzed is narrower than the idealized synchrotron spectrum from a Maxwellian distribution and another ∼30% is even narrower than the single-particle synchrotron spectrum. However, Burgess (2019) recently found that, even when these width measures would reject it, many spectra can be adequately fit by an idealized, physical synchrotron model. This suggests that the empirical ways of estimate the width can not always be safely used to reject the synchrotron model. I will further comment on this issue in Chapter 7.

The problem of the inconsistency of spectral indices has been extensively discussed in the literature and different solutions have been proposed. There are models that invoke a different emission mechanism, such as Comptonization and/or thermal components (Ghisellini and Celotti, 1999; Lazzati et al., 2000; Liang, 1997; Blinnikov, Kozyreva, and Panchenko, 1999; Stern and Poutanen, 2004; Mészáros and Rees, 2000). However, thermal models face the opposite problem as compared to synchrotron models: a thermal spectrum is too hard to explain observations. Various reasonable processes can soften the resulting spectra, such as the convolution of multi-temperature black-bodies (Pe'er and Ryde, 2011), or the composition of an underlying non-thermal spectrum and a thermal component (Pe'er, Mészáros, and Rees 2006; Pe'er et al. 2012, see Pe'er and Ryde 2017 for a recent review).

On the side of synchrotron-based solutions, there are models that suggest modifications of the basic synchrotron scenario to try to reconcile the synchrotron process with the observed GRB prompt spectra, invoking effects that produce a hardening of the low-energy spectral index. For example, a possible solution proposed to explain the observed GRBs spectra takes into account inverse Compton (IC) scattering in Klein–Nishina regime. The influence of the IC cooling on the standard fast cooling synchrotron spectrum can lead to spectra with α between -3/2 and -1 (Derishev, Kocharovsky, and Kocharovsky, 2001; Nakar, Ando, and Sari, 2009; Daigne, Bošnjak, and Dubus, 2011). The key concept behind this solution is that the transition between the Thomson and the Klein–Nishina regime occurs in the range of frequencies observed in the low-energy part of the GRB spectrum, where there is the inconsistency with the predictions. Since the scattering is energy dependent, it becomes progressively less efficient at higher energies and as a net effect this process hardens the emission spectrum at low energies. Since these scatterings are only moderately efficient, a strong IC component at higher energies (GeV) is not expected.

Another possibility is to consider that the emission is in *marginally* fast cooling regime: in this regime ν_c and ν_m are close to each other ($\nu_c \lesssim \nu_m$) and the asymptotic index at low energies $\nu < [\nu_c, \nu_m]$ quickly approaches the value $\alpha_1^{\rm syn} = -2/3$ (Daigne, Bošnjak, and Dubus, 2011; Beniamini, Barniol Duran, and Giannios, 2018). The marginally fast cooling regime could account for values of α up to -2/3. Other scenarios leading to a similar spectral shape invoke a magnetic field that decays downstream with a strength that depends on the distance from the shock front (Pe'er and Zhang, 2006; Derishev, 2007) or on the distance from the central engine (Uhm and Zhang, 2014), or invoke slow particle heating (Asano and Terasawa, 2009) or particle re-acceleration (Murase et al., 2012; Kumar and McMahon, 2008a; Beniamini and Piran, 2013).

The examples considered above can solve the inconsistency of observed spectral slopes with the synchrotron fast cooling predictions only partially. Even though these models

can in principle explain photon indices up to -0.8, -1 or even -2/3, they do not solve the problem of spectra harder than the synchrotron value -2/3 (see e.g. Fig. 2.4).

Other solutions proposed in literature includes anisotropic distribution of the electron pitch angles (Lloyd and Petrosian, 2000), and the so-called jitter radiation (Medvedev, 2000). Under specific configuration of the physical conditions during the emission (e.g. highly non uniform small-scale magnetic fields with inhomogeneities on length scales smaller than the beaming angle and/or the synchrotron self-absorption frequency close to γ-rays), both models could explain spectral slopes as hard as $\alpha \sim 0$. The advantages and difficulties of these and other models have been recently reviewed by Kumar and Zhang (2015). However, in spite of all theoretical efforts, there is still no consensus on the origin of the prompt emission.

All the efforts trying to reconcile the observations with the theory, tried to modify the theoretical models in order to make the predicted slopes compatible with those derived by fitting the GRB prompt emission spectra. Only recently, however, the problem has been tackled from the opposite side, through a revision of the way spectra are modelled, as it will be discussed in the following section.

2.3.1 Recent progress on spectral characterization

As described in Sec. 2.1, the Band function has become the standard spectral function used to describe the prompt emission spectra of GRBs (Band et al., 1993). However, deviations from this function have been recently observed in GRB spectra. These deviations become evident at low energies and have been identified by different authors, who modelled them differently and derived different conclusions.

A common approach to model the deviations is using a thermal component, since the emission from the fireball photosphere is indeed expected (Daigne and Mochkovitch, 2002) (although a pure thermal spectrum has been rarely observed, e.g. Ghirlanda, Celotti, and Ghisellini 2003). The idea of using a composition of an underlying non-thermal spectrum and a blackbody in order to take into account the spectral deviations from the Band function at low energies has been widely used in literature (Ryde et al., 2010; Guiriec et al., 2011; Guiriec et al., 2013; Guiriec et al., 2015; Guiriec et al., 2016; Guiriec et al., 2017). According to these works, when the blackbody component is added to a dominant non-thermal component, it can account for the low energy deviations and improve the spectral modeling. Yu et al. (2015a) have fitted time-resolved spectra of 8 bright GRBs detected by *Fermi* using a physically motivated synchrotron model, and they also add a black-body component at low energies. In this way, the excesses at low-energies were not modeled by the spectral break of the triple power–law predicted by the synchrotron theory but are modeled again by the blackbody peak. Instead, the break and the peak energy of the triple PL take into account the curvature around the νF_ν peak (see an example in Fig. 2.7).

While a blackbody component is useful to model the deviation at low energies observed in γ-rays, its presence might be inconsistent with the data at lower frequencies. In fact, Ghirlanda et al. (2007a), analyzing seven GRBs detected by BATSE and by the Wide Field Camera (WFC) onboard BeppoSAX, showed that the sum of a power–law and a blackbody gives acceptable fits to the time–resolved spectra within the BATSE energy range but overpredicts the flux in the WFC X-ray range. A similar conclusion has been found also by Oganesyan et al. (2019), who found that fitting *Swift* data with CPL+blackbody overestimates the optical data (this will be further discussed in Chap. 7). Moreover, as it will be discussed later in Section 3.1, the approach of the addition of a

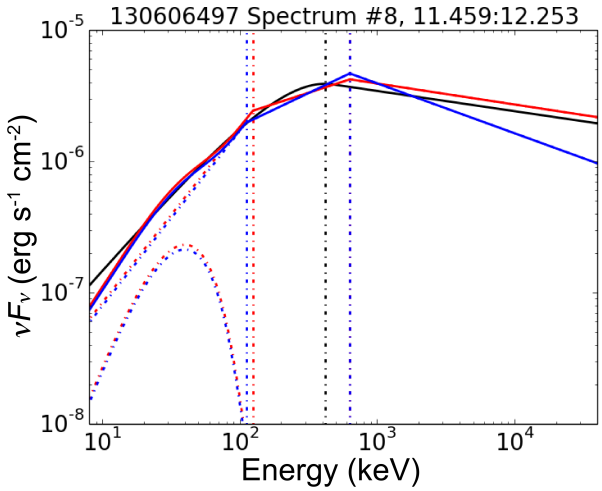

FIGURE 2.7: A selected spectrum from GRB 130606B plotted in νF_ν space from Yu et al., 2015a. The black, red, and blue solid curve show the BAND, SYNC-slow+BB, and SYNC-fast+BB models, respectively, while the dot–dashed curves show individual SYNC or BB component. The vertical dot–dashed black, red, and blue line show the E_{peak} and E_{break} energies for the BAND, SYNC-slow+BB, and SYNC-fast+BB model, respectively.

blackbody requires the coexistence of two emission components, one due to the outflow becoming transparent (thermal component, e.g. Goodman 1986; Paczynski 1986; Daigne and Mochkovitch 2002) and the other due to the non-thermal emission from internal shocks (e.g. Rees and Meszaros, 1994a), whose origin would still be unknown.

However, other attempts to model the same spectral deviation at low energies have been made in the literature. As an example, Tierney et al. (2013) found significant deviations from the Band function at low energies in a sample of bright long bursts detected by *Fermi*/GBM. They found an improvement in the spectral residuals when adding a blackbody or a power-law to the Band function, but also when fitting with a triple broken power-law (with sharp breaks). For example, Fig. 2.8 shows the spectrum of GRB 090424, which displays significant deviations from the Band function. It has two distinct spectral breaks: in addition to the usual peak energy, there is another lower energy break visible in the spectrum. A Band + blackbody fit with $kT \sim$9 keV can be fit throughout the burst, but also a triple broken power-law with break energy at $\sim$33 keV can adequately fit the spectrum. Interestingly, in the latter case the reported photon indices below and above the low-energy break are index$_1$ = -0.59$\pm$0.07 and index$_2$ = -1.52$\pm$0.03, remarkably similar to the ones predicted by synchrotron.

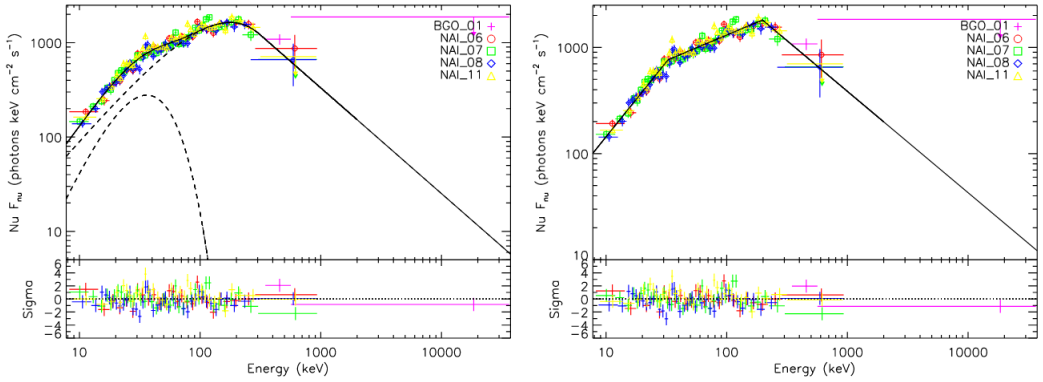

FIGURE 2.8: Two different spectral fits for GRB 090424, whose spectrum shows significant deviations in the low-energy range from the simple Band function. A Band + blackbody fit to the data (left plot) and a double broken power-law fit (right plot) can adequately fit the complex spectral shape. Taken from Tierney et al. 2013.

As pointed out also by the authors, these deviations are found in high fluence GRBs: fainter GRBs may not have sufficient statistics for deviations to be found. The need for a high signal-to-noise ratio in spectral data is crucial and the impact of the fluence parameter in unveiling possible deviations will be subject of investigation in Sec. 3.3.

Recently, a major advancement in the characterisation of prompt spectra has been reported. In two recent studies, Oganesyan et al. (2017) and Oganesyan et al. (2018) extended the investigation of the prompt emission spectra to the soft X-ray band, taking advantage of 34 *Swift* GRBs with prompt emission observed simultaneously by the Burst and Alert Telescope (BAT; 15–150 keV) and by the X-ray Telescope (XRT; 0.3–10 keV). In 11 out of 34 bursts, *Fermi*/GBM data were also available and have been included in the spectral analysis. The time-resolved joint spectral analysis has revealed the necessity of modifying the standard fitting functions, by adding a break at low energies. Fig. 2.9 shows the empirical functions used by the authors to fit the time-resolved spectra. In addition to the standard functions used to fit the prompt spectra (i.e. PL, CPL, and Band), they used the *BandCut* function, a Band function modified to include a high-energy exponential cutoff. This more complex function models the presence of two smooth breaks with two power-laws below the peak energy and an exponential cutoff above the peak energy. In particular, it allows to properly capture the whole spectral shape, especially when also the *Fermi*/GBM data are available.

In the 34 GRBs considered by Oganesyan et al. (2017) and Oganesyan et al. (2018), the low energy break is required with high statistical significance (more than 3σ) in $\sim 62\%$ of the analyzed spectra. The energy $E_{\rm break}$ at which the spectrum breaks is in the range 2–30 keV. The addition of *Fermi* data, when available, helped to constrain the peak energy $E_{\rm peak}$ of these spectra, which were found to have similar values to those of the whole population, i.e. ranging from 20 keV to 1 MeV. The photon index α_1 describing the spectrum below the break energy has a distribution peaked around $\langle \alpha_1 \rangle = -0.51 (\sigma = 0.24)$, while the photon index α_2 describing the spectral segment between $E_{\rm break}$ and $E_{\rm peak}$ has a mean value of $\langle \alpha_2 \rangle = -1.56 (\sigma = 0.26)$. Fig. 2.10 shows the distribution of the low-energy photon indices found in the work of Oganesyan et al. (2017). In particular, for spectra not showing a break, the black and blue empty histograms represents the low energy photon index for the CPL and PL fit, respectively. Consistently with previous spectral catalogs, the mean value for α_{CPL} is around -1, and the mean value of α_{PL} is softer, around -1.5. On the contrary, for those GRBs showing an additional break in the spectrum, the pink

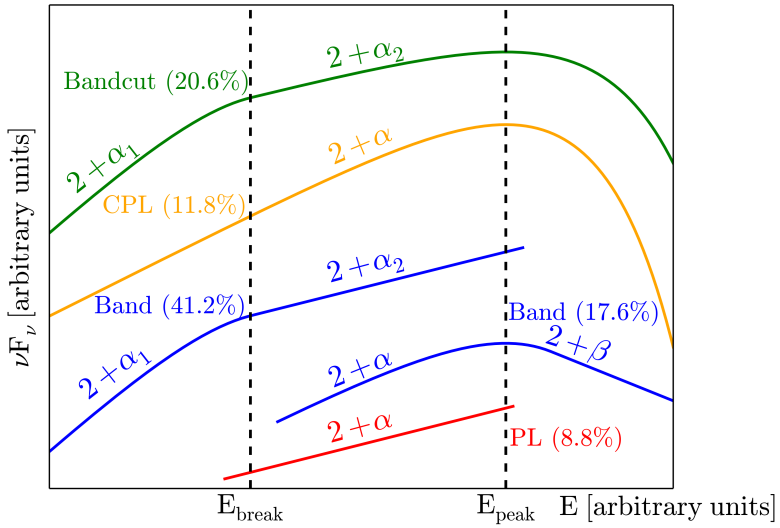

FIGURE 2.9: Functions used in Oganesyan et al. (2018) to fit the GRB prompt spectra observed simultaneously by BAT and by XRT, onboard the *Swift* satellite. Taken from Oganesyan et al. (2018).

and green histograms represent the distributions of the α_1 and α_2 values, respectively. The similarity between the mean values of these distributions and the values expected from synchrotron fast cooling radiation ($\alpha_1^{\rm syn} = -0.67$ and $\alpha_2^{\rm syn} = -1.5$) leads to identify $E_{\rm break}$ with the cooling frequency and $E_{\rm peak}$ with the characteristic synchrotron frequency. Moreover, the relatively low ratio $E_{\rm peak}/E_{\rm break} \sim 30$ found in these spectra indicates a regime in which cooling is *moderate* ($\gamma_{\rm min}/\gamma_{\rm cool} = (E_{\rm peak}/E_{\rm break})^{1/2} \sim 5$). Following e.g. Daigne, Bošnjak, and Dubus (2011) and Beniamini and Piran (2013), the authors suggested that in order to explain such a regime, the dissipation might take place at large radii ($R > 10^{15}$ cm) in a region characterized by a relatively weak magnetic field ($B' \sim$ 10–100 G) and moving with large bulk Lorentz factor ($\Gamma > 400$).

It is interesting to note also that the distribution of α_{CPL} lies between the two distribution of α_1 and α_2. This suggests that when fitting a function with only one possible break, the spectral index found is an intermediate value between the two different indices α_1 and α_2, recovered instead when fitting a function with two possible breaks. The distribution of α_{PL} is consistent with the distribution of α_2, the index of the power-law between the break and the peak energy, suggesting that the part of the spectrum observed at that energy range was the one between $E_{\rm break}$ and $E_{\rm peak}$.

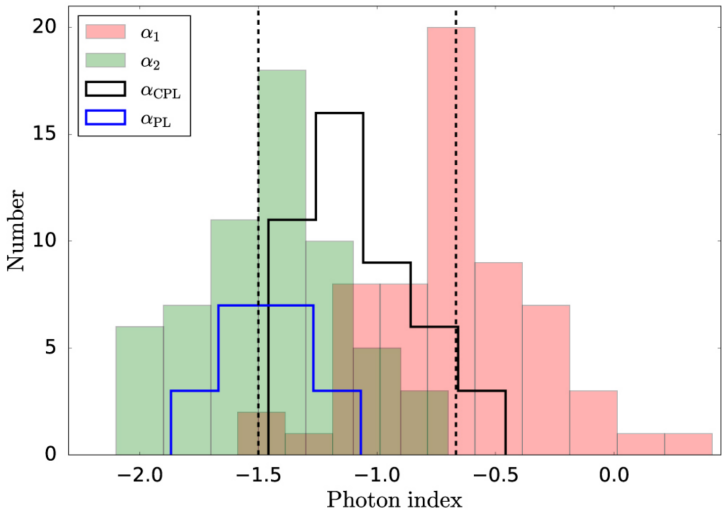

FIGURE 2.10: Distribution of the best-fit parameters α_1 (red) and α_2 (green), representing the photon indices below and above the break energy, resulting from the time-resolved spectral analysis of the 34 GRBs analyzed in Oganesyan et al. (2017). Different histograms refer to different models, as shown in the legend (see Fig. 2.9 for a representation of the models used). The values for α_1 and α_2 predicted from fast cooling synchrotron emission are drawn as dashed black lines. Taken from Oganesyan et al. (2017).

Given the recent detection of an additional spectral break at low-energies in the prompt spectra of GRBs detected by *Swift* and the consistency of the indices below and above it with the synchrotron predictions, it is interesting to study whether such a break is visible also at higher energies or it is related only to the X-ray range. To this aim, I investigated the presence of the additional break in the prompt emission spectrum of *Fermi*/GBM bursts, as it will be described in Chapter 3. In the following section, I focus on the need to introduce a new, more flexible, fitting function in order to fully capture the complex shape of the spectral data collected by *Fermi*/GBM in a broad energy range.

2.3.1.1 Introduction of a new fitting function

In the works of Oganesyan et al. (2017) and Oganesyan et al. (2018), the authors used a set of empirical functions in order to fit the potential presence of an additional break in the low energy part of the *Swift*/BAT and *Swift*/XRT spectra analyzed. In particular, only in a minority of burst the *Fermi*/GBM data were also available and they found that only a few spectra analyzed (20.6% of the sample) were best-fitted by the more complex *BandCut* function. The high energy part of the spectrum above the peak energy was modelled by an exponential cutoff, though. Since in this thesis I focused on investigating the presence of the additional spectral break in the *Fermi*/GBM data, which cover a much wider energy range, it is possible to constrain the peak of the spectrum and also the high–energy power–law above it. Therefore, instead of the *BandCut* function, an empirical function that is able to model the whole spectral shape, with two potential breaks and three power-laws, is needed.

As discussed in Sec. 2.1, the single-component empirical spectral functions traditionally used to fit the GBM spectra (e.g. Kaneko et al., 2006; Gruber et al., 2014) include a PL, a CPL, the Band model, and a SBPL. To test the presence of an additional spectral break, it is necessary to modify the basic SBPL function to include a second break energy and

a third power-law segment. In order to easily extend the definition of the SBPL to have more than one break, in this work I started from a different definition:

$$N_{\rm E}^{\rm SBPL} = A E_{\rm j}^{\alpha} \left[\left(\frac{E}{E_{\rm j}} \right)^{-\alpha n} + \left(\frac{E}{E_{\rm j}} \right)^{-\beta n} \right]^{-\frac{1}{n}} , \tag{2.15}$$

where

$$E_{\rm j} = E_{\rm peak} \cdot \left(-\frac{\alpha+2}{\beta+2} \right)^{\frac{1}{(\beta-\alpha)n}} . \tag{2.16}$$

In Eq. 2.15 $N_{\rm E}$ is the photon spectrum (i.e. number of photons per unit area, per unit time, and per unit energy). The free parameters are the amplitude A, the low-energy spectral index α, the peak energy of the $E^2 N_{\rm E}$ spectrum $E_{\rm peak}$, the high-energy spectral index β, and the smoothness parameter n (higher values of n correspond to sharper curvatures).

The advantage of the SBPL with respect to the Band model is that it gives more flexibility to properly model the curvature around $E_{\rm peak}$, at the expenses of having one additional free parameter. However, introducing a fifth free parameter usually results in ill-determined unconstrained parameters and degeneracy/correlations among them (Kaneko et al., 2006). For this reason, the value describing the curvature is usually kept fixed to a value which has been found to satisfactorily describe most of the spectra (Goldstein et al., 2012; Gruber et al., 2014). In the GBM Catalog the smoothness parameter is called Λ and is kept fixed to $\Lambda = 0.3$ for all GRBs (see Kaneko et al., 2006 for an explanation). In order to perform a fit that can be compared to the one reported in the GBM Catalog, the smoothness parameter n of the SBPL has been fixed to the value $n = 2.69$ (corresponding to $\Lambda = 0.3$).

The following function is the extension of the SBPL mathematical function, namely the double smoothly broken power law (2SBPL):

$$N_{\rm E}^{\rm 2SBPL} = A\, E_{\rm break}^{\alpha_1} \left[\left[\left(\frac{E}{E_{\rm break}} \right)^{-\alpha_1 n_1} + \left(\frac{E}{E_{\rm break}} \right)^{-\alpha_2 n_1} \right]^{\frac{n_2}{n_1}} + \right.$$
$$\left. + \left(\frac{E}{E_{\rm j}} \right)^{-\beta\, n_2} \cdot \left[\left(\frac{E_{\rm j}}{E_{\rm break}} \right)^{-\alpha_1 n_1} + \left(\frac{E_{\rm j}}{E_{\rm break}} \right)^{-\alpha_2 n_1} \right]^{\frac{n_2}{n_1}} \right]^{-\frac{1}{n_2}} , \tag{2.17}$$

where

$$E_{\rm j} = E_{\rm peak} \cdot \left(-\frac{\alpha_2+2}{\beta+2} \right)^{\frac{1}{(\beta-\alpha_2)\, n_2}} . \tag{2.18}$$

The free parameters are the amplitude A, the photon index α_1 below the break energy, the break energy $E_{\rm break}$, the photon index α_2 between the break and the peak energies, the peak energy $E_{\rm peak}$, the high-energy photon index β, and the smoothness parameters n_1 (for the break) and n_2 (for the peak).The 2SBPL model (Eq. 2.17) is nested into the SBPL (Eq. 2.15). The fits obtained from the two models can then be compared through an F-test (Protassov et al., 2002).

These models are shown (assuming typical parameters for the photon indices) in Fig. 2.11 (SBPL in blue and 2SBPL in red), where I also show a SBPL+BB (green line), for comparison. As shown in the plot, the overall effect of adding a (non-dominant) BB is similar to the effect of considering a softer SBPL (i.e. more consistent with synchrotron,

$\alpha_2 = -1.5$) and adding a break at low energies, thus considering a 2SBPL. The final functions have a similar shape (red and green solid lines in Fig. 2.11).

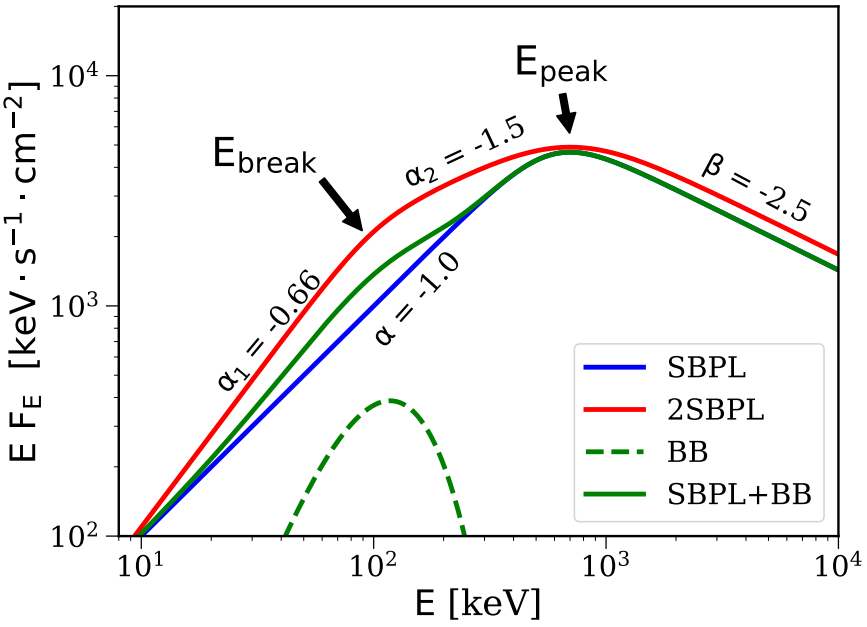

FIGURE 2.11: Comparison between the SBPL model (blue curve), SBPL+BB (green solid curve), and 2SBPL (red curve). Normalizations are arbitrary.

In Chapter 3 I will present the results of the analysis performed using these fitting functions in order to search for the presence of an additional spectral break. Since in my PhD thesis I have made extensive use of GRBs data detected by the *Fermi* satellite, the following section is dedicated to the explanation of its instruments. The description of the procedure for the extraction and the spectral analysis of the Fermi data, both for the LAT and for the GBM instrument, have been reported in the dedicated Appendix A.

2.4 The Fermi Gamma-ray Space Telescope

Launched on a Delta II rocket from Cape Canaveral on June 11, 2008, the Fermi Gamma-Ray Space Telescope (formerly called the Gamma-ray Large Area Space Telescope, GLAST) is a space observatory designed to perform γ-ray astronomy observations. The mission design lifetime (a minimum of 5 years, with a goal of 10 years) was generously overcome already four years ago. Designed in 2001 by NASA and by the space agencies of Italy, France, Japan and Sweden, it was built to shed light on some of the most important mysteries of high-energy astrophysics. Among its main scientific goals, there is understanding the mechanisms of particle acceleration in active galactic nuclei (AGNs), neutron stars and supernova remnants (SNRs), determining the high-energy behavior of gamma-ray bursts (GRBs) and probing dark matter.

Fermi consists of two instrument:

- Large Area Telescope (LAT), which covers the 20 MeV – 300 GeV energy range;
- Gamma-ray Burst Monitor (GBM), which covers the 8 keV – 40 MeV energy range.

FIGURE 2.12: Top: artistic representation of the Fermi satellite in space. Bottom: the two instruments of the *Fermi* satellite (labeled in white) assembled together and prepared for the launch. Credit: NASA (https://fermi.gsfc.nasa.gov/science/eteu/about/)

2.4.1 Large Area Telescope

LAT is a pair-conversion telescope with a wide Field Of View (FOV $>$ 2 sr, $\sim$ 20% of the sky), large effective area ($>$ 8000cm^2) and a good energy resolution ($<$ 10%) (Atwood et al., 2009). Like its predecessor EGRET on board the NASA Compton Gamma-Ray Observatory, LAT performs a gamma-ray sky survey and locates galactic (mainly pulsar) and extragalactic (mainly AGN) sources. LAT is also able to detect the GRBs that light up in its field of view and that have γ–ray emission at energies higher than GeV with detectable flux. It consists of three components (see Fig. 2.13):

- an array of 16 tracker (TKR) modules
- an array of 16 calorimeter (CAL) modules
- a segmented anti-coincidence detector (ACD)

The LAT-Tracker is an array of 4x4 modules and each TKR module consists of 18 XY tracker planes made of a converter, namely tungsten plates, in which gamma-rays incident on the LAT can convert to an e^+e^- pair, and a tracker, namely array of silicon-strip detectors (SSDs) for charged particle detection. The latter actually consists of two planes

of silicon strips, one running in the x and the other in the y direction, thereby localizing the passage of a charged particle.

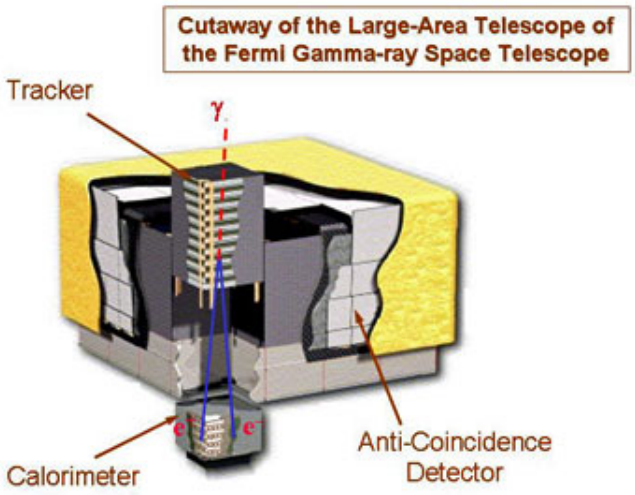

FIGURE 2.13: Schematic diagram of the Large Area Telescope, with the three main components labeled in red.

The Calorimeter is designed to measure the energy deposition due to the e^+e^- produced by the incident photon. It is made by 16 modules and each module consists of 8 planes of 12 CsI(Tl) crystals, with each crystal of size 2.7 cm x 2.0 cm x 32.6 cm. The crystals are read out by photodiodes at each end of the crystal which measure the scintillation light that is transmitted to each end, converting lights into an electrical current. The CAL's segmentation and read-out provide precise three-dimensional localization of the particle shower in the CAL.

Cosmic rays also interact within the TKR modules. To veto these charged particles the LAT is surrounded by an anticoincidence detector (ACD), which rejects 99.97% of unwanted signals produced by cosmic rays that enter the instrument. The ACD is composed of plastic scintillator segmented into tiles. The scintillator is coupled to electronic light sensors such as photomultiplier tubes (PMT), which absorb the light emitted by the scintillator and re-emit it in the form of electrons via the photoelectric effect.

Finally, LAT consists of a data acquisition system, which collects information from the tracker, from the calorimeter, and from the anti-coincidence detector and makes a first distinction between the unwanted signals of cosmic rays and the real signals of γ -rays, which instead must be transmitted to the ground. The Italian collaboration, supported by the Italian Space Agency (ASI), the National Institute of Astrophysics (INAF) and the National Institute of Nuclear Physics (INFN), was responsible for the construction and testing of the Silicon tracker and is actively involved in the scientific investigation of the data of the mission.

2.4.2 Gamma-ray Burst Monitor

The GBM (Meegan et al., 2009) includes two sets of detectors:

- Low-Energy Detectors: 12 sodium iodide (NaI) scintillators, each 12.7 cm in diameter by 1.27 cm thick, are sensitive in the lower end of the energy range, from 8 keV up to about 1 MeV

- High-Energy Detectors: 2 cylindrical bismuth germanate (BGO) scintillators, each 12.7 cm in diameter and 12.7 cm in height, which cover the energy range $\sim$ 150 keV to $\sim$ 30 MeV

The detection of a GRB happens when a significant change in count rate in at least 2 of the 12 NaI scintillators is reported (the on-board trigger threshold is 0.74 photons/cm^2/s). The signals are collected by a central Data Processing Unit (DPU), which packages the resulting data from the instruments into several different types for transmission to the ground (note that the GBM produces an average of 1.4 Gbits/day). The Burst Alert (with data such as intensity, location, and classification) arrives at the Gamma-ray burst Coordinates Network (GCN) within 15 seconds of the burst detection.

The combination of the GBM and the LAT data, which overlap each other in a small energy range between $\sim$30 and 40 MeV, provides a powerful tool for studying GRBs over a very wide range of energies, especially important for the spectral analysis (see Fig. 2.14). In particular, in this thesis I have combined GBM and LAT data, when available, in order to study the behaviour of bright GRB spectra at high energies (see Chapter 4).

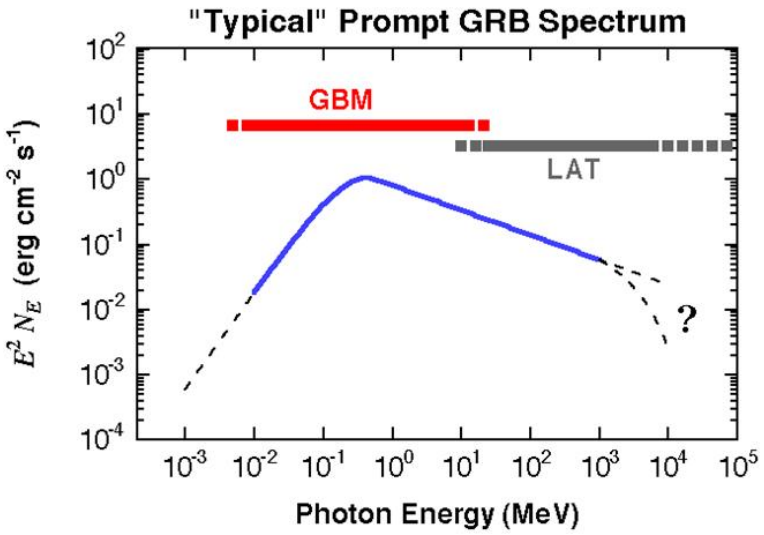

FIGURE 2.14: Gamma-ray burst spectral coverage of the GBM and the LAT instruments. Credit: NASA. From: https://fermi.gsfc.nasa.gov/ssc/data/analysis/documentation/Cicerone/Cicerone_GRBs/Overview_GRB_Spec_Anal.html

Chapter 3

Low–energy spectral breaks in prompt emission spectra

The substantial revision of the empirical functions adopted by Oganesyan et al. (2017) and Oganesyan et al. (2018) to model the prompt phase spectra allowed the authors to find a an additional spectral break at low energies and a better consistency of the indices with the synchrotron theory. A natural consequent question is whether such a break is visible also at higher energies. Indeed, if this break, so far detected in the energy range ∼2-30 keV, is a real spectral feature of GRB spectra, it could be also present at higher energies (in the keV-MeV component). If the presence of such a break at low-energy would be confirmed and the spectral indices would be distributed around the synchrotron predicted values, this would greatly enhance the advancement in the theoretical study of the origin of the prompt emission spectra. It is therefore of paramount importance the characterization of the prompt emission spectral features of GRBs in a broad-band energy range. A broad spectral coverage is crucial to detect both the low-energy spectral break and the peak energy, and also to fully capture the overall shape of the spectrum. To this aim, I performed a systematic search for the presence of such break at higher energies, using the data detected by *Fermi*/GBM. The *Fermi*/GBM data cover a wide energy band (10 keV – 40 MeV) with high spectral resolution (spectra sampled with 128 energy channels): these characteristics enable a systematic study of low-energy spectral deviations in bright *Fermi* bursts.

Moreover, with respect to *Swift*, using GBM data provides some advantages. It could be also possible to study the relation between the break and other quantities of the spectrum (e.g. to the usual peak energy and the isotropic flux). This instead was not always possible in the works of Oganesyan et al. (2017) and Oganesyan et al. (2018), due to the fact that their selection was made on *Swift* burst observed with XRT, and *Fermi* data were available only for a small fraction of bursts in their sample (11 out of 34). In addition, the selection of the sample based on the availability of XRT data allowed the authors to study only one population of GRBs, namely the long ones, since the slewing time of the *Swift* satellite prevents the detection by XRT of short GRBs. We can overcome this difficulty by analyzing the data detected by *Fermi*/GBM, which successfully detects both long and short bursts. The requirement of having XRT data also implied that the presence of a spectral break could be investigated only in late time spectra ($\sim$ a few tens of seconds). This often limited the analysis to the last part of the emission, during the late time peaks of the lightcurve, except for a few cases in which the bursts had a precursor that triggered the satellite before the main emission. Using *Fermi*/GBM instead, it is possible to follow the whole evolution of the burst from its beginning, allowing to study also if and how the spectral break evolves in time. In addition, for the range of interest for the search of the spectral break, the NaI detectors of the GBM instrument (see the description in Sec. 2.4) provide a continuous coverage of a wide energy range (from $\sim$ 8 keV to 900 keV), therefore there is no need to perform a joint analysis of the data detected from two different

instruments, like *Swift*/BAT and *Swift*/XRT. Moreover, XRT data are affected by intrinsic absorption in the soft X-ray band and by strong pile-up effects and both these two effects produce a hardening of the spectrum at low energy. Oganesyan et al. (2017) carefully took into account these effects and demonstrated that they are not sufficient to explain the hardening of the spectrum, and the presence of a spectral break is instead required. Sampling the spectra at higher energies, GBM data are not affected by these two problems, making the low-energy spectral break more confidently detected and identified.

In order to study also if and how the low-energy spectral break evolves in time, it is necessary to analyze the spectrum of a burst not only accumulated over its whole duration (*time-integrated* analysis) but, if possible, also in smaller time intervals of the light curve, namely performing a *time-resolved* analysis. For this reason I performed a selection based on the fluence of the bursts, that ensures a good photon statistic and allows to constrain all the parameters of the fit and eventually to assess the presence of an additional spectral break, with a certain degree of confidence.

In the following sections, I present the main results obtained from the modelling of prompt emission spectra with both an empirical (Ravasio et al., 2018; Ravasio et al., 2019a) and a synchrotron model (Ronchi et al., 2020). In addition, I present the investigation on the possible observational biases hiding the presence of the break and leading to the low energy photon index $\alpha \sim$ -1 typically found in GRBs spectra (Toffano et al., 2021).

The common procedure followed for data extraction and analysis is described in Appendix A.

3.1 GRB 160625B

I sorted GRBs of the Fermi/GBM Catalogue[1], observed in 9.5 years of activity, according to their decreasing fluence (computed in the 10-1000 keV energy range). The top of the list was GRB 130427A, but its brightness caused saturation effects in the detectors (Ackermann et al., 2014) and therefore was not completely suitable for the kind of analysis I wanted to perform. It is interesting to note, however, that a spectral analysis of the first pulse is reported by Preece et al., 2014, who found a physical synchrotron+blackbody model to well fit the spectral data.

I selected GRB 160625B, the second one with the largest fluence (6.4×10^{-4} erg/cm^2) detected by *Fermi* at the time of the search of the candidate (July 2017)[2]. GRB 160625B has also been detected by the LAT on board *Fermi* (Wang et al., 2017; Lü et al., 2017, e.g.).

[1] https://heasarc.gsfc.nasa.gov/W3Browse/fermi/fermigbrst.html

[2] According to the GBM Catalog, GRB 160625B is now (June 2021) the third burst with the largest fluence detected by *Fermi*.

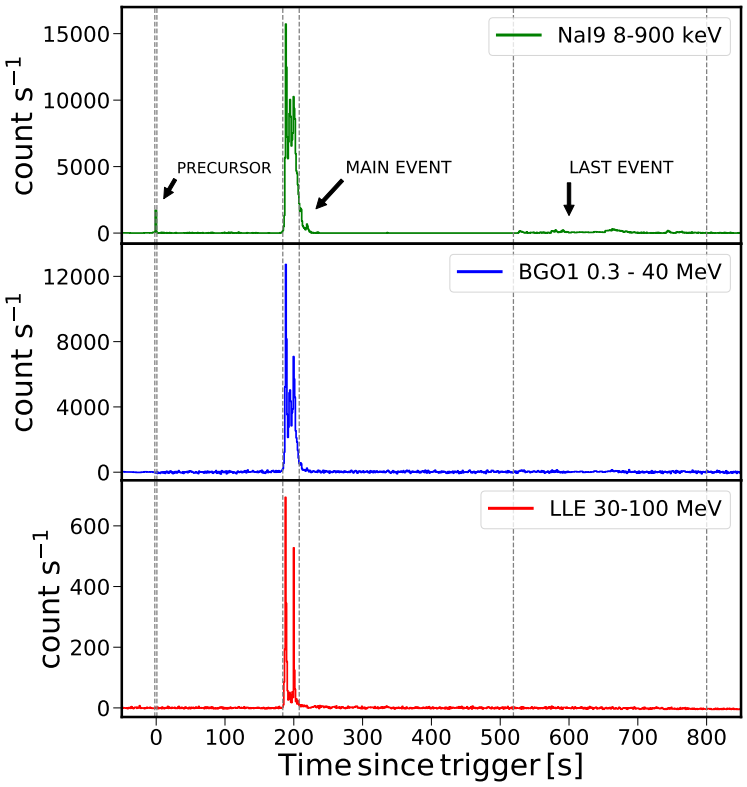

FIGURE 3.1: Background-subtracted lightcurves of GRB 160625B detected by NaI 9 (8 keV–900 keV, top), BGO 1 (300 keV–40 MeV, middle), and LAT Low Energy events (LLE: 30 MeV–100 MeV, bottom). The emission of GRB 160625B is characterized by three episodes: a precursor, a main event and a last dim event. The vertical dashed lines mark the time interval over which the spectrum has been accumulated for the analysis of the three emission episodes.

Figure 3.1 shows the light curve in three energy ranges: 8–900 keV (upper panel, NaI 9), 0.3–40 MeV (middle panel, BGO 1), and 30–100 MeV (bottom panel, LLE). Three different emission episodes separated by long quiescent times are visible: a precursor at $T = T_0$, the main event ~ 180 s later (lasting approximately 30 s), and a faint, soft, long-lasting (~ 300 s) emission starting at $T \sim T_0 + 500$ s.

At a redshift of $z = 1.406$ (Xu et al., 2016), the isotropic energy of GRB 160625B is $E_{\rm iso} \sim 5 \times 10^{54}$ erg, one of the largest ever observed. This GRB has been extensively studied in the literature, due to its extremely large fluence and long duration (Zhang et al., 2016; Wang et al., 2017; Lü et al., 2017), to the rich data sets covering its afterglow emission, and to optical polarization measurements (Alexander et al., 2017a; Troja et al., 2017). Time-resolved prompt spectral analysis performed by Zhang et al., 2016, suggested the presence of a BB spectrum in the first peak (the precursor), and a non-thermal spectrum during the main emission episode. This spectral transition was interpreted as being caused by the transition from a matter-dominated jet to a magnetically dominated jet. Wang et al. (2017) adopted a composition of Band function (Band et al., 1993) with a high-energy cutoff and BB component. A similar two-component model is adopted by Lü et al. (2017). What appears common in these models is the presence, sometimes simultaneous, of a BB and a non-thermal component. Oganesyan et al. (2017) and Oganesyan et al. (2018) suggested that an alternative solution to the presence of a BB is to consider a one-component model with a break in the low-energy part of the spectrum. Following their results, I tested both the possibilities, using the SBPL+BB and the 2SBPL function, defined in Eq. 2.17, and I describe the analysis and the results in the next paragraph.

For the purposes of my work, I focused on the main emission episode of the lightcurve. The time interval for time-integrated spectral analysis was selected requiring a signal-to-noise ratio (S/N) higher than 20 in the most-illuminated BGO (BGO 1). This criterion results in the selection of the time interval 186.40–207.91 s. In addition to the time-integrated analysis, I performed the time-resolved analysis for 21 bins, with time integration of 1.024 s each, distributed within the main event. Nevertheless, spectral analysis of the dimmer precursor and last emission episodes was also performed and will be presented at the end of this Section. For all three episodes, the time interval over which the spectrum has been accumulated is marked with vertical dashed lines in Fig. 3.1.

3.1.1 Time–integrated analysis

The time-integrated analysis over the main event has been performed using GBM data alone and adding, at a later stage, the LAT/LLE data (30–100 MeV), performing a simultaneous fit with the RMFIT software. Regarding the GBM, I analysed the CSPEC data collected by NaI 6, NaI 9, and from both BGO detectors.

3.1.1.1 Evidence of deviation from standard fitting functions

The *Fermi*/GBM GRB Catalog reports the results of the analysis on the spectrum integrated between $T_{\rm start} - T_0 = -44$ s and $T_{\rm stop} - T_0 = 789$ s, i.e. comprising all three episodes. According to this analysis, among a simple power law (PL), a cutoff power law (CPL), a Band model, and a smoothly broken power law (SBPL), the best model is the last one, with $\alpha = -1.021 \pm 0.004$, $E_{\rm peak} = 511 \pm 27$ keV, and $\beta = -2.096 \pm 0.014$. The reduced chi-square is, however, extremely large, $\chi^2_{\rm red} = 4.20$. This suggests that none of the standard models provides a good fit for this spectrum.

First, I analyze the main emission episode to check if the poor fit is caused by strong spectral evolution from the precursor to the late time soft emission. A SBPL function (see equation 2.15) returns $\alpha = -0.722 \pm 0.004$, $E_{\rm peak} = 327.5 \pm 2.8$ keV, $\beta = -2.184 \pm 0.005$, and $\chi^2_{\rm red} = 6.51$. The chi-square is again very large, and the fit has not improved. The spectrum and SBPL fit are shown in the top panel of Fig. 3.2, together with the data-to-model residuals (in units of the data statistical error). Residuals are characterized by a systematic trend, with broad excesses peaking around 60 keV and 600 keV.

A possible solution to improve the fit, which has been typically considered in the literature in this and in similar cases (Zhang et al., 2016; Wang et al., 2017; Lü et al., 2017), is to add a BB component. I tested this possibility and performed a spectral fit with a two-component model, SBPL+BB, shown in the middle panel of Fig. 3.2. The chi-square reduces to $\chi^2_{\rm red} = 1.97$, and the BB temperature is at $kT = 34.45^{+0.39}_{-0.38}$ keV, and accounts for the low-energy excess that was evident around 60 keV in the top panel of Fig. 3.2. The peak energy of the SBPL component shifts to higher energies (almost a factor of 2, $E_{\rm peak} = 576.3^{+6.15}_{-5.99}$ keV), removing the excess that was visible in the one-component SBPL fit at 600 keV. The SBPL photon indices also change considerably after the BB is added, becoming $\alpha = -0.914 \pm 0.005$, $\beta = -2.432 \pm 0.010$.

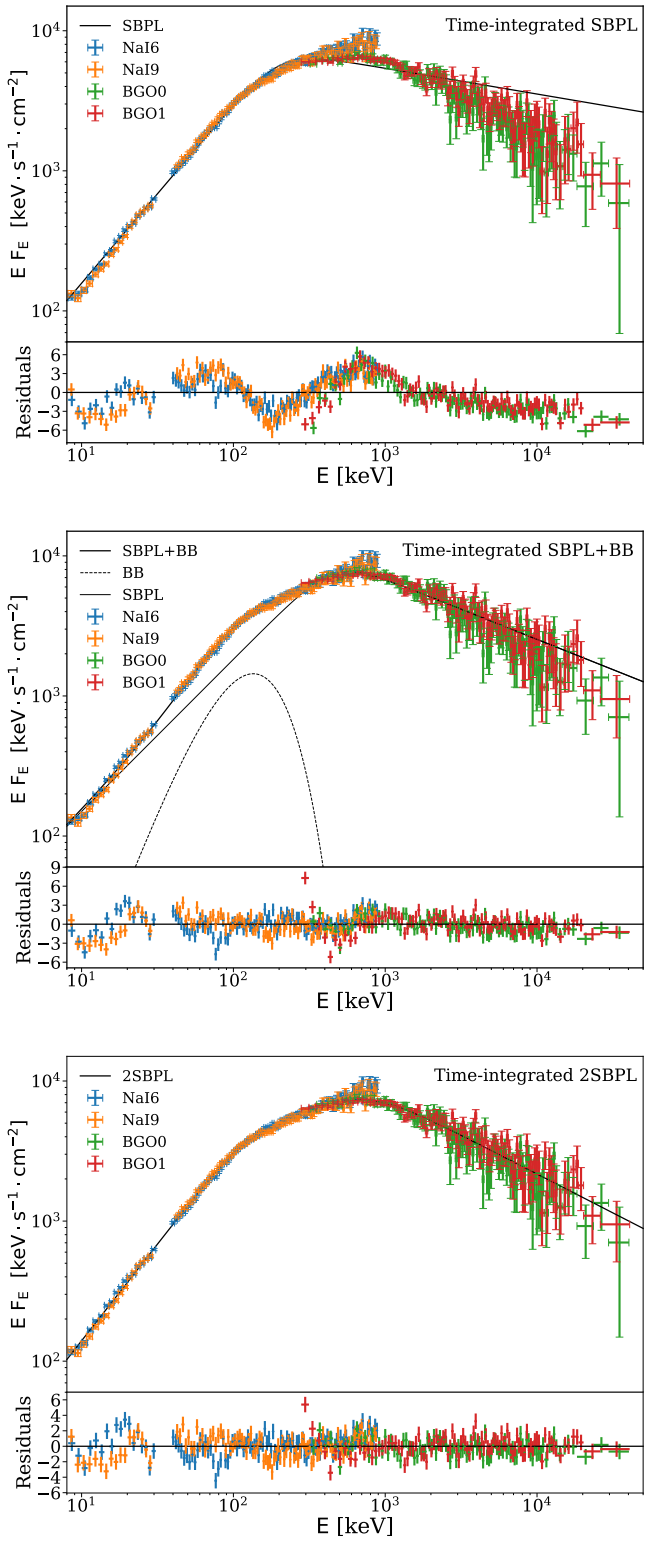

FIGURE 3.2: Time-integrated spectrum of the main event of GRB 160625B (186.40–207.91 s). Three different models are tested: SBPL, SBPL+BB, and 2SBPL (from top to bottom). Different colours refer to different detectors, as explained in the legend. In each plot, the bottom panel shows the model residuals.

3.1.1.2 Fit with the 2SBPL

I fitted the 2SBPL function, defined in equation 2.15, to the time-integrated spectrum of the main emission episode. As for the SBPL, the value of the curvature around the peak energy has been fixed to $n_2 = 2.69$. First, the break curvature n_1 has been left free to vary, but the other parameters of the model were not always constrained during the fit. Therefore, the value of n_1 has been fixed to the average value obtained leaving it free to vary and by fitting the 21 time–resolved spectra: $n_1 = 5.38$. This corresponds to a sharper curvature than the curvature around the peak energy. This value will be used also for the time–resolved analysis.

As shown in the bottom panel of Fig. 3.2, the inclusion of an additional spectral break at low energies significantly improved the fit: the chi-square is $\chi^2_{\rm red} = 701.9/462 = 1.52$, corresponding to an improvement at more than 8σ compared to the SBPL fit. A spectral break is found at $E_{\rm break} = 107.8 \pm 1.9$ keV, while the peak energy increases (compared to previously tested models) to $E_{\rm peak} = 673.5 \pm 10.8$ keV. The photon indices below and above $E_{\rm break}$ have best fit values $\alpha_1 = -0.62 \pm 0.01$ and $\alpha_2 = -1.50 \pm 0.01$, respectively. These values are very close to those expected from synchrotron emission from a cooled population of electrons.

Since the SBPL+BB and 2SBPL are not nested models, but have the same number of degrees of freedom, they can be compared in terms of χ^2 and associated probability. This comparison favours the 2SBPL model. However, both fits have a large reduced chi-square. The main contribution may come from the inconsistency between the two NaI, especially at low energies (i.e. in some energy ranges, one is systematically above/below the other) and the inconsistency between the NaI and the first few points with small errors of the BGO data (i.e. the systematic trend visible in the residuals between 300 and 500 keV may not have been properly taken into account by the response matrix).

3.1.1.3 Inclusion of LLE observations

Since in the time interval considered for the time-integrated analysis, LLE observations are also available, it is worth to add them to the fit to study the shape of the time-integrated spectrum at higher energies, i.e. up to 100 MeV. I found that the LLE data do not lie on the power-law extrapolation of the BGO data: they instead reveal the presence of a spectral softening at high energies. In order to model this softening, I modified the 2SBPL multiplying it by an exponential cutoff at high energy. The fit is shown in Fig. 3.3 with the solid black line, while the LLE data are shown with purple symbols. The best fit value of the cutoff energy (defined as the energy at which the flux is suppressed by a factor $\sim 1/e$ as compared to the simple PL extrapolation) is $E_{\rm cut} = 50.3^{+7.4}_{-13.2}$ MeV, and the reduced chi-square is $\chi^2_{\rm red} = 1.51$. All the other spectral parameters (photon indices, low-energy break and peak energies) are: $\alpha_1 = -0.62 \pm 0.01$, $E_{\rm break} = 107.3^{+1.9}_{-1.6}$ keV, $\alpha_2 = -1.49 \pm 0.02$, $E_{\rm peak} = 668.7^{+14.4}_{-9.2}$ keV, and $\beta = -2.54^{+0.03}_{-0.02}$. These parameters are consistent with those obtained when LLE data are not included. If interpreted as being caused by photon-photon annihilation, the cutoff at ~ 50 MeV corresponds to a Lorentz factor $\sim 200 - 250$, for a variability timescale $\sim 1 - 0.1$ s (Lithwick and Sari, 2001). Similar cutoff energies have been identified, from simultaneous modelling of GBM and LLE data, by Vianello et al. (2018). The bulk Lorentz factors found from this analysis are consistent with those derived in Vianello et al. (2018) and with those derived from the afterglow observations reported in Ghirlanda et al. (2018). In Chapter 4 I will further investigate the presence of exponential cutoffs in the prompt emission spectrum of bright bursts, including GRB 160625B, by adding also LAT data (> 100 MeV).

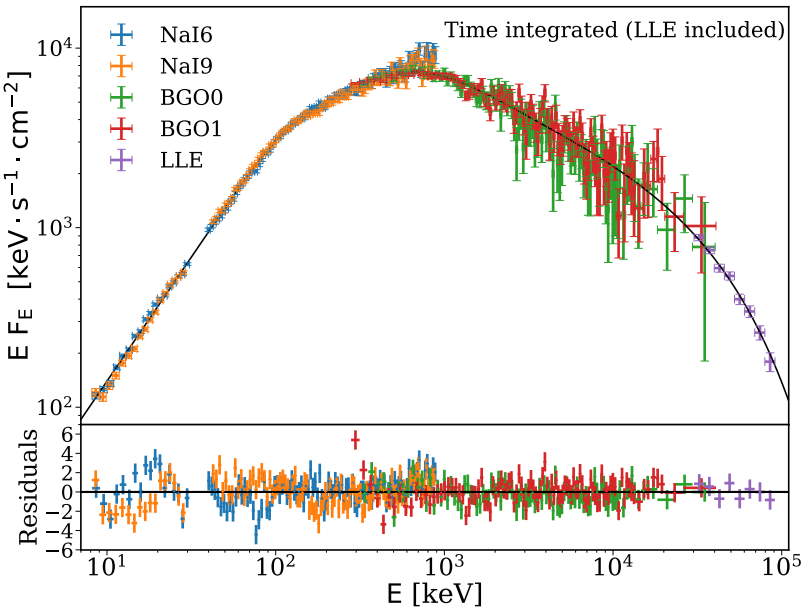

FIGURE 3.3: Time-integrated spectrum of GRB 160625B (186.40–207.91 s) from 8 keV to 100 MeV, including LAT/LLE data. The model (black solid line) is a 2SBPL with a high-energy exponential cutoff.

I also tested a model where the high-energy softening is modelled by an additional power law instead of an exponential cutoff, i.e. a model with four power-law segments smoothly connected by three breaks. This fit has a reduced chi-square $\chi^2_{\rm red} = 1.51$, equal to that obtained when an exponential cutoff is used. The highest energy break (i.e. above the peak energy) is found at $27.3^{+4.8}_{-6.7}$ MeV. The power-law segment above the high-energy break has photon index -3.5 ± 0.2. The values of the other parameters are similar to those found when the softening is modelled using an exponential cutoff. Interpreting the break at 27.3 MeV as being due to photon-photon annihilation, I estimate a $\Gamma \sim 150 - 200$, and the MeV-GeV power-law segment can be explained by emission and absorption taking place in the same region.

For completeness I have also analysed the spectrum of the precursor and of the last dim/long emission episode. I found that for both episodes the best fit model is a CPL. Contrary to what found by Zhang et al. (2016), the fit with a single BB is not favoured, because it is too narrow to account for the observed spectrum. A more detailed description of the analysis has been reported in Ravasio et al. (2018).

3.1.2 Time-resolved analysis

3.1.2.1 Fit results

In order to check whether the low-energy break identified in the time-integrated spectrum is also present in the time-resolved spectra and study its evolution with time, I divided the time interval 186.40–207.91 s into 21 time bins, with 1.024 s integration each. As for the time-integrated analysis, three models have been tested: SBPL, 2SBPL, and SBPL+BB (see Fig. 2.11). The results obtained from the different models (best fit parameters, photon and energy flux, chi-square and degrees of freedom, fit probability, and *F*-test) are listed in Table 3.1 (SBPL), Table 3.2 (2SBPL), and Table 3.3 (SBPL+BB).

First, I compared through an *F*-test the SBPL and 2SBPL models for all 21 time-resolved spectra. In 19 spectra (i.e. all spectra except the last two, where the flux is

TABLE 3.1: Best fit parameters for the SBPL function for the time-resolved analysis of the main emission episode of GRB 160625B. The photon flux and the energy flux have been computed in the energy range 10-1000 keV.

Time Bin $[s]$	Norm. $[ph\,keV^{-1}\,s^{-1}\,cm^{-2}]$	α	E_{peak} $[keV]$	β	Photon Flux $[ph\,s^{-1}\,cm^{-2}]$	Energy Flux (10^{-5}) $[erg\,s^{-1}\,cm^{-2}]$	χ^2/DOF	Prob
186.40 - 187.43	$2.16^{+0.4}_{-0.44}$	$-0.84^{+0.04}_{-0.06}$	$357.0^{+81.9}_{-84.1}$	$-1.81^{+0.03}_{-0.07}$	20.29 ± 0.44	2.6 ± 0.2	464.3 / 464	0.49
187.43 - 188.45	$4.19^{+0.39}_{-0.41}$	$-0.67^{+0.02}_{-0.03}$	$278.5^{+20.1}_{-21.2}$	$-1.9^{+0.02}_{-0.02}$	79.93 ± 0.68	8.5 ± 0.2	634.3 / 464	$6.3 \cdot 10^{-8}$
188.45 - 189.47	$8.93^{+0.5}_{-0.54}$	$-0.6^{+0.01}_{-0.02}$	$230.8^{+7.62}_{-8.47}$	$-1.98^{+0.01}_{-0.01}$	213.0 ± 1.1	17.6 ± 0.2	1053.6 / 464	$8.13 \cdot 10^{-48}$
189.47 - 190.50	$9.91^{+0.6}_{-0.58}$	$-0.65^{+0.01}_{-0.02}$	$456.5^{+29.4}_{-22.4}$	$-2.06^{+0.01}_{-0.01}$	172.84 ± 1.0	10.7 ± 0.2	819.3 / 464	$4.6 \cdot 10^{-22}$
190.50 - 191.52	$7.98^{+0.55}_{-0.65}$	$-0.7^{+0.02}_{-0.02}$	$282.3^{+13.7}_{-9.2}$	$-2.17^{+0.02}_{-0.03}$	98.33 ± 0.78	4.2 ± 0.1	543.3 / 464	0.01
191.52 - 192.55	$8.63^{+0.65}_{-0.8}$	$-0.76^{+0.02}_{-0.03}$	$229.2^{+12.7}_{-7.33}$	$-2.22^{+0.02}_{-0.05}$	77.82 ± 0.72	2.7 ± 0.1	458.4 / 464	0.56
192.55 - 193.57	$8.33^{+0.59}_{-0.64}$	$-0.71^{+0.02}_{-0.02}$	$235.1^{+8.24}_{-6.54}$	$-2.29^{+0.02}_{-0.04}$	92.95 ± 0.77	3.2 ± 0.1	499.6 / 464	0.12
193.57 - 194.59	$9.29^{+0.66}_{-0.57}$	$-0.7^{+0.02}_{-0.02}$	$300.0^{+11.2}_{-7.44}$	$-2.25^{+0.02}_{-0.02}$	122.75 ± 0.86	5.4 ± 0.1	644.3 / 464	$5.5 \cdot 10^{-8}$
194.59 - 195.62	$10.56^{+0.64}_{-0.67}$	$-0.7^{+0.02}_{-0.02}$	$293.6^{+9.6}_{-7.33}$	$-2.26^{+0.01}_{-0.03}$	135.13 ± 0.9	5.7 ± 0.1	694.9 / 464	$1.8 \cdot 10^{-11}$
195.62 - 196.64	$9.46^{+0.58}_{-0.66}$	$-0.71^{+0.02}_{-0.02}$	$279.6^{+8.78}_{-7.63}$	$-2.29^{+0.02}_{-0.03}$	117.21 ± 0.84	4.7 ± 0.1	644.0 / 464	$5.7 \cdot 10^{-8}$
196.64 - 197.67	$10.67^{+0.69}_{-0.85}$	$-0.79^{+0.02}_{-0.02}$	$287.9^{+11.1}_{-9.77}$	$-2.32^{+0.02}_{-0.05}$	94.06 ± 0.79	3.5 ± 0.1	570.3 / 464	$5 \cdot 10^{-4}$
197.67 - 198.69	$10.21^{+0.75}_{-0.7}$	$-0.77^{+0.02}_{-0.02}$	$316.8^{+14.4}_{-9.64}$	$-2.25^{+0.02}_{-0.03}$	99.4 ± 0.8	4.2 ± 0.1	565.2 / 464	$9 \cdot 10^{-4}$
198.69 - 199.71	$9.61^{+0.69}_{-0.63}$	$-0.76^{+0.02}_{-0.02}$	$323.0^{+13.3}_{-9.26}$	$-2.34^{+0.02}_{-0.04}$	103.34 ± 0.8	4.3 ± 0.1	654.9 / 464	$1.1 \cdot 10^{-8}$
199.71 - 200.74	$10.44^{+0.63}_{-0.64}$	$-0.72^{+0.01}_{-0.02}$	$472.3^{+18.5}_{-16.7}$	$-2.13^{+0.01}_{-0.02}$	145.68 ± 0.92	9.1 ± 0.2	688.0 / 464	$5.9 \cdot 10^{-11}$
200.74 - 201.76	$9.74^{+0.6}_{-0.63}$	$-0.7^{+0.02}_{-0.02}$	$368.6^{+14.1}_{-11.8}$	$-2.16^{+0.01}_{-0.02}$	133.83 ± 0.9	7.0 ± 0.1	606.6 / 464	$8.8 \cdot 10^{-6}$
201.76 - 202.79	$12.89^{+0.94}_{-0.73}$	$-0.79^{+0.02}_{-0.01}$	$324.9^{+14.2}_{-8.65}$	$-2.35^{+0.02}_{-0.03}$	118.86 ± 0.86	4.8 ± 0.1	653.5 / 464	$1.4 \cdot 10^{-8}$
202.79 - 203.81	$12.37^{+0.76}_{-1.01}$	$-0.86^{+0.02}_{-0.02}$	$297.4^{+13.0}_{-11.0}$	$-2.35^{+0.02}_{-0.06}$	83.57 ± 0.74	3 ± 0.1	530.4 / 464	0.02
203.81 - 204.83	$9.67^{+0.8}_{-0.79}$	$-0.85^{+0.02}_{-0.02}$	$323.1^{+21.3}_{-12.3}$	$-2.24^{+0.03}_{-0.05}$	67.53 ± 0.68	2.7 ± 0.1	504.3 / 464	0.1
204.83 - 205.86	$8.33^{+0.68}_{-0.59}$	$-0.81^{+0.02}_{-0.02}$	$261.8^{+11.4}_{-8.74}$	$-2.32^{+0.03}_{-0.04}$	64.98 ± 0.67	2.2 ± 0.1	511.7 / 464	0.06
205.86 - 206.88	$6.63^{+0.6}_{-0.77}$	$-0.78^{+0.02}_{-0.03}$	$203.4^{+11.6}_{-7.01}$	$-2.31^{+0.03}_{-0.07}$	54.05 ± 0.64	1.6 ± 0.1	480.4 / 464	0.29
206.88 - 207.91	$6.74^{+0.71}_{-0.92}$	$-0.84^{+0.03}_{-0.04}$	$253.0^{+81.6}_{-14.6}$	$-2.13^{+0.03}_{-0.09}$	42.8 ± 0.58	1.5 ± 0.1	508.3 / 464	0.08

TABLE 3.2: Best fit parameters for the 2SBPL function for the time-resolved analysis of the main emission episode of GRB 160625B. The photon flux and the energy flux have been computed in the energy range 10-1000 keV.

Time Bin $[s]$	Norm.	α_1	E_{break} $[keV]$	α_2	E_{peak} $[keV]$	β	Photon Flux $[ph\,s^{-1}\,cm^{-2}]$	Energy Flux (10^{-5}) $[erg\,s^{-1}\,cm^{-2}]$	χ^2/DOF	Prob.	$\sigma(F_{test})$
186.40 - 187.43	$1.8^{+0.32}_{-0.26}$	$-0.8^{+0.04}_{-0.04}$	$196.7^{+31.2}_{-26.3}$	$-1.53^{+0.04}_{-0.05}$	$6596.0^{+1220.0}_{-1400.0}$	$-3.88^{+1.02}_{-1.03}$	20.16 ± 0.44	2.3 ± 0.1	438.2 / 462	0.78	4.8
187.43 - 188.45	$2.68^{+0.32}_{-0.31}$	$-0.55^{+0.03}_{-0.03}$	$138.1^{+11.5}_{-12.1}$	$-1.45^{+0.04}_{-0.05}$	$2458.0^{+258.0}_{-248.0}$	$-2.4^{+0.09}_{-0.09}$	79.58 ± 0.69	7.7 ± 0.2	487.7 / 462	0.2	> 8.4
188.45 - 189.47	$5.9^{+0.4}_{-0.37}$	$-0.48^{+0.02}_{-0.02}$	$127.7^{+5.25}_{-4.92}$	$-1.49^{+0.03}_{-0.03}$	$1547.0^{+87.2}_{-73.1}$	$-2.54^{+0.05}_{-0.05}$	213.67 ± 1.1	15.8 ± 0.2	494.0 / 462	0.15	> 8.4
189.47 - 190.50	$6.87^{+0.49}_{-0.5}$	$-0.54^{+0.02}_{-0.02}$	$114.4^{+5.16}_{-5.65}$	$-1.52^{+0.03}_{-0.04}$	$1098.0^{+68.6}_{-71.9}$	$-2.54^{+0.04}_{-0.06}$	173.91 ± 1.0	10.0 ± 0.2	505.7 / 462	0.08	> 8.4
190.50 - 191.52	$5.73^{+0.54}_{-0.56}$	$-0.6^{+0.02}_{-0.03}$	$98.17^{+6.33}_{-7.22}$	$-1.54^{+0.05}_{-0.07}$	$621.6^{+45.8}_{-54.4}$	$-2.54^{+0.05}_{-0.09}$	99.09 ± 0.79	4.0 ± 0.1	451.1 / 462	0.63	> 8.4
191.52 - 192.55	$7.76^{+0.72}_{-0.81}$	$-0.73^{+0.02}_{-0.03}$	$107.4^{+6.63}_{-8.89}$	$-1.78^{+0.05}_{-0.1}$	$574.6^{+65.8}_{-114.0}$	$-2.76^{+0.08}_{-0.24}$	78.41 ± 0.73	2.5 ± 0.1	422.9 / 462	0.9	5.8
192.55 - 193.57	$6.26^{+0.69}_{-0.65}$	$-0.63^{+0.03}_{-0.03}$	$99.2^{+8.49}_{-10.2}$	$-1.51^{+0.08}_{-0.12}$	$387.1^{+30.8}_{-39.3}$	$-2.53^{+0.05}_{-0.09}$	93.29 ± 0.78	3.1 ± 0.1	456.6 / 462	0.56	6.1
193.57 - 194.59	$5.97^{+0.53}_{-0.55}$	$-0.57^{+0.02}_{-0.02}$	$102.3^{+6.25}_{-7.2}$	$-1.48^{+0.04}_{-0.05}$	$608.2^{+26.5}_{-24.5}$	$-2.71^{+0.04}_{-0.09}$	123.2 ± 0.87	5.0 ± 0.1	451.8 / 462	0.62	> 8.4
194.59 - 195.62	$6.78^{+0.56}_{-0.58}$	$-0.58^{+0.03}_{-0.03}$	$102.0^{+5.81}_{-6.67}$	$-1.49^{+0.04}_{-0.05}$	$590.8^{+24.1}_{-33.3}$	$-2.72^{+0.04}_{-0.08}$	135.62 ± 0.91	5.3 ± 0.1	485.0 / 462	0.22	> 8.4
195.62 - 196.64	$6.13^{+0.54}_{-0.57}$	$-0.58^{+0.02}_{-0.03}$	$102.1^{+6.15}_{-7.42}$	$-1.51^{+0.04}_{-0.06}$	$559.0^{+23.9}_{-35.4}$	$-2.79^{+0.05}_{-0.1}$	117.59 ± 0.85	4.3 ± 0.1	474.0 / 462	0.34	> 8.4
196.64 - 197.67	$5.76^{+0.73}_{-0.9}$	$-0.61^{+0.04}_{-0.05}$	$83.06^{+8.38}_{-11.8}$	$-1.42^{+0.05}_{-0.08}$	$531.4^{+28.2}_{-48.6}$	$-2.83^{+0.08}_{-0.17}$	94.23 ± 0.79	3.2 ± 0.1	459.4 / 462	0.53	> 8.4
197.67 - 198.69	$6.22^{+0.69}_{-0.76}$	$-0.63^{+0.03}_{-0.04}$	$92.24^{+8.86}_{-11.0}$	$-1.41^{+0.05}_{-0.07}$	$570.5^{+28.9}_{-37.9}$	$-2.62^{+0.04}_{-0.1}$	99.66 ± 0.8	4.0 ± 0.1	453.0 / 462	0.61	> 8.4
198.69 - 199.71	$5.13^{+0.55}_{-0.61}$	$-0.58^{+0.03}_{-0.04}$	$94.75^{+7.6}_{-9.5}$	$-1.42^{+0.04}_{-0.06}$	$606.4^{+23.5}_{-37.7}$	$-2.95^{+0.06}_{-0.14}$	103.02 ± 0.81	3.9 ± 0.1	468.4 / 462	0.41	> 8.4
199.71 - 200.74	$6.19^{+0.56}_{-0.55}$	$-0.57^{+0.02}_{-0.03}$	$108.7^{+8.69}_{-8.86}$	$-1.34^{+0.04}_{-0.05}$	$824.2^{+41.7}_{-40.8}$	$-2.4^{+0.03}_{-0.04}$	145.38 ± 0.93	8.6 ± 0.2	499.0 / 462	0.11	> 8.4
200.74 - 201.76	$6.38^{+0.6}_{-0.58}$	$-0.58^{+0.02}_{-0.03}$	$105.4^{+8.73}_{-9.08}$	$-1.38^{+0.05}_{-0.06}$	$660.5^{+36.5}_{-37.8}$	$-2.39^{+0.03}_{-0.04}$	134.32 ± 0.91	6.8 ± 0.1	476.8 / 462	0.31	> 8.4
201.76 - 202.79	$7.55^{+0.68}_{-0.73}$	$-0.64^{+0.02}_{-0.03}$	$102.2^{+7.29}_{-8.81}$	$-1.48^{+0.04}_{-0.05}$	$621.9^{+22.7}_{-34.4}$	$-3.0^{+0.06}_{-0.13}$	118.41 ± 0.86	4.3 ± 0.1	423.9 / 462	0.9	> 8.4
202.79 - 203.81	$9.27^{+0.89}_{-1.07}$	$-0.77^{+0.03}_{-0.04}$	$113.3^{+12.4}_{-17.5}$	$-1.51^{+0.06}_{-0.12}$	$482.3^{+27.0}_{-50.6}$	$-2.74^{+0.05}_{-0.18}$	83.6 ± 0.75	2.8 ± 0.1	485.3 / 462	0.22	6.1
203.81 - 204.83	$6.62^{+0.87}_{-1.12}$	$-0.74^{+0.04}_{-0.06}$	$94.78^{+14.5}_{-21.8}$	$-1.42^{+0.07}_{-0.13}$	$530.4^{+41.6}_{-59.2}$	$-2.56^{+0.06}_{-0.16}$	67.72 ± 0.69	2.5 ± 0.1	468.3 / 462	0.41	5.5
204.83 - 205.86	$6.28^{+0.71}_{-0.79}$	$-0.73^{+0.03}_{-0.04}$	$105.1^{+10.6}_{-14.0}$	$-1.56^{+0.07}_{-0.12}$	$463.8^{+32.5}_{-55.7}$	$-2.83^{+0.09}_{-0.23}$	65.16 ± 0.68	2.0 ± 0.1	470.7 / 462.0	0.38	5.9
205.86 - 206.88	$4.76^{+0.91}_{-0.98}$	$-0.67^{+0.05}_{-0.08}$	$81.74^{+20.2}_{-25.8}$	$-1.33^{+0.13}_{-0.24}$	$261.8^{+25.5}_{-30.2}$	$-2.44^{+0.05}_{-0.12}$	54.08 ± 0.64	1.5 ± 0.1	472.2 / 462.0	0.36	2.4
206.88 - 207.91	0	0	0	0	0	0	0	0	0	0	0

TABLE 3.3: Best fit parameters for the SBPL+BB function for the time-resolved analysis of the main emission episode of GRB 160625B. The photon flux and the energy flux have been computed in the energy range 10-1000 keV.

Time Bin [s]	Norm.	α	E_{peak} [keV]	β	BB Norm. (10^{-5}) [$ph\,s^{-1}\,cm^{-2}\,keV^{-1}$]	kT [keV]	Photon Flux [$ph\,s^{-1}\,cm^{-2}$]	Energy Flux(10^{-5}) [$erg\,s^{-1}\,cm^{-2}$]	χ^2/DOF	Prob
186.40 - 187.43	$4.67^{+0.72}_{-0.69}$	$-1.11^{+0.03}_{-0.04}$	$3462.0^{+609.0}_{-333.0}$	$-2.46^{+0.2}_{-0.31}$	$0.6^{+0.2}_{-0.2}$	$66.3^{+8.68}_{-6.88}$	20.53 ± 0.44	2.4 ± 0.1	449.2 / 462	0.66
187.43 - 188.45	$5.6^{+0.68}_{-0.68}$	$-0.83^{+0.03}_{-0.03}$	$1450.0^{+152.0}_{-95.5}$	$-2.09^{+0.03}_{-0.04}$	$7.5^{+1.7}_{-1.2}$	$43.7^{+3.07}_{-3.33}$	79.61 ± 0.69	8.0 ± 0.2	523.0 / 462	0.03
188.45 - 189.47	$15.07^{+0.97}_{-0.94}$	$-0.84^{+0.02}_{-0.02}$	$997.2^{+30.1}_{-27.1}$	$-2.28^{+0.02}_{-0.02}$	$25.0^{+2.0}_{-1.9}$	$44.44^{+1.29}_{-1.27}$	213.39 ± 1.1	16.1 ± 0.2	567.1 / 462	$5.8 \cdot 10^{-4}$
189.47 - 190.50	$15.5^{+1.1}_{-1.15}$	$-0.86^{+0.02}_{-0.02}$	$747.2^{+25.6}_{-24.8}$	$-2.31^{+0.02}_{-0.03}$	$33^{+3.5}_{-2.9}$	$37.01^{+1.25}_{-1.35}$	174.25 ± 1.0	10.4 ± 0.2	547.1 / 462	$3.8 \cdot 10^{-3}$
190.50 - 191.52	$12.86^{+1.28}_{-1.28}$	$-0.93^{+0.02}_{-0.03}$	$538.4^{+29.6}_{-29.8}$	$-2.42^{+0.03}_{-0.07}$	$29^{+4.0}_{-3.6}$	$32.04^{+1.48}_{-1.52}$	99.34 ± 0.79	4.1 ± 0.1	458.9 / 462	0.53
191.52 - 192.55	$17.09^{+1.95}_{-2.4}$	$-1.04^{+0.03}_{-0.05}$	$484.0^{+42.0}_{-52.0}$	$-2.47^{+0.05}_{-0.12}$	$26.0^{+3.7}_{-3.3}$	$31.19^{+1.71}_{-1.84}$	78.58 ± 0.73	2.6 ± 0.1	434.7 / 462	0.81
192.55 - 193.57	$12.08^{+1.35}_{-1.71}$	$-0.9^{+0.03}_{-0.05}$	$388.2^{+25.5}_{-34.9}$	$-2.46^{+0.04}_{-0.07}$	$30.0^{+5.5}_{-4.2}$	$30.05^{+1.68}_{-2.27}$	93.47 ± 0.78	3.2 ± 0.1	459.9 / 462	0.52
193.57 - 194.59	$13.52^{+1.02}_{-1.18}$	$-0.9^{+0.02}_{-0.02}$	$553.9^{+17.1}_{-21.4}$	$-2.59^{+0.03}_{-0.06}$	$30.0^{+3.8}_{-3.1}$	$34.22^{+1.23}_{-1.44}$	123.53 ± 0.87	5.1 ± 0.1	456.5 / 462	0.56
194.59 - 195.62	$15.25^{+1.07}_{-1.25}$	$-0.9^{+0.02}_{-0.02}$	$540.6^{+15.8}_{-20.1}$	$-2.6^{+0.03}_{-0.06}$	$34.0^{+4.0}_{-3.3}$	$33.82^{+1.13}_{-1.32}$	136.01 ± 0.91	5.5 ± 0.1	488.6 / 462	0.19
195.62 - 196.64	$13.63^{+1.06}_{-1.27}$	$-0.9^{+0.02}_{-0.02}$	$513.0^{+16.3}_{-22.3}$	$-2.64^{+0.03}_{-0.07}$	$31.0^{+4.1}_{-3.3}$	$33.34^{+1.24}_{-1.49}$	118.0 ± 0.85	4.5 ± 0.1	484.5 / 462	0.23
196.64 - 197.67	$11.59^{+1.74}_{-1.65}$	$-0.9^{+0.02}_{-0.04}$	$451.6^{+20.5}_{-34.5}$	$-2.59^{+0.04}_{-0.1}$	$36.0^{+9.7}_{-5.8}$	$27.5^{+1.59}_{-2.33}$	94.58 ± 0.8	3.4 ± 0.1	476.7 / 462	0.31
197.67 - 198.69	$13.1^{+1.09}_{-1.31}$	$-0.92^{+0.02}_{-0.03}$	$526.7^{+20.2}_{-25.7}$	$-2.53^{+0.03}_{-0.07}$	$26.0^{+4.7}_{-3.6}$	$31.44^{+1.53}_{-1.84}$	99.99 ± 0.81	4.1 ± 0.1	461.0 / 462	0.5
198.69 - 199.71	$11.44^{+1.03}_{-1.04}$	$-0.89^{+0.02}_{-0.02}$	$536.9^{+19.2}_{-20.8}$	$-2.73^{+0.05}_{-0.08}$	$25.0^{+4.0}_{-3.4}$	$32.97^{+1.71}_{-1.72}$	103.42 ± 0.81	4.1 ± 0.1	487.6 / 462	0.2
199.71 - 200.74	$12.47^{+1.03}_{-1.06}$	$-0.84^{+0.02}_{-0.02}$	$683.1^{+24.8}_{-25.4}$	$-2.31^{+0.02}_{-0.03}$	$22.0^{+3.7}_{-2.9}$	$36.65^{+1.99}_{-2.1}$	145.72 ± 0.93	8.8 ± 0.2	518.8 / 462	0.03
200.74 - 201.76	$12.8^{+1.04}_{-1.08}$	$-0.85^{+0.02}_{-0.02}$	$586.9^{+22.7}_{-23.6}$	$-2.33^{+0.02}_{-0.03}$	$25.0^{+3.7}_{-3.1}$	$34.79^{+1.63}_{-1.73}$	134.58 ± 0.91	7.0 ± 0.1	479.8 / 462	0.27
201.76 - 202.79	$16.79^{+1.16}_{-1.37}$	$-0.95^{+0.02}_{-0.02}$	$562.9^{+15.1}_{-21.1}$	$-2.8^{+0.04}_{-0.09}$	$26.0^{+3.7}_{-2.9}$	$34.25^{+1.36}_{-1.6}$	118.77 ± 0.86	4.4 ± 0.1	433.6 / 462	0.82
202.79 - 203.81	$17.12^{+1.36}_{-1.9}$	$-1.01^{+0.02}_{-0.03}$	$470.8^{+21.6}_{-34.5}$	$-2.63^{+0.04}_{-0.13}$	$15^{+3.4}_{-2.5}$	$33.31^{+1.92}_{-2.65}$	83.83 ± 0.75	2.8 ± 0.1	489.0 / 462	0.19
203.81 - 204.83	$12.32^{+1.21}_{-1.76}$	$-0.98^{+0.02}_{-0.04}$	$490.3^{+30.5}_{-44.7}$	$-2.46^{+0.04}_{-0.11}$	$15.0^{+5.1}_{-3.3}$	$30.16^{+2.36}_{-3.36}$	67.95 ± 0.69	2.6 ± 0.1	473.9 / 462	0.34
204.83 - 205.86	$12.75^{+1.19}_{-1.66}$	$-1.0^{+0.02}_{-0.04}$	$458.7^{+22.8}_{-38.2}$	$-2.7^{+0.06}_{-0.17}$	$17.0^{+3.5}_{-2.7}$	$31.93^{+1.75}_{-2.38}$	65.37 ± 0.68	2.1 ± 0.2	472.2 / 462	0.36
205.86 - 206.88	$8.45^{+1.48}_{-2.13}$	$-0.91^{+0.05}_{-0.1}$	$288.4^{+33.6}_{-45.7}$	$-2.43^{+0.04}_{-0.12}$	$23.0^{+10.7}_{-6.3}$	$25.15^{+2.63}_{-4.92}$	54.18 ± 0.64	1.5 ± 0.2	471.0 / 462	0.38
206.88 - 207.91	0	0	0	0	0	0	0	0	0	0

small), the 2SBPL improves the SBPL fit at more than 3σ, which I take as the threshold value for the definition of the best fit model. More specifically, in all these 19 spectra the fit improves at more than 4.8σ (more than 8σ in 13 cases).

Figure 3.4 shows the distributions of the spectral indices of the 2SBPL model fits. If modelled with Gaussian functions, the mean values are $\langle \alpha_1 \rangle = -0.63$ ($\sigma = 0.08$) and $\langle \alpha_2 \rangle = -1.48$ ($\sigma = 0.09$). These values are remarkably consistent with standard synchrotron fast cooling emission, predicting $\alpha_1^{\rm syn} = -2/3$ and $\alpha_2^{\rm syn} = -3/2$, represented with the vertical dashed lines.

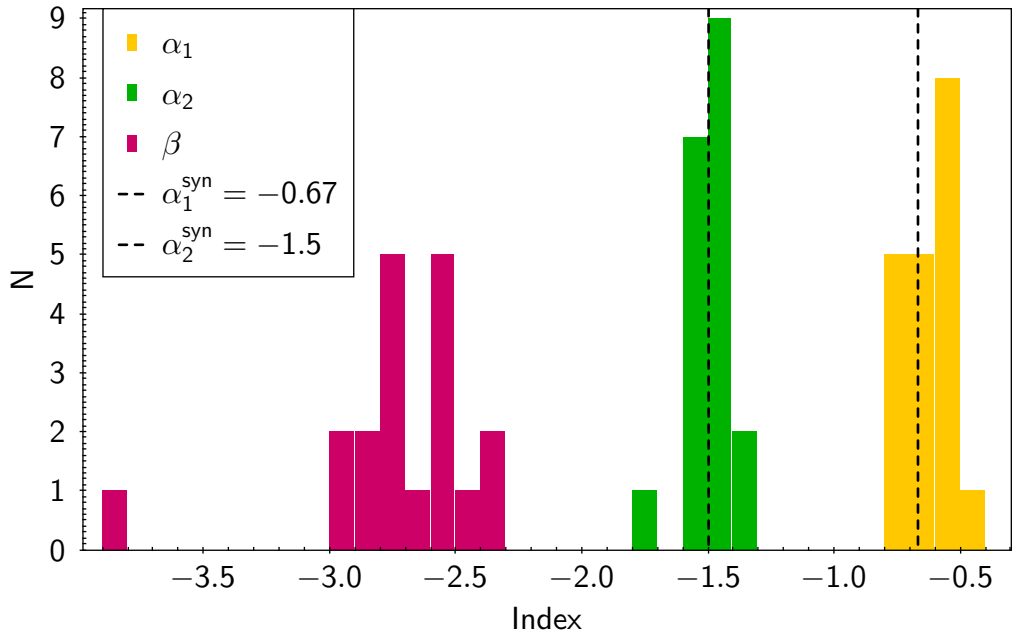

FIGURE 3.4: Distributions of the spectral indices of the three power-law segments of the 2SBPL model (values in Table 3.2) obtained from the time-resolved analysis of GRB 160625B. The vertical dashed lines are the expected values for synchrotron emission in the fast cooling regime.

The SBPL+BB model also leads to similar improvements of the fit over the SBPL. In all

the time-resolved spectra, the fits with the 2SBPL and with the SBPL+BB systematically shift the spectral peak at slightly higher values than the SBPL. A comparison between SBPL and SBPL+BB in terms of F-test, however, cannot be performed. A comparison between 2SBPL and SBPL+BB can instead be performed by comparing the probability of their χ^2. The χ^2 probability is reported in Table 3.2 and Table 3.3 for each time-resolved spectrum, for the 2SBPL and SBPL+BB models, respectively. The two probabilities are compared in Fig. 3.5, where the equality line is shown as a solid black line. The probabilities of the 2SBPL are systematically higher than those resulting from an SBPL+BB fit. In the spectrum accumulated at the peak of the lightcurve (corresponding to the leftmost point in the plot), the statistical comparison firmly favours the 2SBPL model over the SBPL+BB: $\chi^2_{\rm 2SBPL} = 1.07$ ($P_{\rm 2SBPL} = 0.15$) and $\chi^2_{\rm SBPL+BB} = 1.23$ ($P_{\rm 2SBPL} = 6 \times 10^{-4}$). Indeed, the deviation from the equality line happens for spectra in which the observed flux is high ($\gtrsim 8$ erg/cm^2/s^{-1}), not only for the peak of the lightcurve. On the contrary, when the flux is dimmer, the fit probabilities of the 2SBPL and SBPL+BB models are similar.

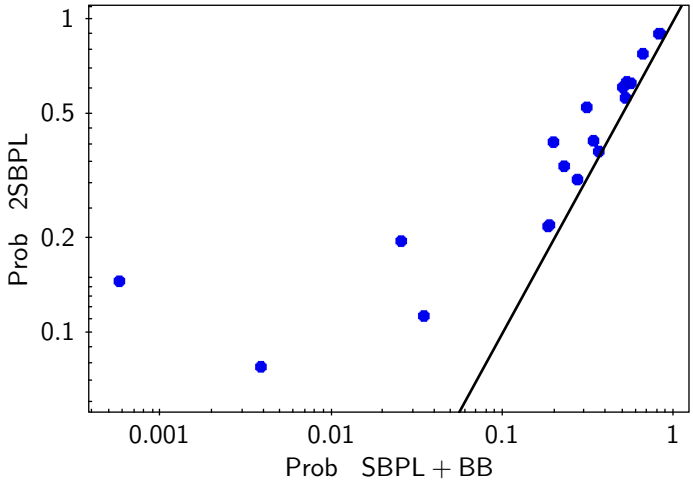

FIGURE 3.5: Fit probability for time-resolved spectra of GRB 160625B: comparison between fits performed with a 2SBPL model (y-axis) and with a SBPL+BB model (x-axis). The two models have the same number of degrees of freedom. The equality line is shown as a solid black line.

3.1.2.2 Spectral evolution of the 2SBPL parameters

The temporal evolution of the spectral parameters inferred from the 2SBPL fits are reported in Fig. 3.6. The upper panel shows the light curve of the main emission episode with a 1.024 s temporal resolution. The vertical dashed lines denote the time bins selected for time-resolved spectral analysis. In the second and third panel, the evolution of the photon indices are displayed. The fourth panel shows the temporal evolution of $E_{\rm peak}$ (red symbols) and $E_{\rm break}$ (blue symbols). Their ratio is given in the bottom panel.

$E_{\rm peak}$ exhibits a strong evolution (a softening) in the first 5 seconds, after which it settles to a nearly constant value ($E_{\rm peak} \sim 500 - 600$ keV). $E_{\rm break}$ displays a similar evolution, but the initial softening is much less pronounced. After the first few seconds, $E_{\rm break}$ also becomes constant (settling on $E_{\rm break} \sim 100$ keV). The ratio $E_{\rm peak}/E_{\rm break}$ varies from ~ 35 at the very beginning to $\sim$5 at later times.

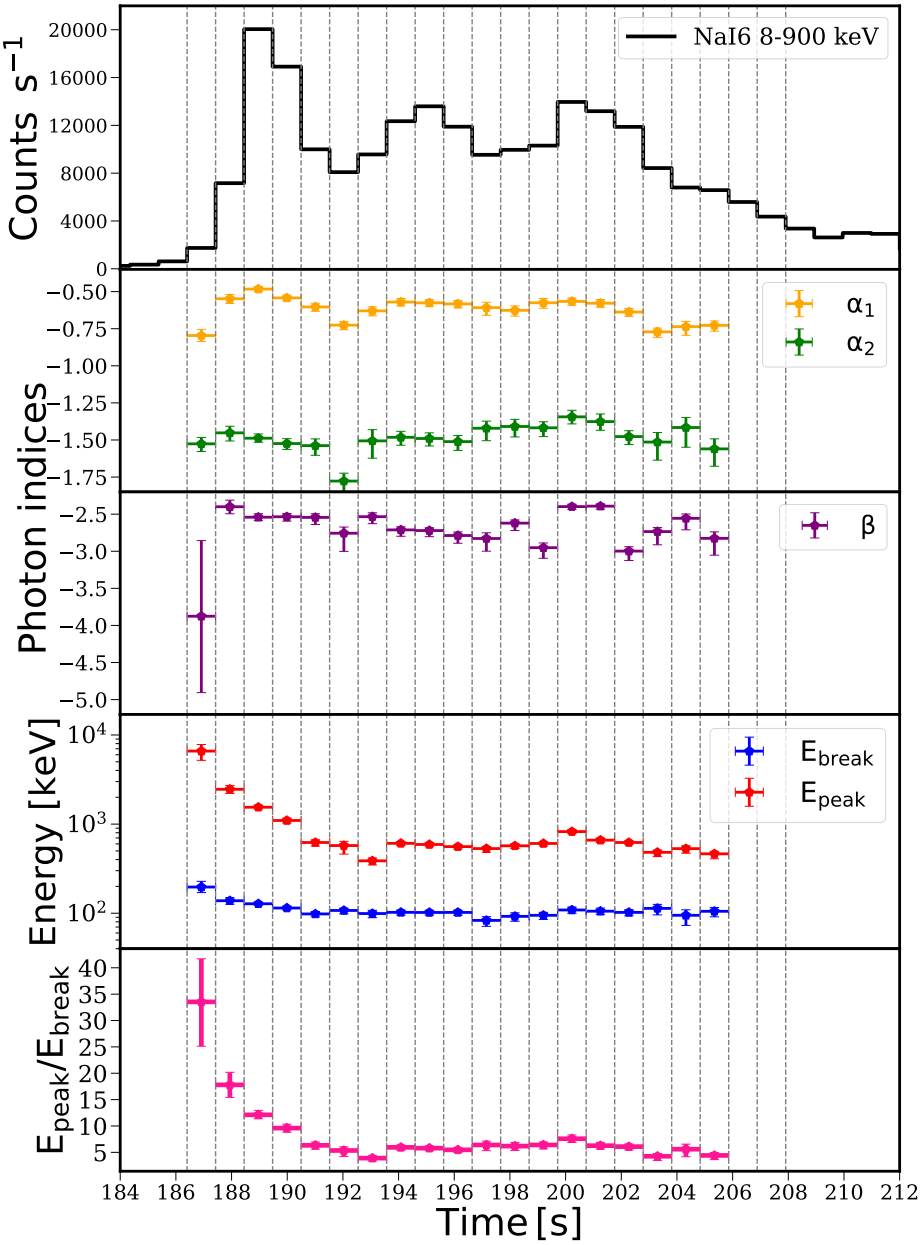

FIGURE 3.6: Time evolution of the spectral parameters of the 2SBPL model (Table 3.1) for the main episode of GRB 160625B. Parameters values are shown only for time-resolved spectra where the 2SBPL fit improves at more than 3σ the SBPL fit (all bins but the last two). From top to bottom: Count rate light curve (with 1.024 s time resolution), photon indices below and above the break (yellow and green symbols, respectively), spectral index above the peak energy (purple symbols), peak and break energy (red and blue symbols, respectively), and ratio between peak and break energy (pink symbols). For an explanation of the notation used for the 2SBPL parameters, see Fig. 2.11 (red line).

I also investigated the presence of a correlation between E_{peak} and E_{break}; E_{peak} versus E_{break} is shown in Fig. 3.7. For all the statistical tests, the significance level is set at 0.05, i.e. the null hypothesis is accepted if $p > 0.05$. The Spearman correlation coefficient is $\rho = 0.61$, with a chance probability $P = 0.009$, thus rejecting the null hypothesis that the

two energies are uncorrelated. Assuming a power-law model, I found:

$$\frac{E_{\rm peak}}{700\,{\rm keV}} = (0.81 \pm 0.06)\left(\frac{E_{\rm break}}{100\,{\rm keV}}\right)^{3.69\pm0.26}. \tag{3.1}$$

The power-law fit is shown in Fig. 3.7 by a solid black line. However, the strong time evolution of $E_{\rm peak}$ occurring in the first four time bins of the emission, which are marked in red in Fig. 3.7, may affect the correlation, which does not seem to persist at later times (blue points).

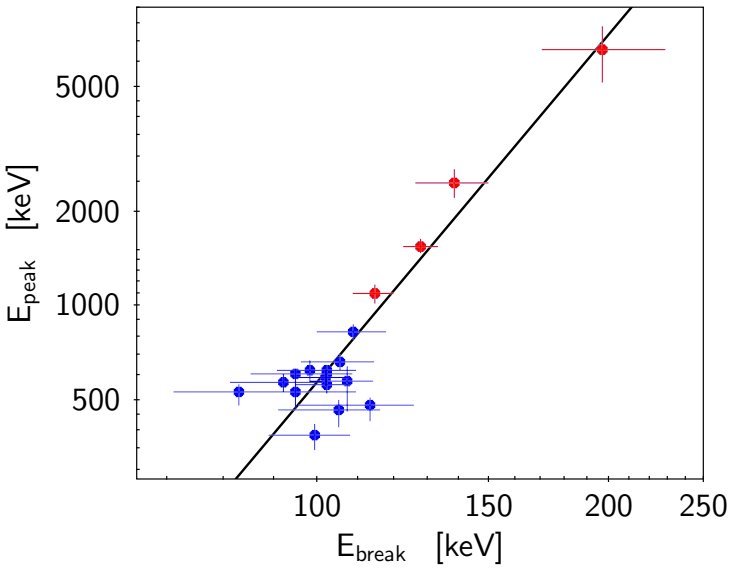

FIGURE 3.7: Correlation between the peak energy $E_{\rm peak}$ and the break energy $E_{\rm break}$ of the 2SBPL model in the time-resolved analysis. The values from the first four time bins are indicated by red symbols, while later times are by blue symbols. Error bars show uncertainties at 1σ.

3.1.2.3 Discussion on BB component

As shown above, the spectral fits largely improve both when a BB component is added to the SBPL (SBPL+BB) and when the SBPL is modified to have another break (2SBPL). Notably, the break energy of the 2SBPL coincides with the peak of the BB component. This is due to the fact that the two competing functions try to model the same feature at low energy. However, as shown in Fig. 3.5, the 2SBPL probability is always larger than the SBPL+BB one. Here I give a tentative explanation of why the data favours the 2SBPL model over the SBPL+BB.

Let's assume that the correct model is a 2SBPL. In the SBPL+BB fit, the BB is used to model the break energy and the peak of the non-thermal component is used to model the peak of the spectrum. When these two features ($E_{\rm break}$ and $E_{\rm peak}$) are far from each other, the SBPL+BB model produces a dip between the BB peak and the SBPL peak. If such a dip is not present in the data, the SBPL+BB model is then forced (in order to minimize the chi-square) to lower the value of the SBPL peak energy in order to explain the continuity, with no deficiency, in the flux between $E_{\rm break}$ and $E_{\rm peak}$. This will result in a slightly worse modelling of the data around the spectral peak. This is indeed what happens in the spectrum at the peak of the light curve: the SBPL+BB function seems to underestimate the energy of the spectral peak ($E_{\rm peak}^{\rm SBPL+BB} \sim 1\,{\rm MeV}$), which is instead better modelled by the 2SBPL function ($E_{\rm peak}^{\rm 2SBPL} \sim 1.5\,{\rm MeV}$).

For all those cases when the 2SBPL and the SBPL+BB return comparable and acceptable fits, another argument can be invoked to support the choice of a 2SBPL. The 2SBPL is a single component model with two breaks and three powerlaws (as the synchrotron emission model above the self–absorption frequency). It returns photon indices, below the break and between the break and the peak, that are remarkably close to those expected in synchrotron spectra (see Fig.3.4). On the other hand the SBPL+BB requires to have two components, a thermal and non–thermal one. While the thermal component is produced at the transparency of the photosphere, the non–thermal component is the result of some non-thermal mechanism that does not have a straightforward interpretation, since its low-energy photon index has a distribution peaked at $\langle\alpha\rangle = -0.88$ ($\sigma = 0.21$).

In the case of GRB 160625B, I also tested how the two models compare when their low-energy power-law slope is fixed to the value expected for synchrotron emission, i.e. $-2/3$. While most (90%) of the fits with the 2SBPL$_{-2/3}$ have a χ^2 probability $> 10^{-2}$, and the best fit parameters are similar to those obtained when the low-energy spectral index is left free to vary, in the case of the SBPL+BB$_{-2/3}$ only 45% of the time-resolved spectra have a probability $> 10^{-2}$.

GRB 160625B: summary of the results

In this section, I showed that both the time-integrated and the time-resolved spectra of GRB 160625B, one of the brightest burst ever detected by *Fermi*/GBM, are characterized by the presence of two spectral breaks, one at low-energy ($E_{\rm break} \sim 80 - 200$ keV) and the other at 5-35 times higher energies, representing the peak in $\nu F\nu$ ($E_{\rm peak} \sim 300$ keV – 6 MeV). While $E_{\rm peak}$ shows a strong softening with time in the first few seconds, $E_{\rm break}$ evolves more slowly and after the first few seconds, both $E_{\rm break}$ and $E_{\rm break}$ becomes constant (settling on $E_{\rm break} \sim 100$ keV and $E_{\rm peak} \sim 500 - 600$ keV). This reflects into the ratio of the two energies: at the beginning $E_{\rm peak}/E_{\rm break} \sim 35$ while at later times it decreases to $\sim$5. The distributions of the spectral indices below and above the break at low energies are consistent with the synchrotron predicted values in marginally fast cooling regime (i.e. with the cooling frequency ν_c smaller but comparable to the characteristic frequency ν_m: $\nu_c \leq \nu_m$).

These results show that the additional spectral breaks found in the X–rays by analyzing *Swift* data (Oganesyan et al., 2017; Oganesyan et al., 2018), can be also present at higher energies, at least in GRB 160625B. These results confirm also the presence of a spectral break in the data of another instrument, the *Fermi*/GBM, which hold some advantages with respect to *Swift*. Using GBM data, there is no need to perform a joint analysis of the data detected from two different instruments, like *Swift*/BAT and *Swift*/XRT. Moreover, GBM data are not affected by the absorption and by strong pile-up effects, two problems that can make XRT data more difficult to be analyzed. Both these two effects produce a hardening of the spectrum at low energy, thus must be carefully taken into account when searching for the presence of a spectral break.

Given the successful results obtained on GRB 160625B, the natural consequent question is whether this feature is present in other bursts detected by *Fermi* or if it is a unique case due to some peculiar properties of GRB 160625B. It is interesting to investigate both the solutions, because in the first case (if it is a common feature in GRBs), it would be a great result but it has to be explained why this feature has never been detected before. The second possibility requires to explain why GRB 160625B has such peculiar properties that makes it to behave in a different way with respect to other GRBs with similar characteristics. In the next Section, I will describe the investigation I performed on a larger sample of bright GRBs.

3.2 Extension of the analysis to a larger sample

To understand if the results from GRB 160625B are peculiar or more general, I extended my research to a larger sample of GRBs detected by the *Fermi*/GBM, to systematically search for the additional low-energy break. Since the presence of this feature has been reported only in long GRBs, I extended the search for the first time also to short GRBs. The aim is searching for the presence of the same feature in two different populations of GRBs, that share some common characteristics but have different progenitors. I sorted the GRBs present in the GBM Catalogue by the fluence of their best fitting model (in the 10-1000 keV energy range) and selected the first 10 GRBs of the list. Therefore, the selection consists of a total of 20 GRBs analyzed, the brightest 10 long and 10 short, listed respectively in Table 3.4 and Table 3.7. This work has been published on the A&A journal (Ravasio et al., 2019a).

In the following sections, I present the results obtained on the long and the short GRBs sub-samples. The data extraction, detectors used, inter–calibration constant factor, channels excluded and background modeling are described in Appendix A. CSPEC data have been used for long GRBs, while Time Tagged Event (TTE) have been used data for short GRBs. For the time-resolved analysis, the light-curves have been rebinned imposing a signal-to-noise ratio $S/N > 60$ on the most illuminated NaI detector. The choice of optimising the S/N of the NaI, regardless of the S/N in the BGO, is motivated by the interest in the low energy break, that (if present) lies around 100 keV, as the analysis of GRB 160625B revealed, i.e. within the energy range of the NaI detectors (8 – 900 keV). Given the relatively large value of the S/N ratio, the χ^2 statistic is used in the fitting procedure.

I analyzed both time–integrated and time–resolved spectra with two different empirical functions, the SBPL and the 2SBPL. As done for GRB 160625B, I fixed the values of the parameters describing the curvatures around the break and the peak energies, both for the SBPL (n) and for the 2SBPL (n_1 and n_2). However, this time I changed the values of the curvatures. Since I wanted to test a synchrotron origin, I chose values of the curvatures that reproduce the shape of synchrotron spectra. I compared the SBPL and 2SBPL functions to a synthetic synchrotron spectrum from a population of partially cooled electrons to find for which values of the curvatures these empirical functions mimic the shape of the synchrotron spectrum. I repeated the test for different cooling efficiencies (i.e., for different values of the ratio $E_{\rm peak}/E_{\rm break}$) and derived that the most suitable value for the curvature is $n = 2$, for both the break and the peak energies. These values correspond to very smooth curvatures.

3.2.1 The 10 brightest long GRBs

Following the selection mentioned above, the resulting sample contains the 10 long GRBs with the largest fluence detected by *Fermi* in its almost 10 years of activity. This selection corresponds to a cut in fluence $F > 1.79 \times 10^{-4}\,{\rm erg\,cm^{-2}}$ (see Table 3.4). From this sample I excluded GRB 090902B (in addition to GRB 130427A), since it shows a prominent high–energy emission detected by the LAT instrument during the prompt phase, which extends to the low energies and dominates the emission below ~ 30 keV (Abdo et al., 2009a). Moreover, as shown in Ryde et al., 2010 and Pe'er et al., 2012, its spectrum seems to be dominated by a thermal photospheric emission component. Both features prevent the identification of a possible low–energy break in the main spectral component, which is the feature I want to investigate.

This selection includes also GRB 160625B. For homogeneity, I reanalysed its spectra with the same new procedure adopted for the other bursts, finding results which are consistent with those presented in Sec. 3.1.

TABLE 3.4: The ten long GRBs with the largest fluence (10–1000 keV) in the GBM catalogue. The last three digits in the name (in square brackets) refer to the naming convention of GBM triggers. The prompt duration and the 10–1000 keV fluence of the time–integrated spectra are listed in columns 2 and 3, and refer to information reported in the online GBM catalogue. The last column reports the redshift, if available.

GRB Name	T_{90} [s]	Fluence [10^{-4} erg cm^{-2}]	Redshift
171010[792]	107.27 ± 0.81	6.72 ± 0.02	0.3285
160625[945]	453.38 ± 0.57	6.68 ± 0.02	1.406
160821[857]	43.01 ± 0.72	5.48 ± 0.02	–
170409[112]	64.0 ± 0.72	3.19 ± 0.01	–
180720[598]	48.9 ± 0.36	3.18 ± 0.01	0.654
171227[000]	37.63 ± 0.57	3.05 ± 0.01	–
090618[353]	112.39 ± 1.09	2.74 ± 0.02	0.54
100724[029]	114.69 ± 3.24	2.43 ± 0.01	–
130606[497]	52.22 ± 0.72	2.15 ± 0.01	–
101014[175]	449.42 ± 1.41	1.79 ± 0.01	–

3.2.1.1 Results of the spectral analysis: time–integrated

The results of the time–integrated analysis for the sample of long GRBs are reported in Table 3.5. For each GRB, the table reports the GRB name (in bold font if the best fit model is a 2SBPL, i.e. if a break is present), the time interval used for the time-integrated spectral analysis, the best fit parameters of the best fit model (either a SBPL or a 2SBPL) chosen according to the significance of the F–test (last column), and the total χ^2/d.o.f. (degrees of freedom).

TABLE 3.5: Best-fit parameters inferred from the time-integrated analysis of the 10 long GRBs. In bold font are highlighted those GRBs with a statistically significant spectral break $E_{\rm break}$ in the low-energy part of their spectrum. The table lists the GRB name, the time interval over which the spectrum has been accumulated, and the results from the spectral analysis: best fit normalization, photon index α_1 (or α when the best fit model is a SBPL), break energy $E_{\rm break}$ (only if the best fit model is a 2SBPL), photon index α_2 (only if the best fit model is a 2SBPL), peak energy $E_{\rm peak}$, photon index β, total chi-square and degrees of freedom (dof), and the significance of the improvement of the fit from a SBPL to a 2SBPL (estimated according to the F-test).

Name	Time interval [s]	Norm [ph/s cm^2 keV]	α_1 (α)	$E_{\rm break}$ [keV]	α_2	$E_{\rm peak}$ [keV]	β	χ^2/dof	$F_{\rm test}$
171010	[0.003 - 100.35 s]	$0.12^{+0.04}_{-0.04}$	$+1.16^{+0.13}_{-0.13}$	$12.39^{+0.13}_{-0.13}$	$-1.4^{+0.01}_{-0.01}$	$182.2^{+1.8}_{-1.8}$	$-2.7^{+0.02}_{-0.02}$	829.22 / 335	$> 8\sigma$
160625	[187.43 - 212.00 s]	$4.58^{+0.15}_{-0.15}$	$-0.56^{+0.01}_{-0.01}$	$119.9^{+3.79}_{-3.79}$	$-1.7^{+0.03}_{-0.03}$	$646.5^{+18.0}_{-18.0}$	$-2.67^{+0.03}_{-0.03}$	638.55 / 342	$> 8\sigma$
160821	[117.76 - 154.63 s]	$9.08^{+0.48}_{-0.51}$	$-0.87^{+0.02}_{-0.02}$	$158.4^{+21.4}_{-22.3}$	$-1.59^{+0.05}_{-0.05}$	$1295.0^{+55.8}_{-50.0}$	$-2.61^{+0.05}_{-0.05}$	411.91 / 226	$> 8\sigma$
170409	[17.66 - 116.99 s]	$1.68^{+0.07}_{-0.07}$	$-0.88^{+0.01}_{-0.01}$	$315.3^{+24.1}_{-24.3}$	$-1.78^{+0.05}_{-0.05}$	$1156.0^{+93.4}_{-81.5}$	$-3.39^{+0.18}_{-0.15}$	527.62 / 347	$> 8\sigma$
180720	[-1.02 - 56.32 s]	$4.19^{+0.85}_{-0.77}$	$-0.73^{+0.08}_{-0.09}$	$38.12^{+12.6}_{-8.32}$	$-1.48^{+0.06}_{-0.05}$	$774.8^{+50.0}_{-36.9}$	$-2.61^{+0.07}_{-0.05}$	589.06 / 343	$> 8\sigma$
171227	[0.003 - 58.24 s]	$1.92^{+0.14}_{-0.14}$	$-0.75^{+0.02}_{-0.02}$	$153.3^{+14.4}_{-14.5}$	$-1.68^{+0.05}_{-0.05}$	$1064.0^{+81.5}_{-69.8}$	$-2.98^{+0.11}_{-0.1}$	466.24 / 344	$> 8\sigma$
090618	[0.003 - 161.28 s]	$2.27^{+0.43}_{-1.1}$	$-0.19^{+0.07}_{-2.83}$	$7.75^{+1.26}_{-0.81}$	$-1.5^{+0.02}_{-0.03}$	$157.2^{+6.8}_{-6.27}$	$-2.87^{+0.1}_{-0.1}$	339.3 / 231	4.1σ
100724	[-5.12 - 137.22 s]	$1.26^{+0.05}_{-0.05}$	$-0.87^{+0.01}_{-0.01}$	-	-	$659.9^{+132.0}_{-75.0}$	$-2.05^{+0.02}_{-0.02}$	444.62 / 339	1.0σ
130606	[-3.07 - 70.66 s]	$10.17^{+0.37}_{-0.36}$	$-1.19^{+0.01}_{-0.01}$	-	-	$600.7^{+69.9}_{-52.4}$	$-2.11^{+0.02}_{-0.02}$	483.38 / 333	2.0σ
101014	[0.003 - 466.44 s]	$0.6^{+0.04}_{-0.1}$	$-0.05^{+0.03}_{-0.0}$	$10.99^{+0.88}_{-0.91}$	$-1.38^{+0.03}_{-0.04}$	$221.7^{+18.3}_{-14.9}$	$-2.35^{+0.08}_{-0.07}$	488.14 / 342	7.4σ

According to the F–test, in 2 long GRBs the improvement of the χ^2 caused by the inclusion of a low-energy break in the fitting function has a significance corresponding to 1σ and 2σ: in these two cases the best fit model is then a SBPL. On the contrary, in all the other 8 long GRBs the 2SBPL function significantly (i.e. at more than 3σ) improves the fit provided by the SBPL model. In particular, the improvement is significant at more than 8σ in six cases and between 4σ and 8σ in two cases. This means that in 8 of the 10 brightest long GRBs the time–integrated spectrum shows the presence of two characteristic energies: a low–energy spectral break $E_{\rm break}$ (typically between few tens and few hundreds of keV) and the usual peak of the νF_ν spectrum $E_{\rm peak}$ (typically between few hundreds and few thousands of keV, see Table 3.5).

In three cases where the presence of the low energy spectral break is highly supported by the significance of the F–test (namely GRB 171010, GRB 090618 and GRB 101014), the break energy is located at $E_{\rm break} \sim 10$ keV, very close to the low–energy edge of the GBM (~ 8 keV): very few data points are available below the break to properly constrain the value of photon index α_1. In all these cases, I found that the best fit value of α_1 reaches very hard values, at odd with results derived when $E_{\rm break}$ is located at higher energies, far from the low–energy edge of the instrument. I will discuss this issue in more details in the next section. In calculating mean values, I therefore included only spectra with $E_{\rm break} > 20$ keV. For the time-integrated analysis, the typical values of the parameters of the 2SBPL model are $\alpha_1 = -0.76^{+0.03}_{-0.03}$, $\alpha_2 = -1.65^{+0.05}_{-0.04}$, $\log(\mathrm{E_{break}}) = 2.11^{+1.11}_{-1.08}$, $\log(\mathrm{E_{peak}}) = 2.98^{+1.72}_{-1.66}$ and $\beta = -2.85^{+0.09}_{-0.08}$.

3.2.1.2 Results of the spectral analysis: time–resolved

For the 8 long GRBs showing a low energy break, I also performed time–resolved analysis, to investigate the presence of the break in shorter time–scales and its temporal evolution. The time–resolved spectral analysis is performed on temporal bins of 1.024 s width, but if there are two (or more) consecutive time bins where the 2SBPL does not produce a better fit (i.e., with significance $< 3\sigma$), I combined them together in order to acquire more statistics and further test the presence of a spectral break. This procedure shows that, in most cases, the break is constrained also in the temporal bins with 1 s resolution. In the other cases, it is sufficient to combine 2–3 consecutive bins to constrain $E_{\rm break}$. This time–rebinning has been applied to $\sim 28\%$ of the time–resolved spectra.

Fig. 3.8 shows the time evolution of the best–fit parameters. In particular, for each GRB the upper panel shows the light–curve, while the lower panels show the results of the spectral analysis: from top to bottom the spectral indices α_1 and α_2 (or α only, if the best fit model is a SBPL), the photon index β, the characteristic energies $E_{\rm break}$ and $E_{\rm peak}$ (or $E_{\rm peak}$ only, if the best fit model is a SBPL), and the ratio $E_{\rm peak}/E_{\rm break}$.

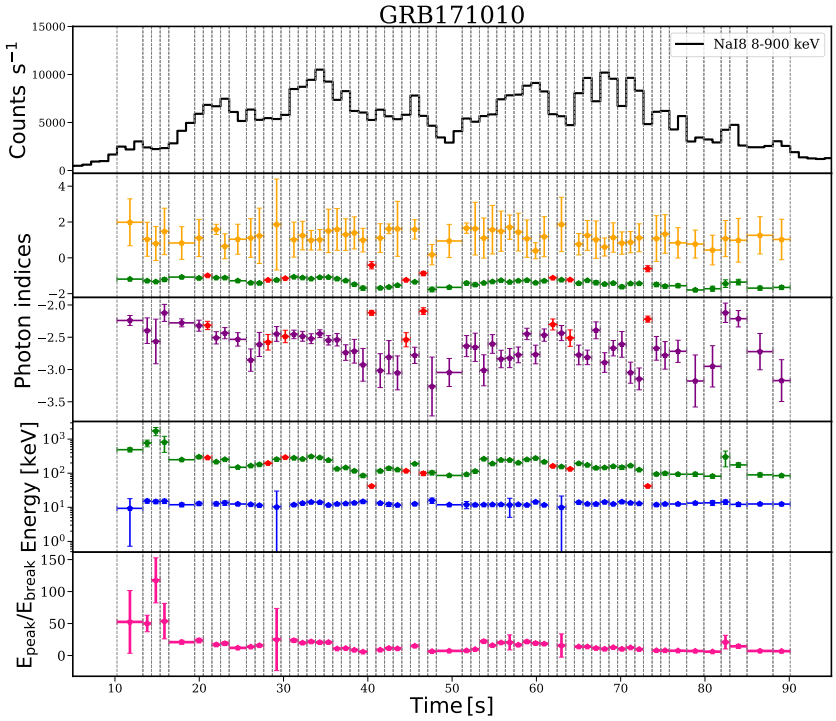
GRB171010
NaI8 8-900 keV
Counts s^{-1}
Photon indices
Energy [keV]
E_{peak}/E_{break}
Time [s]

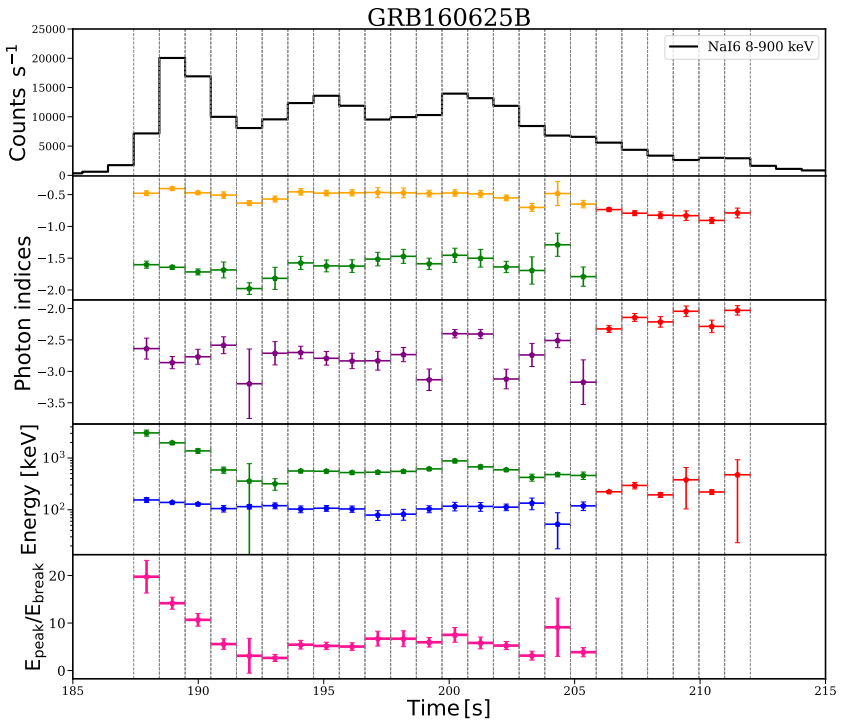
GRB160625B
NaI6 8-900 keV
Counts s^{-1}
Photon indices
Energy [keV]
E_{peak}/E_{break}
Time [s]

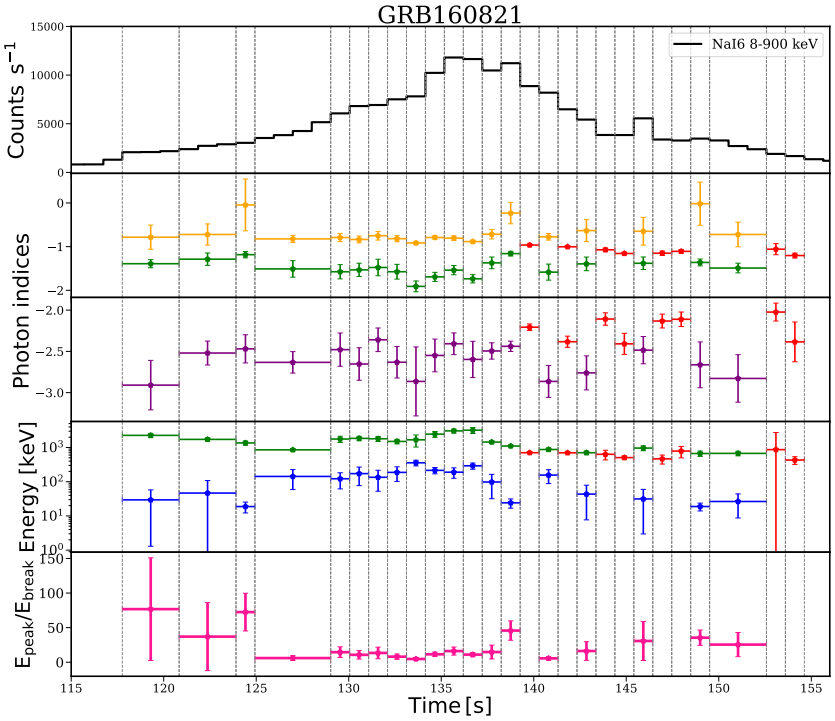
GRB160821
NaI6 8-900 keV
Counts s^{-1}
Photon indices
Energy [keV]
E_{peak}/E_{break}
Time [s]

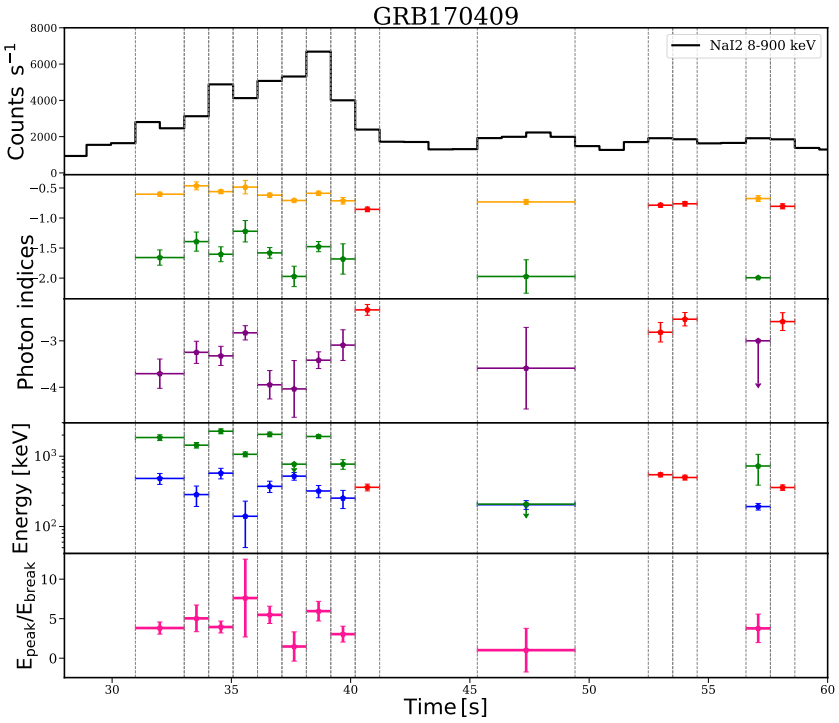
GRB170409
NaI2 8-900 keV
Counts s^{-1}
Photon indices
Energy [keV]
E_{peak}/E_{break}
Time [s]

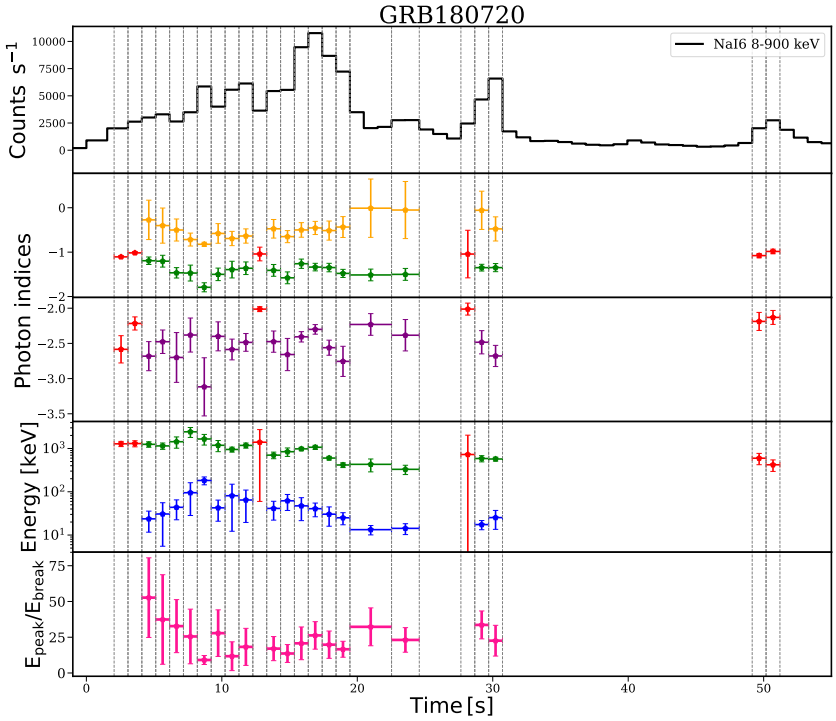
GRB180720
NaI6 8-900 keV
Counts s^{-1}
Photon indices
Energy [keV]
E_{peak}/E_{break}
Time [s]

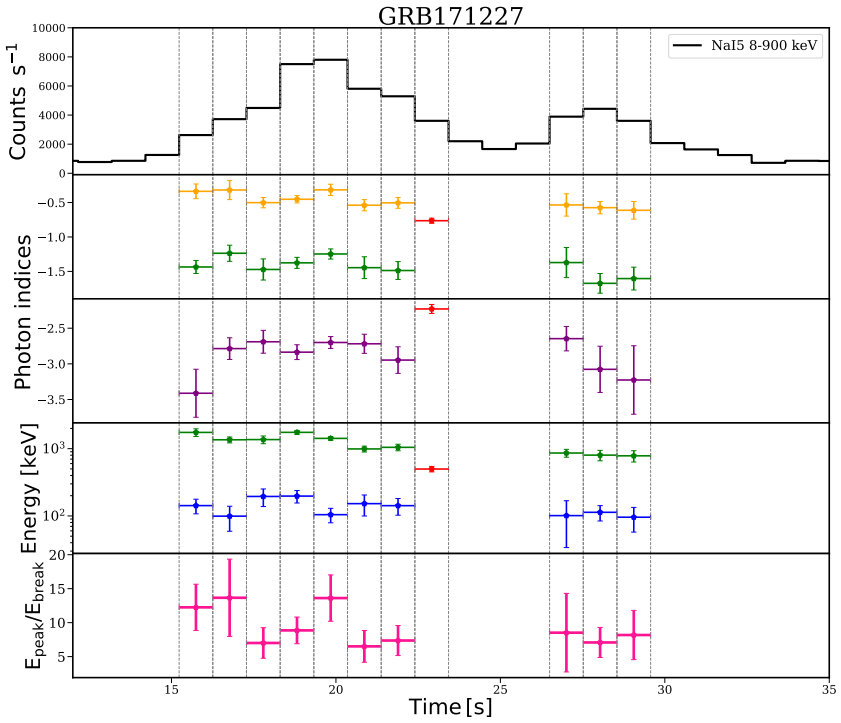
GRB171227
NaI5 8-900 keV
Counts s^{-1}
Photon indices
Energy [keV]
E_{peak}/E_{break}
Time [s]

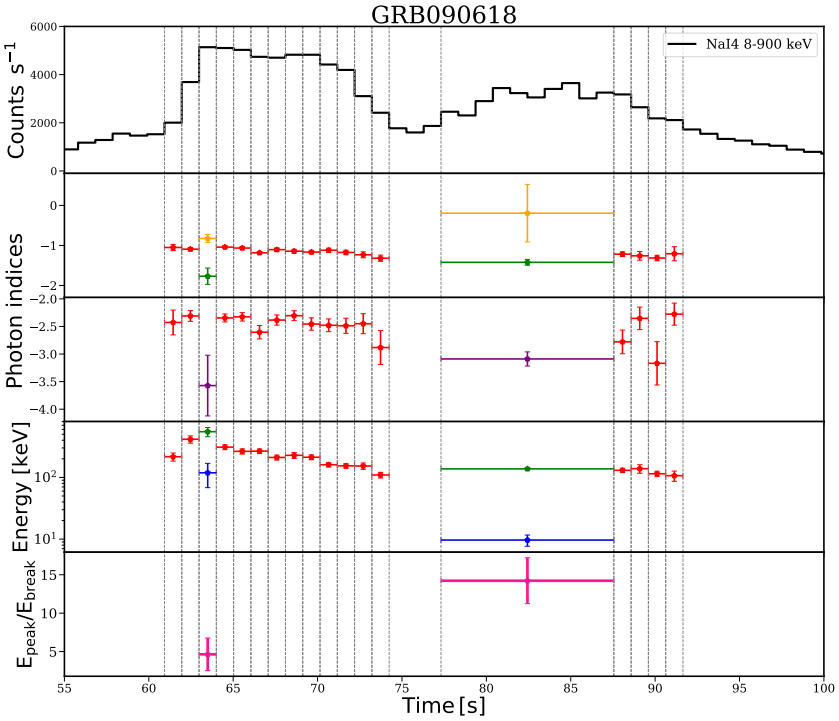
GRB090618
NaI4 8-900 keV
Counts s^{-1}
Photon indices
Energy [keV]
E_{peak}/E_{break}
Time [s]

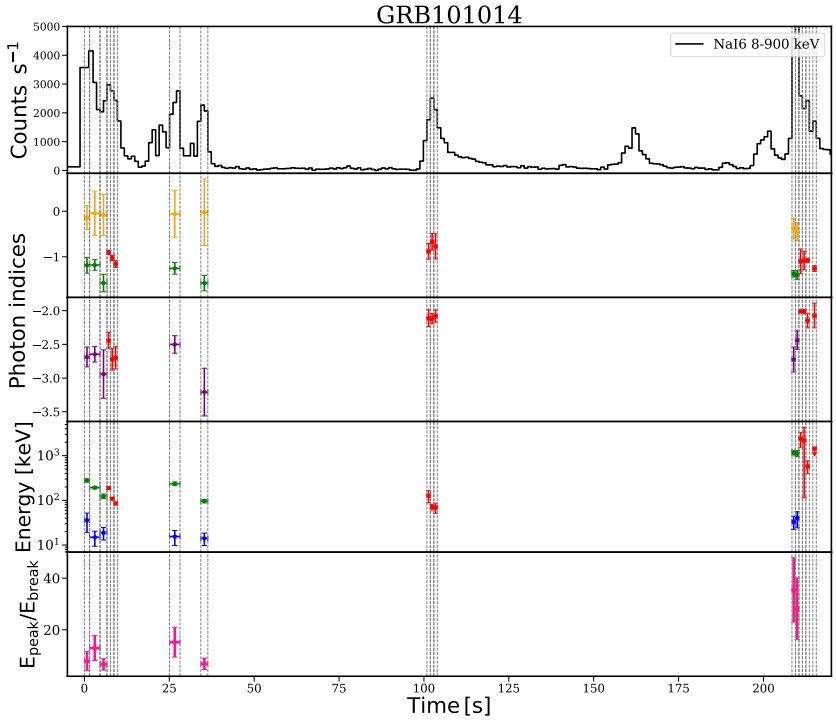

FIGURE 3.8: Lightcurve and temporal evolution of the best fit spectral parameters for each GRB with break energy identified in the time-integrated spectrum (i.e., 8 long GRBs). The vertical lines mark the time bins selected for the time-resolved analysis. In each figure, the top panel shows the lightcurve. In the panels below it is shown the temporal evolution of all best–fit parameters (of the 2SBPL or SBPL function, according to which model fits best the spectrum of the time bin). While all the parameters of the SBPL fit are shown as red points, different colours have been used to represent the parameters of the 2SBPL fit. In particular, from top to bottom, in the second panel there are the photon indices α_1 (yellow points), α_2 (green points) of the 2SBPL function, and α (red points) of the SBPL one. In the third panel there are the two photon indices β (in purple for the 2SBPL function and in red for the SBPL one). The fourth panel shows $E_{\rm break}$ (blue points) and $E_{\rm peak}$ (green points) for the 2SBPL, and $E_{\rm peak}$ for the SBPL (red points). The bottom panel shows the ratio $E_{\rm peak}/E_{\rm break}$.

In most of the time resolved spectra (139/199, i.e. $\sim$70%) the best fit model is the 2SBPL function. An example of a spectrum fitted with the 2SBPL function is shown in Fig. 3.9. In particular it refers to the time bin 7.17 – 8.19 s of GRB 180720B. The best value for the low–energy break is $E_{\rm break} = 93.62^{+91.6}_{-64.1}$ keV and the photon indices of the power–law below and above it are $\alpha_1 = -0.71^{+0.13}_{-0.46}$ and $\alpha_2 = -1.47^{+0.20}_{-0.26}$, while the peak energy is $E_{\rm peak} = 2.42^{+1.02}_{-0.64}$ MeV and the high–energy photon index $\beta = -2.38^{+0.23}_{-0.30}$. The plot also shows for comparison the power–laws expected from synchrotron emission (dashed lines).

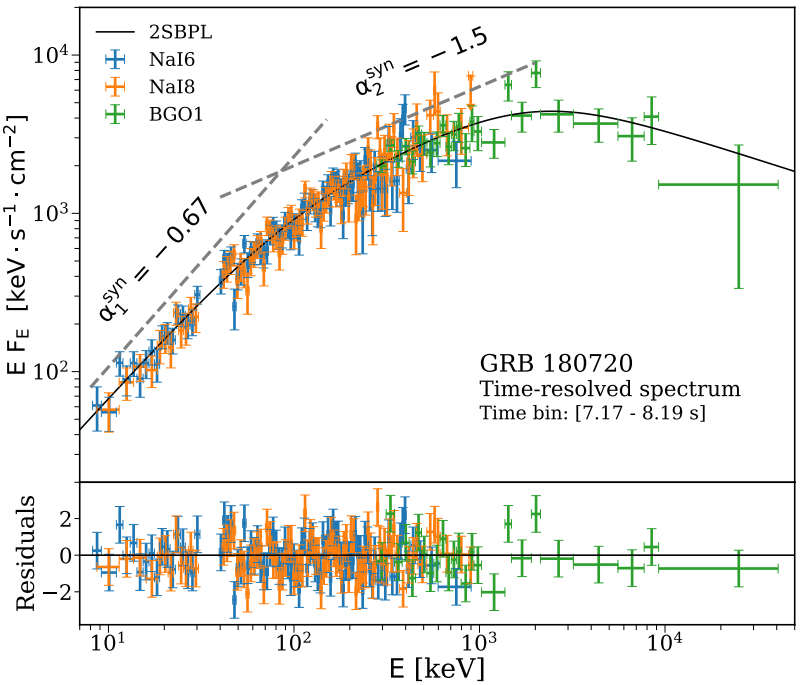

FIGURE 3.9: Example of a time–resolved spectrum of a long GRB best fitted by a 2SBPL (i.e., three power–laws smoothly connected at two breaks). The data correspond to the time interval 7.17 – 8.19 s from the trigger of GRB 180720. Different colours refer to different instruments, as reported in the legend. The best fit values of the 2SBPL model parameters are: $\alpha_1 = -0.71^{+0.13}_{-0.46}$, $E_{\rm break} = 93.62^{+91.6}_{-64.1}$ keV, $\alpha_2 = -1.47^{+0.20}_{-0.26}$, $E_{\rm peak} = 2.42^{+1.02}_{-0.64}$ MeV, and $\beta = -2.38^{+0.23}_{-0.30}$. The two dashed lines show, for comparison, the power–laws (with the photon indices) predicted by synchrotron emission. Data–to–model residuals are shown in the bottom panel.

As for the results of the time–integrated analysis, also in the time–resolved spectra there are cases where $E_{\rm break}$ is close to the low energy threshold of the *Fermi* band ($E_{\rm th} \sim 8$ keV). In particular, $E_{\rm break} < 20$ keV in all time–resolved spectra of GRB 171010 and in 10 of the 35 time–resolved spectra of GRB 090618 and GRB 101014 (note that these three GRBs are the same that have $E_{\rm break} < 20$ keV in the time–integrated spectrum). Before describing the results of the time-resolved analysis, I briefly comment on the spectra with $E_{\rm break} < 20$ keV.

In these spectra, α_1 behaves very differently as compared to typical α_1 values inferred for all the other spectra. Fig. 3.10 shows $E_{\rm break}$ vs. α_1 for the full sample of long GRBs (time-resolved analysis).

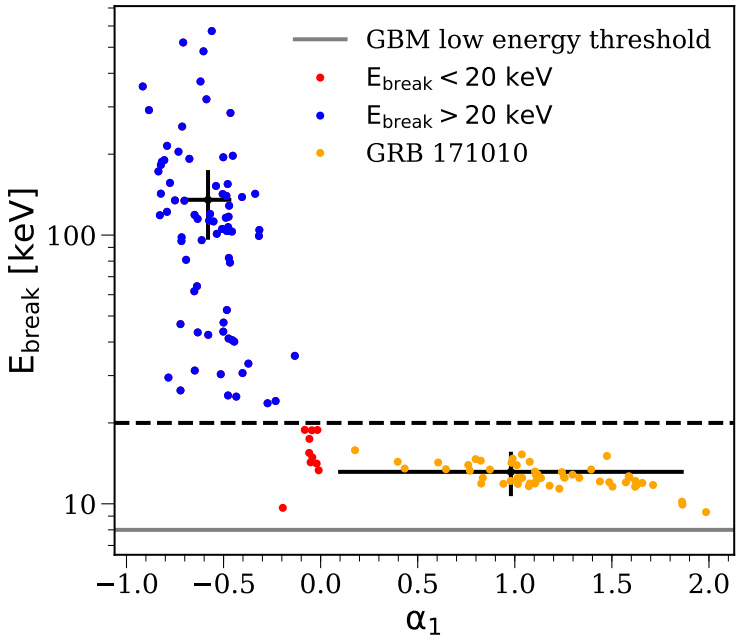

FIGURE 3.10: Relation between the break energy $E_{\rm break}$ and the index α_1 of the power-law describing the spectrum below $E_{\rm break}$. The sample includes all time-resolved spectra of the 10 long GRBs analysed in this work. The dashed black horizontal line marks a difference in behavior, with spectra below this line having very hard and ill-constrained best fit values of α_1. All the parameter distributions and their mean values and standard deviations presented in this Section rely only on spectra with $E_{\rm break}$ larger than this threshold value (blue points). The majority ($\sim$ 85%) of the spectra with $E_{\rm break} < 20$ keV (red points) belong to one specific GRB, namely GRB 171010 (orange points). The mean values of $E_{\rm break}$ and α_1 (along with their average errors) are represented for each sample with the solid black lines. The low energy threshold of the GBM NaI detectors is shown with a grey solid line.

A sudden change in the behaviour of α_1 is visible at low $E_{\rm break}$, with a well defined separation at $E_{\rm break} \sim 20$ keV (dashed horizontal line). In particular, spectra with $E_{\rm break} < 20$ keV (red and orange symbols) have considerably harder values of the low-energy photon index (i.e. $\alpha_1 > -0.2$) and the distribution of α_1 is more scattered. The uncertainty on these values is large, as shown by the black cross plotted on top of the orange/yellow points, which represents the average errors on the two parameters represented. When the break energy is $\gtrsim$20 keV, the distribution of α_1 is completely different, with almost no overlap between the two distributions. Also, the distribution is narrower and the typical error is smaller (black cross plotted on top of the blue points).

The peculiar distribution of the points in the $E_{\rm break}$-α_1 plane strongly suggests an instrumental effect at the origin of the hard values derived when $E_{\rm break} < 20$ keV. The low energy edge of sensitivity of the GBM is $E_{\rm th} \sim 8$ keV (solid grey line in Fig. 3.10), implying that when $E_{\rm break}$ is below 20 keV, a few channels are available for the determination of α_1. Even though this is most certainly true, it is less evident why in these cases α_1 should be systematically overestimated.

I also notice that $\sim$85% of the time resolved spectra with $E_{\rm break} < 20$ keV belong to a single GRB, i.e. 171010 (orange symbols in Fig. 3.10, see also Chand et al. 2018). *Swift*/XRT data (like in the GRBs analyzed by Oganesyan et al. 2017) would be of paramount importance in cases like this one, to better characterise the low-energy photon index. Unfortunately, for GRB 171010 there are no *Swift*/XRT data simultaneous to the GBM ones.

For the motivations explained above, I will consider in the following analysis the time resolved spectra with $E_{\rm break} > 20\,$keV. Table 3.6 summarizes all the results of the time–resolved analysis, showing the mean values and standard deviations of the best–fit parameters for each of the 7 long GRBs with the break energy $E_{\rm break} > 20\,$keV.

TABLE 3.6: Average results of the time-resolved analysis for the 7 long GRBs that display a low-energy break $E_{\rm break}$ in their time-integrated spectrum (see GRBs with name in bold font in Table 3.4; GRB 171010 is not included, because all time-resolved spectra have $E_{\rm break} < 20\,$keV). For each GRB, the table lists the mean value and standard deviation σ of the best-fit parameter distribution inferred from the time-resolved analysis for spectra with best fit model given by a 2SBPL and with $E_{\rm break} > 20\,$keV. The second column reports the number of spectra satisfying these conditions over the total number of spectra analysed.

Name	# of spectra	$\langle\alpha_1\rangle$	$\langle\alpha_2\rangle$	$\langle E_{\rm break}\rangle$ [keV]	$\langle E_{\rm peak}\rangle$ [keV]	$\langle\beta\rangle$
160625	18/24	−0.51 (0.08)	−1.62 (0.15)	110.66 (22.65)	805.98 (668.66)	−2.79 (0.24)
160821	17/27	−0.74 (0.15)	−1.51 (0.17)	133.49 (94.49)	1643.16 (745.55)	−2.62 (0.17)
170409	10/14	−0.62 (0.0)	−1.66 (0.25)	334.60 (141.47)	1304.06 (656.459)	−3.47 (0.37)
180720	15/24	−0.54 (0.14)	−1.41 (0.15)	55.67 (39.43)	1093.26 (481.31)	−2.58 (0.20)
171227	10/11	−0.47 (0.10)	−1.43 (0.13)	134.29 (36.39)	1212.26 (348.01)	−2.90 (0.24)
090618	1/18	−0.83 (0.10)	−1.77 (0.20)	118.56 (50.36)	550.05 (93.29)	−3.57 (0.55)
101014	3/17	−0.32 (0.23)	−1.32 (0.11)	36.31 (14.36)	862.77 (113.23)	−2.62 (0.16)
Mean values:		−0.58 (0.16)	−1.52 (0.20)	135.31 (112.15)	1177.59 (679.28)	−2.81 (0.37)

Figure 3.11 shows the distribution of the spectral indices α_1, α_2, and β of the 2SBPL model fits (filled histograms). These histograms are built considering the time–resolved spectra for which the 2SBPL is the best fit model. The inferred mean values are $\langle\alpha_1\rangle = -0.58$ (with standard deviation $\sigma_{\alpha_1} = 0.16$) and $\langle\alpha_2\rangle = -1.52$ ($\sigma_{\alpha_2} = 0.20$). These values are remarkably consistent with those predicted for a population of electrons emitting synchrotron radiation in the so–called "marginally fast cooling regime".

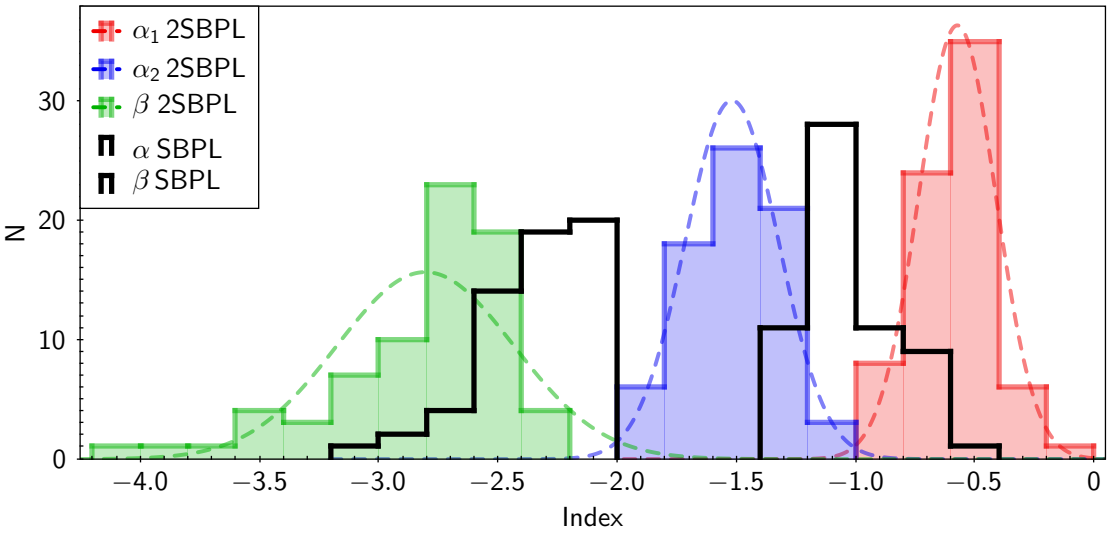

FIGURE 3.11: Long GRBs, time–resolved analysis: distribution of the spectral indices, according to the best fit model, for the time–resolved fits of the 8 long GRBs showing a spectral break. The spectral indices α_1, α_2 and β of the 2SBPL model are shown with red, blue and green filled histograms, respectively. Gaussian functions showing the central value and standard deviation of the distributions are overlapped to the histograms (color–coded dashed curves). The black empty histograms represent the distributions of the two photon indices α and β of the SBPL model, for spectra where the SBPL is the best fit model.

For comparison, Fig. 3.11 also shows the distributions (solid line, black histograms) of the spectral indices α and β (i.e. below and above the peak energy $E_{\rm peak}$, respectively) for those spectra sufficiently well fitted by the SBPL (i.e. $E_{\rm break}$ is not required according to the F–test). The distribution of the spectral index α of the SBPL model is consistent with the value $\langle\alpha\rangle = -1.02$ (σ_α = 0.19) typically reported in the literature which is obtained employing single break fitting functions (e.g. SBPL or Band). It is interesting to note that this distribution is placed almost in the middle of the two distributions of the spectral indices α_1 and α_2 of the 2SBPL model, namely of the two power–laws below and above $E_{\rm break}$. This seems to suggest that the underlying spectrum is made of two power–laws connected by a broad curvature. Since the change in the slopes is smooth rather than sharp, the spectrum below the peak energy is curved and the change in the slopes could be hidden by the broad curvature. Fitting the spectrum with only one power–law may return an intermediate slope between the two different components. This issue will be widely investigated and discussed in Sec. 3.3.

As done for GRB 160625B, I also performed the fit of the time resolved spectra by fixing the slope of the low-energy power-law index to the value $\alpha_1 = -2/3$ predicted by the synchrotron theory. I did this analysis for the spectra in which the low-energy power-law index is harder, at more than 1-σ, than -2/3. These represent 47% of the spectra. When α_1 is fixed to -2/3 in the 2SBPL model, most ($\sim$ 85%) of the time resolved spectra can still be adequately fitted (fit probability $> 10^{-2}$) and the other free parameters of the model assume values which are consistent, within their errors, with those obtained leaving α_1 free. This suggests that a power–law with photon index $\alpha_1 = -2/3$ is indeed allowed to be present in the data, without a significant change in the other parameters' values.

The spectral index β, describing the high energy part of the spectrum (i.e. above

$E_{\rm peak}$), has a distribution centered around $\langle\beta\rangle = -2.33$ ($\sigma_\beta = 0.24$) for the spectra fitted by the SBPL while the 2SBPL fits provide a distribution centered at $\langle\beta\rangle = -2.81$ ($\sigma_\beta = 0.37$). Thus, when the spectrum requires the presence of two breaks (i.e. three power–laws) the high energy power–law is steeper than the cases when only one break is present. This could be related to the fact that the SBPL has only one possibility to model a change in the slope. If the spectrum is characterized by two spectral breaks, then the SBPL is forced to underestimate the spectral peak energy, in order to model the part of the spectrum between the two breaks and reduce the fit statistic. The remaining high energy part of the spectrum has to be modelled with one power–law with the slope β, but the early positioning of the spectral peak cannot account for the still high flux of the spectrum. Therefore the SBPL fit will model that part of the spectrum near the peak energy with a harder beta index, which keep the flux high. This would result in an overall worse modeling of the steeper high energy tail of the spectrum, but the typically large error bars at the end of the BGO detectors energy range often makes this effect negligible. The fact that the high-energy slope β for the SBPL function is typically harder than the one recovered by the 2SBPL fits is important, because it affects the inferred values of the spectral index of the underlying emitting particle distribution. A steeper high–energy power–law slope β would imply also a steeper index p of the particle distribution accelerated by the relativistic shocks. This will be investigated and discussed also in Chapter 4 and Sec. 5.2.

Figure 3.12 shows the distributions of the two characteristic energies of the 2SBPL fits (blue histograms for $E_{\rm break}$ and red histograms for $E_{\rm peak}$), and $E_{\rm peak}$ of the SBPL fit (black empty histogram). $E_{\rm peak}^{\rm SBPL}$ has a log–normal distribution centered at $\langle\log(E_{\rm peak}^{\rm SBPL}/{\rm keV})\rangle = 2.46$ ($\sigma_{E_{peak}} = 0.40$). Instead, when a second break in the fitting function is introduced and its presence in the spectrum is statistically significant, the distributions of $E_{\rm break}$ and $E_{\rm peak}$ are centered at the mean values $\langle\log(E_{\rm break}/{\rm keV})\rangle = 2.00$ ($\sigma_{E_{break}} = 0.34$) and $\langle\log(E_{\rm peak}^{\rm 2SBPL}/{\rm keV})\rangle = 3.00$ ($\sigma_{E_{peak}} = 0.26$).

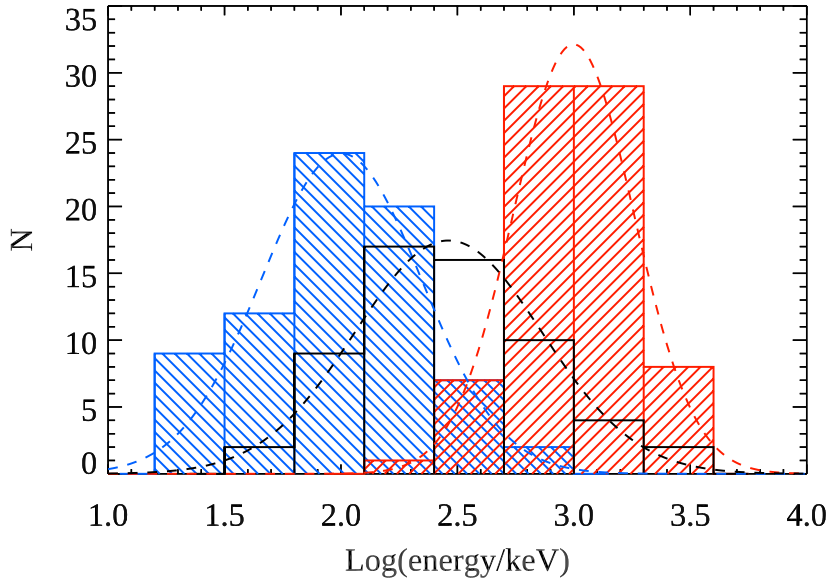

FIGURE 3.12: Distributions of the characteristic energies $E_{\rm beak}$ and $E_{\rm peak}$ for the 2SBPL (blue and red hatched histogram, respectively) and $E_{\rm peak}$ for the SBPL model (black empty histogram), obtained from the time–resolved analysis of long GRBs. Gaussian functions showing the central value and standard deviation for each distribution are overplotted to the histograms (with the same color coding).

Summarizing, from the comparison of the best fit values obtained when the best fit model is a SBPL and when is a 2SBPL (Fig. 3.11 and Fig. 3.12), I notice that:

- the distribution of $\alpha^{\rm SBPL}$ lies in between the distributions of α_1 and α_2 (see also Oganesyan et al. 2018). This will be carefully investigated in Sec. 3.3.
- the distribution of $E^{\rm SBPL}_{\rm peak}$ lies in between the distributions of the new feature $E^{\rm 2SBPL}_{\rm break}$ and $E^{\rm 2SBPL}_{\rm peak}$ (the νF_ν peak energy is now shifted to higher energies);
- $\beta^{\rm SBPL} > \beta^{\rm 2SBPL}$. The high energy part of the spectrum will be studied in Chapter 4.

3.2.2 The 10 brightest short GRBs

Sorting the *Fermi*/GBM Catalogue of short GRBs for decreasing fluence of the best-fit model and selecting the first 10, provides a cut in fluence at $5.72 \pm 0.11 \times 10^{-6}\,{\rm erg\,cm^{-2}}$. Table 3.7 lists the 10 GRBs of the sample. For each of these 10 GRBs, I performed only time-integrated analysis, due to the low statistic in the time-resolved bins.

TABLE 3.7: The ten short GRBs with the largest fluence (10–1000 keV) in the GBM catalogue. The last three digits in the name (in square brackets) refer to the naming convention of GBM triggers. The prompt duration and the fluence of the time–integrated spectra are listed in columns 2 and 3, and refer to information reported in the online GBM catalogue.

GRB Name	T_{90} [s]	Fluence [$10^{-6}\,{\rm erg\,cm^{-2}}$]
170206[453]	1.17 ± 0.10	10.80 ± 0.16
120323[507]	0.38 ± 0.04	10.66 ± 0.13
140209[313]	1.41 ± 0.26	9.52 ± 0.18
090227[772]	0.30 ± 0.02	8.93 ± 0.17
150819[440]	0.96 ± 0.09	7.75 ± 0.15
170127[067]	0.13 ± 0.04	7.41 ± 0.21
120624[309]	0.64 ± 0.16	7.14 ± 0.16
130701[761]	1.60 ± 0.14	6.30 ± 0.14
130504[314]	0.38 ± 0.18	6.01 ± 0.14
090228[204]	0.45 ± 0.14	5.72 ± 0.11

3.2.2.1 Results of the time–integrated analysis of short GRBs

The results of the spectral analysis are reported in Table 3.8. For each GRB, the table lists the name, the time interval over which the spectrum has been integrated, the best–fit parameters of the analysis, the χ^2/d.o.f. and the associated probability.

TABLE 3.8: Best-fit parameters for the time-integrated analysis of the 10 short brightest GRBs analysed in this work. The best fit model is always a SBPL.

Name	Time interval [s]	Norm [ph/s cm^2 keV]	α	E_{peak} [keV]	β	χ^2/dof	Prob
170206	[-0.128 - 1.664 s]	$1.41^{+0.21}_{-0.20}$	$-0.62^{+0.03}_{-0.04}$	$280.4^{+18.1}_{-13.3}$	$-2.38^{+0.06}_{-0.08}$	361.63 / 346	0.2707
120323	[-0.064 - 0.576 s]	$98.11^{+22.6}_{-14.1}$	$-1.04^{+0.08}_{-0.06}$	$109.5^{+20.5}_{-4.87}$	$-2.11^{+0.03}_{-0.05}$	372.44 / 353	0.2286
090227	[-0.064 - 0.256 s]	$1.68^{+0.19}_{-0.23}$	$-0.60^{+0.02}_{-0.03}$	$1576.0^{+67.3}_{-67.1}$	$-2.82^{+0.06}_{-0.20}$	358.17 / 349	0.3559
150819	[-0.064 - 1.152 s]	$25.21^{+2.3}_{-2.52}$	$-1.24^{+0.02}_{-0.03}$	$595.3^{+188.0}_{-73.8}$	$-2.41^{+0.16}_{-0.19}$	349.53 / 347	0.4518
170127	[-0.064 - 0.256 s]	$0.78^{+0.19}_{-0.39}$	$-0.47^{+0.05}_{-0.11}$	$755.5^{+23.4}_{-56.0}$	$-3.29^{+0.06}_{-0.59}$	312.4 / 348	0.9151
120624	[0.000 - 0.320 s]	$5.1^{+0.62}_{-0.62}$	$-0.83^{+0.02}_{-0.02}$	$2892.0^{+299.0}_{-205.0}$	$-2.49^{+0.12}_{-0.17}$	344.93 / 345	0.491
130701	[-0.064 - 1.600 s]	$0.46^{+0.12}_{-0.11}$	$-0.69^{+0.04}_{-0.06}$	$892.3^{+90.9}_{-74.0}$	$-2.68^{+0.21}_{-0.26}$	324.75 / 347	0.7989
130504	[-0.032 - 0.384 s]	$0.87^{+0.15}_{-0.17}$	$-0.57^{+0.03}_{-0.04}$	$1033.0^{+74.9}_{-46.9}$	$-2.79^{+0.10}_{-0.25}$	375.6 / 352	0.1853
090228	[-0.064 - 0.512 s]	$2.29^{+0.32}_{-0.33}$	$-0.76^{+0.03}_{-0.03}$	$663.7^{+51.3}_{-38.0}$	$-2.87^{+0.17}_{-0.28}$	346.76 / 349	0.5238

The results are quite interesting: contrary to what found in long GRBs, no one of the 10 time-integrated short GRBs spectra shows evidence of a spectral hardening at low energies. They are all well fitted by the SBPL function, thus with two power–laws smoothly connected at the νF_ν peak, not requiring another spectral break. The peak energy has typical value $\langle \log(E_{peak}/keV) \rangle = 2.70$ and standard deviation $\sigma_{E_{peak}} = 0.47$. The distribution of the two photon indices α and β are shown in Fig. 3.13. It is interesting to note that α, which describes the index of the power–law below E_{peak}, has typical value $\langle \alpha \rangle = -0.78$ ($\sigma_\alpha = 0.23$), i.e. consistent within 1σ with the synchrotron value $\alpha_1^{syn} - 2/3$. In a synchrotron scenario, this would imply that the cooling frequency ν_{cool} is very close to the injection frequency ν_{min} and we can observe only one power–law below the peak energy.

The photon index β of the spectral power–law above E_{peak} has mean value $\langle \beta \rangle = -2.59$, with $\sigma_\beta = 0.33$.

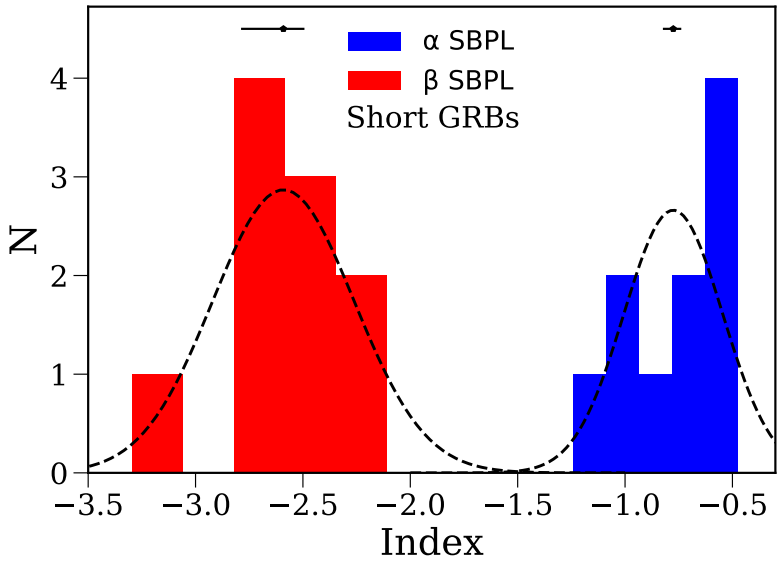

FIGURE 3.13: Short GRBs, time–integrated spectra: distributions of the spectral indices α and β for the best fit model (that is always a SBPL) for all 10 short GRBs reported in Table 3.8. The mean values and typical errors are shown on the top of the corresponding distributions (black symbols). Gaussian functions showing the mean value and standard deviation are overplotted to the histograms.

3.2.3 Summary of the results

In this section, I presented the spectral analysis of the brightest 10 long and 10 short GRBs detected by *Fermi*/GBM in 10 years of activity. I systematically fitted two empirical functions to the spectra: a smoothly broken power-law (SBPL) and a double smoothly broken power-law (2SBPL). The reason for testing a 2SBPL model is to identify the possible presence of two characteristic energies in the prompt emission spectra: the usual peak energy $E_{\rm peak}$ and a spectral break $E_{\rm break}$ at lower energies, recently identified in a sample of *Swift* bursts (Oganesyan et al., 2017; Oganesyan et al., 2018) and in one *Fermi*/GBM bright burst (Ravasio et al. 2018, see Sec. 3.1).

For long GRBs, the time–integrated analysis shows that in 8 of the 10 brightest GBM GRBs, the SBPL fails to provide an acceptable fit: the data require an additional spectral break $E_{\rm break}$, located between $\sim 10\,$keV and 300 keV. For these 8 GRBs I also performed a time–resolved analysis, finding that $\sim$ 70% of the time-resolved spectra also show strong evidence for a low–energy spectral break. For this sample of time–resolved spectra, the log–normal distributions of $E_{\rm break}$ and $E_{\rm peak}$ are centered around the mean values $\langle \log(E_{\rm break}/{\rm keV})\rangle = 2.00 \pm 0.34$ and $\langle \log(E_{\rm peak}/{\rm keV})\rangle = 3.00 \pm 0.26$. Moreover, the fit with the 2SBPL model returns higher values of $E_{\rm peak}$ thus also resulting in a steeper values of β with respect to the SBPL fits (see Fig. 3.11). Steeper values of the slope β imply steeper values of the slope p of the shock–accelerated particles distribution. I will perform a deeper study of the high-energy part of the spectrum in Chapter 4 and discuss the implications on the shape of the emitting particles distribution in Chapter 5.

The photon indices of the power–laws below $E_{\rm break}$ and between $E_{\rm break}$ and $E_{\rm peak}$ are respectively $\langle \alpha_1 \rangle = -0.58 \pm 0.16$ and $\langle \alpha_2 \rangle = -1.52 \pm 0.20$. These values are remarkably consistent with the predicted values for synchrotron emission in marginally fast cooling regime (for an example of typical spectrum see Fig. 3.9). These results confirm the presence of the break in the brightest long GRBs observed by *Fermi* and the values of the indices strongly suggest that the underlying emission mechanism is synchrotron. Even though the natural evolution of this analysis would require to build a physically motivated synchrotron model and fit it to the spectral data to test the synchrotron interpretation (see Sec. 3.4), these results obtained from empirical functions represent a first consistency check. This is important because, assuming that the emission is due to synchrotron radiation, the position of the break energy can be interpreted as the synchrotron cooling frequency, implying that the relativistic particles do not cool completely. It is therefore possible to derive estimates of the physical parameters characterizing the GRB emitting region, such as the magnetic field B and the energies of the emitting particles. I will derive the parameters of the emitting region and discuss the physical implications of these results in Chapter 5.

For short GRBs, none of the time–integrated spectra of the 10 brightest events shows a break at low energies. The best fit model is always a SBPL, but, as for long GRBs, the distribution of the index α_1 below $E_{\rm peak}$ is consistent within 1σ with the low–energy synchrotron photon index $\alpha_1^{\rm syn} = -2/3$. In a synchrotron scenario, this would imply that what we are observing is the low energy power–law below the cooling frequency $\nu_{\rm cool}$, that is so close to the minimum frequency $\nu_{\rm min}$ (corresponding to $E_{\rm peak}$) that we cannot distinguish them. This, in turn, implies an even more incomplete cooling of the emitting particles, as it will be discussed in Chap. 5.

Given the successful results obtained on the brightest bursts detected by *Fermi*, it is clear now that the presence of an additional spectral break in GRB 160625B is not due to some peculiar properties of that GRB, but instead it could be a more common feature in GRBs spectra, at least in the brightest ones. These results now pose impelling questions:

how common is this low energy break? Could it be present also in other, dimmer, bursts of the GRB population detected by the *Fermi* Catalog? Why this feature has never been detected before? There could be a link between the presence of a break in the spectrum and the value of the low–energy photon index α. Indeed, in those spectra best fitted by a simple SBPL, I recover the typical value of the low–energy photon index, $\langle \alpha \rangle = -1.02 \pm 0.19$. Interestingly, this value lies between the values of α_1 and α_2, as shown in Fig. 3.11. Speculating that most of the spectra present a break below $E_{\rm peak}$, the value of α can be understood as a sort of average value between the α_1 and α_2: these are indeed asymptotic values that can be reached if $E_{\rm break}$ and $E_{\rm peak}$ are far from each other. In a work led by Mattia Toffano (Toffano et al., 2021), we have tried to investigate these issues through both spectral analysis and simulations. I will describe our results in the next section.

3.3 Observational biases hiding the low energy break

While the presence of a low-energy spectral break has been identified in a sub–sample of *Fermi* GRBs, as shown in the previous Sections, a sizable fraction of GRB spectra are still well fitted by single break functions. As described in Chap. 2, the most commonly used is the Band function (Band et al., 1993), which consists of two smoothly connected power laws $N(E) \propto E^{\alpha}$ and $N(E) \propto E^{\beta}$ describing the photon spectrum at low and high energies, respectively. The habit of fitting spectra with a single break function may have played a major role in preventing the discovery of the break. However, the brightest events offered the possibility to see a deviation from the standard modeling and to discover the presence of low energy spectral breaks.

On the other hand, the non-detection of breaks could be due to several factors. For spectra with a low signal-to-noise ratio (S/N) the identification of a change in slope below the peak energy might be difficult and the best–fit might be a single break function with low–energy index α between α_1 and α_2. Also, the non-detection could be due to the position of the break: if the break is either close to the peak energy or below the low-energy edge of the instrument sensitivity, a spectral fit would be unable to identify the break.

In this section, I describe the investigation we performed about the possibility that the low-energy spectral break is a common feature in GRB spectra, and that the typical spectral index $\alpha_{\rm Band} \sim -1$ is an average value between the two power-law segments below and above the break energy. To this aim, we analyzed bright long and short GRBs detected by *Fermi* in search for statistically significant evidence of the low-energy spectral break. I will briefly describe the sample, which have been selected with different criteria with respect to those of the previous section, and the results of the spectral analysis. Then, I will focus on the spectral simulations performed to study how the value of $\alpha_{\rm Band}$ becomes harder (softer) by moving the break closer to (farther from) the peak energy. We derived limits on the possible location of the break energy in GRBs whose spectrum is best fitted by the Band function (i.e., with no evidence of a break). The complete description of the methods and the results described in this section have been published in Toffano et al. 2021.

3.3.1 The sample

To perform our investigation, we first need to characterize the low-energy part of GRB spectra, searching for possible spectral breaks. To this aim, we selected GRBs detected by the GBM and applied selection criteria that are different from those used in the previous Section. In particular, we wanted to maximize the probability of (i) performing reliable spectral analysis and (ii) identifying the presence of a spectral break at low energies, well distinguished from the spectral peak energy. This can be achieved by selecting GRBs with large fluence, as done before, but also with large $E_{\rm peak}$ values, as they are more likely to display the low-energy break $E_{\rm break}$ within the energy range of the GBM, given that their typical separation is $E_{\rm break}/E_{\rm peak} \sim 0.1$ (see Section 3.2).

For these reasons, from the online *Fermi* Catalog, which contains 2669 GRBs up to April 2020, we selected long GRBs with fluence $> 10^{-4}\,{\rm erg\,cm^{-2}}$ (integrated over the 10–1000 keV energy range) and observed peak energy $E_{\rm peak} > 300\,{\rm keV}$, and short GRBs with fluence $> 5 \times 10^{-6}\,{\rm erg\,cm^{-2}}$ and $E_{\rm peak} > 300\,{\rm keV}$. This selection is based on the values of fluence and peak energy reported in the Catalog and corresponding to the fit of the time-integrated spectrum with the Band function. Our selection resulted in 27 long and 9 short GRBs.

All spectra were fitted with two different spectral models: the Band function, often used to fit GRB spectra (Preece et al., 1998; Kaneko et al., 2006; Ghirlanda, Celotti, and Ghisellini, 2002; Nava et al., 2011a; Sakamoto et al., 2011b; Gruber et al., 2014; Yu et al., 2016; Lien et al., 2016b; Goldstein et al., 2012; Frontera et al., 2000) (see the definition in Chap. 1) and the double smoothly broken power-law function 2SBPL (equation 2.17 defined in Sec. 3.1), keeping the curvature values $n_1 = n_2 = 2$ previously assumed.

In order to distinguish the spectral parameters of these two fitting functions, in the following I refer to the photon indices of the Band function as $\alpha_{\rm Band}$ and $\beta_{\rm Band}$, the photon indices of the 2SBPL below the peak energy as $\alpha_{1,\rm 2SBPL}$ and $\alpha_{2,\rm 2SBPL}$, and the photon index of the 2SBPL above the peak energy as $\beta_{\rm 2SBPL}$.

We adopted the Akaike information criterion (AIC - Akaike 1974) to compare the fits obtained with the 2SBPL and Band functions and choose the best one. We recall that $\rm AIC = 2k - 2\ln(\hat{L})$, where k is the number of free parameters in the model and $\hat{L}$ is the maximum value of the likelihood function L obtained by varying the free parameters. For Gaussian-distributed variables $\chi^2 \propto -2\ln(L)$. If $\Delta\rm AIC = AIC_{Band} - AIC_{2SBPL} \geq 6$, the Band fit has $\lesssim 5\%$ probability of describing the observed spectrum better than the 2SBPL function (Akaike, 1974): in such a case, we considered the 2SBPL a better fit and thus considered the presence of a break as statistically significant at the 95% confidence level.

3.3.2 Fit results

Here I summarize the results of the spectral analysis on the 27 long GRBs and 9 short GRBs spectra. We found that:

- of the 27 long GRBs, 12 have a low-energy break, namely, their spectra are best fitted by the 2SBPL function ($\Delta\rm AIC \geq 6$); the distributions of $\alpha_{1,\rm 2SBPL}$ and $\alpha_{2,\rm 2SBPL}$ are centered around –0.71 and –1.71, close to the typical values –2/3 and –3/2 expected for synchrotron spectrum from marginally fast cooling electrons;
- the remaining 15 long GRBs are well fitted by the Band function and, according to the AIC criterion, there is no improvement using the 2SBPL function;
- long GRBs without a break have an $\alpha_{\rm Band}$ distribution that is slightly softer than $\alpha_{1,\rm 2SBPL}$ but harder than $\alpha_{2,\rm 2SBPL}$ This might suggest that when the spectral data are not sufficient to constrain and identify a spectral break, the Band function returns a value of the low-energy index that is an average between the index $\alpha_{1,\rm 2SBPL}$ and $\alpha_{2,\rm 2SBPL}$. This possibility is investigated with simulations in the following section;
- all short GRBs are well fitted by the Band function. In six short GRBs we could only derive an upper limit on $\beta_{\rm Band}$, indicating that also a cutoff power-law function could be a good fit to the spectra (see e.g., Ghirlanda, Ghisellini, and Celotti 2004). the distribution of $\alpha_{\rm Band}$ of short GRBs is similar to the $\alpha_{1,\rm 2SBPL}$ distribution of long GRBs with a break: a KS test between the two returns $p = 0.16$[3]. This confirms the results found in the previous section, suggesting that the power-law segment $\alpha_{2,\rm 2SBPL}$ separating $E_{\rm break}$from $E_{\rm peak}$is not present in short GRBs, i.e., $E_{\rm break}\sim E_{\rm peak}$.

3.3.3 Origin of the value $\alpha_{\rm Band} \sim -1$

The results of the spectral analysis described above confirm the presence of two classes of long GRBs: those requiring two power-law segments ($\alpha_{1,\rm 2SBPL}$ and $\alpha_{2,\rm 2SBPL}$) to describe

[3]For all the statistical tests we have set the significance level at 0.05, i.e. we accept the null hypothesis if $p > 0.05$.

the spectrum at energies $E < E_{\rm peak}$, and those for which this part of the spectrum is well described by a single power law ($\alpha_{\rm Band}$). As the values of $\alpha_{\rm Band}$ are typically softer than $\alpha_{\rm 1,2SBPL}$ but harder than $\alpha_{\rm 2,2SBPL}$, we investigate the possibility that spectra best fitted by Band are hiding a spectral break that is difficult to identify with a certain statistical significance due to the lack of enough signal at low energies, and/or to the proximity of $E_{\rm break}$ to $E_{\rm peak}$, and/or to the proximity of $E_{\rm break}$ to the low-energy edge of the GBM sensitivity. If this is correct, we would expect to see a dependence of $\alpha_{\rm Band}$ on the values of $E_{\rm break}$ and $E_{\rm peak}$ and on their separation. Specifically, we expect that when the underlying spectrum has a break, the fit with the Band function will return a hard $\alpha_{\rm Band} \sim \alpha_{\rm 1,2SBPL}$ when $E_{\rm break} \sim E_{\rm peak}$, and, conversely, a soft $\alpha_{\rm Band} \sim \alpha_{\rm 2,2SBPL}$ when $E_{\rm break} \ll E_{\rm peak}$.

A strong correlation is not expected, as the value of $\alpha_{\rm Band}$ should depend not only on the ratio $R_{\rm E} = E_{\rm break}/E_{\rm peak}$, but also on the absolute value of $E_{\rm peak}$(or, equivalently, $E_{\rm break}$), and also on the specific values of $\alpha_{\rm 1,2SBPL}$ and $\alpha_{\rm 2,2SBPL}$. To better investigate this effect and its presence in the spectra, we performed a set of simulations that are described in the following sections.

3.3.3.1 Band function response to a spectral break

We now investigate how the presence of a spectral break generally affects the results of a fit performed using the Band function. We simulated[4] GRB prompt spectra with input model 2SBPL, keeping fixed all the parameters and varying solely $E_{\rm break}$. The adopted input parameters are $\alpha_{\rm 1,2SBPL} = -0.65$, $\alpha_{\rm 2,2SBPL} = -1.67$, $E_{\rm peak}$=1000 keV, $\beta_{\rm 2SBPL} = -2.5$. These input values have been chosen in order to reproduce a typical long GRB of our sample. For these simulations, we used the GBM background and response matrix files from one of the GRBs in our sample. We verified that choosing different background and response matrix files belonging to any other GRB in our sample does not affect the simulation results.

Each simulated spectrum is then fitted with the input model (a 2SBPL with parameters free to vary) and also with a Band function. For each value of $E_{\rm break}$, we repeated the simulation 200 times, obtaining (for each parameter and for the reduced chi-square) a distribution of values. From these distributions we extracted the mean value and its 68% confidence interval. Figure 3.14 shows the parameters returned by the Band fits as a function of the position of the energy break. This exercise is repeated for two different cases, with a rather high average S/N [5] ($\sim$ 21, left-hand panel) and a S/N ratio that is approximately a factor 10 lower ($\sim$ 2.7, right-hand panel). They represent simulated spectra of a GRB with a fluence of $\sim 3.5 \cdot 10^{-4}$ erg cm^{-2} and $\sim 3.5 \cdot 10^{-5}$ erg cm^{-2}, respectively. The input parameters used for the 2SBPL function ($\alpha_{\rm 1,2SBPL}$, $\alpha_{\rm 2,2SBPL}$, $E_{\rm peak}$, $\beta_{\rm 2SBPL}$) are marked by dashed horizontal lines. We distinguish the best-fitting model according to our criterion based on the AIC (in Fig. 3.14, diamonds: 2SBPL, circles: Band).

[4] Spectral simulation performed within `XSPEC` with the `fakeit` tool.

[5] calculated as $(s-b)/\sqrt{b}$, where s and b are the source and background estimated counts, respectively (see e.g. Dereli-Bégué, Pe'er, and Ryde 2020).

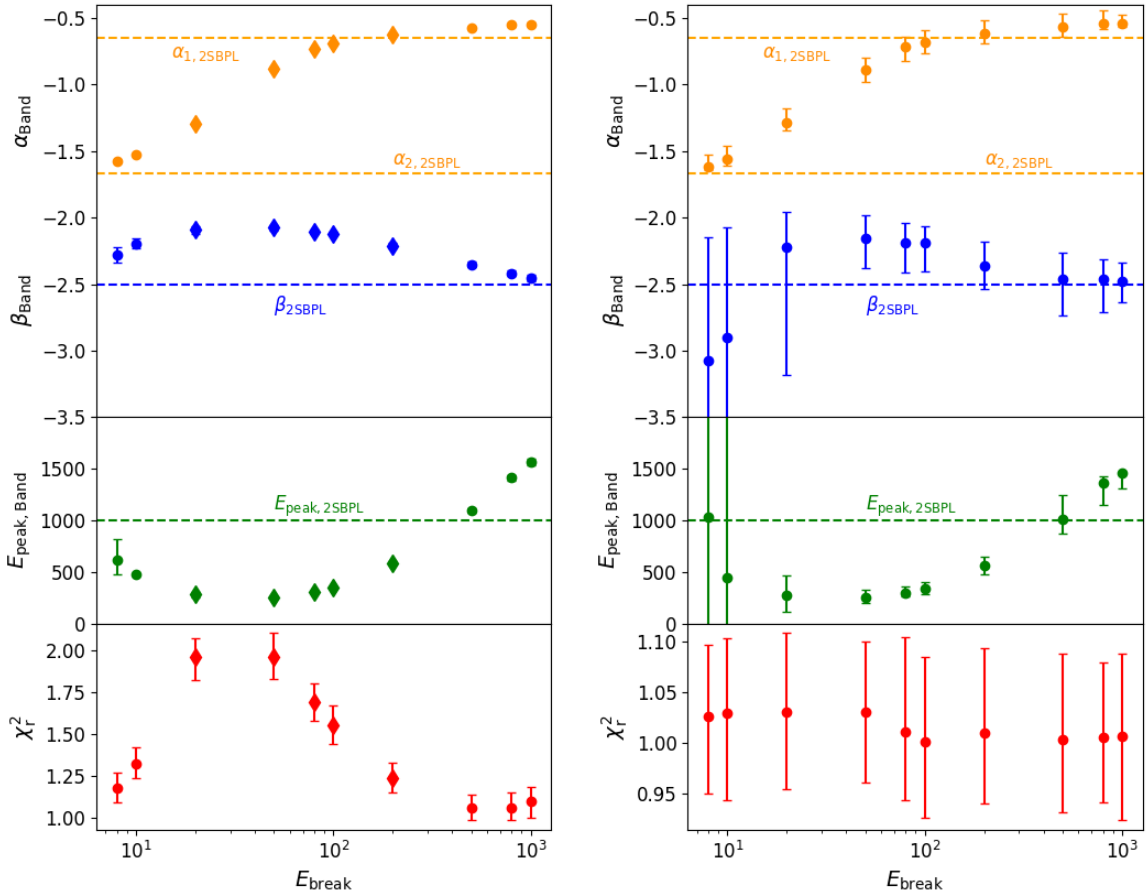

FIGURE 3.14: Band function parameters as a function of the position of the energy break E_{break} of the 2SBPL function. Each plot shows the parameters of the Band function fitted to a series of spectra simulated assuming the 2SBPL function whose parameter values are marked by the horizontal dashed lines. Top: Low-energy slope α_{Band} (orange symbols) and high-energy slope β_{Band} (blue symbols). Middle: Energy peak $E_{peak,Band}$ (green symbols). Bottom: Fit χ^2_r (red symbols). Left: Spectrum characterized by a S/N $\sim$ 21 (fluence $\sim$ $3.5 \cdot 10^{-4}$ erg cm^{-2}). Right: Spectrum characterized by S/N $\sim$ 2.7 (fluence $\sim$ $3.5 \cdot 10^{-5}$ erg cm^{-2}). Data are represented as circles when the best-fitting model is Band and as diamonds when the best-fitting model is 2SBPL.

The values of α_{Band} obtained by fitting the simulated spectra with the Band function (orange symbols in the top panel) correlate with E_{break}: a low value of E_{break} makes $\alpha_{Band} \approx \alpha_{2,2SBPL}$. On the other hand, as E_{break} increases (and approaches E_{peak} which in this example is 1 MeV) $\alpha_{Band} \approx \alpha_{1,2SBPL}$. In between, the value of α_{Band} is an average of $\alpha_{1,2SBPL}$ and $\alpha_{2,2SBPL}$, depending on the position of E_{break}. Given the presence of only a single break in the Band function (i.e., $E_{peak,Band}$) the other parameters (β_{Band} and $E_{peak,Band}$) also depend on the position of the break: β_{Band} (blue symbols) always assumes softer values compared to the input one, unless $E_{break} \sim E_{peak}$. The peak energy $E_{peak,Band}$ (green symbols) is an average of E_{break} and E_{peak} of the 2SBPL function and approaches the input value when E_{break} is very low or when $E_{break} \sim E_{peak}$.

These results hold for both S/N ratios. The main difference is in the uncertainties on the best fit parameters (larger for the case with lower S/N) and, most notably, on the behavior of the χ^2_r. In the case with lower S/N, the χ^2_r of the Band fit is always acceptable ($\sim$ 1), regardless of the value of E_{break}. This shows that, even though the input spectrum has a spectral break and this break falls within the GBM energy range, identification of

the break is not possible in a spectrum with a relatively low S/N, and the best-fit model is a Band function. We note that a fluence of $3.5 \cdot 10^{-5}$ erg cm^{-2} or less is representative of the majority of long GRBs detected by Fermi/GBM. If the S/N is increased by a factor of ten (left-hand panel), the χ^2_r of the fit with the Band function depends on E_{break} : only when the break is at the low-energy end of the GBM spectral range ($E_{break} \lesssim 10$ keV) or close to E_{peak} ($E_{break} \gtrsim 500$ keV), the fit with the Band function returns an acceptable χ^2_r. Despite the high S/N, in such cases the break is hardly identifiable ($\Delta AIC < 6$).

Finally, we notice that even when the Band function returns an adequate fit, (i.e., when $E_{break} \lesssim 10$ keV or $E_{break} \sim E_{peak}$) the resulting values of α_{Band}, β_{Band}, and $E_{peak,Band}$ might largely deviate from the values of the input spectrum.

3.3.3.2 Spectral simulations: $R_E - \alpha_{Band}$ trend

In order to further investigate the $R_E - \alpha_{Band}$ trend, we focused first on the 12 long GRBs analyzed in this work that have a spectral break E_{break}. In Fig. 3.15 we show (orange symbols) their ratio $R_E = E_{break}/E_{peak}$ (from the fits of the 2SBPL) versus α_{Band} (from the fit of the same spectrum with the Band function). Long GRBs with a break are located in the range $R_E \in [0.04, 0.5]$ and, if their spectra are fitted with the Band function, the resulting α_{Band} is in the range $\alpha_{Band} \in [-1.1, -0.2]$. A broad trend in the $R_E - \alpha_{Band}$ plane appears among the points. A correlation analysis returns a Pearson correlation coefficient of 0.56 and an associated chance probability value of $p = 0.05$, suggesting a correlation between R_E and α_{Band}.

For each of these GRBs, we simulated spectra with the 2SBPL function with parameter values fixed to the best-fit values obtained from the spectral fits except for E_{break}, which we vary between $0.01 E_{peak}$ and E_{peak}. For each GRB, we used the corresponding GBM background and response matrix files for the corresponding simulations. Simulated spectra were renormalized in order to maintain the energy-integrated flux of the real spectrum constant while moving E_{break}. Low values of R_E place the break below the GBM low-energy threshold, i.e., 8 keV, in those GRBs with $E_{peak,2SBPL} < 800$ keV. We then refit the simulated spectra with the Band function and derive α_{Band}. The simulation of each spectrum is repeated 200 times to build the distribution of α_{Band} and estimate its mean value and 68% confidence interval.

In Fig. 3.15 the orange dashed lines show, for each of the 12 long GRBs, the corresponding α_{Band} returned by the fit with the Band function for each input value of R_E. These curves show that α_{Band} depends on the relative position between break and peak energy, with small ratios resulting in soft spectra and large ratios resulting in harder spectra, as expected. These simulations show that the value of α_{Band} is a "weighted" mean of the $\alpha_{1,2SBPL}$ and $\alpha_{2,2SBPL}$ slopes. Moreover, different curves show similar trends, showing that the different values of E_{peak} and input $\alpha_{1,2SBPL}$ and $\alpha_{2,2SBPL}$ are responsible for the dispersion in the plane. The dispersion of the curves is similar to the dispersion in the real data.

From the tracks of the orange dashed lines shown in Fig. 3.15 we can speculate that, when the best-fit model is a Band function, values of α_{Band} harder than ~ -1.0 could be consistent with the presence of an E_{break} in the proximity of E_{peak} (i.e., $0.1\, E_{peak} < E_{break} \lesssim E_{peak}$), while values softer than ~ -1.0 could indicate the presence of E_{break} far from E_{peak}(i.e., $E_{break} \lesssim 0.1 E_{peak}$). This possibility is investigated in the following section, through spectral simulations.

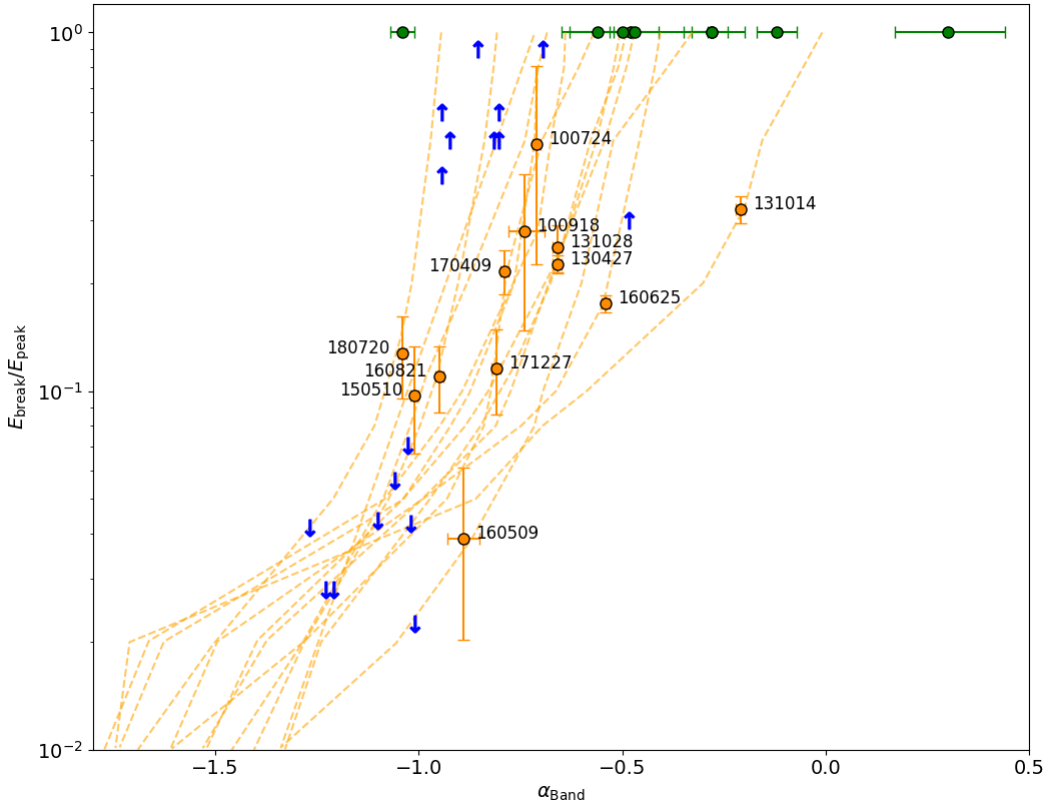

FIGURE 3.15: The 12 long GRBs best fitted by a 2SBPL shown with orange symbols. Their value of $R_E = E_{break}/E_{peak}$ is shown vs. the value of the index α_{Band} that is obtained by fitting their spectrum with a Band function. Short GRBs (whose spectrum is always best fitted by the Band function) are represented here assuming that, if the underlying spectrum were 2SBPL, it would be expected to have $E_{break} \sim E_{peak}$ (green symbols). The orange dashed lines show the results of simulations; blue arrows represent the upper and lower limits on R_E for the 15 long GRBs whose spectra are best fitted by Band.

3.3.3.3 Spectral simulations: investigation of the spectra without a low-energy break

As shown in the fit results section, 15 long GRBs in our sample do not show the presence of a low-energy spectral break. Through spectral simulations, we now propose to investigate whether or not it is still possible for these GRBs to have a low-energy break, even though the best-fit model is a simple Band function. The simulation now assumes that also in these 15 GRBs the spectrum has the shape of the 2SBPL function and infers constraints on its parameters by requiring that the fit with the Band function is not only acceptable but also preferred over a 2SBPL, and returns best-fit values which are consistent with those of the real spectrum.

Based on the trend found between R_E and α_{Band}, we would expect that if the spectrum is intrinsically a 2SBPL and E_{break}lies at low energies, the Band function could adequately fit the simulated spectrum and result in $\alpha_{Band} \sim \alpha_{2,2SBPL}$. Similarly, if the spectrum is intrinsically a 2SBPL and E_{break}lies close to E_{peak}, the Band function could return $\alpha_{Band} \sim \alpha_{1,2SBPL}$. For each burst, the spectra simulated with the 2SBPL function maintain the same fluence of the real GRB.

We repeated the simulations for different values of the 2SBPL parameters. In particular:

- $\alpha_{1,2SBPL}$ is sampled uniformly within the range $[-0.3, -1.05]$ with steps of 0.03;

- $\alpha_{2,2SBPL}$ is sampled uniformly in the interval $\in [-1.1, -1.9]$ with steps of 0.03;
- E_{break} is sampled between 2 keV and the energy peak with steps of 2 keV;
- β_{2SBPL} is fixed to the value obtained from the fit with the Band function.

For each combination of parameters, we simulated ten spectra. We assumed the background and response matrix files of each GRB for these simulations. These simulated spectra are then refitted with both the 2SBPL and Band functions. From the built parameter distributions we derived the mean values and 68% confidence interval. Once we refitted the spectrum with a Band function, we accepted the simulation if the Band fit satisfies the following conditions:

- it is statistically equivalent to the fit with the 2SBPL, i.e., $\Delta AIC < 6$;
- its α_{Band} and β_{Band} are consistent, within 1σ, with the values inferred from the real spectrum;
- its E_{peak} is consistent, within 3σ, with the value inferred from the real spectrum.

For each of the 15 long GRBs that do not explicitly show a break, we found a significant number of parameter combinations for which the 2SBPL functions were able to satisfactorily reproduce the real spectrum.

In particular, for all these long GRBs we were able to set either a plausible maximum or minimum value for E_{break} and constrain either $\alpha_{2,2SBPL}$ or $\alpha_{1,2SBPL}$ in an interval. These are represented with the blue arrows in Fig. 3.15. The limits for E_{break} and the low-energy slope intervals are listed in Table 3.9 and Table 3.10.

TABLE 3.9: Constraints on $\alpha_{2,2SBPL}$ and maximum E_{break}(in keV) for GRBs with soft α_{Band} that did not show an energy break in their time-integrated spectrum.

Name	$\alpha_{2,2SBPL}$ Range	$E_{break,Max}$
090323(002)	$[-1.48, -1.18]$	30
130504(978)	$[-1.42, -1.28]$	12
130606(497)	$[-1.24, -1.12]$	12
140206(275)	$[-1.60, -1.36]$	18
170210(116)	$[-1.37, -1.14]$	24
170527(480)	$[-1.34, -1.15]$	24

TABLE 3.10: Constraints on $\alpha_{1,2SBPL}$ and minimum E_{break}(in keV) for GRBs with hard α_{Band} that did not show an energy break in their time-integrated spectrum.

Name	$\alpha_{1,2SBPL}$ Range	$E_{break,Min}$
090926(181)	$[-0.83, -0.80]$	220
100414(097)	$[-0.68, -0.54]$	126
101123(952)	$[-1.02, -0.94]$	182
120526(303)	$[-0.90, -0.83]$	372
120624(933)	$[-1.05, -0.93]$	320
120711(115)	-0.95	440
130306(991)	$[-0.98, -0.72]$	86
160905(471)	$[-0.90, -0.84]$	572
170214(649)	$[-0.92, -0.86]$	158

3.3.4 Discussion and Conclusions

If the input spectrum is a 2SBPL, simulations described in Sec. 3.3.3.1 show that when $E_{\rm break}$ is close to $E_{\rm peak}$ or below the low-energy threshold ($E_{\rm min}$) of the instrument, the Band function gives $\alpha_{\rm Band} \sim \alpha_{\rm 2,2SBPL}$ and $\alpha_{\rm Band} \sim \alpha_{\rm 1,2SBPL}$, respectively (see Fig. 3.14). Values of $\alpha_{\rm Band} \sim -1$ correspond to $E_{\rm break}$ between $E_{\rm min}$ and $E_{\rm peak}$. Through the spectral analysis of a sample of GRBs selected with different criteria, Burgess et al., 2020 found that, when $E_{\rm break} \lesssim E_{\rm peak}$, the values of $\alpha_{\rm Band}$ are distributed approximately $\in [-1.7, -0.5]$. We argue that, if the break is a common feature of GRB spectra, the value of $\alpha_{\rm Band}$ is a proxy of its position with respect to $E_{\rm peak}$.

This hypothesis is verified through the spectral analysis of a sample of 27 long and 9 short GRBs selected within the *Fermi* sample of GRBs with large fluence and large $E_{\rm peak}$ in order to ease the search for $E_{\rm break}$, if present. In 12 out of the 27 long GRBs, we found $E_{\rm break}$ (i.e., the 2SBPL fits the data better than Band). Through spectral simulations, using these events as templates, we found that if the break is moved within the range delimited by $E_{\rm peak}$ and $E_{\rm min}$, the fit with Band results in a softer (if $E_{\rm break}$ departs from $E_{\rm peak}$) or harder (if $E_{\rm break}$ approaches $E_{\rm peak}$) low-energy index $\alpha_{\rm Band}$ (dashed orange lines in Fig. 3.15). At the extremes, the values of $\alpha_{\rm 1,2SBPL}$ and $\alpha_{\rm 2,2SBPL}$ are found. Instead, none of the short GRBs analyzed have a break, but they all have a relatively hard $\alpha_{\rm Band}$ which we suggest implies $E_{\rm break}$ lying close to $E_{\rm peak}$. Through dedicated spectral simulations we showed that the 15 long GRBs best fitted by the Band function (i.e., apparently without a break) could instead have a break close to $E_{\rm peak}$, corresponding to $\alpha_{\rm Band} > -1$ (upward arrows in Fig. 3.15), or close to $E_{\rm min}$ if $\alpha_{\rm Band} < -1$ (downward arrows in Fig. 3.15).

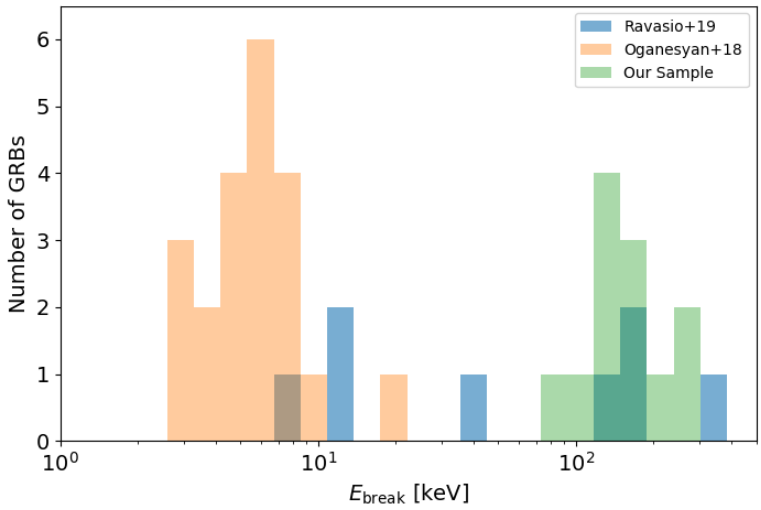

FIGURE 3.16: Energy distribution of the spectral breaks identified in prompt spectra of GRBs, combining the results of Oganesyan et al. (2018), Ravasio et al. (2019a), and Toffano et al. (2021).

The identification of the break in the spectra of GRBs detected by *Fermi* or *Swift* has been currently possible only for a limited number of events. Combining the results presented in this thesis and in Oganesyan et al. (2017) and Oganesyan et al. (2018), the distribution of the break energy observed so far is represented in Fig. 3.16. The distribution shows that the breaks have been found in the X–rays ($\sim$ few keV) and at γ–ray ($\sim$ hundreds keV) energies. Our analysis indicates instead that the low-energy break could be a more common feature than what suggested by direct spectral analysis. Indeed, we showed that the detection of the break energy is hampered by (1) the separation of $E_{\rm break}$

from $E_{\rm peak}$ and (2) the spectral signal-to-noise ratio. A burst with a typical fluence (e.g. $3.5 \cdot 10^{-5}\,{\rm erg\,cm^{-2}}$) detected by Fermi/GBM can be fitted by Band even though it has an additional break (right panel of Fig. 3.14). Combined together, these effects can explain why we were not able to find $E_{\rm break}$ in approximately half of the selected GRBs but, through simulations, were able to set an upper or lower limit on its possible value.

Our results show that the distributions of $\alpha_{1,\rm 2SBPL}$ and $\alpha_{2,\rm 2SBPL}$ are close to but slightly softer than the values predicted by synchrotron emission in the moderate fast cooling regime (Daigne, Bošnjak, and Dubus, 2011), namely -3/2 and -2/3. This is partly due to our fits with the 2SBPL function rather than with the synchrotron model (see e.g., Burgess, Ryde, and Yu 2015; Burgess et al. 2020) and to the fact that we analyze time-integrated spectra to exploit the highest S/N in search of $E_{\rm break}$. Time-resolved spectral analysis, indeed, often finds harder spectral slopes (Nava et al., 2011b; Acuner and Ryde, 2017) and, as shown in Section 3.2, the distributions of $\alpha_{1,\rm 2SBPL}$ and $\alpha_{2,\rm 2SBPL}$ are closer to the typical synchrotron values. In the next section, I focus on testing the synchrotron interpretation of the GRB prompt emission spectra, by fitting the data with a physical synchrotron model.

3.4 Testing the consistency of the synchrotron model with data

The presence of an additional spectral break has been demonstrated at different energies (in X–rays by Oganesyan et al., 2017; Oganesyan et al., 2018 and in γ-rays by Zheng et al. 2012; Ravasio et al. 2018; Ravasio et al. 2019a; Toffano et al. 2021) and using different instruments (*Swift* and *Fermi*). These findings on the spectral break point towards a common origin of the GRB prompt emission spectra and the consistency of the indices strongly suggests a synchrotron origin. However, comparing the photon indices derived from the empirical model and the synchrotron predictions represents a first consistency check, but it does not fully prove the validity of the synchrotron interpretation. At this stage, a more detailed, theory-driven analysis is required in order to assess the validity of the synchrotron interpretation. A necessary step forward consist in building a physically motivated synchrotron model and using it to fit the data. As described in Sec. 2, some attempts in this direction have been made recently (Oganesyan et al., 2019; Burgess et al., 2020), proving the ability of the synchrotron model to adequately fit at least some prompt emission spectra of *Swift* and *Fermi* bursts.

Therefore, in Ronchi et al. 2020 we built a physical model of synchrotron emission from a relativistic population of injected electrons and fitted it to the data of a test case event: GRB 180720B. This GRB belongs to the sample of the 10 brightest long GRBs studied in Ravasio et al. 2019a. As shown in the previous Section 3.2, its prompt spectrum in the keV–MeV energy range is characterized by the presence of an additional spectral break ($\langle E_{\rm break} \rangle \sim 55$ keV, see Table 3.6 and Fig. 3.9). On top of having an exceptional fluence, this burst offered also a rare observational dataset. Indeed, GRB 180720B was detected at VHE (in the energy range 100–440 GeV) by the High Energy Stereoscopic System (H.E.S.S.) telescope (Ruiz-Velasco, 2019; Abdalla et al., 2019). This burst was also detected by LAT and LLE data are also available. Moreover, it was detected by *Swift*/BAT and XRT (Siegel et al., 2018) and followed up in the optical band by many on-ground facilities (see the Section 6.1 for a description of the observations). Therefore, our interest in this GRB lies in the possibility to fit the synchrotron model to one of the richest datasets collected for the prompt emission of a GRB, and constrain the physical parameters of the emission process.

3.4.1 Spectral analysis

The left panel of Fig. 3.17 shows the light curves (counts s^{-1}) of GRB 180720B detected by three different instruments sensitive to increasing photon energies from top to bottom: NaI (8–900 keV), BGO (0.3–40 MeV), and LLE (30–100 MeV). These light curves show a main event lasting $\sim$ 35 s with numerous overlapping pulses and a very bright peak at $t \simeq 15$ s, followed by another peak at $t \simeq 50$ s. The pulses show the typical fast rise exponential decay (FRED) shape.

We considered five time intervals for the analysis of the burst emission[6]: 0–35 s, 35–70 s, 70–120 s, 120–200 s, and 200–500 s. The choice of these large time intervals for the spectral analysis is motivated by the fact that we also wanted to study the transition from the prompt to the afterglow emission. A more detailed explanation of this time binning will be given in Sec. 6.1. These time intervals are identified in red, yellow, green, blue, and purple, respectively, and this color-code is used in Figs. 3.17 and it will be used also in Fig. 6.1, Fig. 6.2, and Fig. 6.3 in Sec. 6.1.

The first two time intervals 0-35 s and 35-70 s contain the two main emission peaks of the prompt emission. The time–resolved analysis showed that: 1) the first time interval can be fitted by the synchrotron model; 2) the second time interval requires the presence

[6]Every time interval reported in this section on GRB 180720B is referred to GBM trigger time.

of an additional non–thermal spectral component. We interpret the latter as the rising afterglow emission, and it will be described in Chapter 6.

For the purposes of this Chapter, in the following we concentrate on results relative to the first and second time intervals, from 0 to 70 s.

In addition to the standard procedure reported in Appendix A, for the LAT data, we selected photons with energies in the 100 MeV – 100 GeV range and a zenith angle from the spacecraft axis $< 100^{\circ}$ to reduce the contamination of photons coming from the Earth limb. A power-law model was used to fit the LAT spectrum in each time interval. The results of the first two time intervals are resumed in Table 3.11. For GBM data, the two NaI detectors and the BGO detector with the highest count rates, namely NaI#6, NaI#8 and BGO#1, were used for the analysis. Spectra were extracted with `gtburst`. The first two time intervals were analyzed by combining the GBM with the LAT/LLE data (Pelassa et al., 2010). To perform a joint spectral analysis of GBM and LLE data, we used the software XSPEC (v12.10.0c).

3.4.2 Synchrotron model

The first three time intervals are fitted with a physical model for the synchrotron emission from relativistic electrons. We considered relativistic electrons injected with an energy distribution $dN(\gamma)/d\gamma \propto \gamma^{-p}$ between $\gamma_{\rm min}$ and $\gamma_{\rm max}$ and solved the continuity equation accounting for synchrotron losses. The spectral shape at any time t is determined by the ratio of $\gamma_{\rm min}$ to the electron cooling energy $\gamma_{\rm c}$, and by the value of p. In addition to the spectral shape, the model spectrum is specified by two other parameters that determine the energy $E_{\rm m}$ of the photons emitted by electrons of energy $\gamma_{\rm min}$ and the normalisation $F_{\rm m}$ of the $F(E)$ spectrum evaluated at $E_{\rm m}$, respectively. Such a model is not present in the XSPEC library, therefore a table model spectra for different combination of the free parameters was built and implemented in XSPEC.

From the value of $E_{\rm m}$ and the ratio $\gamma_{\rm min}/\gamma_{\rm c}$ it is possible to derive the cooling energy $E_{\rm c}$ of the photons emitted by the electrons cooled down to $\gamma_{\rm c}$ using the relation $E_{\rm c} = E_{\rm m}\,(\gamma_{\rm c}/\gamma_{\rm min})^2$. So the four free parameters can be redefined to be $E_{\rm c}$, $E_{\rm m}$, p, and the normalisation $F_{\rm m}$. Confidence ranges on these parameters were then derived within XSPEC, through the built-in Markov chain Monte Carlo algorithm (`chain` command).

The four free parameters defined above are also associated with the five physical quantities describing the emitting region, namely the co-moving magnetic field B', the total number of emitting electrons $N_{\rm e}$, the bulk Lorentz factor Γ, and the values of $\gamma_{\rm c}$ and $\gamma_{\rm min}$. The value of the bulk Lorentz factor Γ is an additional unknown to the general problem. In the specific case of GRB 180720B this parameter can be derived from the onset of the afterglow (see the Section 6.1). The other four physical quantities can be constrained using this value of Γ and the results of the spectral fitting (see Chapter 5).

3.4.3 Results

In the following, I describe the results of the spectral analysis for SED I and SED II.

3.4.3.1 SED I (0-35 sec): Evidence of synchrotron prompt spectrum

The first SED, corresponding to the time interval 0–35 seconds, is represented in red in Fig. 3.17 and shows a spectrum which extends from 10 keV up to 100 GeV with a single emission component. These spectral results are reported in Table 3.11.

TABLE 3.11: Best-fit parameters for each different model used in the first two SEDs reported in Fig. 3.17 of GRB 180720B. The first column reports the time interval over which the spectrum has been integrated, the second column the detector whose data have been used to build the SED along with the energy range, and the third column represents the different models used to fit that data. From the fourth column onwards: energy flux computed in the energy range reported in the second column, photon energy corresponding to the electron cooling Lorentz factor E_c, photon energy corresponding to the electron injection Lorentz factor E_m, electron energy distribution slope p (corresponding high-energy photon index $\beta = -p/2 - 1$ in parentheses), power-law photon index of the LLE/LAT data, and the reduced χ^2 of the fit with the degrees of freedom in parentheses.

Time interval	Data	Model	Flux $[10^{-7}\mathrm{erg/s\,cm^2}]$	E_c [keV]	E_m [keV]	$p(\beta)$	Γ_{PL}	χ^2_{red}(d.o.f.)
0-35 s	GBM [10 keV - 40 MeV]	Sync	142^{+7}_{-2}	75^{+5}_{-2}	2380^{+24}_{-524}	$> 3.95 (< -2.98)$ @ 3σ	-	1.56 (293)
	LLE [30 - 100 MeV]	PL	$1.73^{+0.17}_{-0.24}$	-	-	-	$-3.44^{+0.36}_{-0.29}$	0.39 (11)
	GBM+LLE [10 keV - 100 MeV]	Sync	142^{+3}_{-1}	79^{+2}_{-3}	1898^{+314}_{-58}	$4.77^{+0.49}_{-0.15}$ $(-3.39^{+0.08}_{-0.25})$	-	1.52 (305)
	LAT [100 MeV - 100 GeV]	PL	$0.34^{+0.10}_{-0.10}$	-	-	-	$-3.87^{+0.71}_{-0.71}$	-
35-70 s	GBM+LLE [10 keV - 100 MeV]	Sync	$13.0^{+0.04}_{-2.2}$	25^{+83}_{-2}	519^{+57}_{-417}	$3.26^{+0.19}_{-0.64}$ $(-2.63^{+0.32}_{-0.1})$	-	0.97(286)
	LAT [100 MeV - 100 GeV]	PL	$1.41^{+0.49}_{-0.49}$	-	-	-	$-2.3^{+0.21}_{-0.21}$	-

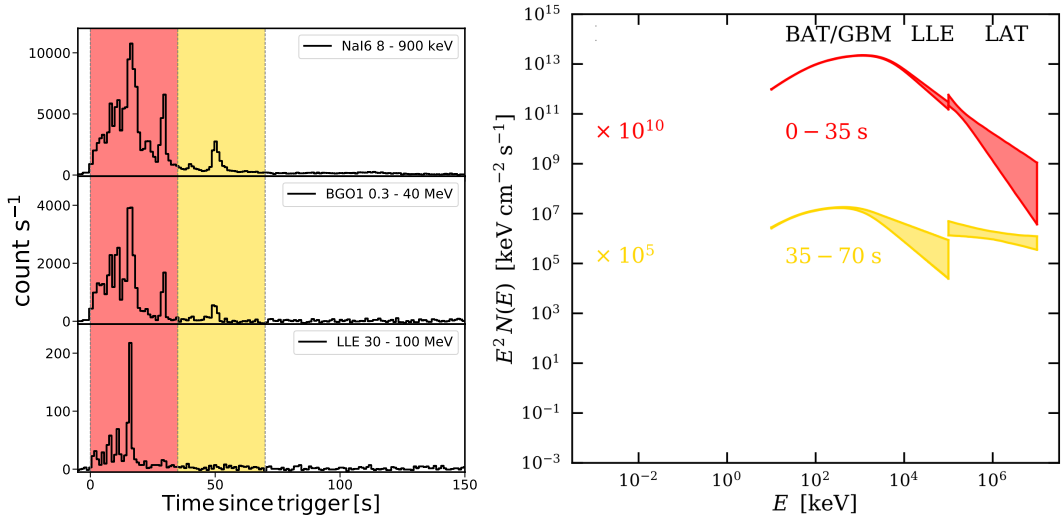

FIGURE 3.17: Left panel: background-subtracted light curves of GRB 180720B, detected by NaI#6 (8–900 keV, top), BGO#1 (0.3–40 MeV, middle), and LAT–LLE (30–100 MeV, bottom). Different time intervals are highlighted with different colours, corresponding to the colour code that will be used also in Fig. 6.1. Right panel: evolution of the first two SEDs of GRB 180720B. Each curve corresponds to a specific time interval and has been rescaled for presentation purposes by the scaling factor reported in the figure. For reference, the top labels denote the instruments providing data in the corresponding energy ranges.

We fitted the GBM and LLE data together and the best-fit model is shown in Fig. 3.18 by the solid black line, with a shaded yellow region representing the 68% confidence interval. The corner plot of the posterior distributions of the parameters of the fit is shown in Fig. 3.19, where no strong residual correlation between the free parameters is evident. The best fit, corresponding to the lowest χ^2, lies in the region characterised by

the larger probability.

The best-fit model returns a steep slope $p = 4.77^{+0.49}_{-0.15}$ of the injected electron distribution. In empirical models (e.g. Band model) this corresponds to a spectral photon index $\beta = -p/2 - 1 = -3.39^{+0.08}_{-0.25}$, which is consistent with the value obtained from the independent fit of the LLE data alone (i.e. $\Gamma_{\rm PL} = -3.44^{+0.36}_{-0.29}$). The independent analysis of the LAT data with a power law results in a consistent soft emission component with slope $\Gamma_{\rm PL} = -3.87 \pm 0.71$. Indeed, the addition of the LLE and LAT data plays a major role in constraining the high energy slope of the spectrum. When fitting the GBM data alone (NaI+BGO) with the synchrotron model described above, we cannot constrain the high energy part of the spectrum, but only set a lower limit on the p parameter, as reported in Table 3.11.

The steep value found when jointly fitting GBM+LLE data is peculiar with respect to the typical β $\sim$-2.3 of the Fermi bursts (Gruber et al., 2014; Goldstein et al., 2012; Nava et al., 2011a) and implies that the population of electrons is distributed over a narrow energy range. The full implication of this relatively steep p value found will be discussed in Chapter 5.

These results show that the photon spectrum $N(E)$ displays a slope $N(E) \propto E^{-2/3}$ below the break energy $E_{\rm break} \sim E_{\rm c}$ and a slope $N(E) \propto E^{-3/2}$ between the break and the peak energy $E_{\rm peak} \sim E_{\rm m}$. These results are similar to the ones reported in Ravasio et al. 2018; Ravasio et al. 2019a and to those recently found in other GRBs detected by *Swift* and *Fermi* with either empirical (e.g. Zheng et al. 2012; Oganesyan et al. 2017; Oganesyan et al. 2018) or physically motivated synchrotron models (Zhang et al., 2016; Burgess et al., 2020; Oganesyan et al., 2019). The emission is in fast cooling regime, even though the cooling is not complete (moderately fast cooling, see Kumar and McMahon 2008b; Daigne, Bošnjak, and Dubus 2011; Beniamini and Piran 2013). The full implication of these results will be discussed in Chapter 5 .

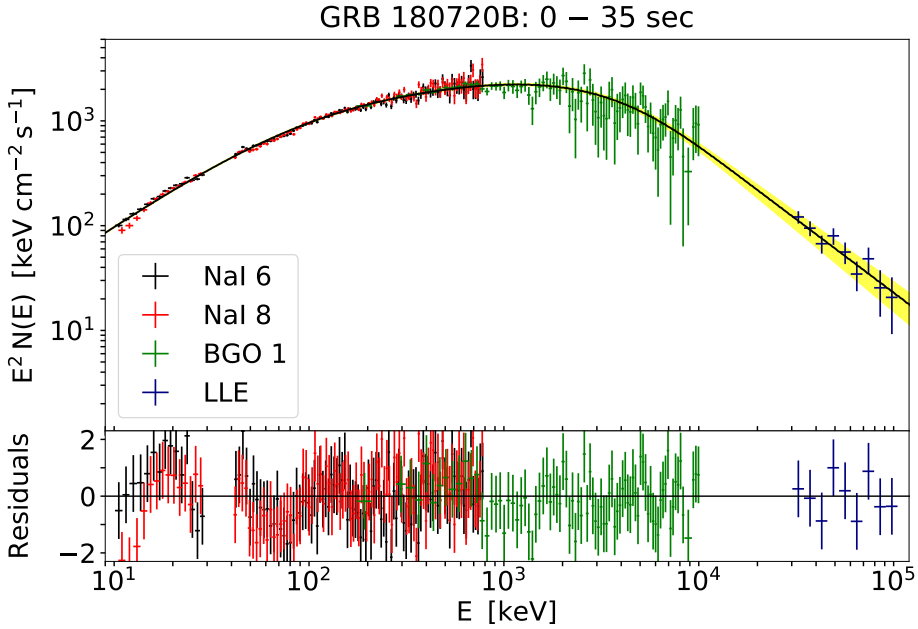

FIGURE 3.18: Spectrum corresponding to the 0-35 s time interval of GRB 180720B. The GBM and LLE data are fitted jointly with the model (shown by the solid line) of synchrotron emission from relativistic electrons. The shaded yellow region represents the 68% confidence region of the best-fit model. The bottom panel shows the data–to–model residuals. The best-fit spectral parameters are reported in Table 3.11

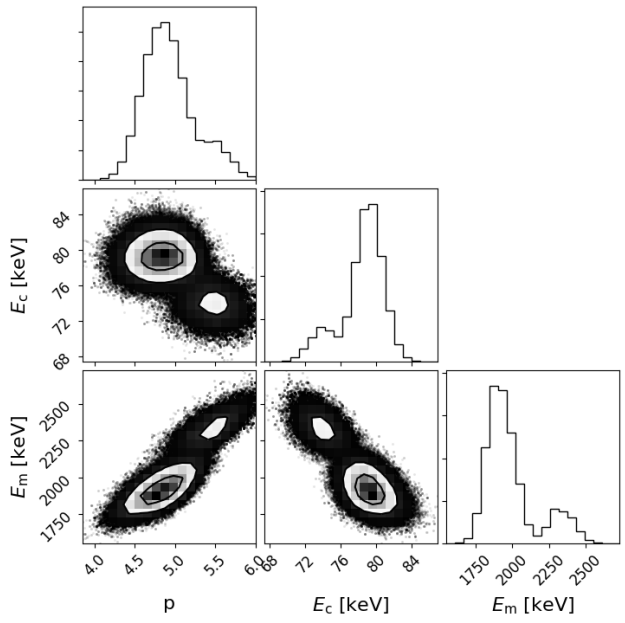

FIGURE 3.19: Posterior distribution corner plot for the free parameters of the synchrotron model used to fit SED I of GRB 180720B. The 1D marginalised posterior distributions are shown on the diagonal, while the 2D marginalised distributions are shown below the diagonal. Contours in the 2D plots are at 1 and 2σ. Outside the 2σ contour, individual samples from our MCMC are shown as black dots.

The residuals of the fit (bottom panel of Fig. 3.18) show that the model properly fits the data over almost the entire spectral range. However, systematic residuals are present below ∼30 keV over a narrow energy range. These residuals could be the reason behind the quite large $\chi^2_{\rm red} \sim 1.5$ obtained in the analysis of the GBM+LLE data in the first time interval. The nature of such residuals could be a poorly calibrated response matrix and/or the break evolution within the considered time bin (Ravasio et al., 2019a). Since SED I includes the main event of the burst, which is characterised by several overlapping pulses, a spectral analysis over such a large temporal interval (∼ 35 s) could be affected by spectral evolution, with the result of producing a time averaged spectrum with a broader shape around the break energy and the peak energy. In order to explore this issue and find out if this could alter the results, we performed a spectral analysis on a finer temporal resolution, by subdividing the first time interval in three bins. These time bins were chosen to have enough signal in the LLE energy range to be able to constrain the high-energy part of the spectra.

The best-fit parameters for the synchrotron model in the three time bins are shown in Table 3.12.

TABLE 3.12: Best-fit parameters for the synchrotron model obtained in the three time intervals in which the first SED of GRB 180720B has been split. For these time intervals, we used GBM and LLE data together, modelling the spectrum from 10 keV up to 100 MeV. The first column reports the time interval over which the spectrum has been integrated. The second column onwards list the following fit parameters: energy flux computed in the energy range 10 keV - 100 MeV, photon energy $E_{\rm c}$ corresponding to the electron cooling Lorentz factor γ_c, photon energy $E_{\rm m}$corresponding to the electron injection Lorentz factor γ_m, electron energy distribution slope p (corresponding high-energy photon index $\beta = -p/2 - 1$ in parentheses), and the reduced χ^2 of the fit with the degrees of freedom in parentheses.

Time interval	Flux $[10^{-7}$erg/s cm$^2]$	$E_{\rm c}$ [keV]	$E_{\rm m}$ [keV]	$p(\beta)$	$\chi^2_{\rm red}$(d.o.f.)
0-14 s	170^{+4}_{-4}	156^{+5}_{-10}	2278^{+418}_{-37}	$4.98^{+0.85}_{-0.002}(-3.49^{+0.001}_{-0.43})$	1.11(341)
14-21 s	228^{+6}_{-1}	99^{+4}_{-3}	1283^{+85}_{-92}	$3.97^{+0.07}_{-0.18}(-2.99^{+0.09}_{-0.04})$	1.17(341)
27-35 s	47^{+1}_{-4}	41^{+1}_{-5}	913^{+195}_{-76}	$5.06^{+0.64}_{-0.54}(-3.53^{+0.27}_{-0.32})$	1.12(341)

The synchrotron spectrum provides a good modeling of the data also in these three time intervals, and the reduced χ^2 are smaller than the one obtained from the analysis of the larger time interval. From this analysis, it is possible to note that the spectral break and peak tend to evolve towards lower energies as also found in Ravasio et al. (2019a). This introduces a broadening of the spectral shape, as suspected. The high-energy part of the spectra is still characterised by a very steep slope, even though we note a significant change in the p value (becoming softer) in the second time bin, which corresponds to the peak of the lightcurve.

It is interesting to compare these results with the ones obtained from the time-resolved analysis of GRB 180720B with the empirical function 2SBPL (see Section 3.2). The comparison is not completely fair, since the time-integrated analysis was performed on a larger timescale (from -1 to 56 s) than the one considered here (from 0 to 35 s) and the time–resolved fits were performed on smaller time bins (of 1.024 s), where no strong spectral evolution is evident. However, some conclusions can still be drawn, since the time-resolved analysis timescale (on which I will focus the comparison) was similar (4–31 s) and the 2SBPL function qualitatively reproduces the same shape of the synchrotron spectrum in fast cooling regime. Regarding the presence of an additional spectral break, the mean value of $\langle E_{\rm break} \rangle$= 56±39 keV (spanning from 24 to 182 keV, see Section 3.2)

found with the 2SBPL is consistent with the cooling frequency E_c= 79^{+2}_{-3} keV (spanning from 41 to 156 keV, see Table 3.12) of the synchrotron spectrum found in this analysis. The peak energies found from the empirical fits are instead systematically smaller than the ones found from the synchrotron fits: the time-resolved analysis with 2SBPL reported a mean value of $\langle E_{\rm peak} \rangle$= 1093±481 keV (spanning from 416 to 2426 keV), while the synchrotron fits return a time-integrated value of $E_{\rm peak}$= 1898^{+314}_{-58} keV (spanning from 913 to 2278 keV). This could be due to the fact that the synchrotron spectrum is indeed wider than the 2SBPL function and it takes a few orders of magnitude in energy to reach the asymptotic values of the slopes, while the 2SBPL width is regulated by the curvature parameters, kept fixed during the fit procedure. In addition, the steep high–energy slope β= $-3.39^{+0.08}_{-0.25}$ found in this analysis significantly differs from the empirical fits results, where I found $\langle \beta \rangle$ = -2.58 ± 0.20. This is presumably due to the fact that in the previous analysis I did not consider the LLE data, that instead help in constraining the shape of the high energy end of the spectrum.

3.4.3.2 SED II (35-70 sec): transition between prompt and afterglow emission

The second SED, represented in yellow in Fig. 3.17, shows the presence of two emission components. The spectrum below 100 MeV (obtained combining GBM and LLE data) is still well fitted by the synchrotron model, with values of the peak and break energies a factor $\sim$ 2 smaller than those of SED I. The slope of the electron energy distribution is harder than the value in the previous SED ($p = 3.26^{+0.19}_{-0.64}$). Also the LAT data, when fitted alone using a power–law model, show a harder spectrum, with $\Gamma_{\rm PL} = -2.3 \pm 0.2$. In the following time intervals, as it will be shown in the Section 6.1, the photon index of the LAT spectrum is even harder, settling around $\Gamma_{\rm PL} \sim -2$ (as reported in Fig. 6.2). The prompt synchrotron emission dominates in the GBM+LLE energy range and above 100 MeV the LAT spectrum flux is inconsistent with the low-energy spectrum flux. This could indicate that the afterglow component, which is characterised by a typical photon index $\Gamma_{\rm PL} \sim -2$, is rising and contributing at higher energies.

In conclusion, the SED in the time interval 35-70 s shows the coexistence of two different components. The superposition of this harder emission component with the peaked prompt emission spectrum as seen by the GBM can account for the harder p value obtained from the fit of the GBM+LLE data with the synchrotron model.

3.4.4 Conclusions

In this section I reported the study of the prompt emission of GRB 180720B, whose spectral evolution has been followed up to 70 s after the trigger time. The SED evolution (Fig. 3.17) shows the progressive turning off of the prompt emission, which dominates up to 70 seconds in the 0.01–100 MeV energy range.

The SEDs of the first two time intervals were fitted with a physical model of synchrotron emission from a relativistic population of injected electrons. The synchrotron model provided an acceptable fit of the data, highlighting the presence of two different break energies in the prompt spectra, E_c and E_m. These energies evolve with time, becoming softer, while keeping an average ratio of $\sim$17. The ordering of these energies indicates a fast cooling regime. These results are consistent with those obtained with an empirical function described in the Section 3.2, regarding GRB 180720B, which belongs to selected sample of the 10 long brightest GRBs detected by *Fermi*.

These results are consistent with those found by Oganesyan et al. (2017), Oganesyan et al. (2018), Ravasio et al. (2018), and Ravasio et al. (2019a) using an empirical function and with those found in Oganesyan et al. (2019), who found acceptable fits of the

broadband spectral shape with a physical synchrotron model. In particular, these results demonstrate the validity of the synchrotron physical model to properly fit the spectral data of the prompt emission of a GRB. Inside the considered energy band, the synchrotron model well describes a complex spectral shape that requires two break energies and three power–laws. In the fast cooling regime, the slopes of the two power–laws below the peak energy of the spectrum are fixed and are not able to adapt to a different spectral shape, contrary to the fit with the empirical function, where the slopes were free to vary.

A synchrotron model was also found to be a good description of the spectral data in 19 single–pulse *Fermi*/GBM bursts in Burgess et al. (2020). However, the majority of spectra analysed by the authors displays a regime of slow cooling, namely $\gamma_{\rm cool}/\gamma_{\rm min} > 1$, as shown in their Figure 3. The vast majority of the p values they found are greater than 3, which in the slow cooling regime allows to have the synchrotron minimum frequency $\nu_{\rm min}$ corresponding to the peak energy of the νF_ν spectrum. Below the peak energy, they do not observe an additional spectral break, but rather a single power–law with slope -2/3, while the cooling frequency is located in the BGO/LLE energy range. The spectral shape found by the authors is therefore different from the one found in the results presented in this thesis and also in the work of Oganesyan et al. (2019). Moreover, the authors claimed the presence of a transition between slow and fast cooling at late times in the prompt emission, and especially during the decay of the luminosity, which is counter intuitive. Contrary to the results reported by the authors, we did not find any transition of cooling regimes in the spectra analyzed, which we always interpret as $\gamma_{\rm cool}/\gamma_{\rm min} < 1$. However, the transition from a dominant slow cooling regime to the fast cooling one, observed so far only for the single-pulse bursts analyzed in Burgess et al. (2020), is an interesting feature to investigate, as it would be indicative of a transition of physical conditions in the GRB outflow.

The results obtained in this Section have fundamental implications for the understanding of the physical conditions occurring during the prompt phase of GRBs. Thanks to the synchrotron modeling, it is possible to estimate the intrinsic physical parameters of the emission region during the prompt phase, such as the co-moving magnetic field B', the minimum electron Lorentz factor $\gamma_{\rm min}$, and the total number of electrons N_e. From the modeling, we found also that the emitting electrons should be injected with a steep power-law energy distribution with $p \sim 4.8$, which is unusual and implies that electrons are narrowly distributed. I will discuss this issue and the emission region parameters in the context of the standard GRB prompt emission model in Chapter 5.

Chapter 4

The high–energy extension of prompt emission spectra

Instruments like GBM or BATSE provided the opportunity to study in detail thousands of GRB prompt emission spectra, but their spectral coverage is limited to the keV–MeV energy range. Over the years, the extension of the accessible range up to GeV energies allowed to study the GRB prompt emission spectrum at higher energies (above $\sim$ 40 MeV). Besides the first few detections of radiation above several tens of MeV provided by the CGRO/EGRET and AGILE/GRID instruments, most of our present knowledge on GRB high–energy emission comes from the *Fermi*/LAT instrument. Its larger field of view and effective area with respect to its predecessors allow to detect an average of 14 GRBs per year. Nevertheless, this leads to have LAT detections of GRBs available only for $\sim$ 12% GBM-detected bursts (see Nava 2018 for a recent review on the high–energy emission of GRBs). In the majority of cases, the LAT data, when available, reveals the presence of an extra power–law component, which rises with a small delay ($\sim$ a few seconds) after the prompt emission, it lasts longer, it is less variable and in some cases it has been observed rising also during the prompt emission (e.g. see the GRBs emission described in Chap. 6). This emission is thought to be of external origin and therefore interpreted as the afterglow emission of the burst. Instead, the early emission detected by LAT, simultaneous to the prompt phase and characterized by variability, can be interpreted as the extension of the prompt emission. Therefore, the study of the early emission detected by LAT offers the rare opportunity to investigate the high–energy extension of the prompt emission spectrum, without the contamination from the afterglow component.

However, there is a grey area between the peak energy of the spectrum and $\sim$100 MeV, where the poor statistics of the prompt spectrum (decaying as a power–law with a typical β $\sim$-2.5 of the Band function) and the low effective area of the available detectors (BGO) make it difficult to characterize the spectrum at high energy. The inclusion of the LLE (30–100 MeV) and LAT data (>100 MeV) in turn can reveal interesting features of the prompt emission spectrum. Several works found that the high–energy part of the prompt spectrum lie on the extrapolation of the keV–MeV (GBM) one, thus consisting of a single power–law up to $\sim$ GeV energies, although with a softer index than the one inferred from fitting the GBM data alone (e.g. Fermi Large Area Telescope Team et al. 2012; Abdo et al. 2009b; Axelsson et al. 2012). Assuming that the spectrum of accelerated electrons is a power–law and that the cooling is dominated by the synchrotron emission, the photon index of the power–law describing the spectrum above the peak energy allows to constrain the spectral index p of the electrons' energy distribution, providing fundamental insights on the acceleration mechanism (Baring, 2009; Shen, Kumar, and Robinson, 2006).

On the other hand, it was also shown that the spectrum of a handful of GRBs requires a high–energy break between the GBM and LAT energy bands, revealing a statistically significant presence of an exponential spectral cutoff from a few tens to hundreds of MeV (Fermi Large Area Telescope Team et al., 2012; Tang et al., 2015; Vianello et al., 2018). The

cutoff energy could be interpreted as a sign of the maximum energy γ_{max} of the parent electrons' distribution, although it is expected at higher energies for typical GRB parameters. A more likely alternative is to interpret the cutoff as due to the pair-production opacity, which allows to derive the estimate of the bulk Lorentz factor Γ of the jet (Lithwick and Sari, 2001). Knowing Γ is crucial as it allows to infer the comoving frame properties of the emitting region, shedding light on many interesting (but still unknown) physical quantities (e.g. the nature of the radiation process, the location of the emitting region, the ejecta mass). Therefore, from the study of the extension to high energies of GRB prompt emission spectra, we can gain valuable information regarding the physics underlying the GRB emission. The combination of GBM and LAT data offers a powerful tool to study GRB spectra over a wide energy range, spanning about 6 decades of gamma-ray energy.

In order to characterize the high–energy part of GRB prompt emission spectra, I analyzed a sample of GRBs whose prompt emission has been detected up to GeV energies. In this Chapter I describe the results of the preliminary analysis of the spectra obtained combining GBM and LAT data. The interpretation of these results will be given in Chapter 5. The complete description and the full implication of the preliminary results discussed in this Chapter will be presented in a paper, which is in preparation.

4.1 The sample

The second catalog of LAT-detected GRBs contains 186 events (Ajello et al., 2019), revealed during the first 10 years of activity of *Fermi*. From the LAT online Catalog[1], we selected those GRBs detected by LAT in the energy range 30-100 MeV, namely those with LLE data available. There are 91 GRBs following this criterion. We sorted these 91 GRBs according to their significance in the LLE data, which is measured in terms of σ using the bayesian blocks detection algorithm, according to the catalog. Since we are interested in investigating the high-energy part of GRB spectra, we required to have enough signal in the LLE data, namely we selected GRBs with $\sigma \geq 20$. Moreover, to ensure a good photon statistics also in the GBM energy range, we required a fluence $F > 10^{-5}\,\mathrm{erg\,cm^{-2}}$ measured in the 10-1000 keV energy range over the total duration of the burst, as reported in the GBM Catalog. Applying these criteria, we obtained 22 GRBs. All the selected events belong to the long class.

Fig. 4.1 shows the fluence measured in the 10-1000 keV energy range (i.e. detected by GBM) vs. the significance of the signal in the LLE data, in units of σ, for the 91 GRBs of the LAT Catalog with LLE data available, represented by the red points. The selected sample of 22 GRBs is represented by the blue points. The selection criteria described above are represented by the two black dashed lines. From our selection we excluded GRB 090926A (represented with the red point falling in the selected region in Fig. 4.1). This GRB has an additional high-energy power-law component detected by the LAT during the prompt phase, which shows also a spectral cutoff at 1.4 GeV (Ackermann et al., 2011; Yassine et al., 2017). This prevents the identification of a possible high–energy cutoff on the main spectral component and the accurate determination of the slope of the high–energy power–law.

[1] https://heasarc.gsfc.nasa.gov/W3Browse/all/fermilgrb.html

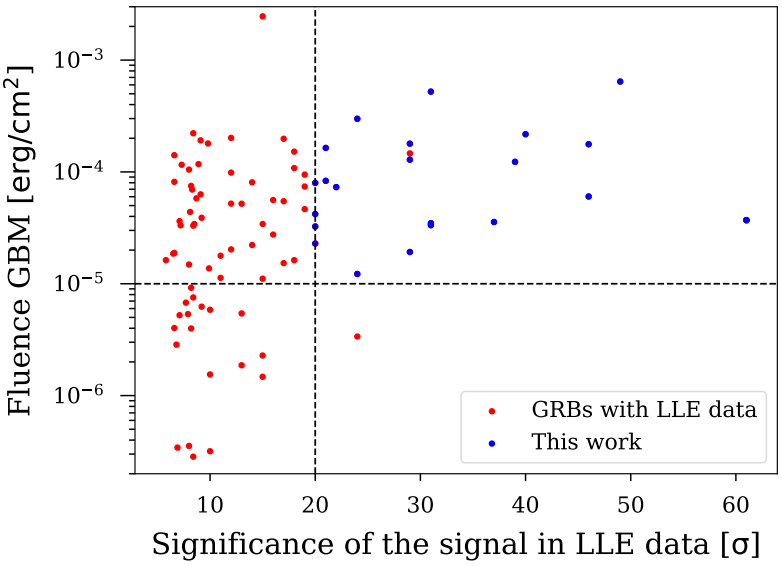

FIGURE 4.1: The sample of 22 GRBs analyzed (blue points) among the 91 events (red points) detected in the LLE energy range (30–100 MeV), in 10 years of *Fermi* activity, according to the LAT Catalog. We selected the events applying a cut on the fluence in the 10-1000 keV energy range and a cut on the significance of the signal in the LLE data, both represented by the two black dashed lines. The red point falling in the selected region represents GRB 090926A, which has been excluded from the selection (see the text for an explanation).

Table 4.1 lists the name, the fluence in the 10-1000 keV energy range, the significance of the LLE signal and the redshift, if available, for each selected event.

TABLE 4.1: The sample of 22 long GRBs selected to study the high–energy extension of the spectrum. The events satisfies two selection criteria: they have a significance in the LLE signal $\sigma \geq 20$, as reported in the LAT Catalog, and a fluence measured in the energy range 10–1000 keV over the total duration of the burst $F > 10^{-5}$ erg cm^{-2}, as reported in the GBM Catalog. The first column lists the name of the GRB (with the last three digits referring to the naming convention of GBM triggers), the second column reports the fluence of the burst (10–1000 keV), the third column reports the significance of the signal in the LLE data, in terms of σ. The last column reports the redshift of the burst, if available. The events are listed in order of decreasing significance of the signal in the LLE data.

GRB Name	GBM Fluence [10^{-4} erg cm^{-2}]	Significance of LLE signal σ	Redshift
110721[200]	0.370	61	–
160625[945]	6.43	49	1.406
080916[009]	0.603	46	4.35
170214[649]	1.77	46	2.53
100724[029]	2.17	40	–
140206[275]	1.23	39	–
131108[862]	0.357	37	2.4
141028[455]	0.348	31	2.332
100116[897]	0.334	31	–
160821[857]	5.22	31	–
130504[978]	1.29	29	–
110328[520]	0.192	29	–
160509[374]	1.79	29	1.17
180720[598]	2.99	24	0.654
151006[413]	0.122	24	–
160905[471]	0.732	22	–
150902[733]	0.832	21	–
100826[957]	1.64	21	–
090328[401]	0.420	20	0.736
110731[465]	0.229	20	2.83
160910[722]	0.797	20	–
150202[999]	0.325	20	–

In addition to the procedure reported in Appendix A, I describe here specific details of the data analysis. Spectra were extracted with the public software GTBURST. While the time interval selection is typically performed on the most illuminated NaI detector, for the purpose of this analysis, which aims at investigating the high-energy extension of the prompt spectrum, we selected the time interval according to the lightcurve detected in the LLE energy range. Fig. 4.2 shows an example of the selection performed. The three panels display the lightcurve of GRB 140206 in progressively higher energy ranges in the NaI, BGO and LLE data. The red vertical dotted lines mark the time interval analyzed. As it can be seen, the selection includes most of the emission detected in the LLE data, which extends up to ∼26 s. On the other hand, the last dimmer emission pulse present in the NaI lightcurve, which extends up to ∼45 s, does not have a counterpart signal in the LLE data, and it is not included in the temporal selection.

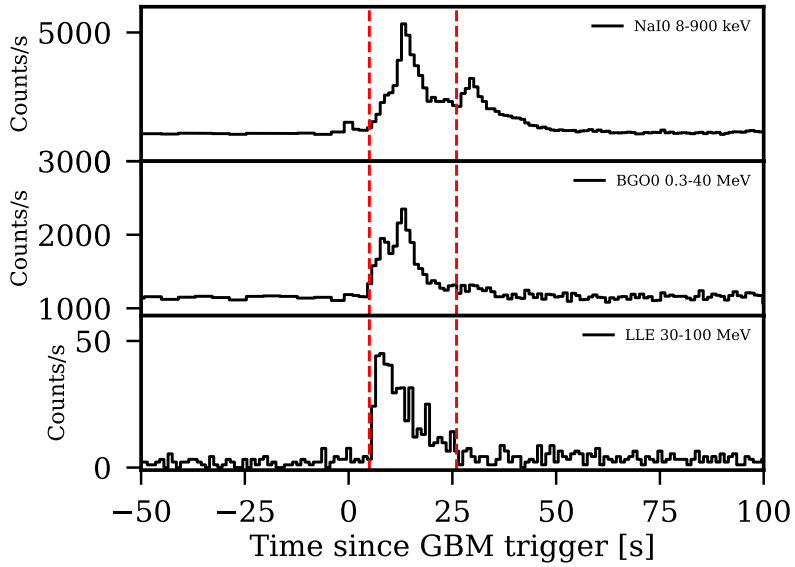

FIGURE 4.2: Example of the time interval selection performed in this analysis. Since we want to study the high–energy part of the spectrum, the selection, highlighted by the red dashed vertical lines, is based on the emission in the LLE data and not in the GBM ones. As clearly visible in this example, the selected time interval includes most of the emission detected in the LLE energy range, excluding time intervals where there is no emission in the 30–100 MeV energy range (e.g. the last dimmer pulse in the NaI energy range). This example refers to the lightcurve of GRB 140206 detected in different energy bands, from the lowest (8-900 keV, NaI detectors) to the highest (30-100 MeV, LLE data) available. In this example plot, data are not background-subtracted.

Regarding the LAT data, we selected P8R3_TRANSIENT020 class events, filtering photons in the 100 MeV – 10 GeV energy range. For those GRBs whose LAT data (100 MeV - 10 GeV) revealed to be an upper limit, we decided to slightly extend the energy range of LLE data, otherwise analyzed in the energy range 30–100 MeV, up to 150 MeV. This choice concerns a total of 5 GRBs.

For each GRB, we performed a joint spectral analysis of the GBM (10 keV – 10 MeV), LLE (30 - 100 MeV) and LAT (100 MeV - 10 GeV) data, with the public software XSPEC (v. 12.10.1f).

4.1.0.1 Fitting models

We analyzed each time–integrated spectrum with four different empirical functions: SBPL, 2SBPL (see Chapter 2 for the description of their functional form), and their modified versions including the presence of a high–energy cutoff, *SBPLCUTOFF* and *2SBPLCUTOFF*, respectively, which are described in the following. Fig. 4.3 shows the four different spectral shapes that we want to test in this analysis, including the relative instrument we used to cover each energy range. The choice of fitting also with the 2SBPL is motivated by the fact that, besides searching for the presence of a cutoff at high energies, we also want to test the possibility of having a spectral break below the peak energy, as found in the previous analysis (see Chapter 3).

In order to identify the possible presence of a cutoff at high energies, we multiplied both SBPL and 2SBPL by an exponential cutoff function available among XSPEC models, called *highecut*. This piecewise function is defined as:

$$highecut(E) = \begin{cases} 1 & \text{for } E \leq E_c \\ e^{(E_c - E)/E_{fold}} & \text{for } E \geq E_c \end{cases}$$

with E_c representing the energy at which the function starts to modify the basic model and E_{fold} regulating the sharpness of the exponential drop. The combination of the two quantities provides the energy at which the drop in the flux reaches a value of $1/e$, namely at $E_{cutoff} = E_c + E_{fold}$. We consider E_{cutoff} as the relevant energy at which the spectrum shows a significant change with respect to the extrapolation of the power–law. The relative errors of E_c and E_{fold} have been summed in quadrature.

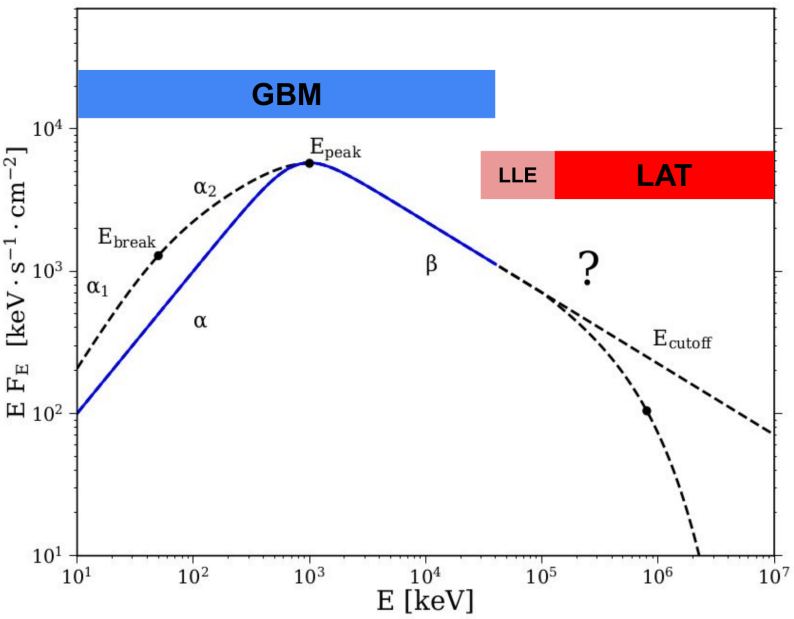

FIGURE 4.3: Representation of the four possible GRBs prompt emission spectral shapes tested in this analysis and the relative spectral coverage of the GBM and the LAT instruments on board *Fermi*. The typical GRBs spectrum is shown with the blue solid line, characterized by the usual α, β and E_{peak} parameters. Below the peak energy, the dashed black line shows the possible presence of a spectral break, modelled with the additional parameters α_1, α_2 and E_{break}(as shown in Chap. 3). At higher energies, above E_{peak}, the spectrum could show either the presence of a exponential cutoff, highlighted by E_{cutoff}, or the extension of the power-law with slope β (dashed black lines). The positions of the relevant energies for each model are marked with black dots. Combining the GBM and the LAT data, the analyzed spectra span 6 orders of magnitude in energy. The y-axis scale is arbitrary.

We used the PG-Statistic, valid for Poisson data with a Gaussian background, in the fitting procedure. The best-fit model is selected by minimizing the Akaike information criterion (AIC, Akaike 1974). In particular, we select the more complex model only if the improvement of the fit corresponds to $\Delta AIC \geq 6$ (Burnham and Anderson, 2004) [2]. The best–fit parameters and their uncertainties have been estimated through Markov Chain Monte Carlo (MCMC) approach.

[2]The quantity $e^{-(AIC_i - AIC_{min})/2} = e^{-\Delta AIC/2} \sim 0.05$ represents the relative likelihood of the i-th model with respect to the model with the lowest AIC value. It is proportional to the probability of the i-th model to minimize the information loss, namely the i-th model is 0.05 times as probable as the first model to represent the data (Burnham and Anderson, 2004)

4.2 Results of the spectral analysis

In Table 4.2, we present the results of the time-integrated analysis from 10 keV up to 10 GeV of the selected sample of LLE-detected GRBs. For each GRB, the table lists the name, the best fit model (according to the ΔAIC criterion), the best fit parameters, the value of the PG-Statistic and, for those cases in which the spectrum is better fitted with the addition of a cutoff, the related difference in AIC. The reported errors are at the 1-σ level.

TABLE 4.2: Best–fit parameters for the 22 long GRBs analyzed. The first column displays the name of the burst, the second column reports the best–fit model, and the following columns report the corresponding best–fit parameters. If the best–fit model is the 2SBPL, the third and fifth columns show the indices α_1 and α_2 above and below the break energy $E_{\rm break}$, which is reported in the fourth column. If the best–fit model is the SBPL, the photon index α is reported in the third column. The peak energy $E_{\rm peak}$ and the high energy slope β are reported for all best–fit models in the fourth and seventh column, respectively. The cutoff energy, both as an estimate or as a lower limit, is reported in the eight column. GRBs showing a significant cutoff in the spectrum have been highlighted in boldface. The PG–Stat value is given for each GRB in column 9, while the corresponding improvement (ΔAIC) of the fit with respect to the basic model (SBPL or 2SBPL) is reported in the last column only for GRBs showing a cutoff.

Name	Best fit model	$\alpha_1(\alpha)$	$E_{\rm break}$ [keV]	α_2	$E_{\rm peak}$ [keV]	β	$E_{\rm cutoff}$ [MeV]	PG–Stat	ΔAIC
110721	2SBPL	$-0.67^{+0.09}_{-0.07}$	$60.9^{+15.8}_{-13.0}$	$-1.51^{+0.05}_{-0.05}$	$2349.3^{+287.8}_{-251.2}$	$-2.74^{+0.06}_{-0.09}$	$\geq$689.7	360.3	-
160625	**2SBPLCUTOFF**	$-0.55^{+0.01}_{-0.01}$	$123.6^{+3.3}_{-4.3}$	$-1.71^{+0.02}_{-0.02}$	$738.1^{+20.7}_{-23.2}$	$-2.72^{+0.01}_{-0.03}$	$297.6^{+77.4}_{-30.6}$	**655.7**	**17.5**
080916	SBPL	$-1.05^{+0.02}_{-0.02}$	-	-	$555.0^{+66.2}_{-24.1}$	$-2.22^{+0.05}_{-0.02}$	$\geq$3468	385.4	-
170214	**SBPLCUTOFF**	$-0.86^{+0.01}_{-0.01}$	-	-	$369.6^{+14.4}_{-15.2}$	$-2.31^{+0.03}_{-0.01}$	$236.1^{+83.7}_{-31.5}$	447.8	24.2
100724	**SBPLCUTOFF**	$-0.82^{+0.01}_{-0.01}$	-	-	$600.0^{+154.3}_{-54.0}$	$-2.06^{+0.03}_{-0.01}$	$45.4^{+12.2}_{-5.6}$	438.6	167.7
140206	**SBPLCUTOFF**	$-0.98^{+0.01}_{-0.01}$	-	-	$395.2^{+29.1}_{-23.1}$	$-2.18^{+0.03}_{-0.03}$	$88.3^{+18.2}_{-12.5}$	**429.8**	**69.1**
131108	SBPL	$-0.98^{+0.02}_{-0.02}$	-	-	$360.2^{+15.5}_{-13.8}$	$-2.23^{+0.01}_{-0.01}$	$\geq$825.1	470.9	-
141028	2SBPL	$-0.83^{+0.03}_{-0.03}$	$124.4^{+11.2}_{-7.2}$	$-1.97^{+0.05}_{-0.02}$	$1256.5^{+1531.8}_{--2.0}$	$-2.92^{+0.03}_{-0.32}$	$\geq$488.5	345.6	-
100116	SBPL	$-1.11^{+0.02}_{-0.01}$	-	-	$702.6^{+64.6}_{-67.8}$	$-2.69^{+0.06}_{-0.04}$	$\geq$502.2	458.3	-
160821	**2SBPLCUTOFF**	$-0.91^{+-0.0}_{-0.02}$	$149.1^{+19.5}_{---0.3}$	$-1.53^{+-0.0}_{-0.04}$	$1341.8^{+63.9}_{-29.7}$	$-2.5^{+-0.01}_{-0.09}$	$46.5^{+4.6}_{-2.2}$	**1004.8**	**200.9**
130504	2SBPL	$-1.03^{+0.03}_{-0.02}$	$204.7^{+21.2}_{-26.1}$	$-1.95^{+0.06}_{---1.95}$	$1405.8^{+573.5}_{-712.9}$	$-3.29^{+0.19}_{-0.4}$	$\geq$86.51	587.0	-
110328	2SBPL	$-0.95^{+0.05}_{-0.1}$	$131.6^{+96.8}_{-26.3}$	$-1.74^{+0.06}_{-0.13}$	$10559.9^{+1162.3}_{-3710.5}$	$-4.6^{+0.95}_{-0.28}$	$\geq$128.6	360.3	-
160509	**SBPLCUTOFF**	$-0.89^{+0.01}_{-0.01}$	-	-	$392.0^{+17.1}_{-15.1}$	$-2.16^{+0.02}_{-0.02}$	$100.7^{+9.9}_{-16.8}$	**388.0**	**171.0**
180720	**2SBPLCUTOFF**	$-0.52^{+0.07}_{-0.09}$	$24.2^{+3.7}_{-1.6}$	$-1.36^{+0.01}_{-0.02}$	$788.1^{+42.1}_{-20.3}$	$-2.39^{+0.03}_{-0.05}$	$37.4^{+2.2}_{-4.3}$	**517.8**	**42.2**
151006	2SBPL	$-0.86^{+0.01}_{-0.11}$	$50.3^{+34.7}_{-3.3}$	$-1.67^{+0.03}_{-0.14}$	$5319.3^{+5399.2}_{-170.6}$	$-3.39^{+0.18}_{-0.64}$	$\geq$188.9	310.4	-
160905	**SBPLCUTOFF**	$-0.9^{+0.02}_{-0.02}$	-	-	$794.5^{+90.6}_{-59.0}$	$-2.4^{+0.12}_{-0.13}$	$14.3^{+4.7}_{-2.8}$	**398.1**	**20.6**
150902	2SBPL	$-0.58^{+0.03}_{-0.03}$	$139.3^{+10.7}_{-11.1}$	$-1.78^{+0.08}_{-0.08}$	$368.7^{+39.5}_{-51.1}$	$-2.82^{+0.04}_{-0.06}$	$\geq$495.3	379.5	-
090328	**SBPLCUTOFF**	$-1.08^{+0.02}_{-0.03}$	-	-	$651.3^{+63.0}_{-51.7}$	$-2.2^{+0.04}_{-0.05}$	$109.5^{+35.3}_{-6.3}$	**325.0**	**25.8**
100826	2SBPL	$-0.76^{+0.03}_{-0.02}$	$125.7^{+8.1}_{-11.1}$	$-1.89^{+0.08}_{-0.03}$	$1261.7^{+530.4}_{-332.1}$	$-2.72^{+0.18}_{-0.13}$	$\geq$235.4	543.0	-
110731	SBPL	$-1.04^{+0.03}_{-0.02}$	-	-	$336.5^{+7.7}_{-19.0}$	$-2.37^{+0.05}_{-0.02}$	$\geq$1942	380.2	-
160910	**2SBPLCUTOFF**	$-0.7^{+0.05}_{-0.07}$	$94.1^{+52.9}_{-26.2}$	$-1.38^{+0.12}_{-0.26}$	$340.3^{+18.3}_{-48.6}$	$-2.37^{+0.04}_{-0.05}$	$98.2^{+12.5}_{-5.6}$	**420.7**	**8.3**
150202	SBPL	$-0.94^{+0.01}_{-0.04}$	-	-	$216.8^{+12.1}_{-4.7}$	$-2.46^{+0.02}_{-0.07}$	$\geq$56.72	388.6	-

Since we want to investigate the shape of the high–energy part of the spectrum, in the following sections we will focus on the evidence of an exponential cutoff at high energies and on the slope of the spectrum above the peak energy.

4.2.1 GRBs with high-energy spectral cutoff

In 10 out of 22 GRBs the addition of an exponential cutoff largely improved the fit, namely their time-integrated spectrum shows a statistically significant exponential drop at high energies with respect to the basic model. The cutoff energy $E_{\rm cutoff}$ is well constrained in all the 10 spectra and its distribution spans a wide range of values, from $\sim$ 14 up to 298

MeV. In 4 GRB spectra the cutoff energy is above 100 MeV, while for the remaining 6 it falls in the LLE energy range, namely it is below 100 MeV.

Fig. 4.4 shows an example of a GRB spectrum showing a cutoff at high–energy. In particular, the data refer the νF_ν representation of the time-integrated spectrum of GRB 140206. Data from different detectors have been color-coded as shown in the legend. The top plot shows the fit with the SBPL function (solid black line), which models the spectral shape with the following best–fit parameters: $\alpha = -1.01 \pm 0.01$, $\beta = -2.35 \pm 0.01$ and $E_{\rm peak} = 326.1^{+8.8}_{-6.6}$ keV. However, both the LLE and LAT data are not properly modelled by the high–energy power–law with slope β, and this produces a systematic trend visible in the residuals from $\sim$ 80 MeV onwards, indicating that the function is overestimating the data (see the panel below). The bottom plot shows the fit with the SBPLCUTOFF function. For comparison, it is also represented with a dashed black line the SBPL function without the exponential cutoff term. It is possible to note that the addition of an exponential cutoff provides a significant improvement of the fit (statistically evaluated in this case by a ΔAIC = 69.1). When fitted with the SBPLCUTOFF function, the spectral data are modelled by a larger peak energy $E_{\rm peak} = 395.2^{+29.1}_{-23.1}$ keV and a softer β parameter $\beta = -2.18 \pm 0.03$ with respect to the fit with the SBPL. The exponential cutoff, parametrized by a cutoff energy at $E_{\rm cutoff} = 88.3^{+18.2}_{-12.5}$ MeV, absorbs the previously visible trend in the residuals.

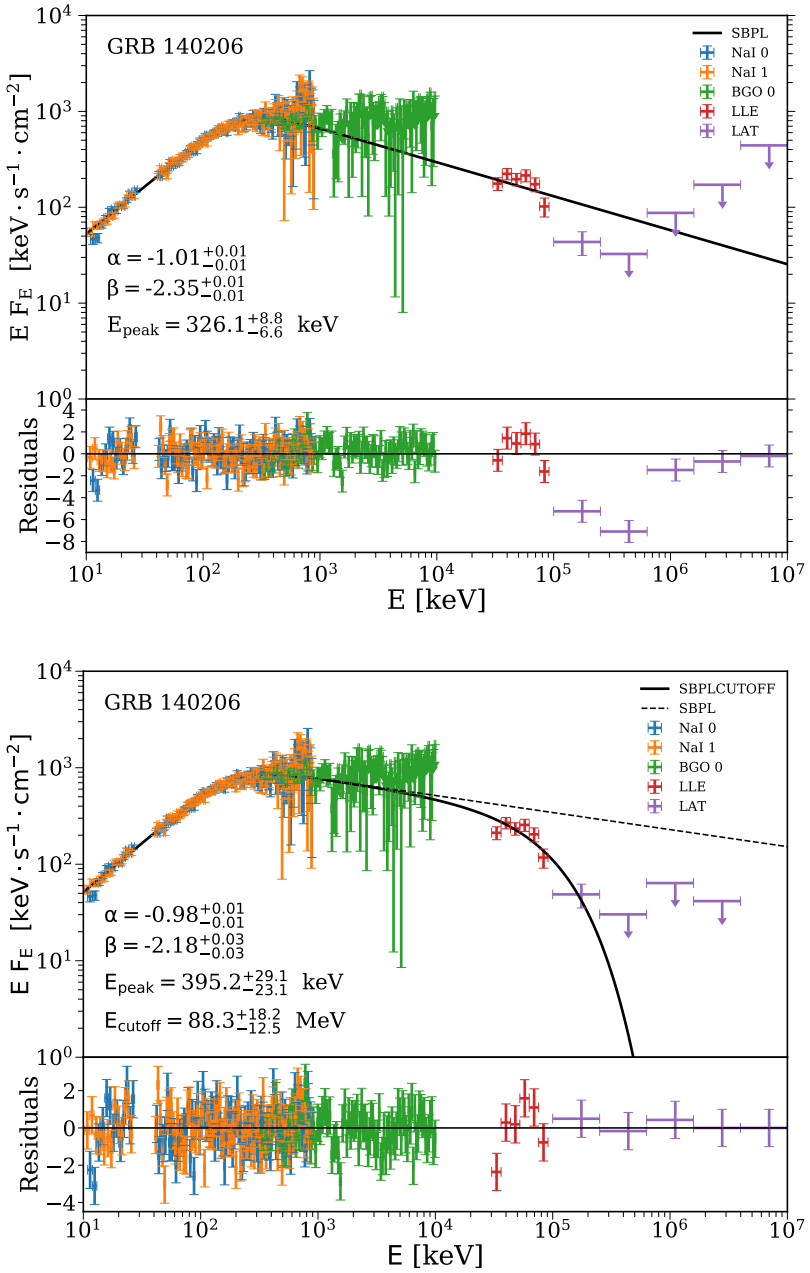

FIGURE 4.4: Example of a time-integrated spectrum showing a cutoff at high–energy. Data correspond to the signal detected by different instruments (colour-coded as shown in the legend) for GRB 140206. The top plot shows the fit with the SBPL function, represented by the solid black line. The bottom plot shows the same spectral data fitted with the addition of an exponential cutoff, namely with the SBPLCUTOFF function, represented with the solid black line. The dashed black line displays the SBPL function without the exponential cutoff term. The parameters of the best–fitting models and their 1-σ errors are reported in each plot (see also Tab. 4.2). The bottom panel of each plot shows the residuals of the spectral fit, namely the distance of the data from the model in units of the errors. Data have been rebinned for graphical purposes.

For 6 of the 10 GRBs showing a cutoff, the basic model that best describes the spectrum below the cutoff energy is the SBPL, while for the other 4 GRBs the best fit model

is the 2SBPL. This means that for 4 GRBs, the spectrum from 10 keV to 10 GeV is characterized by 3 spectral breaks: the break energy $E_{\rm break}$, the peak energy $E_{\rm peak}$ and the cutoff energy $E_{\rm cutoff}$. This result shows how crucial it is a wide and continuous energy coverage of the GRBs prompt emission spectrum to systematically characterize the whole spectral shape.

Combining the 4 GRBs best fitted by the *2SBPLCUTOFF* with the 7 GRBs best fitted by the 2SBPL, the presence of a low-energy break is reported in a total of 11 out of 22 GRBs. We note that, of these 11 GRBs, only 3 GRBs were already found to have a break in Ravasio et al. 2018; Ravasio et al. 2019a; Toffano et al. 2021.

4.2.1.1 Simulations

We performed spectral simulations in order to support the evidence of an exponential cutoff found in the 10 time-integrated GRBs spectra. The adopted procedure is the following: for each GRB showing a cutoff, we simulated a fake spectrum adopting as input model the basic one (either SBPL or 2SBPL) with the best–fit parameters obtained fitting the real data, and then we fitted it with the more complex model (either SBPLCUTOFF or 2SBPLCUTOFF, respectively). We repeated this procedure 1000 times and built the distributions of the improvement of the fit when adding a cutoff ΔPG–Stat$^{\rm sim}$, to be compared with the ΔPG–Stat$^{\rm fit}$ obtained in the fit with real data. We found that, simulating a spectrum without the cutoff, in all but one GRB in our sample the addition of a cutoff does not provide an improvement of the fit greater or equal to the one found in our analysis using real data, reporting chance probabilities smaller than 0.2%.

As an example, we show in Fig. 4.5 the distributions of ΔPG–Stat$^{\rm sim}$ obtained from the simulations of the worst case, GRB 160910, and of the best case, GRB 160821, the lowest and the highest value of ΔAIC in our sample, respectively. For GRB 160821, the ΔAIC found in the fit with the real data (represented by the vertical dashed line) is much greater than the mean of the distribution of ΔPG–Stat$^{\rm sim}$ obtained simulating and re-fitting 1000 spectra, corresponding to a chance probability much smaller than 0.2%. In the worst case, corresponding to GRB 160910, the improvement of the fit obtained with the addition of a cutoff in the real data ΔPG–Stat$^{\rm fit}$=12.3 is greater than the 97.2% of the distribution of the ΔPG–Stat$^{\rm sim}$ obtained from simulations, corresponding to a chance probability smaller than 2.8%.

We therefore reject the null hypothesis that each of the 10 GRB spectra analyzed shows the presence of an exponential cutoff by chance, namely all the cutoff observed are highly significant.

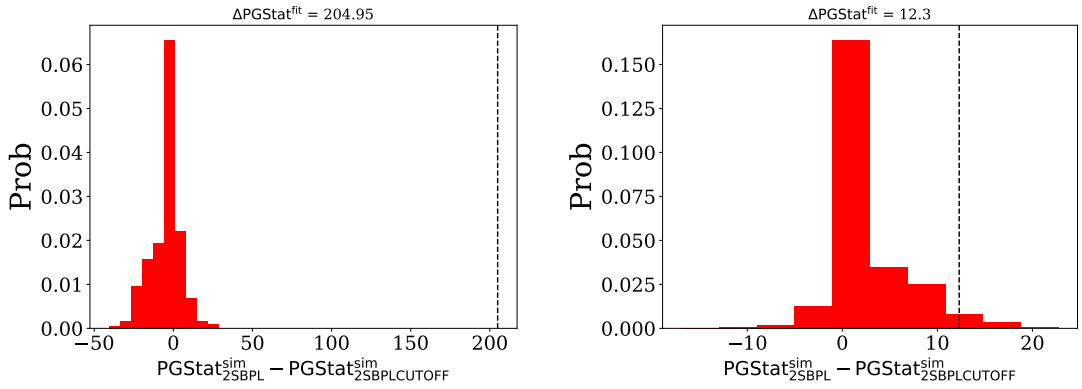

FIGURE 4.5: Distributions of the improvement ΔPG–Stat of the fit when adding a cutoff with respect to the basic model, for 1000 simulated spectra of GRB 160821 (left plot) and of GRB 160910 (right plot), corresponding to the highest and the lowest values of ΔAIC of our sample (see Table 4.2). The best–fit parameters of the basic model obtained from fitting the real data are used as input for all fake spectra. The vertical dashed lines mark the value of ΔPG–Stat^{fit} obtained from fitting the observed spectrum with 2SBPL and with 2SBPLCUTOFF.

4.2.1.2 Comparison with previous detections of exponential cutoff

We now compare the obtained results with the evidences of spectral cutoff previously reported in the literature. We focus the comparison on published works that found the presence of an exponential cutoff in the main emission component of the prompt emission spectrum, excluding those reporting a cutoff in the extra power–law components in the spectrum (e.g. see Ackermann et al. 2010; Ackermann et al. 2011; Ackermann et al. 2013; Abdo et al. 2009a; Abdo et al. 2009b).

Fermi Large Area Telescope Team et al. 2012 analyzed 288 GRBs detected by GBM that do not show evidence of emission above 100 MeV. They compared the computed flux upper limits in the LAT energy band with the extrapolations of the spectral fits of GBM data, finding that 6 GRBs of the sample required the presence of a spectral cutoff between GBM and LAT data. However, lacking a direct evidence of a spectral cutoff, they set $E = 100$ MeV as the cutoff energy for all 6 the burst.

Tang et al. 2015 systematically searched for a high-energy spectral cutoff combining GBM and LAT data of 28 GRBs prompt emission spectra. They fitted the main emission component with the Band function with and without a high–energy cutoff. From a time-integrated analysis, they found 5 GRBs showing a cutoff at energies between ∼13 and ∼62 MeV on the main emission component and one GRB (GRB 131108) with a cutoff at ∼347 MeV on the extra power–law component. Three of the five GRBs reported to have a cutoff by Tang et al. 2015 are also present in our sample. Only in one of them, namely GRB 140206, we found evidence of a spectral cutoff, although at higher energies with respect to what found by the authors (we found $E_{\rm cutoff} = 88.3^{+18.2}_{-12.5}$ MeV, while the authors found it at 50.1 ± 6.8 MeV). For the remaining 2 GRBs, our best–fitting model is the 2SBPL. These discrepancies can be ascribed to the use of different fitting models, although a more quantitative comparison should be performed to support this speculation. GRB 131108 belongs to our sample and from our analysis its spectrum is best fitted by a SBPL: we did not find any systematic trend in the residuals that may suggest the presence of an extra power–law component.

GRB 160625B, included in our sample, has been reported by Wang et al. 2017 to have an exponential cutoff of tens of MeV in six out of eight time-resolved intervals. This is

consistent with the time-integrated result reported also in Chap. 3 and with the results obtained in this Chapter.

In a more recent work, Vianello et al. 2018 studied the prompt emission spectra of GRB 100724B and GRB 160509A, both included in our sample. Their time-resolved analysis revealed the significant presence of high-energy cutoff at $E_{\rm cutoff} \sim$ 20–60 MeV for GRB 100724B and ∼80–150 MeV for GRB 160509A, with $E_{\rm cutoff}$ slightly increasing with time in both cases. We found consistent results from the time-integrated analysis on similar time intervals, reporting a $E_{\rm cutoff} = 45.4^{+12.2}_{-5.6}$ MeV for GRB 100724B and $E_{\rm cutoff} = 100.7^{+9.9}_{-16.8}$ MeV for GRB 160509A.

Combining all the previous detections reported in the literature, we conclude that this analysis revealed 5 new cases of GRB prompt spectra showing the presence of an exponential cutoff: GRB 170214, GRB 160821, GRB 180720, GRB 160905, GRB 090328, GRB 160910.

4.2.2 GRBs with high-energy spectral power–law

For 12 out of 22 GRBs, the spectrum is well fitted with a single power–law up to 10 GeV. In these spectra, the presence of a spectral cutoff at high energies is not supported by the data. In 5 out of these 12 GRBs, the best fit model is the SBPL. This means that nor the addition of a low-energy break or of a high-energy cutoff provides a significant improvement of the fit and their spectrum is described by two power-laws smoothly connected at the νF_ν peak of the spectrum.

In 7 out of 12 GRBs, the best fit model is the 2SBPL. For those GRBs, the spectrum below the peak energy $E_{\rm peak}$ is better described by two power-laws smoothly connected at $E_{\rm break}$. The distributions of the indices α_1, α_2, β and of the energies $E_{\rm break}$ and $E_{\rm peak}$ for the 2SBPL function are consistent with the corresponding distributions derived in Section 3.1, 3.2 and 3.3.

Since the high–energy data are often characterized by large error bars, they can possibly hide the presence of a cutoff, which may be allowed by the fit statistic until a given energy. Therefore, for the 12 GRBs not showing a cutoff, we aimed at setting a lower–limit on the position of $E_{\rm cutoff}$. The procedure adopted is the following: we fitted the data with the basic model (SBPL or 2SBPL) fixing all the best–fitting parameters, and we added the presence of a cutoff at progressively smaller energies[3], until the fit statistic allows to consider the addition of the cutoff as statistically equivalent. Using the same criterion adopted for choosing the best–fitting model, the presence of a cutoff is no longer supported by the data when it leads to a ΔAIC$\geq$4 with respect to the best-fit statistic. The value of the cutoff energy $E_{\rm cutoff}$ corresponding to the first fit with ΔAIC$\geq$4 is considered as the lower–limit of the cutoff energy for the analyzed spectrum. This procedure has been followed for the 12 GRBs not showing a cutoff, obtaining 12 lower–limits, that are reported in Table 4.2.

4.2.3 Beta distribution

For all the models tested, the shape of the spectrum above the peak energy is modelled by a power–law with slope β. Combining the results from all the best–fitting models shown in Table 4.2, we built the distribution of the β parameter, which is shown with the black empty histogram in the left plot of Fig. 4.6: it spans a quite wide range, from -4.60 to -2.06, and it is has a median value of $\langle\beta\rangle$ = -2.43 (standard deviation of 0.55).

[3]To perform these tests we used the command *steppar* implemented in XSPEC, which performs a fit while stepping the value of a parameter through a given range.

The distribution does not show values greater than -2. This is due to the hard limit we set on the upper boundary of the range of acceptable values for the β parameter. In order to have a peak in the νF_ν spectrum, the spectral indices below and above the peak energy are greater and smaller than -2, respectively.[4]

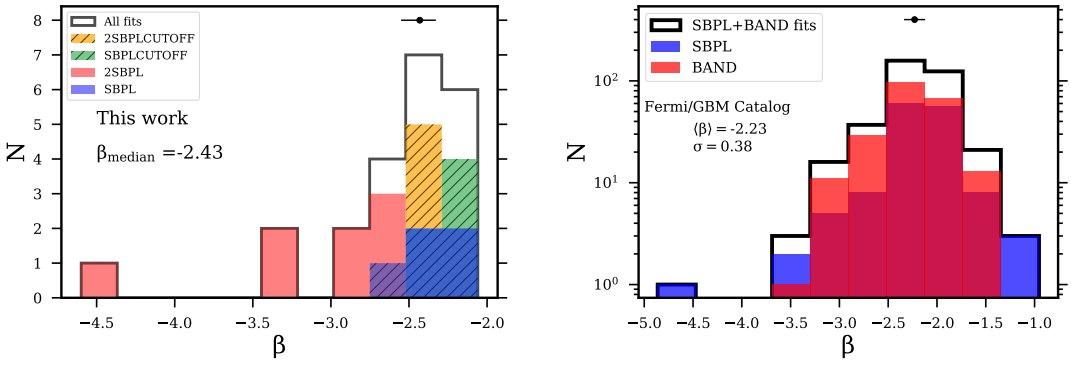

FIGURE 4.6: Left: distributions of the high-energy slope β for the 22 GRBs spectra analyzed. Different colors represent the different best–fitting models, while the black empty histogram represents the combination of all the β values derived from the spectral fits. On the top of the distributions we over–plotted the median value and the mean error on the β parameter of all the sample. Right: distribution of the β parameter of GRBs included in the *Fermi*/GBM Catalog (black empty histogram). The red and blue histograms represent those GRB spectra best–fitted by the Band and the SBPL function, respectively. Also in this plot we show on the top of the distributions the mean value of β for the black empty histogram, together with the average error.

In the left plot of Figure 4.6, the red and blue histograms represent the β parameter when the best–fitting models are 2SBPL and SBPL, respectively. The orange and green histograms display the β values of the spectra best–fitted by the 2SBPLCUTOFF or the SBPLCUTOFF model, respectively.

Comparing the β values of the spectra best–fitted by the SBPL with the ones best fitted by the 2SBPL, we note that the latter ones are steeper (see the blue and the red histograms in the plot). This confirms the results found in the previous Sec. 3.1 and Sec. 3.2, and it is likely due to the addition of the low energy break, that allows the 2SBPL function to better model the peak energy and the remaining high–energy part of the spectrum.

Moreover, despite the two distributions are consistent within one sigma, the β parameters for the 12 GRB spectra not showing a cutoff (see the red and blue histograms in the left plot of Fig. 4.6) are steeper than the ones derived for the 10 GRBs showing a cutoff (see the orange and green distributions). A K–S test comparing the β distribution for the 12 GRB spectra not showing a cutoff and the β distribution for the 10 GRBs showing a cutoff returns a p-value=0.036. This indicates that the two distributions are not drawn from the same distribution[5]. The mean value of β for the 12 GRB spectra not showing a cutoff is $\langle\beta_{\rm no\,cutoff}\rangle$ = -2.73 (σ= 0.63), while for the 10 GRBs showing a cutoff is $\langle\beta_{\rm cutoff}\rangle$ = -2.34 (σ= 0.18). This could be an effect of the presence of the exponential cutoff. Under

[4]Our sample contains bursts which have been selected with a criterion based on the signal of the LLE data and all the corresponding spectra analyzed showed a well defined peak in the broad energy band studied. Therefore, if the constraint on the β parameter would be relaxed, we would still have β values smaller than -2.

[5]I recall here that for the statistical tests we have set the significance level at 0.05, i.e. we accept the null hypothesis if $p > 0.05$.

the assumption that the intrinsic high–energy slope is the same, when an exponential cutoff is present in the spectrum the power–law segment between the peak energy and the cutoff energy is truncated earlier, allowing to constrain β on a smaller energy range. This effect, combined with the broad curvature of the spectrum, likely provides harder values of the high–energy slope of GRBs showing a cutoff.

We now compare these results on the high-energy power–law slope β with the Fermi GBM Catalog. Among the four functions used to fit the spectra in the Catalog, only the Band and the SBPL ones provide a β parameter for the modelling of the high-energy part of the spectrum. In the right plot of Fig. 4.6 we collected all the β slopes of the Fermi GBM Catalog bursts whose time–integrated spectrum has been best–fitted by Band (red histogram) or SBPL (blue histogram) function. The black empty histogram represents the total distribution of β, regardless the best–fitting model. The total β distribution is centered around $\langle\beta\rangle = -2.23$ ($\sigma = 0.38$). The average error on the β values together with the mean value are represented by the horizontal bars over-plotted above the histograms.

Differently from our results, the *Fermi*/GBM distribution β extends beyond values of $\beta \sim$ -2 ($\sim$18% of the values are greater than -2, at more than 1σ). Due to the necessity of fitting a large variety of spectral shapes, in the Fermi Catalog no constraints on the spectral indices of both Band and SBPL functions are introduced, therefore there can be cases with β values greater than -2. When excluding values greater than -2 from the *Fermi*/GBM Catalog distribution, we find that the β values obtained in this analysis are slightly steeper than the ones reported in the Catalog. A K-S test comparing the β distribution found in this analysis with that of the *Fermi* Catalog but selecting only those values of $\beta < -2$ returns a p-value=0.028. This probability indicates that the two distributions are not drawn from the same parent distribution. This can reflect the use of more complex fitting models in our analysis, as compared to the simpler Band and SBPL function of the Catalog. As mentioned above, especially the 2SBPL function typically returns steeper values of the slope β with respect to the simpler SBPL function. Moreover, the diversity in the β distributions can be ascribed to the addition of the LLE and LAT data to the GBM ones in our analysis. While in the *Fermi*/GBM Catalog are reported the parameters of the fit obtained considering spectral data up to $\sim$ 40 MeV, in this analysis we extended the characterization of the spectra up to 10 GeV. This may suggest that high-energy slope of the GRBs prompt emission spectrum is indeed softer than what commonly deduced from fits made with lower energy data alone (e.g. from BATSE or GBM). A similar conclusion has been drawn also by Fermi Large Area Telescope Team et al. 2012, where it was shown that in 24 bursts co-detected by GBM and LAT the β values are systematically softer than the values found from fitting the GBM data alone. Also, when performing the joint fit of GBM and LAT data, they found no cases of spectra with $\beta >$ -2, in agreement with the constraint we set on this parameter.

4.3 Conclusions

In this Section, I presented the results of the joint analysis of GBM and LAT data of prompt emission spectra for 22 bright GRBs, covering a wide energy range, from 10 keV up to 10 GeV.

We found that in 10 out of 22 bursts, the spectral data significantly deviate from the extrapolation of the high–energy power–law, requiring the presence of an exponential cutoff at high energies, between $\sim$14 and 298 MeV. These results are consistent with the previous detections of exponential cutoffs in GRB prompt spectra reported in the literature. Considering those bursts, we report the presence of a spectral cutoff not previously

detected in a total of 5 GRBs. In the remaining 12 out of 22 GRBs, there is no evidence of a spectral cutoff in the data. Since the poor signal in the highest part of the spectrum might hamper the evidence of a cutoff, we performed a test to derive the lower–limit on its position, for each of the 12 GRBs not showing a cutoff.

However, these estimates of the cutoff energy strongly depend on the modeling of the prompt emission spectrum. Of course, a different modeling could provide different estimates of the cutoff energy (and therefore could affect the estimates of Γ, if interpreting the cutoff as due to pair-production). As an example, the prompt emission spectrum of GRB 180720B has been well fitted by the synchrotron model in Sec. 3.4. The synchrotron fit did not require the presence of an additional cutoff to model the spectrum at high-energies, which was instead modelled by a steep power–law with $\beta \sim 3.4$ (corresponding to a slope $p \sim 4.8$ of the particle energy distribution). Instead, the analysis of the prompt emission spectrum of GRB 180720B with the four empirical functions adopted in this Section revealed that the 2SBPLCUTOFF is the best fitting model, reporting a cutoff energy at $E_{\rm cutoff} = 37.4^{+2.2}_{-4.3}$ MeV. This inconsistency is due to fitting the same data with an empirical function and the synchrotron spectrum, that leads to a different modeling of the high-energy spectrum. I provide a tentative explanation of such a difference, which may be related to the curvature parameters of the empirical function. Indeed, in the synchrotron spectrum, once the two fixed spectral slopes below the peak match the data, the high energy part can be steepened by increasing the value of p, without affecting the slopes below the peak. In the empirical function 2SBPL instead, the width is regulated by the two curvature parameters, which are kept fixed during the fitting procedure and are linked to the slope values. Increasing the value of the β parameter, as required to match the high-energy part of the spectrum, affects also the modeling of the spectrum below the peak, making it more inconsistent with the spectral data. The inclusion of a cutoff in the function allows to model the broad curvature around the peak with a relatively flat β parameter, while the exponential cutoff takes into account the steep high-energy part of the spectrum, returning an overall better consistency with the data. This shows that a deeper investigation of the influence of the curvature of the empirical function on the spectral slopes is required (this issue will be further discussed in Chapter 7).

Combining all the spectral fits, we derived the distribution of the slope β of the high-energy power–law, with median value $\langle\beta\rangle$ = -2.43 (standard deviation of 0.55). We compared this distribution with the distribution of β from the *Fermi*/GBM Catalog, finding that our β values are steeper than the ones reported in the Catalog. This can be due to the addition of the LLE and LAT data in our analysis, that allow to better constrain the high–energy power–law slope of spectrum. This could be an indication that the true slope of the GRBs prompt emission spectrum is softer than what is usually found.

Our results show how crucial is the inclusion, when possible, of the LLE (30–100 MeV) and LAT data (>100 MeV) to the study of a GRB spectrum detected by the GBM (typically in the energy range 10 keV–10 MeV). A broadband study of the prompt emission spectrum can reveal significant deviations from the standard spectral shape often found when analyzing the spectra in a narrower energy range and with simpler functions (see the solid blue line in Fig. 4.3). From these results we can derive important constraints on the physical quantities characterizing the GRB emitting region. From the estimate (lower–limit) of the cutoff energy, if interpreted as a sign of pair-production opacity, it is possible to derive an estimate (lower–limit) of the bulk Lorentz factor of the jet during the prompt phase. Moreover, the distribution of the high–energy slope β allows to constrain the slope of the population of relativistic electrons accelerated by the shocks or via magnetic reconnection. I will derive and discuss the theoretical implications of these results in Chapter 5.

The complete description and the full implications of the preliminary results discussed in this Chapter will be presented in Ravasio M.E., et al. *The high-energy extension of prompt emission spectra of bright Fermi GRBs*, in preparation.

Chapter 5

Interpretation

In Chapter 3, I have shown the results of the study of bright long and short GRB prompt emission spectra, fitted both with empirical functions and with a physical synchrotron model. The main observational results are:

- the presence of an additional spectral break below the peak energy, first discovered in *Swift* data, is found in the majority ($\sim$ 70%) of the time–resolved prompt emission spectra of bright *Fermi*/GBM long GRBs;
- the distribution of the break energy $E_{\rm break}$ is centered at $\langle \log(E_{\rm break}/{\rm keV}) \rangle = 2.00$ ($\sigma_{E_{break}} = 0.34$) and the peak energy $E_{\rm peak}$ is distributed around $\langle \log(E_{\rm peak}/{\rm keV}) \rangle = 3.00$ ($\sigma_{E_{peak}} = 0.26$);
- the distribution of the spectral slopes below and above $E_{\rm break}$ are respectively $\langle \alpha_1 \rangle = -0.58 \pm 0.16$ and $\langle \alpha_2 \rangle = -1.52 \pm 0.20$, consistent with the -2/3 and -3/2 slopes as predicted by synchrotron emission;
- in short GRBs, no evidence for an additional spectral break was found, but the low energy photon index is consistent with -2/3;
- a physical synchrotron model provides a successful modeling of the prompt emission spectra of GRB 180720B.

The average values of the photon indices of the empirical functions and the consistency of the synchrotron model with data allow me to investigate about a possible synchrotron origin. I therefore identify $E_{\rm break}$ with the cooling frequency $\nu_{\rm cool}$ and $E_{\rm peak}$ with the characteristic synchrotron frequency $\nu_{\rm min}$. These characteristic frequencies correspond to the cooling Lorentz factor $\gamma_{\rm cool}$ and the minimum Lorentz factor $\gamma_{\rm min}$ of the shock–accelerated population of particles, respectively.

As shown in Fig. 5.1 (see also the bottom panels of Fig. 3.8 for the time evolution in each GRB), $E_{\rm break}$ and $E_{\rm peak}$ are fairly close to each other, with a ratio $E_{\rm peak}/E_{\rm break}$ which is roughly a factor ~ 14, implying a ratio $\gamma_{\rm min}/\gamma_{\rm cool} = (E_{\rm peak}/E_{\rm break})^{1/2} \sim 3$.

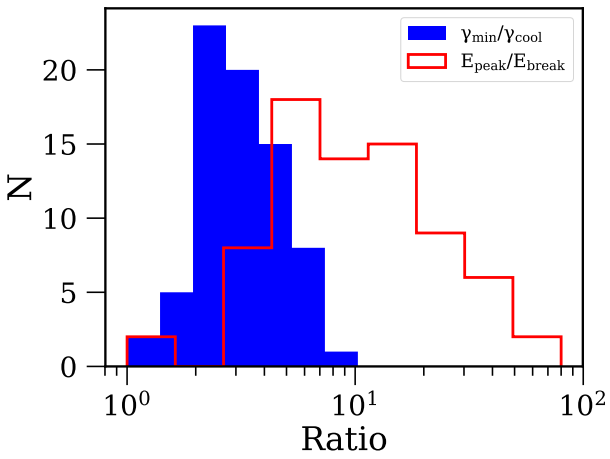

FIGURE 5.1: Distribution of the ratio of $E_{\rm peak}/E_{\rm break}$ and the corresponding energies $\gamma_{\rm min}/\gamma_{\rm cool}$ of the population of relativistic electrons in the synchrotron interpretation, as derived from the analysis of 10 bright long GRBs (see Chap. 3)

.

The relatively small ratio between $E_{\rm peak}$ and $E_{\rm break}$ corresponds to what is generally referred to as a *marginally fast cooling regime*, i.e. a situation in which $\nu_{\rm cool} \lesssim \nu_{\rm min}$ and not $\nu_{\rm cool} \ll \nu_{\rm min}$ as in the fast cooling regime (Daigne, Bošnjak, and Dubus, 2011; Beniamini, Barniol Duran, and Giannios, 2018). The *marginally fast cooling regime* is at odd with respect to the radiative regime commonly expected in the GRB standard model where, as I will show below, the cooling timescale is much smaller than the dynamical timescale (and surely, of the timescale of integration of individual time resolved spectra, $\sim$ 1 s). Instead, the marginally fast cooling regime, which is still efficient in terms of radiated energy (Daigne, Bošnjak, and Dubus, 2011), requires a relatively long cooling timescale so that the two characteristic frequencies lie closer one to each other.

In Chapter 4, I focused on the high-energy extension of the prompt emission spectra. In particular, I showed the results of the analysis of the prompt emission spectra for 22 bright GRBs, covering a wide energy range, from 10 keV up to 10 GeV. Here I summarize the main observational results:

- in 10 out of 22 bursts, the spectral data significantly deviate from a simple power–law at high–energies, requiring the presence of an exponential cutoff, marked by the characteristic energy $E_{\rm cutoff}$ between $\sim$14 and 298 MeV;
- in 12 out of 22 GRBs, there is no evidence of a spectral cutoff in the data. For each of these bursts, we set a lower–limit on its position, which might not necessarily be 10 GeV, due to the poor statistic at high energies;
- from all the spectral fits, we derived the distribution of the slope β of the high-energy power–law, with median value $\langle\beta\rangle$ = -2.43 (standard deviation of 0.55);

These results show the relevance of extending the study of the prompt emission spectra up to high energies, by including, when possible, the LLE (30–100 MeV) and LAT data (>100 MeV) to the typical GBM spectrum.

In this Chapter, I discuss the physical interpretation of the results obtained in the two previous Chapters from the analysis of the prompt emission spectra of GRBs and summarized above. The first Section 5.1 is dedicated to the interpretation of the low–energy breaks found in Chap. 3 in the context of synchrotron emission, while the second Section 5.2 is devoted to the main implications derived from either the observations of exponential cutoff and the spectral slope of the high-energy extension of the prompt emission spectra, described in Chap. 4.

5.1 Low–energy breaks

In the following, I will assume that the emission is produced by optically thin synchrotron radiation in marginally fast cooling regime and I will derive the parameter values characterizing the emission region and discuss their physical implications. In the first part of this Section, I will consider a leptonic origin of the synchrotron emission, which is the commonly adopted scenario for the prompt emission due to the high radiative efficiency of electrons. However, as it will be shown in Section 5.1.1, the observed variability timescale and the expected magnetic field value in the emission region represent major challenges for the leptonic synchrotron interpretation, in light of the parameter values obtained in Chapter 3. Therefore, in Section 5.1.2 I will describe an alternative scenario we proposed (Ghisellini et al., 2020), which instead assumes a hadronic origin of GRBs prompt emission spectra.

5.1.1 Synchrotron radiation from non-thermal electrons

Ghisellini, Celotti, and Lazzati 2000 argued that, for the typical physical conditions of the prompt emission of GRBs, the radiative cooling timescale of electrons is much shorter than the dynamical timescale. Due to the relative ordering of the cooling and minimum frequencies $\nu_c \ll \nu_m$, the flux density between these two characteristic frequencies is $F_\nu \propto \nu^{-1/2}$, as discussed in Chap. 2. Considering an electron of energy $\gamma_e m_e c^2$, moving towards the observer with bulk Lorentz factor Γ in a region with comoving magnetic field B', the radiative cooling timescale (in the observer frame) for synchrotron and Compton emission is

$$t_{\rm cool}^{\rm obs} = \frac{\gamma'}{\dot{\gamma}'}\frac{(1+z)}{\Gamma} = \frac{6\pi m_e c}{\sigma_T B'^2 \gamma'_e (1+U'_{\rm rad}/U'_B)}\frac{(1+z)}{\Gamma}\,, \tag{5.1}$$

where $U'_{\rm rad}$ and U'_B are the radiation and magnetic energy densities, respectively. The typical frequency of photons emitted by synchrotron (ignoring inverse Compton emission for the moment) is

$$\nu^{\rm obs} = \frac{4}{3}\frac{eB'}{2\pi m_e c}\gamma_e'^2\frac{\Gamma}{1+z}\,, \tag{5.2}$$

implying that a given photon frequency $\nu^{\rm obs}$ is mainly produced by electrons with Lorentz factor

$$\gamma'_e = \left[\frac{3\pi m_e c \nu^{\rm obs}}{2eB'}\frac{(1+z)}{\Gamma}\right]^{1/2} \tag{5.3}$$

Substituting γ'_e in Equation 5.1, we can obtain:

$$t_{\rm cool}^{\rm obs} = \frac{(24\pi m_e c e)^{1/2}}{\sigma_T\,(1+U'_{\rm rad}/U'_B)}\sqrt{\frac{(1+z)}{\Gamma}}\,\nu^{\rm obs\,-1/2} B'^{-3/2}. \tag{5.4}$$

According to the standard model, the typical GRB emitting region should be located at $R \sim 10^{13}$–10^{14} cm from the central engine. Considering a value of $B'_0 \sim 10^{15}$ Gauss at $R_0 = 10^6$ cm (Piran, 2005), close to the central powerhouse, the conservation of the Poynting flux implies that:

$$P_{B'_0} \propto R_0^2 \Gamma_0^2 {B'_0}^2 = R^2\ \Gamma^2\ {B'}^2 \propto P_{B'} \tag{5.5}$$

$$\Longrightarrow B' \simeq 10^6 \frac{B'_{0,15}\ R_{0,6}\ \Gamma_0}{\Gamma_2\ R_{13}} \tag{5.6}$$

If we lower the magnetic field value at R_0, or increase the radius of the emission region or the bulk Lorentz factor Γ of one order of magnitude, the corresponding magnetic field in the emitting region is still strong, namely in the range $B' \sim 10^4 - 10^6$ Gauss. For the typical range of values of B', $\Gamma = 100$ and $\nu^{\rm obs} \sim 100$ keV, and considering only the synchrotron process, the observed cooling timescale is of the order of $\sim 10^{-5} - 10^{-8}$ s[1].

The other quantity useful to characterize the cooling of the particles is the dynamical timescale $t_{\rm ad} \sim R/2c\Gamma^2$, which is the typical timescale associated with the adiabatic cooling due to the spherical expansion. Given the radius $R \sim 10^{13}$ cm typically assumed for internal shocks and $\Gamma = 100$, the dynamical timescale is $t_{\rm ad} \sim 1.6 \times 10^{-2}$ s (see also Chapter 2). For the typical parameters of the emitting region derived above, it is clear that $t_{\rm cool} \ll t_{\rm ad}$, namely the particles efficiently radiate most of their energy on a timescale much smaller than the dynamical one and they are in the so-called *fast-cooling regime*.

5.1.1.1 Estimate of the magnetic field in the emitting region

The individual time-resolved spectra that I have analyzed represent a sort of snapshot of the emission region: during the integration time, the electrons had the possibility to cool and reach the cooling frequency $\nu_{\rm cool}$, producing the spectral break I found. Therefore, imposing a timescale comparable to the spectral integration timescale (namely $t^{\rm obs}$ =1 s), it is possible to derive a limit on the magnetic field B' in the region where the emission is produced. Considering the mean value of $E_{\rm break} \sim 100$ keV found in my analysis and assuming a typical bulk Lorentz factor of the emission region $\Gamma = 100$, we can invert Eq. 5.4 and obtain:

$$B' \sim 10\ \ \Gamma_2^{-1/3} {\nu^{\rm obs}_{100\,\rm keV}}^{-1/3}\ \ {t^{\rm obs}_{1s}}^{-2/3}\ \ (1+z)^{1/3}\ \ \text{Gauss}\,. \tag{5.7}$$

Considering that the break energy $E_{\rm break}$ found in the brightest *Fermi* bursts is distributed in the range $\sim$20 – 600 keV (Fig. 3.12) and that the distribution of bulk Lorentz factors Γ (as obtained in Ghirlanda et al. 2018) spans two orders of magnitude from $\sim$20 – 2000, we derive an estimate of the corresponding distribution of the comoving magnetic field $B' \in [1, 40]$ G. In this estimate we have used the spectral integration timescale of 1 s as the reference timescale. Since the magnetic field depends on the cooling timescale as $B' \propto t^{-2/3}$, if instead we would consider the dynamical timescale, we would obtain a magnetic field $B' \sim 600$ G. This value is still a few orders of magnitude lower than the expected value in the GRB emission region.

In the textbook case of GRB 180720B, we have fitted directly a synchrotron model to the prompt emission spectra and it provided an acceptable modeling in the energy range

[1]The redshift value used in this computation is $z = 2$, corresponding to the average value for long GRBs. However, the redshift value does not affect the cooling timescale estimate for more than a factor of order 1.

between 10 keV and 100 MeV. Under the assumption of one-shot electron acceleration and applying the standard synchrotron theory, we can derive the minimum energy of the injected non–thermal distribution of relativistic electrons $\gamma_{\rm min}$ and the total number of electrons $N_{\rm e,iso}$ contributing to the observed emission.

Following Kumar and McMahon (2008b) (see also Beniamini and Piran 2013) and considering only synchrotron cooling, we can find the unknowns $\gamma_{\rm min}$ and $N_{\rm e,iso}$ in terms of the observables obtained from the fit, in particular the cooling energy $E_{\rm cool}$, injection energy $E_{\rm min}$, and flux density at the cooling energy $F_{\rm cool}$[2]:

$$\gamma_{\rm min} = \left(\frac{4\pi\, m_e\, c\, E_{\rm min}\,(1+z)}{3\,h\,e\,B'\,\Gamma}\right)^{1/2} \simeq 6.3\times10^{5}\; E_{\rm min,3}^{1/2}\, B'^{-1/2}\, \Gamma_2^{-1/2}\,(1+z)^{1/2} \tag{5.8}$$

$$N_{\rm e,iso} = \frac{4\pi d_L^2\, m_e\, c^2\, F_{\rm cool}}{\sqrt{3}\, e^3\, B'\,\Gamma\,(1+z)} \simeq 10^{50}\; F_{\rm cool,mJy}\, B'^{-1}\, \Gamma_2^{-1}\, d_{L,28}^2\,(1+z)^{-1}, \tag{5.9}$$

where $E_{\rm cool}$ is expressed in units of 10^2 keV, $E_{\rm min}$ in units of 10^3 keV, Γ in units of 100, $F_{\rm cool}$ in mJy, and d_L is the luminosity distance of the GRB in units of 10^{28} cm. The fit of the spectrum corresponding to SED I (see Fig. 3.18) returned a cooling energy $E_{\rm cool} \sim 79$ keV and an injection energy $E_{\rm min} \sim 1898$ keV, while the flux at the cooling energy is $F_{\rm cool} \sim 6$ mJy. The integration time of 35 s of SED I corresponds to the time (in the observer frame) taken by the injected electrons to cool down to $\gamma_{\rm cool}$ and to produce a spectral break at the observed energy $\sim E_{\rm cool}$. The relative positions of the cooling energy $E_{\rm cool}$ and of the injection energy $E_{\rm min}$ in SED I lead to a value of the Lorentz factor $\gamma_{\rm cool}$ of the cooled electrons which is only a factor of 5 lower than the injection Lorentz factor $\gamma_{\rm min}$. This again indicates that the electrons are in a moderately fast cooling regime, consistently with the previous results obtained from empirical functions. Therefore, in Eq. 5.7 we use $E_{\rm cool} = 79$ keV and $t_{\rm cool}^{\rm obs} = 35$ s. Considering the maximum range of possible values of Γ found from the analysis of the LAT lightcurve of GRB 180720B (see Chap. 6), i.e. 294 (80) in the homogeneous (wind) medium case, we found $B' \sim 0.8\ (1.3)$ G, $\gamma_{\rm min} \sim 0.9\ (1.3)\times10^6$ and $N_{\rm e,iso} \sim 1.2\ (2.9)\times10^{51}$. The uncertainties on the measured quantities $E_{\rm cool}$, $E_{\rm min}$, $F_{\rm cool}$ give an uncertainty of 20% on the physical parameters. Also the values of B', $\gamma_{\rm min}$, and $N_{\rm e,iso}$ inferred from a finer time resolved analysis (on similar timescales, ∼10 s) are consistent with the values inferred from the spectrum integrated over the first 35 s. This is an indication that the physical properties of the outflow do not change significantly during the prompt emission. These values are also consistent with the ranges estimated by Oganesyan et al. (2019) for a sample of 21 *Swift* GRBs.

As found above, the low-energy break identified in the spectrum of long GRBs, associated to the radiative cooling break, inevitably implies a low value of the magnetic field.

The result of the spectral analysis of short GRBs is even more puzzling, when interpreted within the synchrotron scenario. As shown in Sec. 3.2.2, conversely to the long ones, no bright short GRB out 10 analyzed shows a spectral break. Instead they present a single power-law below the νF_ν peak, characterized by a hard photon index: $\alpha = -0.78 \pm 0.23$, consistent with the expected synchrotron photon index $-2/3$ of the power-law below $\nu_{\rm cool}$. If interpreted in the same scenario of synchrotron cooling supposed for long GRBs, this seems to indicate that the power-law with photon index -1.5 between the $\nu_{\rm cool}$ and the $\nu_{\rm min}$, namely the footprint of the cooling of the electrons via synchrotron process, is not present in short GRBs. This means that in the case of short

[2]Here the quantities $E_{\rm cool}$ and $E_{\rm min}$ related to the synchrotron modeling correspond qualitatively to the break energy $E_{\rm break}$ and the peak energy $E_{\rm peak}$ respectively, of the empirical modeling considered above.

GRBs the situation is even worse, since $E_{\rm break}/E_{\rm peak} \sim 1$, implying that the magnetic field should be even smaller than the value calculated for long GRBs.

The above mentioned low values of the comoving magnetic field B' are at odds with expectations for the magnetic field in the typical GRB emitting region, which should be ∼3–5 orders of magnitude higher at $R \sim 10^{13}$–10^{14} cm from the central engine (see Equation 5.1.1). In other words, such a high value of the magnetic field expected from the standard model would not be compatible with the relatively long timescales found in the results presented in this thesis (i.e. ∼1 s) (Ghisellini, Celotti, and Lazzati, 2000). Therefore, while these results positively solve the issue of the inconsistency of observed spectra and theoretical prediction of synchrotron radiation, they open a new challenging question: within the standard GRB model and synchrotron theory, having the cooling break at few hundreds of keV implies that the magnetic field of the emission region is very small, which is at odd with the MGauss value expected according to the standard model. The problem then shifts on the search for a way to fit such a low magnetic field in the framework of the GRB standard model.

5.1.1.2 Consequences of a low magnetic field in the leptonic scenario

Keeping such small values of the magnetic field (∼10 G) in a relatively compact emitting region consistent with the standard model ($R \sim 10^{13}$–10^{14} cm) is not a viable solution. In fact, for the combinations of bursts luminosity and low magnetic field found from my results, the density of the electrons would be so high that the Compton process would be dominant with respect to the synchrotron one and the electrons should cool completely via Compton process. Moreover, it would require a mechanism that can justify such a low magnetic field in the emission region.

To better understand the problem, we can look at the Fig. 5.2, that allows to study the parameter space of the main physical quantities involved in the discussion. In particular, in order to explain the observed spectra, I assumed that the time the electrons need to cool down to $\gamma_{\rm cool}$ via synchrotron process is of the same order of the adiabatic timescale, namely $t_{\rm cool} = t_{\rm ad} = R/2c\Gamma^2$. From this assumption, it is possible to derive self-consistent constraints on the distance from the central engine R, the bulk Lorentz factor Γ and the magnetic field B' in the emitting region. Indeed, let us now express the magnetic field as a function of the distance R and the bulk Lorentz factor Γ of the jet:

$$
\begin{aligned}
B_{\rm syn}(R,\Gamma) &= \left(\frac{24\pi\, e\, h\, m_e\, c\,(1+z)}{(1+Y)^2\,\sigma_T^2}\right)^{1/3} E_{\rm break}^{-1/3}\,(t_{\rm ad})^{-2/3}\,\Gamma^{-1/3} \\
&= \left(\frac{24\pi\, e\, h\, m_e\, c\,(1+z)}{(1+Y)^2\,\sigma_T^2}\right)^{1/3} E_{\rm break}^{-1/3}\left(\frac{R}{2c\Gamma^2}\right)^{-2/3}\Gamma^{-1/3} \\
&= \left(\frac{96\pi\, e\, h\, m_e\, c^3\,(1+z)}{(1+Y)^2\,\sigma_T^2}\right)^{1/3} E_{\rm break}^{-1/3}\,R^{-2/3}\,\Gamma
\end{aligned}
\tag{5.10}
$$

where Y=$U'_{\rm rad}/U'_{\rm B}$ is the ratio of the radiation energy density and the magnetic energy density. For simplicity, we now consider only the synchrotron process, namely setting Y=0. However, as we will see later, for the combinations of parameters involved, the Compton process plays an important role in the cooling process.

In the case of a Poynting flux dominated jet, the associated luminosity can be computed as $L_{\rm poyn} = cR^2 B_{\rm syn}^2 \Gamma^2$, given the magnetic field defined in Eq. 5.10. This luminosity

L_{poyn} is required to be at least equal to the observed isotropic luminosity L_{iso} of the burst, namely $L_{poyn} \geq L_{iso}$, and this has been included in Fig. 5.2 with a yellow region to represent the energetic constraints implied by the considered parameter space.

Regarding the relevant timescale, it is useful to select a range of times that may represent the variety of variability timescale of the prompt emission lightcurve. Following e.g. Golkhou, Butler, and Littlejohns 2015 (see Fig. 5.4 in the following), I choose as representative timescales those in the range $t \in [0.01, 1]$ s.

Therefore, assuming a burst with typical spectral break E_{break}=100 keV and an isotropic luminosity $L_{iso} = 10^{52}$ erg/s, for every couple of values of distance R and bulk Lorentz factor Γ, Fig. 5.2 shows the values of magnetic field B_{syn} (contour levels), the relevant adiabatic timescale (red band) and the minimum Poynting luminosity needed to accommodate L_{iso} (yellow region) in case of a magnetically dominated jet.

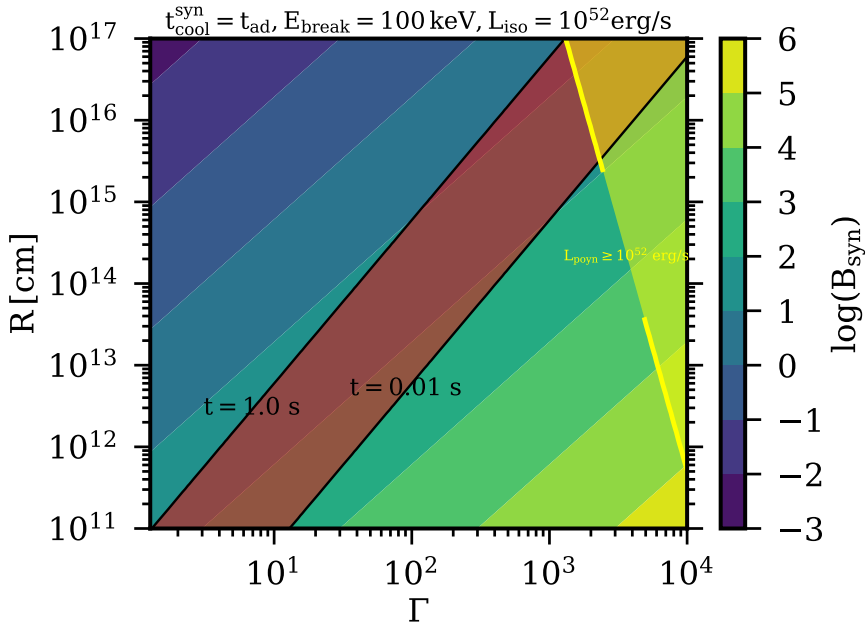

FIGURE 5.2: Contour plot showing the parameter space of the magnetic field B_{syn}, adiabatic timescale t_{ad} and Poynting luminosity L_{poyn} computed for a given bulk Lorentz factor Γ and radius R, for a burst with E_{break}=100 keV and $L_{iso} = 10^{52}$ erg/s. The values of the magnetic field are computed assuming the synchrotron cooling timescale equal to the adiabatic one.

From Fig. 5.2 we can recover the results obtained above: if we consider the emitting region located at $R \sim 10^{13-14}$ cm and typical values of the bulk Lorentz factor ($\Gamma \sim$100), the relevant timescales require a small magnetic field ($B_{syn} \sim$10–100 G). As discussed in Sec. 5.1.1, for the conservation of the Poynting flux, such a low magnetic field at $R \sim 10^{13-14}$ cm would imply a B' at the base of the jet which is 5-7 orders of magnitude smaller than the predictions. Since the power of the Blandford-Znajek process, thought to be the leading mechanism for the extraction of the rotational energy of the black hole (Blandford and Znajek, 1977), is $P_{BZ} \propto B'^2$, the lower is the value of the magnetic field and the lower will be the energy extracted, and we can no more explain the total energy observed in GRBs. In fact, from Fig. 5.2 it can be seen that for the typical parameters considered above, the Poynting flux would be lower than the observed isotropic luminosity L_{iso}, and it cannot justify the energetics we see in γ-rays. This suggest that the Poynting

flux would not be the dominant form of power that can be converted into radiation. In order to obtain the required Poynting flux (the yellow area), one should assume extremely high values of the bulk Lorentz factor $\Gamma \sim 10^3$.

However, as anticipated before, the most problematic issue when dealing with a low magnetic field in a small emitting region is the Compton process. For the combinations of bursts luminosity and low magnetic field that we have derived, it plays a major role and dominate the cooling of the particles. In the work of Ghisellini et al. 2020, we investigated this problem computing the ratio of Synchrotron-Self-Compton to synchrotron luminosity L_C/L_{Syn} as a function of the magnetic field. When treating the inverse Compton (IC) scattering, it is convenient to adopt dimensionless photon energies $x = h\nu/(m_e c^2)$. In the comoving frame, the scattering is described by the Klein–Nishina cross section σ_{KN} which equals the Thomson one σ_T for $x' \ll 1/\gamma$. For simplicity, we then assume that

$$\begin{aligned} \sigma_{KN} &= \sigma_T, \quad x' \leq 1/\gamma \\ \sigma_{KN} &= 0, \quad x' > 1/\gamma. \end{aligned} \tag{5.11}$$

This overestimates somewhat the cross section when $x' \sim 1/\gamma$ (in this case $\sigma_{KN} = 0.43\sigma_T$) and of course underestimates it at high energies. However, this approximation is reasonable when considering scatterings between rather wide distributions of photon and electron energies, becoming more inaccurate when these are narrow.

According to such approximation, an electron of random Lorentz factor γ loses energy by scattering a fraction of the total radiation energy density U'_{rad}, given by

$$U'_{rad} = \frac{L'_{iso}}{4\pi R^2 \Delta R'} \frac{\Delta R'}{c} = \frac{L_{iso}}{4\pi R^2 c \Gamma^2}. \tag{5.12}$$

Not all this radiation energy density is available for scattering in the Thomson regime. The larger γ the smaller the fraction $f(\gamma)$ of scattered photons:

$$f(\gamma) = \frac{\int_0^{1/\gamma} U'_r(x')\, dx'}{U'_r}. \tag{5.13}$$

Therefore, for the generic electron of random Lorentz factor γ that cool by synchrotron and inverse Compton, the ratio of the two loss rates is:

$$\frac{\dot{\gamma}_{IC}}{\dot{\gamma}_{Syn}} = \frac{U'_{rad}}{U'_B} f(\gamma). \tag{5.14}$$

where $U'_B = B'^2/8\pi$ is the magnetic field energy density. To find the ratio L_C/L_{Syn} we must integrate over the particle energy distribution:

$$\frac{L_C}{L_{Syn}} = \frac{U'_r}{U'_B} \frac{\int_1^{\gamma_{max}} N(\gamma)\gamma^2 f(\gamma) d\gamma}{\int_1^{\gamma_{max}} N(\gamma)\gamma^2 d\gamma} \tag{5.15}$$

The typical spectral shape found in my analysis is emitted by electrons distributed in energy as a broken power law:

$$\begin{aligned} N(\gamma) &= K\gamma^{-2}, \quad \gamma_{cool} \leq \gamma \leq \gamma_{min} \\ N(\gamma) &= K\gamma_{min}^{p-2}\gamma^{-(p+1)}, \quad \gamma > \gamma_{min}, \end{aligned} \tag{5.16}$$

where γ_{cool} and γ_{min} are the energies of the electrons emitting mainly at ν_{cool} and ν_{peak}.

Calculating Eq. 5.15 assuming the particle energy distribution in Eq. 5.16, we built Fig. 5.3, showing the ratio of the Compton and synchrotron luminosity as a function of the magnetic field and for different distances from the central engine (assuming $L_{\rm iso}$=10^{52} erg/s, $\Gamma = 100$ and $E_{\rm break}$=100 keV). It can be seen that an emitting region at $R \sim 10^{13} - 10^{14}$ cm with a magnetic field of $B' < 100$ G would imply a Compton component a factor $\sim 10^5 - 10^7$ brighter than the synchrotron one. However, a strong Compton spectral component of the prompt emission has not been distinctly detected so far in the GeV energy range (e.g. by the LAT instrument, Zhang et al. 2011; Abdo et al. 2009a). The observations limit the Y parameter to be small (of the order of ~ 10 at maximum, e.g. Oganesyan et al. 2019; Beniamini and Piran 2013), which in turn limits the emitting region to be larger than the standard values of $R \sim 10^{13} - 10^{14}$ cm. From Fig. 5.3, it can be seen that in order to have unimportant Compton emission (i.e. a ratio smaller than unity, represented by the orange line) for magnetic fields $B' < 100$ G, the distance R must be larger than $\sim 10^{16}$ cm.

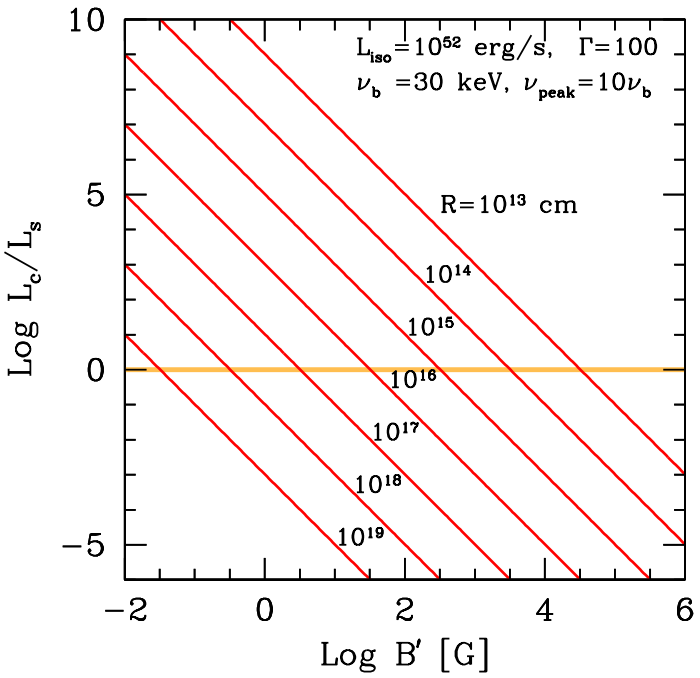

FIGURE 5.3: Ratio of the Compton to synchrotron luminosity predicted for a burst with $L_{\rm iso}$=10^{52} erg/s, $\Gamma = 100$ and $E_{\rm break}$=100 keV. The horizontal orange line corresponds to equal synchrotron and self-Compton luminosities. Figure taken from Ghisellini et al. 2020.

Summarizing, the scenario with a small magnetic field of $\sim$ 10–100 G in a compact emitting region located at $R \sim 10^{13} - 10^{14}$ cm is not a viable solution to explain the observations. The hardest problem to face is the Compton emission, which would dominate the cooling rate for small emission regions. In particular, the Compton-to-synchrotron luminosity would be so high that we expect the emission in the GeV energy range to be dominated by the SSC component (whose low-energy part would be visible also in the MeV–GeV energy range), while it is instead limited by the existing observations. The other problem is related to the energetic involved in the jet: in the case of a magnetically dominated jet, the Poynting flux would be too small to justify the energetics observed in

γ-rays (unless we assume extremely high Γ), pointing towards a matter-dominated jet.

A larger emitting region, at a distance $\sim 10^{16-18}$ cm, would reconcile the estimated low value of magnetic field with the transport from the central compact magnetized object through Poynting flux conservation. This in turn implies a reduced radiation energy density and therefore a reduced SSC luminosity.

As an example, from the synchrotron modelling of GRB 180720B, we derived a magnetic field of 1 G, $\Gamma \sim 300$ and $t^{\rm obs} \sim 35$ s, that lead to the estimate of a distance $R \sim 2ct^{\rm obs}\Gamma^2 \sim 10^{17}$ cm. Moreover, the large values of $\gamma_{\rm min}$ and $\gamma_{\rm cool}$ ensure that the self-Compton emission occurs in the Klein-Nishina regime, further limiting the SSC component and most of it would be produced at very large frequencies. Indeed, the SSC luminosity would exceed the synchrotron one by a factor 100 if the scatterings occur in the Thomson regime. Taking into account the reduction by a factor 10^4 because of the Klein-Nishina regime (Ghisellini et al., 2020), eventually the bolometric SSC prompt luminosity is expected to be a factor of 100 lower than the synchrotron luminosity, and most of it would be produced at around 100 TeV, well above the Fermi/LAT energy range. Therefore the SSC contribution in the LAT energy range and below could be safely neglected.

However, the alternative of moving the emitting region at larger radii has to overcome two major difficulties. First, such a large distance is comparable if not even beyond the typical distance where external shocks develop and the afterglow radiation is produced ($R \sim 10^{16}$ cm). To have a self-consistent picture, one should require to move the region of the external shock even further away (at $R > 10^{18}$ cm) from the central engine. For typical parameters, this would be possible only in a very low–density external medium (e.g. $n \sim 10^{-6}$ cm^{-3} for an homogeneous medium). Second, if the prompt emission site is moved at such large distances from the central engine, it becomes hard to obtain the fast variability timescale typically observed in the prompt light curve. Estimates of the observed minimum variability timescale of the prompt emission has been performed for *CGRO*/BATSE, *Swift*/BAT (Golkhou and Butler, 2014) and *Fermi*/GBM bursts (MacLachlan et al., 2013; Golkhou, Butler, and Littlejohns, 2015), finding values ranging from $\sim 10^{-3}$ to 10 s. As an example, Fig. 5.4 (taken from Golkhou, Butler, and Littlejohns 2015) shows the observed variability timescale for a sample of 938 GRBs detected by *Fermi*/GBM. The reported median of the distribution of the observed minimum timescales for long and short GRBs are 134 ms and 18 ms.

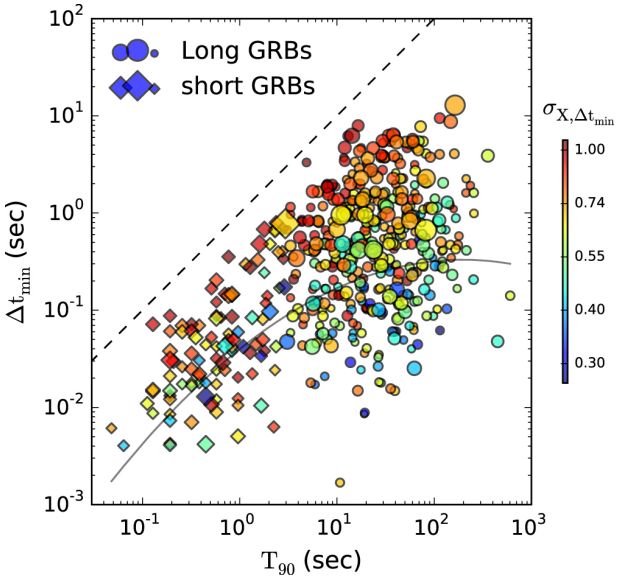

FIGURE 5.4: Minimum variability timescale of the prompt emission lightcurve vs duration time T_{90} for 938 GRBs observed by Fermi/GBM. Figure taken from Golkhou, Butler, and Littlejohns 2015.

Such short variability timescales require compact emitting regions. From Fig. 5.2, it is clear that we can obtain such short timescales at such a large radii only assuming very large bulk Lorentz factor values, $\Gamma \gtrsim 10^3$. Although these values are not theoretically excluded, they are rather extreme, lying on the high end of the distribution of Γ derived from the observations of the afterglow onset (Ghirlanda et al., 2018).

These considerations show how difficult it is finding a simple self consistent picture which explains all the observed properties of the prompt emission. In particular:

- spectra with two breaks (which have been found in both X–rays and γ–rays for long GRBs Oganesyan et al. 2017; Oganesyan et al. 2018; Ravasio et al. 2018; Ravasio et al. 2019a; Ronchi et al. 2020; Burgess et al. 2020) ;
- the variability of the prompt emission (of the order of $\sim$ tens of ms) ;
- the huge amount of energy radiated during the prompt (of the order of $\sim 10^{52-54}$ erg) :
- the lack of a strong SSC component in the $\sim$GeV energy range.

We cautiously stress, however, that these considerations are drawn under the hypothesis of the synchrotron process: if the emission is not due to this process, then one should invoke some other radiation mechanism that has to explain the current findings. In any case, this demands a revision of the so-called standard model of GRBs.

In the next section, I will describe the alternative we proposed to explain the current findings, which involves protons rather than electrons as synchrotron emitters (Ghisellini et al., 2020).

5.1.2 Synchrotron from protons

A possible solution to the problematic set of parameters implied by the incomplete cooling of the electrons is to assume that the spectra are produced by synchrotron radiation from protons, not from leptons (see Gupta and Zhang 2007 for a discussion of lepton

and hadronic models for the high energy prompt emission in GRBs). In fact, as it will be shown in the following, protons allows to keep a large magnetic field in a relatively small emitting region, as predicted by the standard model. Protons are also accelerated efficiently in shocks, and should receive most of the shock energy, more than the leptons. Applying the synchrotron theory to protons, we obtain that the typical synchrotron frequency emitted by a proton with Lorentz factor γ_p in the comoving frame is:

$$\nu'_{\rm p} = \frac{4}{3}\frac{eB'}{2\pi\, m_{\rm p}c}\,\gamma_{\rm p}^2 \rightarrow \gamma_{\rm p} = \left[\frac{3\pi\,\nu'_{\rm p} m_{\rm p} c}{2eB'}\right]^{1/2} \sim 10^4 \left[\frac{\nu'_{\rm p,keV}}{B'_6}\right]^{1/2}. \tag{5.17}$$

The total power emitted for a tangled magnetic field and an isotropic distribution of pitch angles is:

$$P_{\rm p} = \frac{4}{3}\sigma_{\rm T} c \left(\frac{m_{\rm e}}{m_{\rm p}}\right)^2 \frac{B'^2}{8\pi}\gamma_{\rm p}^2. \tag{5.18}$$

The synchrotron cooling time (in the observer frame) is:

$$\begin{aligned} t^{\rm obs}_{\rm cool,p} &= \frac{\gamma_{\rm p} m_{\rm p} c^2}{P_{\rm p}} = \frac{6\pi m_{\rm p} c^2}{\sigma_{\rm T} c B'^2 \gamma_{\rm p}} \left(\frac{m_{\rm p}}{m_{\rm e}}\right)^2 \frac{1+z}{\Gamma} \\ &= \frac{6\pi m_{\rm e} c^2}{\sigma_{\rm T} c B'^{3/2}} \left(\frac{m_{\rm p}}{m_{\rm e}}\right)^{5/2} \left[\frac{2e}{3\pi\, c \nu^{\rm obs}_e} \frac{1+z}{\Gamma}\right]^{1/2} \\ &= t^{\rm obs}_{\rm cool,e} \left(\frac{m_{\rm p}}{m_{\rm e}}\right)^{5/2} \sim 1.44 \times 10^8 t^{\rm obs}_{\rm cool,e} \text{ for the same } \nu^{\rm obs}. \end{aligned} \tag{5.19}$$

Comparing with the electron synchrotron cooling timescale of Eq. 5.4 ($t^{\rm obs}_{\rm cool,e} \sim 10^{-8}$ s) we have values close to ∼1 s, corresponding to the integration timescale of the analyzed spectra. Having an observed cooling timescale of ~ 1 s for particles emitting at the observed frequency of 100 keV then requires different physical parameters for electrons and protons. In particular, if we consider electrons, the emission region must be weakly magnetised ($B' \sim 1$ G) and it has to be at a large distance ($R \sim 10^{16}$ cm), to avoid overly fast self-Compton cooling, as discussed above. If instead the emitting particles are protons, in order to explain the observed cooling frequency the emitting should be highly magnetized with a standard value of $B' \sim 10^6$ G and lie at a standard distance $R \sim 10^{13}$ cm. Therefore, the proton-synchrotron scenario may help in solving the inconsistencies we found when interpreting the observational evidences presented in this thesis in the leptonic scenario.

It is interesting to derive what is the maximum frequency that can be emitted by protons via synchrotron process, in order to check if there are inconsistencies with the photon energies that we observe. The argument, suggested by Guilbert, Fabian, and Rees 1983 for shock-accelerated electrons, was that at each shock crossing, the electrons double their energy, until their gyro-radius becomes so large that synchrotron cooling limits the maximum attainable γ, leading to a maximum comoving frequency of $\sim$ 50 MeV. Repeating the original argument for the protons, we find that, since the maximum comoving frequency is proportional to the mass of the particle, this quantity is $m_{\rm p}/m_{\rm e}$ times bigger, namely ∼93 GeV. Thus, the protons could take into account the spectrum at even higher photon energies.

5.1.2.1 Radiative cooling and adiabatic timescales

The proton-synchrotron scenario can work because the radiative cooling timescale for protons is much longer than for leptons, and this can naturally explain the large cooling frequency $\nu_{\rm cool}$. On the other hand, one might wonder how we can have a very fast variability (tens of milliseconds) in this scenario. The answer lies in the adiabatic timescale, $t_{\rm ad} \sim R/(2c\Gamma^2)$, which is of the same order of the minimum variability timescale. After $t_{\rm ad}$, the size of the emitting region roughly doubles, all particle energies halve, and the normalisation of the particle distribution decreases (to conserve the number of emitting particles), along with the magnetic field. As a result, the emitting flux, even though the radiative cooling is not particularly severe, is bound to decrease. The $\nu_{\rm cool}$ break continues to evolve (becoming smaller) but the flux decreases, making this evolution difficult to observe. In addition, when using a relatively long exposure timescale (~ 1 s), we can see the superposition of several events, each lasting for $t_{\rm ad}$. If all these events have a similar $\nu_{\rm cool}$ we will observe a non-evolving break frequency (as in the case of GRB 160625B discussed in Chap. 3). However, contrary to the electrons case, for the protons the adiabatic timescale could be too short for some combination of the radius R and the bulk Lorentz factor Γ in order to be able to explain the observed cooling frequency. This issue will be further discussed in Chapter 7.

5.1.2.2 Electrons contribution in a proton–synchrotron scenario

We consider the case in which the number of injected electrons and protons is the same. We also consider that the observed spectrum is due to the proton–synchrotron process. We then ask if the emission produced by electrons can contribute to the observed prompt flux. Two cases are considered:

1. Electrons and protons are injected with the same random Lorenz factor distribution.
2. Electrons and protons are injected with the same energy distribution.

In case (1), the total injected power associated to the electron would be a factor $m_{\rm p}/m_{\rm e}$ smaller, making the electron–synchrotron luminosity negligible with respect to the proton–synchrotron one. Furthermore, the typical frequencies emitted by electron–synchrotron would be larger by a factor of $m_{\rm p}/m_{\rm e}$ with respect to the proton–synchrotron case.

In case (2), if a similar number of electrons and protons are injected with the same typical energies, then the two kinds of bolometric luminosities would also be equal, but the random Lorentz factors of the electrons would be $m_{\rm p}/m_{\rm e}$ times larger. The typical electron–synchrotron frequencies would be a factor $(m_{\rm p}/m_{\rm e})^3$ larger. Here we are assuming that the argument leading to a maximum synchrotron emitted frequency does not apply, requiring an acceleration mechanism different from shocks. In this case it is likely that this extremely high-energy emission ($\sim 10^3$ TeV) would produce a pair cascade, partly inside the emitting region, and partly outside. The fraction of luminosity absorbed within the emitting region would reprocess the power to smaller energies, but a detailed calculation is needed to quantify this statement. The fraction of high-energy photons that escape the source can pair-produce in the intergalactic medium interacting with the cosmic background light. In this case the luminosity initially collimated into the jet angle is dispersed because the produced pairs would be de-collimated by the intergalactic magnetic field. It is then likely that the reprocessed light would not contribute to the observed flux, but further investigations are required to support this speculation.

5.1.2.3 Implications on the jet nature

In the standard scenario, the emitting particles are accelerated at the shocks and cool, and are not re-accelerated. An estimate of the number of emitting electrons was already presented in Equation 5.1.1.1. Here I report a different derivation, still consistent with the previous one, and apply it to the case of the electrons and the protons. In particular, the total number of particles $N_{\rm iso}$ contributing to the observed emission is:

$$N_{\rm iso} \sim \frac{E_{\rm iso}}{\Gamma mc^2(\gamma_{\rm inj}-\gamma_{\rm cool})}. \tag{5.20}$$

This assumes that the slope of the injected distribution is $p > 2$. We now compare case A (electrons) and case B (protons) assuming in any case $\Gamma = 10^2\Gamma_2$.

Case A: electrons — From Eq. 5.2 the typical Lorentz factor $\gamma_{\rm cool}$ of the electrons emitting at $\nu_{\rm cool}$ is

$$\gamma_{\rm cool} = 2.5\times10^4 \left[\frac{\nu^{\rm obs}_{\rm cool,keV}}{B'}\frac{(1+z)}{\Gamma_2}\right]^{1/2}. \tag{5.21}$$

This leads to a total number of emitting electrons:

$$N_{\rm e,iso} \sim 4.9\times10^{52}\frac{E_{\rm iso,53}}{(\gamma_{\rm inj}/\gamma_{\rm cool}-1)}\left[\frac{B'}{\nu^{\rm obs}_{\rm cool,keV}\Gamma_2(1+z)}\right]^{1/2}. \tag{5.22}$$

Observationally, the break at $E_{\rm break} = h\nu_{\rm break}$, interpreted as the cooling break $\nu_{\rm cool}$, is a factor of approximately ten smaller than $\nu_{\rm peak}$. This corresponds to $\gamma_{\rm inj}/\gamma_{\rm cool} \sim 3$ (see Fig. 5.1).

Case B: protons — In this case we assume $B' = 10^6 B'_6$ G. From Eq. 5.17 we have that protons emitting at 1 keV have $\gamma \sim 10^4$. From Eq. 5.20, the total number of emitting protons producing $E_{\rm iso}$ is:

$$N_{\rm p,iso} \sim 6.9\times10^{49}\frac{E_{\rm iso,53}}{(\gamma_{\rm inj}/\gamma_{\rm cool}-1)}\left[\frac{B'_6}{\nu^{\rm obs}_{\rm cool,keV}\Gamma_2(1+z)}\right]^{1/2}. \tag{5.23}$$

In terms of total mass, this corresponds to only $M = N_{\rm p,iso}m_p \sim 5.5\times10^{-8}M_\odot$.

Since the emitting protons have $\gamma \sim 10^4$, which is greater than Γ, it is not possible that they derive their energy from the conversion of bulk kinetic energy into random energy, unless only a minority of protons are accelerated at the expense of a much larger population of cold protons. This requires a not-yet-specified mechanism able to channel a fraction of the total bulk kinetic energy into a few selected protons. In the case of a matter-dominated jet, we can compare the estimate in Eq. 5.23 with the distribution of the fireball baryon loading derived from the afterglow observations reported in Ghirlanda et al. (2018). Correcting for a typical opening angle of 5 degrees (Ghirlanda et al., 2007b; Ghirlanda et al., 2018) and assuming an efficiency of conversion from bulk kinetic energy to random energy η=0.1, our estimate of the baryon loading is $\sim 5\times10^{-7}M_\odot$, which falls inside the baryon loading distribution reported in their Figure 11. Our value is a factor of 10 smaller than the peak of their distribution, located at a few $10^{-6}M_\odot$.

Another more likely possibility could be a partial magnetic reconnection of a dominant magnetic field. In this case we would have a magnetically dominated flow with a small baryon loading, and we would expect three possible observational consequences. The first is the absence of a thermal prompt emission, the 'fossil' radiation remaining after

the conversion of the internal energy into bulk motion (see, e.g. Daigne and Mochkovitch 2002). The second is polarisation of the prompt emission, if part of the magnetic field, besides being dominant, is also ordered (see e.g. Lyutikov, Pariev, and Blandford 2003). The third consequence is a weak or absent reverse shock when the flow starts to decelerate (see e.g. Nakar and Piran 2004).

5.1.3 Conclusions

In this Section I have investigated the synchrotron interpretation of the results presented in Chapter 3, according to two different scenarios: leptonic and hadronic.

The results obtained in Chap. 3 demonstrated the presence of a low-energy break in the prompt spectrum of GRBs and, coupled with the values of the slopes below and above the break, strongly suggest that the emission process is synchrotron originating from particles that cannot completely cool. In a leptonic scenario, this is at odds with respect to the expected efficient cooling of the emitting particles given the compact highly magnetized region where prompt emission is envisaged to originate. The size of the emitting region should be relatively large in order to avoid a strong self-Compton emission. Furthermore, the inferred lower limits on the size can start to significantly conflict with the limits posed by the onset of the afterglow and by the fast variability timescale of the prompt lightcurve. In a leptonic scenario we find no simple solution to this problem. We consider this to be serious and to require a substantial revision of the common and standard scenario assumed for the GRB prompt emission (i.e. emitting region located just beyond the transparency radius, with strong magnetic field, and limited importance of the self–Compton emission).

One possibility that is capable of preserving the standard scenario is to assume that the radiation we observe is still synchrotron but produced by protons. Due to their heavier mass, the cooling timescale of protons is much longer than the one of the electrons, explaining the observed cooling frequency with a standard value of the magnetic field at standard radii. Since their random energy exceeds the bulk one, this possibility likely requires that the dominant form of energy carried by the jet is magnetic. If the magnetic field is also ordered, then we expect a largely polarised prompt emission. A magnetically dominated jet should also imply a limited importance of any thermal component in the prompt emission, as well as a weak (or null) reverse shock at the start of the deceleration phase.

These first simple estimates concerning the presence of emitting, ultra-relativistic protons are very promising in explaining the prompt emission spectra found from the analysis of *Swift* and *Fermi* GRBs. It is interesting now to proceed with more refined and extended calculations in order to constrain the limits and the feasibility of the proton-synchrotron scenario, regarding for example the energetic involved in the jet and the possible contribution of GRBs to ultra-high-energy cosmic rays and to IceCube neutrinos (produced by the photomeson process). I will further discuss some issues regarding the newly proposed proton-synchrotron scenario in Chapter 7.

5.2 High–energy spectrum

In this Section I provide the interpretation of the results obtained in Chap. 4 from the analysis of the high-energy extension of GRBs prompt emission spectrum. This section is divided in two parts. The first one regards the exponential cutoff observed, whose interpretation will be focused on the pair-production opacity argument.

In the second part I focus on the interpretation of the results about the slope of the high-energy power–law above the peak of the spectrum (including the result on GRB 180720B obtained in Sec. 3.4), which allows us to constrain the slope of the underlying distribution of the accelerated particles.

5.2.1 Estimate of Γ from the pair-production opacity

When the compactness argument, introduced in Chapter 1, is applied to the prompt emission spectra, it allows to derive a constraint on the bulk Lorentz factor Γ of the jet. In particular, if interpreted as the result of opacity to pair-production within the source, the observed exponential cutoff can provide an estimate of the bulk Lorentz factor Γ of the jet during the prompt emission phase.

We can derive a more detailed computation of the optical depth for pair–production in the emitting region, which depends on the spectral parameters derived from the analysis in Chap. 4, and use it to set a lower limit or an estimate of Γ, depending on whether an exponential cutoff is present or not in the spectrum, respectively.

For a photon with energy $h\nu$, the energy $h\nu_{\rm T}$ of the target photon for the $\gamma\gamma \rightarrow e^+e^-$ process is such that $\epsilon'_T = 1/\epsilon'$, where $\epsilon' = h\nu'/(m_e c^2)$ and $\epsilon'_{\rm T} = h\nu'_{\rm T}/(m_e c^2)$ [3]. Following Equation B3 reported in Svensson 1987, we can express the optical depth for pair-production for a photon of energy ϵ' as:

$$\tau_{\gamma\gamma}(\epsilon') = \eta(\beta_e)\sigma_T \frac{1}{\epsilon'} n(\frac{1}{\epsilon'})\Delta R' = \eta(\beta)\sigma_T \frac{U'_{rad}(1/\epsilon')}{m_e c^2}\Delta R' \tag{5.24}$$

where we are assuming a spectral photon density $n(\epsilon') \propto \epsilon'^{-\beta_e}$, where β_e is the energy spectral index, σ_T the Thomson cross-section, $\Delta R'$ the width of the shell and $U'_{\rm rad}$ the radiation energy density. The term $\eta(\beta_e)$ depends on the slope of the spectrum and encapsulates the numerical factors ahead of the result of the integral $\int'_{\epsilon_T} \sigma_{\gamma\gamma}(\epsilon')L'(\epsilon')d\epsilon' \sim \eta(\beta_e)\sigma_T L'(\epsilon'_T)$. The analytical expression for the term $\eta(\beta_e)$ is given in Equation B5 in Svensson 1987: for the range of interest in our calculations, a typical β_e = 1–1.5 returns $\eta(\beta_e)$=0.122–0.072. Assuming the usual expression that links the width of the shell $\Delta R'$ to the distance from the black hole R, namely $\Delta R' = R/\Gamma$, and rewriting the optical depth as a function of the frequency ν, we obtain:

$$\tau_{\gamma\gamma}(\nu) = \eta(\beta_e)\sigma_T \frac{L'(\nu_T)}{4\pi R^2 ch}\frac{R}{\Gamma}. \tag{5.25}$$

Assuming that $R = 2ct_{var}\Gamma^2$ and using the relativistic transformation $L'(\nu_T) = L(\nu_T)/\Gamma$, we derive:

$$\tau_{\gamma\gamma}(\nu) = \eta(\beta_e)\sigma_T \frac{d_L^2 F(\nu_T)}{2c^2 h t_{var}\Gamma^4} \tag{5.26}$$

[3] Unless otherwise stated, in this Section the quantities expressed with a prime refer to the comoving frame, otherwise they refer to the observer frame.

Assuming that the spectrum of the target photons is a power–law with spectral energy index β_e, namely $F(\nu_T) = F(\nu_{peak}) \left(\frac{\nu_T}{\nu_{peak}}\right)^{-\beta_e}$, we can write the optical depth as:

$$\tau_{\gamma\gamma}(\nu) = \eta(\beta_e)\sigma_T d_L^2 F(\nu_{peak}) \left[\frac{(m_e c^2)^2}{h\nu_{peak}}\right]^{-\beta_e} \frac{h\nu_{cutoff}^{\beta_e}}{2c^2 h t_{var}} \Gamma^{-4-2\beta_e} \tag{5.27}$$

This equation would allow to compute the optical depth for every GRB whose parameters $F(\nu_{\rm peak})$, β_e, $\nu_{\rm peak}$, $\nu_{\rm cutoff}$, $t_{\rm var}$ and Γ are known. Instead of using $F(\nu_{peak})$, namely the monochromatic flux at the peak energy $h\nu_{\rm peak}$ of the spectrum, we can further rewrite this equation using more common parameters for GRBs spectra, such as the isotropic luminosity $L_{\rm iso}$ and the spectral energy indices of the Band function α and β, converted in energy indices α_e and β_e. If the spectrum is described by two power–laws with energy indices α_e and β_e connected at the peak energy $h\nu_{\rm peak}$, we can express the optical depth as:

$$\tau_{\gamma\gamma}(E_{cutoff}) = \eta(\beta_e)\sigma_T \frac{L_{iso}}{4\pi} \frac{(1-\alpha_e)(\beta_e-1)}{(\beta_e-\alpha_e)} \left[\frac{(m_e c^2)^2}{E_{peak}}\right]^{-\beta_e} \frac{E_{cutoff}^{\beta_e}}{2c^2 E_{peak} t_{var}} \Gamma^{-4-2\beta_e} \tag{5.28}$$

The requirement that $\tau_{\gamma\gamma}(E_{cutoff}) = 1$ in Eq. 5.28 leads to the estimate of Γ:

$$\Gamma = \left[\eta(\beta_e)\sigma_T \frac{L_{iso}}{4\pi} \frac{(1-\alpha_e)(\beta_e-1)}{(\beta_e-\alpha_e)} \left[\frac{(m_e c^2)^2}{E_{peak}}\right]^{-\beta_e} \frac{E_{cutoff}^{\beta_e}}{2c^2 E_{peak} t_{var}}\right]^{\frac{1}{4+2\beta_e}} \tag{5.29}$$

For the computation of the bulk Lorentz factor it is required the knowledge of the redshift z of the source, which is naturally included in the isotropic luminosity term but the correction also applies to the energies and the variability timescale in the equation. For 9 GRBs in our sample, the redshift has been spectroscopically measured (see Table 4.1), and we used it in the computation of Γ. For those GRBs without a redshift measurement, we used $z = 2$ as representative value of the redshift distribution of long GRBs.

Each GRBs lightcurve shows different temporal behaviours and varies on different timescales. For the sake of simplicity, I use the same value of the variability timescale for all the GRBs, namely $t_{\rm var}$=0.1 s, which corresponds to the mean value of the variability timescales for long bursts observed by *Fermi* (Golkhou, Butler, and Littlejohns 2015 – see previous Section).

Setting $\tau_{\gamma\gamma}(E_{\rm cutoff}) = 1$ in Eq. 5.28 allows us to derive an estimate of Γ for those 10 GRBs showing a cutoff in their spectrum, as reported in Chap. 4. For the remaining 12 GRBs not showing a cutoff, we used the lower–limit on $E_{\rm cutoff}$ derived from the spectral fits in order to set a lower–limit on their Γ. These values of Γ must be compared with $\Gamma_{\rm max} = (1+z)E_{\rm cutoff}/m_e c^2$. This limit corresponds to the maximum bulk Lorentz factor attainable for a given observed cutoff energy and for which the cutoff energy in the comoving frame is at the self-annihilation threshold ($E'_{\rm cutoff} = m_e c^2$) [4]. The true bulk Lorentz factor is then the minimum of the obtained values.

[4] This is due the fact that, when we observe a cutoff energy in the spectrum, it could correspond at last to $m_e c^2$ in the comoving frame, which immediately gives a limit to the maximum value of bulk Lorentz factor Γ_0.

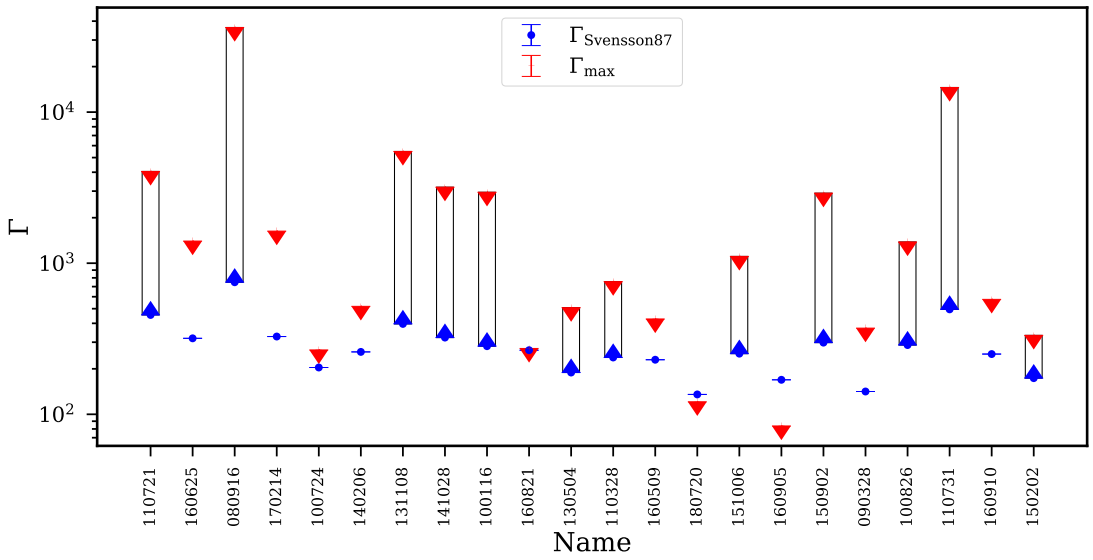

FIGURE 5.5: Bulk Lorentz factor Γ obtained from the pair-production opacity argument, applied the sample of 22 GRB prompt emission spectra analyzed. The name of each GRB is displayed on the x–axis. On the y–axis, the blue points display the estimates of Γ for those GRBs showing an exponential cutoff in their spectrum. The red downward arrows show the values of $\Gamma_{\rm max}$, namely the maximum value of Γ attainable for the pair-production interpretation of the cutoff energy. The blue upward arrows represent the lower–limit on Γ from those GRBs not showing a cutoff in their spectrum. For those GRBs, the lower–limit on Γ has been computed using the lower–limit on the position of the cutoff energy. The black empty bars represent the allowed range of values for Γ between the upper– and the lower–limits.

The estimates and the lower-limits of Γ and the upper-limits given by $\Gamma_{\rm max}$ are shown in Fig. 5.5. For all GRBs in our sample, represented with their names on the x–axis, the red downward arrows on the y-axis show the maximum value $\Gamma_{\rm max}$. The blue upward arrows represent the lower–limit on Γ derived from those GRBs not showing a cutoff in their spectrum. For these GRBs, the black vertical bars represent the range of possible values of the bulk Lorentz factor, namely between the lower–limit imposed by the absence of a cutoff in the spectrum and the upper–limit imposed by $\Gamma_{\rm max}$. The blue points represent the value of Γ derived from those GRBs showing a cutoff in their spectrum. The uncertainties on the measured quantities $E_{\rm cutoff}$, $E_{\rm peak}$, $L_{\rm iso}$, $\alpha_{\rm e}$ and $\beta_{\rm e}$ give a relative uncertainty of the order of 3.5% on the estimates of Γ. We note that in all but two GRBs the estimate of Γ is below the maximum value $\Gamma_{\rm max}$: we therefore consider the value derived from Eq. 5.28 as the estimate of their bulk Lorentz factor. For two GRBs, 180720B and 160905, the estimate of Γ from the cutoff energy is above the maximum value $\Gamma_{\rm max}$, thus the relative bulk Lorentz factor is $\Gamma_{\rm max}$.

The distribution of the estimates of Γ for the 10 GRBs showing a cutoff is centered around $\langle\Gamma\rangle = 230\,(\sigma = 64)$, while the distribution of the 12 lower–limits on Γ has a mean value of $\langle\Gamma\rangle = 345\,(\sigma = 154)$. The main reason for the difference in the distributions can be due to the fact that, for the 12 GRBs without the detection of a cutoff, we used the lower–limits on the cutoff energy and their values are of the order of several hundreds of MeV, thus typically larger than the estimates of $E_{\rm cutoff}$ for the 10 GRBs with a detected exponential cutoff. The lower–limits on $E_{\rm cutoff}$ imply that there could be a cutoff at higher energies. In turn this would imply that the distribution of Γ derived with the 10 GRBs

would be broader, extending towards larger values. This is indeed inferred from the afterglow observations, as it will be discussed in the following section.

We can now focus on the comparison of the estimates of Γ with those derived in literature for other GRBs using the pair-production opacity argument. In the work of Tang et al. 2015, the computation of pair-production opacity $\tau_{\gamma\gamma}$ is similar to the one in this thesis and also to the one presented in Lithwick and Sari (2001), namely assuming a simple one–zone model where the photon field in the emitting region is uniform, isotropic, and time independent. However, since the cutoff energies in the main spectral components they reported were below $\sim$ 60 MeV, in the majority of the cases their estimates of Γ exceeded the maximum attainable values $\Gamma_{\rm max}$. This led the authors to use $\Gamma_{\rm max}$ as the actual bulk Lorentz factor for the majority bursts analyzed, finding values of Γ between $\sim$ 50 and $\sim$150. These values are systematically lower than the values inferred in this thesis.

For the remarkable cases of GRB 100724B and GRB 160509A, showing cutoff energies from $\sim$ few tens of MeV up to 150 MeV, Vianello et al. (2018) reported bulk Lorentz factors in the range $\Gamma \sim 100 - 400$, consistent with our results. The authors used two different time-dependent models to derive the values of the bulk Lorentz factors (i.e. an internal–shocks motivated model by Granot, Cohen-Tanugi, and Silva 2008 and a photospheric model by Gill and Thompson 2014).

It is important to note that simplified one-zone models, as the one used in this thesis and in Lithwick and Sari (2001), Tang et al. (2015) and Fermi Large Area Telescope Team et al. (2012), may provide systematic differences in the inferred Lorentz factors as compared to more detailed time-dependent multi-zone models that consider the case of multiple emitting regions and that take into account the time variability of $\tau_{\gamma\gamma}$. Granot, Cohen-Tanugi, and Silva (2008), and more recently Hascoët et al. (2012), have shown that such time-dependent models can yield inferred Γ estimates that are reduced by a factor of 2–3 compared to estimates made using single-zone models. In the context of these time-dependent model, the estimates of Γ presented in Fig. 5.5 should all be rescaled downward by a factor of 2–3. For a discussion of single and multi-zone models, see also Zou, Fan, and Piran (2011).

5.2.1.1 Comparison with Γ derived from the afterglow

Most of the available estimates of the value of Γ have been inferred from the measurement of the time of the peak of the afterglow lightcurve. When the jet collides with the interstellar medium and it starts to accumulate mass, it starts to decelerate and a peak in the afterglow lightcurve is expected, due to the transition from the coasting to the deceleration phases.

We now focus on the comparison of our estimates of Γ obtained from the pair–production opacity argument with the values inferred from the afterglow onset times, which have been measured for a sample of 50 GRBs and reported in Ghirlanda et al. 2018. This comparison gives us the possibility to build the intrinsic distributions of bulk Lorentz factors of GRBs from two different and independent methods, using two different physical processes (pair-production on one side and deceleration of the jet on the other side).

Fig. 5.6 shows the distributions of the values of the bulk Lorentz factors inferred from the two methods. The filled blue histograms represents the estimates of Γ derived from the $\gamma\gamma$ opacity argument applied in this work, while the empty histograms represent the values derived from the measurement of the afterglow onset time as reported in Ghirlanda et al. 2018, and with the green (orange) color the ones computed assuming the homogeneous (wind-like) medium. For the homogeneous medium case, the authors

assumed a typical medium density of $n_0 = 1$ cm^{-3}. For the wind-like medium case, they used a normalization of $n_0 = 10^{35} \dot{M}_{-5}\, v_{w,3}^{-1}$ cm^{-3}, following the relation $n_0 = \dot{M}/4\pi m_p v_w$ where typical values of the mass-loss rate $\dot{M} = 10^{-5} M_\odot$ yr^{-1} and of the wind velocity $v_w = 10^3$ km s^{-1} have been assumed (Chevalier and Li, 2000).

We show in Fig. 5.6 only the estimates of Γ derived from either the measurement of a cutoff energy in the prompt spectrum or of the time of the peak of the afterglow lightcurve, namely we exclude the lower–limits on the values of Γ derived from both independent methods.

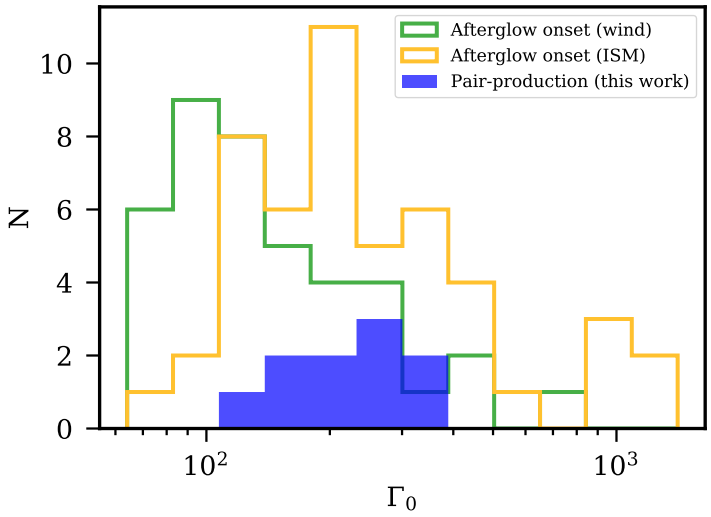

FIGURE 5.6: Distributions of bulk Lorentz factors of GRBs obtained from independent methods. The blue filled histogram represents the distribution of Γ values inferred from the pair-production opacity argument applied to the prompt spectra of 22 GRBs analyzed in this work. The empty histograms show the distributions of Γ values derived from the measurement of the afterglow onset time for a sample of 50 GRBs, as reported in Ghirlanda et al. 2018. The orange histogram represents the values of the bulk Lorentz factor derived assuming a constant medium density, while the green histogram shows the values inferred from the wind–like medium case.

We note that the values of Γ derived in this work are consistent with those derived from the afterglow onset reported in Ghirlanda et al. 2018. Our results are well included in the 68% of the distribution of Γ derived from the afterglow onset time assuming an homogeneous medium. A K–S test performed between the constant ISM case and our Γ distributions returns a p-value = 0.66, indicating that they might be drawn from the same underlying distribution of bulk Lorentz factors. Our results are instead located in the higher tail of the distribution related to the wind–like medium, and a K–S test returns a p-value = 0.002. Since in the wind case the assumed density of the circumburst medium is higher, the Γ values related to the wind–like case are typically smaller than the ones related to the homogeneous case. Keeping fixed all the other parameters in Eq. 5.29, smaller values of Γ would imply smaller values of the cutoff energy E_{cutoff}, which in turn implies that the GRB may not be detected in the LAT energy band. In turn, this may indicate there may be a selection effect in favor of faster GRBs when analyzing GRBs in the LAT sample. Moreover, there may be a bias also on the other side of the distribution, namely towards higher values of the bulk Lorentz factor. The distribution of Γ found applying the pair-production argument may extend towards higher values, as indicated

by the yellow distribution of Γ derived from the afterglow in the ISM case. This is indeed already suggested by the distribution of Γ found from the lower-limits on the cutoff energy $E_{\rm cutoff}$, which is centered around $\Gamma = 345$ and extends up to ∼750. However, keeping fixed all the other parameters of Equation 5.29, such higher values of Γ imply higher values of $E_{\rm cutoff}$, which cannot be observed with the current instruments.

Since the equation for the estimate of Γ from the afterglow onset time strongly depends on the medium density, it would be interesting to repeat this comparison assuming different medium densities, wind velocities and mass loss rates and compare the corresponding Γ values to the ones we found in our analysis. For example, in order to reproduce the blue distribution we found in our analysis, the green distribution related to the wind case should be moved towards higher values of Γ and this implies to assume higher densities of the external medium, which depends on the wind velocity and mass loss rate parameters. However, even though the dependence of the bulk Lorentz factor on the wind parameters is $\Gamma \propto n^{-1/4}$ (see e.g. Equation 6.2 in Chap. 6), the poor knowledge on the wind parameters values (based essentially on the work of Chevalier and Li 2000) limits the range of possible values of the bulk Lorentz factor. For the ISM case, the dependence of the bulk Lorentz factor on the medium density parameter is instead weaker ($\Gamma \propto n^{-1/8}$), thus a change of e.g. a factor 10 in the medium density would not significantly affect the corresponding estimate of the bulk Lorentz factor.

In the work of Nava et al. (2017), the authors suggested another method to derive upper limits on the bulk Lorentz factor, exploiting again the afterglow lightcurve. In particular, since the high-energy synchrotron afterglow flux strongly depends on Γ, they used 190 *Fermi* GRBs which were not detected by *Fermi*/LAT to place upper limits on the flux, and then on Γ. The derived values of the order of $\Gamma \sim 200$ for a homogeneous density medium, and in the range $\Gamma \sim 100$–400 for a wind-like medium, which are consistent with those inferred using other methods (e.g. afterglow onset time and/or pair-production).

5.2.1.2 Estimate of the radius R

We found that two GRBs, GRB 080916 and GRB 110731, in the sample analyzed in Ghirlanda et al. (2018) are also present in our GRB sample. Therefore, for both GRBs a direct comparison of the bulk Lorentz factors derived from the two independent methods can be performed.

From our analysis, their prompt emission spectra do not show the presence of a cutoff. They are both best–fitted by the SBPL. Therefore, we can only set a lower–limit on their Γ values from the pair–production argument. On the other hand, from the peak time of their afterglow lightcurve Ghirlanda et al. (2018) derived an estimate of Γ. Table 5.1 shows the lower–limit and the estimate of the Γ values inferred from the pair-production interpretation and from the afterglow onset, respectively. For the latter, we report both the value derived for the homogeneous and the wind–like cases. The pair-production interpretation implies a Γ greater than the one derived from the afterglow in the wind–like medium case, while the value relative to the constant medium case is in agreement. This could be due to the fact that the value of Γ provided by the pair-production opacity argument depends on the assumption we made on the variability timescale, which we set $t_{\rm var} = 0.1$ s for all GRBs. The corresponding value for the radius R, implicitly assumed, is reported in the fourth column of the Table 5.1.

Since the radius R is of one least known and often assumed parameters of the GRB prompt emission framework, for those GRBs belonging to both samples, we can take the advantage of having the bulk Lorentz factor constrained from an independent method and use it in Eq. 5.28 to estimate the distance R of the emitting region from the black hole. Instead of substituting $R = 2ct_{\rm var}\Gamma^2$, we can invert Eq. 5.28 and use the Γ value

inferred from the afterglow onset to derive the value (or a lower–limit) of the radius R, without making assumptions on the variability timescale. In particular, solving Eq. 5.28 for the radius R, we obtain:

$$R = \eta(\beta_e)\sigma_T \frac{L_{iso}}{4\pi} \frac{(1-\alpha_e)(\beta_e-1)}{(\beta_e-\alpha_e)} \left[\frac{(m_e c^2)^2}{E_{peak}}\right]^{-\beta_e} \frac{E_{cutoff}^{\beta_e}}{cE_{peak}} \Gamma^{-2-2\beta_e}. \quad (5.30)$$

If the GRB spectrum shows an exponential cutoff, then we can set $\tau_{\gamma\gamma}(E_{\rm cutoff})$ as before, and solve for the radius R. If instead the spectrum is a single power–law above the peak, we can use the lower–limit on the cutoff energy to derive a lower–limit on R. This procedure holds only under the assumption that the bulk Lorentz factor Γ of the jet derived from the afterglow onset is the same bulk Lorentz factor of the jet during the prompt emission. However, after having released the energy of the prompt emission, the jet should proceed in the coasting phase and as long as it does not undergo any changes in its kinetic energy, we are allowed to safely associate the two estimates of bulk Lorentz factors.

We can apply this procedure only for two GRBs of our sample, namely GRB 080916 and GRB 110731. We report in Table 5.1 the comparison of the bulk Lorentz factors derived from the prompt and the afterglow phases, and the relative estimate of R, using either the value of Γ obtained for the homogeneous and for the wind–like medium. We note that the two estimates of the radius in the homogeneous and wind cases are different, with the wind–like case greater of a factor of $\sim$50–160 than the homogeneous case. This difference reflects the factor of $\sim$2–3 of difference in the Γ values and it is due to the fact that the radius $R \propto \Gamma^{-2-2\beta_e}$, which, for a typical energy index $\beta_e \sim 1.5$, means that $R \propto \Gamma^{-5}$. The fact that values of the radius R in both cases are R$\gtrsim 10^{13-15}$ cm imply that the distance of the emitting region from the central engine should be slightly larger than the typical radius assumed for the internal shocks to occur ($R \sim 10^{14}$ cm), although still consistent with it.

In our analysis, this procedure for the estimate of the radius R was possible for only two GRBs of our sample. However, Eq. 5.30 is general and can be applied to any other GRB which has the bulk Lorentz factor inferred from an independent method and whose spectral parameters are known. We plan to find other candidates to apply this procedure to and derive the distribution of values for the radius R of the prompt emission region for GRBs.

TABLE 5.1: Comparison of the lower–limits on the radius R of the GRB prompt emission region derived from the pair–production opacity argument, but assuming different estimates of the bulk Lorentz factor Γ. The values of Γ are obtained from two independent methods: the pair–production argument and the afterglow onset time. For each burst, the values of Γ obtained in this Chapter by applying the pair–production argument (assuming $t_{var} = 0.1$s) are reported in the first row, while those obtained from the afterglow onset, taken from Ghirlanda et al. 2018, are reported in the second and third row, for the ISM and wind–like cases, respectively. These values of Γ are then used to estimate the radius R (see Eq. 5.30 in the text), using the pair–production opacity argument. The only 2 out of 22 GRBs of the sample analyzed in Chap. 4 with an estimate of Γ provided by the afterglow onset are GRB 080916C and GRB 110131, thus the estimate of R was possible only for these two GRBs. For each burst, the table shows in the first column the name of the GRB, in the second column the method used to derive Γ, either pair–production or afterglow onset, in the third column the estimates of Γ, according to the different methods, and in the fourth column the corresponding estimates of R according to the pair–production argument.

Name	Method	Γ	R
GRB 080916C	$\gamma\gamma \rightarrow e^+e^-$	> 748.13	$> 6.3 \times 10^{14}$ cm
	Afterglow onset (ISM)	1410 ± 151	$> 3.7 \times 10^{13}$ cm
	Afterglow onset (Wind)	660 ± 49	$> 1.8 \times 10^{15}$ cm
GRB 110731	$\gamma\gamma \rightarrow e^+e^-$	> 494.98	$> 3.8 \times 10^{14}$ cm
	Afterglow onset (ISM)	971.2 ± 12.1	$> 1.5 \times 10^{13}$ cm
	Afterglow onset (Wind)	331.5 ± 8.3	$> 2.4 \times 10^{15}$ cm

5.2.2 Estimate of the slope p of the accelerated particle's distribution

From the same sample of 22 GRBs co-detected by GBM and LAT (see Chap. 4), we derived the distribution of the slope β of the high-energy power–law above E_{peak}. Combining all the results of the spectral analysis, the distribution of β has a median value of $\beta = -2.43$, with a standard deviation of 0.55. The spectral photon index β can be associated to the spectral index p of the population of shock–accelerated electrons, which are assumed to be distributed as a power–law $N(\gamma_e) \propto \gamma_e^{-p}$, for $\gamma_{min} < \gamma < \gamma_{max}$. If the radiative process is synchrotron, for $\nu_m < \nu < \nu_{max}$ (corresponding to γ_{min} and γ_{max}, respectively) the spectrum $F_\nu \propto -p/2$ in fast cooling regime, while in slow cooling regime for $\nu_m < \nu < \nu_c$ (where ν_c corresponds to the cooling frequency) $F_\nu \propto -(p-1)/2$.

In 11 out of 22 GRBs analyzed the spectrum shows the presence of two characteristic energies, E_{break} and E_{peak}, which we associate to the synchrotron cooling frequency ν_c and the injection frequency ν_m, respectively, indicating a fast cooling regime. Given the previous results on the brightest bursts observed by *Fermi*/GBM (see Chap. 3), showing a cooling frequency $\nu_c < \nu_m$, and on the simulations performed, demonstrating that there can be observational biases preventing the cooling break identification, we can reasonably assume that all the 22 GRBs spectra analyzed have a cooling break below the peak energy, i.e. that all the spectra analyzed are in fast cooling regime.

Under this assumption, we associate each spectral slope β to the slope of the accelerated particle distribution using the relation p = -2 -2β [5]. Fig. 5.7 shows the distribution

[5] If, on the contrary, we would have assumed that the spectrum of those GRBs not showing a break is in slow cooling regime, the corresponding p values would have been greater than the ones in fast cooling

of p (right panel) resulting from the β distribution (left panel) derived from the 22 GRBs analyzed. Each color represents the distribution of the slope obtained from the 4 spectral models fitted to the data, while the black empty histograms represent the total distribution, from which the median and standard deviations values are derived. Combining all the fit results, the distribution of p has a median value of p = 2.86, with a standard deviation of 1.1. I recall here that the fact that distribution of β values (and the corresponding p ones) is truncated at -2 (2, respectively) is due to the requirement that the spectrum has a peak in the νF_ν representation. This in turn means that the spectral indices below and above the peak energy are greater and smaller than -2, respectively.

As discussed in Chap. 4, this assumption instead does not hold if we deal with the whole *Fermi*/GBM Catalog, where there can be cases with β values greater than -2. This can be clearly seen in the left panel of Fig. 5.8, reporting all the β slopes of the Fermi GBM catalog bursts whose time–integrated spectrum has been best–fitted by Band (red histogram) or SBPL (blue histogram) function. Following the same relation used in the previous paragraph, we derived the corresponding distribution of p for the *Fermi*/GBM Catalog, which is shown in the right panel of Fig. 5.8. The distribution of p obtained from our analysis is slightly steeper than the one derived from the *Fermi*/GBM Catalog. This can be due to the fact that we studied the extension of the spectrum at higher energies with respect to the GBM, adding crucial data from 30 MeV up to 10 GeV to constraint the high–energy slope of the spectrum.

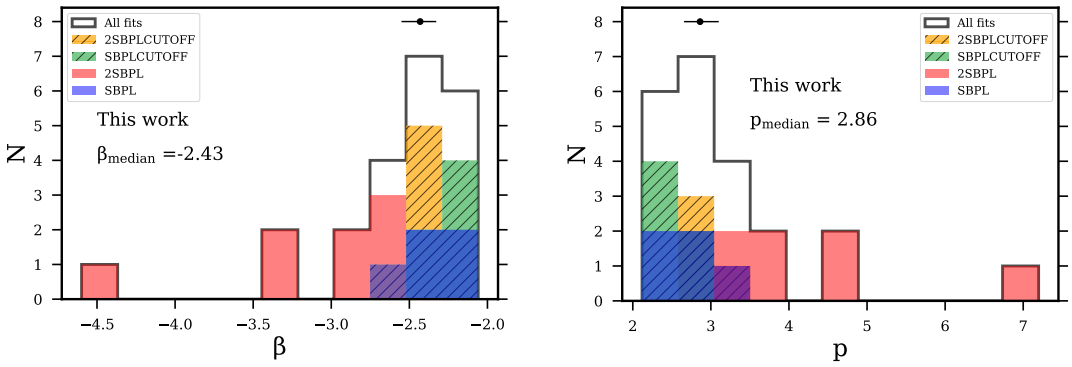

FIGURE 5.7: Distributions of β (left panel) and of the corresponding p (right panel) for the sample of 22 GRBs spectra analyzed in Chapter 4, according to the relation p = -2 -2β (assuming synchrotron in fast cooling regime).

regime, specifically the difference is of 1 ($p_{\text{slow cooling}} = p_{\text{fast cooling}} + 1$), pushing even more to the right the p distribution.

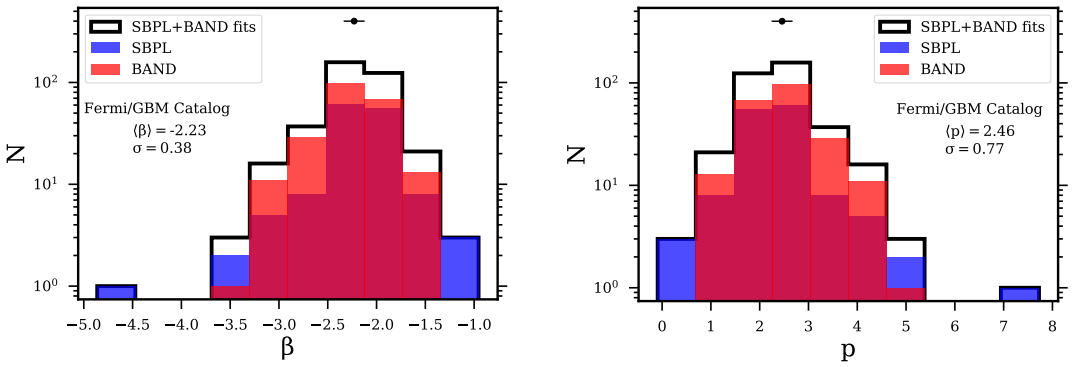

FIGURE 5.8: Distributions of β (left panel) and of the corresponding p (right panel) for the sample of *Fermi*/GBM catalog bursts best–fitted by either Band (red histograms) or SBPL functions (blue histograms), according to the relation p = -2 -2β.

There are two main considerations that we can draw from these results. The first one regards the width of the p distribution. In Fig. 5.7 (confirmed also in Fig. 5.8) is clearly visible that the distribution of p is quite broad and, although the majority of p values are clustered within p=3.5, there is also a non-negligible tail extending towards steep values. This result suggests that the acceleration mechanism does not produce relativistic electrons distributed as a power–law with a unique slope, but rather with a quite wide variety of slopes. A similar conclusion has been drawn for bursts detected by BATSE (Shen, Kumar, and Robinson, 2006), where the observed distribution of p, centered around $\langle p \rangle = 2.50$ with $\sigma = 0.49$, were found to be inconsistent with a universal p value.

The second consideration regards the fact that the distribution of p shows steep values, generously extending at p $\sim$ 5 (up to one case at 7). This result is confirmed also by the independent synchrotron modeling of the prompt emission spectrum of GRB 180720B, shown in Chap. 3. In the specific case of the SED I (0-35 s), the synchrotron modeling returned a slope $p = 4.8$ of the injected population of electrons (see Fig. 3.18). This in turn produced a soft photon spectrum ($\beta \sim -3.4$) at high energies, as confirmed also by the fit of the high-energy spectrum with a single power law. Also SED II (35-70 s) was characterized by a steep slope, even though with a smaller value of $p \sim 3.4$, which corresponds to a harder electron energy distribution producing the synchrotron spectrum. However, we cannot exclude that also in SED II the value of p was large because of the contamination of the high-energy part of the spectrum by the harder spectral component arising in the LAT energy range. Moreover, from the synchrotron modeling of the spectral data, we also derived the value of the minimum energy of the injected non–thermal distribution of relativistic electrons $\gamma_{\rm min}$ (see Section 5.1), which was found to be of the order of $\gamma_{\rm min} \sim 10^6$. Such steep values of p, coupled with large values of $\gamma_{\rm min}$, are strong constraints for the the accelerations mechanism, either internal shocks or magnetic reconnection. Indeed, the acceleration mechanism responsible for the injection of non-thermal electrons must be really efficient in accelerating electrons to high energies, but it also should give rise to a steep electron energy distribution.

On the one hand, both analytic computations and numerical simulations, obtained by several groups using different approaches, predicts that accelerated electrons in relativistic shocks have a power–law distribution with a universal p $\sim$2.2–2.3 (Bednarz and Ostrowski 1998; Achterberg et al. 2001; Lemoine and Pelletier 2003, see Sironi, Keshet,

and Lemoine 2015 for a recent review). On the other hand, relativistic magnetic reconnection (Spruit, Daigne, and Drenkhahn, 2001; Drenkhahn and Spruit, 2002), as also recently shown by particle in cell (PIC) simulations (Sironi and Spitkovsky, 2014; Sironi, Petropoulou, and Giannios, 2015; Petropoulou et al., 2019), can produce a steep electron energy distributions (i.e. $p \sim 4-5$) in the case of a moderate magnetisation, but the electrons can only attain a moderately large $\gamma_e \sim 10^2 - 10^3$. However, it is not possible to extrapolate the predictions of the works mentioned above to our studies on the prompt emission, since they investigated the theory of particle acceleration in ultra-relativistic unmagnetized (or weakly magnetized) plasma. The prompt emission is thought to be produced by mildly relativistic shocks in a magnetized plasma, which belong to a parameter space not yet fully explored. The theory of acceleration in the physical conditions occuring during the prompt emission is still under development (see the recent study of Ligorini et al. 2021), and what kind of energy distribution is expected is still an open question. Given the poor knowledge of the physics underlying the mildly relativistic shock in a magnetized plasma, it is even more important to tackle this problem from an observational point of view. To this aim, the study of the slope of the observed spectrum at high energies reported in this Section is crucial, as it provides meaningful constraints on energy distribution of the particles the acceleration mechanism has to produce.

5.2.3 Conclusion

In this Section I presented the interpretation of the results of the analysis up to 10 GeV of 22 bright GRBs prompt emission spectra observed by *Fermi*, shown in Chap. 4.

We interpret the exponential cutoff observed in 10 out of 22 GRBs as a sign of the pair-production opacity and derive an estimate of the bulk Lorentz factor Γ (or its lower–limit for the remaining 12 GRBs not showing the cutoff). We found reasonable values for the bulk Lorentz factor Γ of the jet during the prompt emission phase (see Fig. 5.5), that are consistent with those derived from the same opacity argument present in the literature. Moreover, we compared our Γ values with the ones inferred from the afterglow onset time reported in Ghirlanda et al. 2018, finding that our results are consistent with those related to the homogeneous medium case (see Fig. 5.6). Signs of pair–production opacity from slower GRBs jet could be difficult to be detected by the LAT instrument, implying a selection effect in our sample, and this hampers the consistency with the bulk Lorentz factors derived in the wind case.

For those GRBs with Γ inferred from any other independent method, we showed that it is possible to derive the estimate of the distance R of the emitting region from the central engine by using that Γ value in the pair–production opacity equation. In the only two GRBs of our sample where it was possible, we used the values of Γ derived from the afterglow onset reported in Ghirlanda et al. 2018. We found values of $R > 10^{13} - 10^{15}$ cm, according to the different estimates of Γ in the homogeneous and wind–like cases. Despite being lower–limits, the inferred values of the radius are compatible with those predicted by the GRB standard model for the prompt emission.

From the slopes β of the power–laws modelling the high–energy spectrum of the 22 GRBs analyzed, we derived the corresponding slopes p of the underlying distribution of non-thermal accelerated particles, assuming the relation p=-2-2β. We note that the distribution of p is quite broad and does not cluster around a universal value. Moreover, we found that the distribution of p has a median value of $p = 2.86$ with a tail reaching values $p \sim$ 5–7. Steep values of p, coupled also with the large values of $\gamma_{\rm min}$ found from the synchrotron modeling of GRB 180720B, require an efficient acceleration mechanism and a steep energy distribution of accelerated particles, providing meaningful constraints to

the theory of particle acceleration through mildly relativistic shocks or magnetic reconnection.

The full implication of the preliminary results discussed in this thesis will be presented in Ravasio M.E., et al. *The high-energy extension of prompt emission spectra of bright Fermi GRBs*, in preparation.

Chapter 6

GRBs detected at VHE

Until 2018, the emission from GRBs has been detected only below 100 GeV, especially from *Fermi*/LAT and the AGILE satellite. Whether or not GRBs are capable of producing Very High Energy (VHE, E>100 GeV) gamma-rays remained an open question (see e.g. Nava 2018). The LAT instrument has detected several photons with energies above 10 GeV coming from bright bursts, which translate into photons exceeding 100 GeV in the case of large redshift of the progenitor. The strongest indication of VHE emission from GRBs was the detection in GRB 130427A (z=0.34) of a 95 GeV photon at 244 s after the trigger time using the LAT instrument (Ackermann et al., 2014). The detection of these photons challenges the interpretation of the VHE emission as due to the same emission component of the lower energy photons, namely the synchrotron one, since they significantly exceeded the synchrotron limit $E_{\rm syn,max}$ (obtained by equating the cooling to the acceleration rate of particles in a decelerating blast wave, see e.g. Piran and Nakar 2010). A possibility is to interpret these photons as belonging to a separated component (e.g. inverse Compton) dominating at high energies. However, these detections did not provide a clear evidence for the rise of a new spectral component. Indeed, the tension between observations and synchrotron model could be relaxed by considering a more complicated scenario for particle acceleration, e.g. a magnetic field decaying downstream on a length scale smaller than the region occupied by shocked particles (Kumar et al., 2012).

The detection of VHE photons, coupled with observations at other wavelengths, can provide strong constraints on the circumburst medium properties, bulk Lorentz factor of the jet, magnetic field strength and they can provide insights into the emission and particle acceleration mechanisms at relativistic shocks (e.g. unveiling the energy of the accelerated electrons involved in the radiation process). For this reason, over the years there were extensive efforts towards follow-up observations at VHE, which unfortunately provided only upper limits until 2018 (Acciari et al., 2011; Berti et al., 2019; Piel et al., 2019).Among many challenges that the Imaging Atmospheric Cherenkov telescopes (IACT) have to overcome, there are the small field of view (a few degrees) combined with the poor localization capabilities of the space detectors such as *Fermi*/GBM, and the attenuation by pair–production on the extra-galactic background light (EBL).

The follow-up programs were finally and richly rewarded since 2018 with the afterglow detection of GRB 180720B (HESS Collaboration et al., 2019), GRB 190114C (MAGIC Collaboration et al., 2019b), GRB 190829A (HESS collaboration, Abdalla, et al., 2021), and GRB 201216C (Blanch et al., 2020a). All these GRBs belong to the long class and are relatively close with respect to the redshift distribution of GRBs (the most distant GRB detected at VHE so far is GRB 201216C, with a redshift of z=1.1). These detections were possible also thanks to the overcome of some critical observational issues such as observations during moonlight periods or after long time delays, a very fast repositioning speed of the telescopes, and finally the increased sensitivity of the IACTs instruments. These VHE emission has been so far detected during the afterglow phase of the GRB and they prove that GRBs are capable of producing VHE radiation up to $\sim$10 hours after the

prompt emission trigger, a key information to completely understand the acceleration mechanisms and emission processes of these events.

These discoveries represent also a success for GRB theories. For typical shock-microphysical parameters inferred from afterglow modeling of other GRBs, there is a general consensus that the leptonic synchrotron self-Compton emission (SSC), where the same accelerated electrons that emit synchrotron photons can scatter off some of these photons, should produce a bright component at TeV energies that can be accessible to the current generation of IACTs. One key prediction of the SSC mechanism is that there should be two bumps in the spectral energy distribution (SED) of the afterglow spectrum (Sari and Esin, 2001), often observed in blazars (Ghisellini et al., 2017). This second component has been firmly established, for the first time, by the MAGIC detection of GRB 190114C, coupled with the X–ray and γ–ray observations (MAGIC Collaboration et al., 2019a). In that case, the LAT detections played a fundamental role in constraining the presence of an additional, rising, spectral component at higher energy. LAT data did not instead help in identifying the double-hump feature, comparatively less evident, in the spectral energy distribution obtained by HESS Collaboration et al. 2019 for GRB 180720B and for GRB 190829A. However, the SSC component could still be the favoured explanation for the H.E.S.S. data (obtained in the late afterglow phase), since the synchrotron emission would instead require exotic particle–acceleration mechanisms to explain photon energies above 100 GeV.

Since we are at the dawn of the VHE era in GRBs, it is crucial to study the properties of the first bursts not specifically related to the VHE emission, in order to investigate their possible common characteristics and to start to study the population of GRB emitting at TeV energies. This would help in finding which kind of physical conditions (such as the external medium density, the kinetic energy of the jet, the bulk Lorentz factor, etc.) are required to produce the newly discovered SSC component, how common are these conditions and if the SSC interpretation holds for all detected GRBs.

In this chapter I describe my contribution to the study of the first three GRBs detected at VHE, GRB 180720B, GRB 190114C and GRB 190829A, not from the VHE perspective but rather from the analysis and interpretation of their multi-wavelength data. In both GRB 180720B (Sec. 6.1) and GRB 190114C (Sec. 6.2), basing on the study of the temporal and spectral evolution of the solely high-energy emission, we sampled the smooth transition from the prompt to the afterglow phase and pinpointed the peak of the afterglow lightcurve (in *Fermi*/LAT for GRB 180720B and in *Fermi*/GBM energy range for GRB 190114C). Interpreting the observed peak as the sign marking the deceleration of the outflow, we derived the bulk Lorentz factor of the jet Γ for both bursts. In the case of GRB 190829A (Sec. 6.3), we obtained high-resolution VLBI images of its radio counterpart and we combined them with the theoretical modeling of the multi-wavelength afterglow emission (including the VHE data detected by the H.E.S.S. Telescopes), inferring interesting constraints on the GRB micro-physical parameters.

6.1 GRB 180720B

While the widely applied Band function fits the dominant component in the 10 keV – 1 MeV range (observed by *Fermi*/GBM), the inclusion of high-energy data (>100 MeV with *Fermi*/LAT) can challenge the modeling of the GRB spectrum and reveal other spectral components (see e.g. Chap. 4). The high–energy data can be the extension of the keV-MeV component, but sometimes they require an additional non-thermal component, fitted by a single power-law function. While the early high-energy emission (simultaneous to the keV–MeV component) shows some variability, the long-lasting LAT emission, detected in some cases up to hours after the end of the prompt, exhibits a smooth decay in time and seems to have an external origin. However, the GRB emission detected by LAT within T_{90} may include contributions of different emission region, i.e. internal or external, and the distinction between an internal and an external origin of emission is not always straightforward. Therefore, it is interesting to follow the evolution of the emission at high-energies, since it can reveal the transition between the prompt and the afterglow component. Moreover, the deceleration of the jet by the interstellar medium is expected to produce a peak in the afterglow light curve at a time $t_{\rm p}$, corresponding to the transition from the coasting to the deceleration phase (Sari and Piran, 1999). If this peak is observed, by deducing $E_{\rm K}$ from the prompt emission and making an assumption on the circum-burst medium density, it is possible to estimate the bulk Lorentz factor of the jet Γ. This has been done for large samples of GRBs (Molinari et al., 2007; Ghirlanda et al., 2012; Ghirlanda et al., 2018). Therefore, following the afterglow evolution from its rise to its decay is fundamental, as it allows to pinpoint the beginning of the deceleration phase and derive the maximum velocity that the jet attained.

GRB 180720B is a bright GRB that has been followed up by an intensive observational campaign (see Section 6.1.1) and this allowed us to track the interplay in the spectrum and the lightcurve of the prompt and the afterglow components. In Section 3.4 I described the prompt emission component dominating the first ∼70 s of GRB 180720B. In this Section I will focus on the rise and the fall of its afterglow component, extending the analysis up to 500 s. Combined evidence from lightcurves (Fig. 6.1 and Fig. 6.2) and SEDs (Fig. 6.3) shows the emergence of the afterglow component in the LAT energy range and the progressive turning off of the prompt emission. From the peak of the afterglow lightcurve, which we interpret as the onset of the deceleration of the blastwave, we derived the estimate of the bulk Lorentz factor Γ of the jet during the coasting phase. I also briefly discuss the consistency of our results with the H.E.S.S. ones.

6.1.1 Observations and data analysis

On 20 July 2018 at 14:21:39 UT, *Fermi*/GBM detected GRB 180720B (Roberts and Meegan, 2018), which was also detected by *Swift*/BAT (Siegel et al., 2018) and *Fermi*/LAT (Bissaldi and Racusin, 2018a). The observed burst duration T_{90} is 49 s in the energy range 50–300 keV (Roberts and Meegan, 2018). GRB 180720B was observed by an intensive follow-up campaign. *Swift*/XRT began observing the source 86.5 seconds after the BAT trigger. Sasada et al. (2018) detected a bright optical counterpart, 73 seconds after the trigger using the 1.5 m Kanata telescope. Several other optical ground telescopes observed this burst (Reva et al., 2018; Itoh et al., 2018; Kann, Izzo, and Casanova, 2018; Crouzet and Malesani, 2018; Horiuchi et al., 2018; Watson et al., 2018; Schmalz et al., 2018; Covino and Fugazza, 2018; Lipunov et al., 2018; Jelinek et al., 2018; Zheng and Filippenko, 2018; Izzo et al., 2018). The redshift $z = 0.654$ was measured with the spectrograph X-shooter on VLT UT2 telescope (Vreeswijk et al., 2018). *Fermi*/LAT detected the emission at higher energies (100 MeV–100 GeV) from GRB 180720B up to 900 s after the trigger time, with a

maximum photon energy of 5 GeV at 137 s (Bissaldi and Racusin, 2018a). GRB 180720B was detected at VHE (in the energy range 100–440 GeV) by the H.E.S.S. telescope (Ruiz-Velasco, 2019; Abdalla et al., 2019) at around 10 hours after the trigger time. Despite the statistical significance of the detection is $\sim 5\sigma$ (Abdalla et al., 2019), this burst is a good candidate to study the properties of GRBs emitting at VHE, and the origin of that emission.

Thanks to the wide energy coverage and high cadence of the observations, it is possible to unveil the afterglow emergence and follow–up the transition from the prompt to the afterglow phase, hardly assessed in γ–rays. As discussed in Section 3.4, in order to study this transition, we considered five time intervals [1]: 0–35 s, 35–70 s, 70–120 s, 120–200 s, and 200–500 s (see Fig. 6.1). According to the same color-code used in Section 3.4, we identified these time intervals with the red, yellow, green, blue, and purple colors, respectively, and this color-code is used in Figs. 6.1 and 6.2. The choice of these large time intervals for the spectral analysis is determined by two requirements: 1) having a sufficient signal in the energy range of the LAT/LLE data ($>$ 30 MeV) where the spectral transition from the prompt to the afterglow is best highlighted; 2) combining, when possible, *Fermi* data with *Swift* and optical data, maximising the temporal overlap to have the combination of data from different spectral bands. Moreover, from a first analysis of the *Fermi*/LAT data, it appeared that the lightcurve shows a rise, a peak, and an initial decay. Therefore, the refinement of the temporal selection was made in order to separate these phases of the *Fermi*/LAT light curve and follow the spectral evolution in the LAT energy range.

The LAT data were extracted and analysed for all the five time intervals shown in the left plot of Fig. 6.1 and filtered selecting photons with energies in the 100 MeV – 100 GeV range. The description of the LAT, GBM, BAT and XRT analysis is reported in Section 3.4. To perform a joint spectral analysis which combined any of the data sets of BAT, XRT, GBM, or LLE in all the time intervals, the spectral analysis software XSPEC (v12.10.0c) was used. To include the XRT spectra to the joint broad-band spectral modelling, the energy channels have been grouped using the *grppha* tool to have at least 20 counts per bin.

6.1.2 Results: temporal evolution of the emission

In the left panel of Fig. 6.1, we denoted the instruments used for the analysis of each time interval. Using the same color-code, the right panel of Fig. 6.1 shows the light curves (counts s^{-1}) of GRB 180720B detected by three different instruments sensitive to increasing photon energies from top to bottom: NaI (8–900 keV), BGO (0.3–40 MeV), and LLE (30–100 MeV). The first two time intervals are characterized by several overlapping pulses, and, as shown in Section 3.4, they are associated to synchrotron radiation during the prompt emission phase (see Section 3.4). From the third time interval onwards, the signal in the BAT and GBM energy range is weaker and there are no more bumps in the GBM light curves (see the right panel of Fig. 6.1). This may be an indication that the prompt emission is ceasing, leaving the stage to the afterglow component. In principle, a possible signature of the transition between the prompt and the afterglow could be a change in the variability of the light curve of the LLE data. However, given the low statistics of the LLE data from 35 seconds onwards, it is difficult to evaluate quantitatively the variability when the afterglow starts to dominate.

[1] Every time interval reported in this section on GRB 180720B is referred to GBM trigger time.

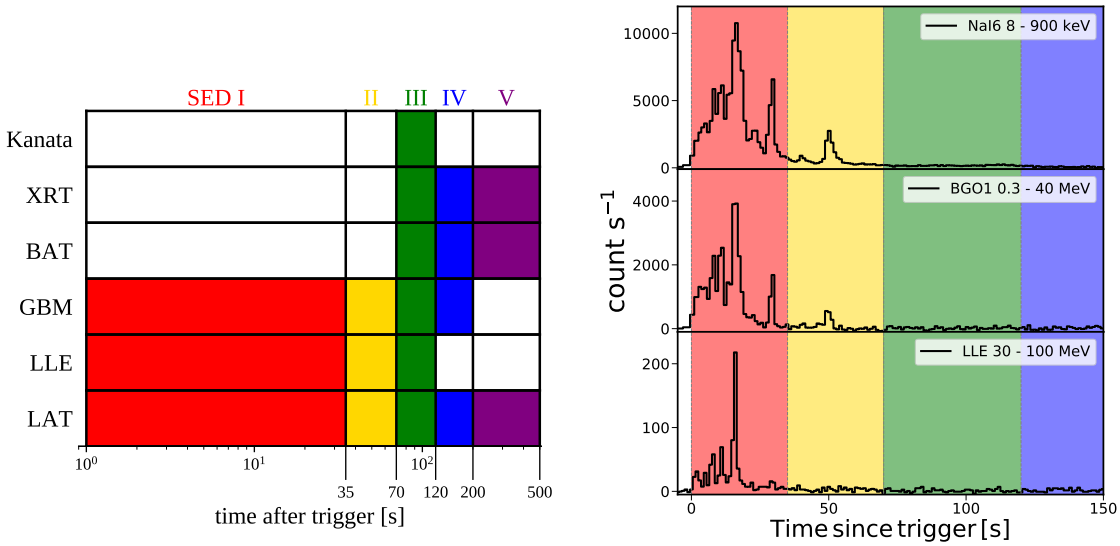

FIGURE 6.1: *Left:* Time intervals and corresponding instruments providing the spectra used for the spectral analysis of GRB 180720B. *Right:* Background-subtracted light curves of GRB 180720B, detected by NaI#6 (8–900 keV, top), BGO#1 (0.3–40 MeV, middle), and LAT–LLE (30–100 MeV, bottom). Different time intervals are highlighted with different colours, and the same colour code is used also in Fig. 6.2 and Fig. 6.3.

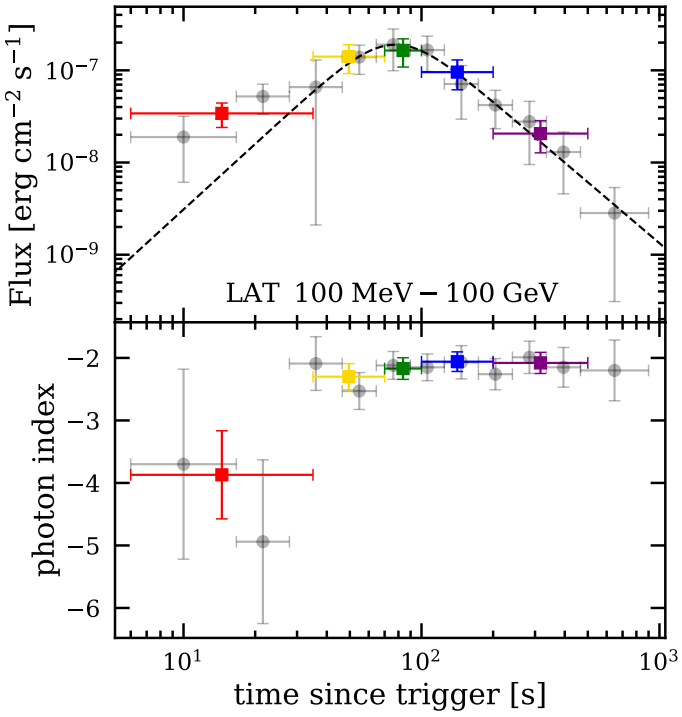

FIGURE 6.2: *Top*: LAT light curve. The energy flux is integrated over the 100 MeV – 100 GeV energy range. Coloured square symbols correspond to the time intervals defined in 6.1; grey circles show the results of the analysis with a higher time resolution. *Bottom*: Photon indices of the power-law model used for the LAT data analysis. Same colour coding and symbols as the top panel.

In order to build the LAT lightcurve, it is necessary to model the spectra in each time

interval. A power-law model was used to fit the LAT spectrum an the results are resumed in Table 6.1. The bottom panel of Fig. 6.2 shows the evolution of the power-law photon spectral index. The spectrum of the emission detected by LAT up to 35 s is characterised by a soft spectrum with spectral index $\Gamma_{\rm PL} < -3$. We attribute this spectral behaviour to the tail of the prompt emission spectrum extending into the LAT energy range. From 35 s onwards, the LAT photon index sets on the constant value ~ -2. This spectral change is confirmed also by a finer time-resolved analysis. This can be an indication that in the LAT data is happening the transition from the prompt to the afterglow emission phases. As shown in Fig. 6.2, the spectral index of ∼–2 remains constant until 900 s, i.e. long after the prompt emission has ceased. The harder spectral slope ∼ -2 of the long–lived LAT emission after 35 s is a common feature of LAT GRBs (Ajello et al., 2019; Nava, 2018). We interpreted this as the emission produced by the external forward shock.

Fig. 6.2 shows the light curve (top panel) and the photon index evolution (bottom panel) obtained from the analysis of the LAT data in the energy range 100 MeV - 100 GeV. The colour-coded symbols correspond to the five time intervals defined in Fig. 6.1, while the grey points show the results of the analysis of the LAT data on a finer temporal binning using equally spaced logarithmic temporal bins, except for the first and last time bins, which are longer to have higher photon statistics. The delay between the first photon detected by LAT in the 100 MeV – 100 GeV range and the GBM trigger is approximately 5 s. The highest photon energy is 4.9 GeV and the corresponding photon was detected by LAT 137 s after the GBM trigger (corresponding to SED IV). These values are consistent with those reported by the *Fermi*/LAT Collaboration (Bissaldi and Racusin, 2018b).

The LAT lightcurve in the 35–70 s time interval possibly includes the superposition of a dominant prompt emission soft tail and a rising harder afterglow components. To characterise the time profile of only the afterglow component, it is useful to consider the light curve beyond 35 s (i.e. excluding the first two grey data points in Fig. 6.2) and to fit with a smooth-joint double power law (see e.g. Ghirlanda, Ghisellini, and Nava, 2010), as follows:

$$R(t) = \frac{A(t/t_{\rm b})^{\alpha}}{1+(t/t_{\rm b})^{\alpha+\beta}}, \tag{6.1}$$

where the free parameters are the rise and decay slopes α and β respectively, characteristic time $t_{\rm b}$, and normalisation factor A. This fit is shown by the dashed line in the top panel of Fig. 6.2. The best–fit parameters are $A = (3.8 \pm 0.4) \times 10^{-7}$ erg s^{-1} cm^{-2}, $\alpha = 2.4 \pm 0.7$, $\beta = 2.2 \pm 0.2$, and $t_{\rm b} = 76.5 \pm 8.0$ s. The LAT flux rises consistently with $\sim t^2$, that is the expected behaviour in case of synchrotron emission (in the fast cooling regime) from the external shock prior to the deceleration radius in a constant ambient medium (e.g. Sari and Piran, 1999). The peak of the light curve is given by $t_{\rm peak} = t_{\rm b}(\alpha/\beta)^{1/(\alpha+\beta)} = 78 \pm 8$ s. We interpreted this peak as the onset time of the afterglow emission and inferred the bulk Lorentz factor of the outflow (see the derivation in Section 6.1.4).

6.1.3 Results: evidence of afterglow emission from SEDs

Fig. 6.3 shows the whole evolution of the SED from the trigger time up to 500 seconds, including the first two SEDs described in Section §3.4. This plot shows the SED obtained from the combined analysis of the XRT, GBM, and LAT/LLE data when available (first three SEDs) together with the independent analysis of the LAT data (for all the five time intervals). Since the photon with the highest energy detected by LAT is ∼ 5 GeV, the LAT SEDs are limited over the 0.1–10 GeV energy range. The shaded regions corresponding to each SED show the 68% confidence interval on the model fits. These are obtained

by combining the errors on the best-fit parameters and accounting for their covariance through a Monte Carlo sampling of the parameter space.

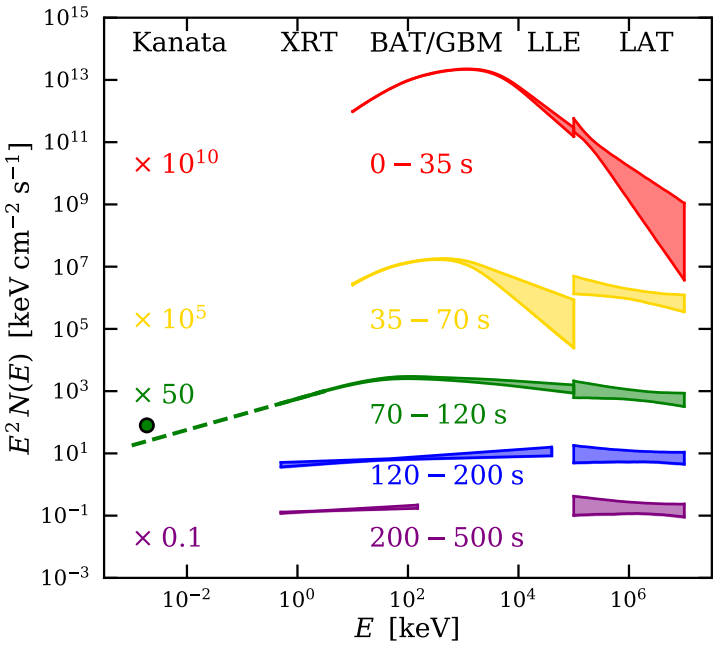

FIGURE 6.3: Evolution of the SED of GRB 180720B, which shows the smooth transition from the prompt (first 70s – red and yellow curves) to the afterglow phase, dominating from 70 s onward (green, blue and purple curves). Each curve corresponds to a specific time interval and has been rescaled for presentation purposes by the scaling factor reported in the figure. For reference, the top labels denote the instruments providing data in the corresponding energy ranges.

The time interval of the green SED from 70 s to 120 s contains the peak of the LAT light curve ($t_{\rm peak} \sim 78$ s, Fig. 6.2) and represents the moment when the afterglow begins to dominate the observed emission. At this epoch, X–ray data from *Swift*/XRT ranging from 0.5 keV to 10 keV are also available, allowing us to extend the analysis to lower energies. The synchrotron model, used to fit the first two SEDs and described in Section §3.4, is also used to fit the combined data of XRT+BAT+GBM+LLE. The best fit is a synchrotron spectrum in fast cooling, with $E_{\rm cool}$ constrained to be below 0.5 keV, $E_{\rm min} \sim 44$ keV and a high-energy slope which is consistent with the LAT spectrum (see also Table 6.1). The spectrum shows no evidence of a break down to the XRT energy range. Therefore, under the assumption that the emission is still in the fast cooling regime, at this epoch the cooling energy $E_{\rm cool}$ has to be very low, less than 0.5 keV. Furthermore, extrapolating the spectrum down to the optical range with a power law $N(E) \propto E^{-3/2}$ (dashed green line in Fig. 6.3), it is marginally consistent with the optical detection reported by Sasada et al. 2018.

In the remaining two SEDs from 120 s up to 500 s the afterglow emission is dominant. Indeed data from X-rays up to gigelectronvolt are well fitted by a single power-law function with $\Gamma_{\rm PL} \sim -2$, which is the expected value of the synchrotron afterglow spectral photon index (Burrows et al., 2005; Zhang et al., 2006).

TABLE 6.1: Best-fit parameters for each different model used in the five SEDs reported in Fig. 6.3 of GRB 180720B. The first column reports the time interval over which the spectrum has been integrated, the second column the detector whose data have been used to build the SED along with the energy range, and the third column represents the different models used to fit that data. From the fourth column onwards: energy flux computed in the energy range reported in the second column, photon energy corresponding to the electron cooling Lorentz factor E_c, photon energy corresponding to the electron injection Lorentz factor E_m, electron energy distribution slope p (corresponding high-energy photon index $\beta = -p/2 - 1$ in parentheses), power-law photon index of the LLE/LAT data, and the reduced χ^2 of the fit with the degrees of freedom in parentheses.

Time interval	Data	Model	Flux [10^{-7}erg/s cm^2]	E_c [keV]	E_m [keV]	$p(\beta)$	Γ_{PL}	χ^2_{red}(d.o.f.)
0-35 s	GBM [10 keV - 40 MeV]	Sync	142^{+7}_{-2}	75^{+5}_{-2}	2380^{+24}_{-524}	$> 3.95 (< -2.98)$ @ 3σ	-	1.56 (293)
	LLE [30 - 100 MeV]	PL	$1.73^{+0.17}_{-0.24}$	-	-	-	$-3.44^{+0.36}_{-0.29}$	0.39 (11)
	GBM+LLE [10 keV - 100 MeV]	Sync	142^{+3}_{-1}	79^{+2}_{-3}	1898^{+314}_{-58}	$4.77^{+0.49}_{-0.15}$ $(-3.39^{+0.08}_{-0.25})$	-	1.52 (305)
	LAT [100 MeV - 100 GeV]	PL	$0.34^{+0.10}_{-0.10}$	-	-	-	$-3.87^{+0.71}_{-0.71}$	-
35-70 s	GBM+LLE [10 keV - 100 MeV]	Sync	$13.0^{+0.04}_{-2.2}$	25^{+83}_{-2}	519^{+57}_{-417}	$3.26^{+0.19}_{-0.64}$ $(-2.63^{+0.32}_{-0.1})$	-	0.97(286)
	LAT [100 MeV - 100 GeV]	PL	$1.41^{+0.49}_{-0.49}$	-	-	-	$-2.3^{+0.21}_{-0.21}$	-
70-120 s	XRT+BAT+GBM+LLE [0.5 keV - 100 MeV]	Sync	$7.26^{+0.21}_{-0.8}$	-	$43.55^{+10.48}_{-7.9}$	$2.08^{+0.19}_{-0.04}$ $(-2.04^{+0.1}_{-0.02})$	-	0.91 (465)
	LAT [100 MeV - 100 GeV]	PL	$1.64^{+0.56}_{-0.56}$	-	-	-	$-2.17^{+0.17}_{-0.17}$	-
120-200 s	XRT+BAT+GBM [0.5 keV - 40 MeV]	PL	$1.38^{+0.20}_{-0.15}$	-	-	-	-1.91 ± 0.05	0.86 (490)
	LAT [100 MeV - 100 GeV]	PL	$0.96^{+0.34}_{-0.34}$	-	-	-	$-2.06^{+0.16}_{-0.16}$	-
200-500 s	XRT+BAT [0.5 - 150 keV]	PL	0.06 ± 0.01	-	-	-	-1.86 ± 0.03	1.03 (276)
	LAT [100 MeV - 100 GeV]	PL	$0.21^{+0.08}_{-0.08}$	-	-	-	$-2.08^{+0.17}_{-0.17}$	-

6.1.4 Estimate of the bulk Lorentz factor Γ

The light curve of the LAT flux (Fig. 6.2 top panel) shows a peak at ~ 80 s from the trigger. As shown in Fig. 6.3, after 35-40 s the prompt emission is already too weak to contribute substantially to the observed emission in the LAT energy range. Indeed, the spectral slope of the LAT emission changes from soft to hard (Fig. 6.2 bottom panel).

If the long-lasting LAT emission is of external origin, it is possible to derive the bulk Lorentz factor just before the deceleration phase, conventionally Γ, from the interpretation of the peak of the LAT light curves as the deceleration time. The required quantities are: i) the time of the peak of the light curve t_p; ii) the isotropic equivalent kinetic energy of the jet E_k after the emission of the prompt radiation; iii) the circum-burst density n, responsible for the deceleration of the jet, and iv) its radial profile.

The different derivation of Γ from the afterglow onset proposed in the literature have been summarised and compared recently in Ghirlanda et al. 2018, where it has been shown that the different methods differ at most by a factor of 2. We therefore chose the following equation, derived by Nava et al. 2013 :

$$\Gamma = \left[\frac{(17-4s)(9-2s)3^{2-s}}{2^{10-2s}\pi(4-s)}\left(\frac{E_k}{n_0 m_p c^{5-s}}\right)\right]^{1/(8-2s)} t_{p,z}^{-\frac{3-s}{8-2s}}. \quad (6.2)$$

In this equation, $t_{p,z}$ is the onset time measured in the source cosmological rest frame, i.e. $t_{p,z} = t_p/(1+z)$ and m_p is the proton mass. Since the jet is assumed to be cold,

the energy that is still in the jet after the prompt emission is in the form of the kinetic energy E_k. Thus, the kinetic energy of the fireball is inferred as $E_k = E_{\rm iso}(1-\eta)/\eta$, where η is the efficiency of conversion of the initial energy into radiation during the prompt phase, typically assumed to be of few tens percent (Fan and Piran, 2006; Zhang et al., 2007; Wygoda et al., 2016; Beniamini, Nava, and Piran, 2016; Kumar, 1999). The density is assumed to have a radial profile parametrised as $n(R) = n_0 R^{-s}$, where R is the distance from the central engine and $s = 0$ represents the uniform density case while $s = 2$ describe the scenario of a stellar wind density profile. In the latter case $n_0 = \dot{M}_{\rm w}/(4\pi v_{\rm w} m_p)$, where $\dot{M}_{\rm w}$ is the rate of mass loss and $v_{\rm w}$ is the wind speed (Chevalier and Li, 2000).

For the two different cases of homogeneous medium ($s = 0$) and wind density profile ($s = 2$), Eq. 6.2 becomes:

$$\Gamma \propto \left(\frac{E_{\rm iso}}{\eta n_0 m_{\rm p} c^5}\right)^{\frac{1}{8}} t_{\rm p,z}^{-\frac{3}{8}} \qquad (s=0) \tag{6.3}$$

$$\Gamma \propto \left(\frac{E_{\rm iso}}{\eta n_0 m_{\rm p} c^3}\right)^{\frac{1}{4}} t_{\rm p,z}^{-\frac{1}{4}} \qquad (s=2) \tag{6.4}$$

Assuming a redshift $z = 0.654$ as reported in Vreeswijk et al. (2018), an isotropic equivalent energy $E_{\rm iso} = 6 \times 10^{53}$ erg (Frederiks et al., 2018), $\eta = 0.2$, $t_{\rm p} = 80$ s, the resulting estimate of the bulk Lorentz factor is $\Gamma = 294$ (220) for $n_0 = 1$ (10) cm^{-3} in the case of a constant external medium density ($s = 0$). For a wind medium ($s = 2$), assuming a wind mass–loss rate $\dot{M}_{\rm w} = 10^{-5}$ M$_\odot$ yr^{-1}, $\Gamma = 142$ (80) for $v_{\rm w} = 10^3$ (10^2) km s^{-1}. Such values are consistent with the distributions of Γ in both scenarios obtained from the analysis of a large sample of bursts with measured onset time (Ghirlanda et al., 2018).

6.1.5 Connections between LAT and H.E.S.S. emissions

The H.E.S.S. telescope detected high-energy photons (100–440 GeV) from GRB 180720B at ~ 10.5 h after the trigger time. At the time of the work, Abdalla et al. (2019) reported a H.E.S.S. $EF(E)$ flux of 5×10^{-11} erg cm^{-2} s^{-1} in the energy range 100-440 GeV.

By analysing the LAT data from 8 to 12 hours after the trigger, we obtained[2] a 1σ upper limit of 8.5×10^{-10} erg cm^{-2} s^{-1} (integrated in the 0.1–100 GeV energy range). By extrapolating the LAT light curve of Fig. 6.2 at $t \sim 10.5$ h, we predicted a 0.1–100 GeV $EF(E)$ flux of $\sim 5 \times 10^{-13}$ erg cm^{-2} s^{-1} if the flux decays $\propto t^{-2.2}$ (as found in the first 500 seconds). Instead, if after ~ 500 s the flux temporal decay becomes shallower (e.g. $\propto t^{-1}$, consistently with the X–ray data[3]), the flux at 10.5 hours would be $\sim 8 \times 10^{-11}$ erg cm^{-2} s^{-1}.

Therefore, the true LAT flux at around 10 h should be between $\sim 5 \times 10^{-13}$ erg cm^{-2} s^{-1} and the upper limit 8.5×10^{-10} erg cm^{-2} s^{-1}. We note that if the flux decays $\propto t^{-1}$, its value at 10.5 hours is similar to that reported by Wang et al. (2019) and Abdalla et al. (2019) for the H.E.S.S. detection at higher energies. The similarity in the $EF(E)$ flux values leads to the possible interpretation that the afterglow spectrum above 100 MeV could extend up to energies around 300 GeV as a single component. However the VHE emission is unlikely to be synchrotron emission because of the limiting maximum synchrotron frequency (Guilbert, Fabian, and Rees, 1983). This VHE emission can be more easily explained as a SSC component (Meszaros, Rees, and Papathanassiou, 1994; Waxman, 1997; Wei and Lu, 1998) as also suggested by Abdalla et al. (2019) and Wang et al. (2019).

[2] We assumed that the spectral index of the LAT emission component is -2 as observed before.

[3] https://www.swift.ac.uk/xrt_curves/00848890/

6.1.6 Discussion and conclusion

In this section I described the study of the early afterglow emission of GRB 180720B, whose spectral evolution has been followed up to 500 s after the trigger time. In particular, in the first time interval (0–35 s), which includes the main event of the prompt emission, the high-energy LAT spectrum presents different behaviour with respect to the rest of the burst (see bottom panel in Fig. 6.2). The photon index in this time interval is steep ($\sim$-4) and it is consistent with the photon index of the spectrum at lower energies obtained from the analysis of the GBM+LLE data. Therefore, we identified the LAT emission observed in the first time interval as the continuation of the prompt emission spectrum, thus associating it an internal origin (see Section 3.4). From the second time interval onward, the LAT emission shows a gradual hardening of the spectrum, whose photon index settles around -2 and remains constant up to $\sim$500 s. This is an indication of the rise of another spectral component, superimposed to the prompt emission one. The lightcurve of the LAT data allows to follow the flux evolution of this component: in the second and third time interval, the flux rises $\propto t^{2.4}$, it shows a peak at $\sim$ 78 s and then it follows a decay $\propto t^{-2.2}$ in the last two time intervals (120-200 s and 200-500 s), as shown in Fig. 6.2.

We interpret the component rising and falling in the LAT energy band as due to the afterglow of the burst, because: i) it appeared well after the start of the prompt emission (in the second time interval, 35-70 s); ii) it dominates up to late times ($\sim$ 500 s); iii) its spectral photon index $\Gamma_{\rm PL}$ $\sim$-2 is consistent with the ones of the typical afterglows observed in γ-rays, and iv) its lightcurve observed in the LAT energy range shows a smooth rise and decay of the flux, differently from the highly variable lightcurve observed at lower energies typically associated to the prompt phase.

Therefore, interpreting the GeV component of GRB 18720B rising after $\sim$35 s as afterglow due to the external shock, we identified the LAT lightcurve peak as the onset of the deceleration of the outflow (Fig. 6.2). Using the measured time of the lightcurve peak $t_{\rm p}$ allows us to derive the estimate of the bulk Lorentz factor of the jet $\Gamma \sim 300\ (150)$, for a homogeneous (wind-like) circum-burst medium. We have used this crucial information on the value of Γ, instead often assumed in GRBs, in the estimate of the intrinsic physical parameters of the emission region related to the synchrotron modeling, as described in Chapter 5.

An alternative interpretation of the peak of the LAT lightcurve could be the passage of the characteristic frequency of the synchrotron spectrum inside the observed energy range. This would produce a rise, a peak and a subsequent decay similar to the one observed in Fig. 6.2. In this case, the characteristic synchrotron frequency should lie very close to the observation band at the time of the peak and when it is crosses the band, the spectrum should reveal its presence (i.e. displaying a broken power–law behaviour). However, the spectral analysis of the LAT emission revealed that at the time of the peak of the LAT lightcurve (third time interval), the XRT+BAT+GBM+LLE spectrum is well fitted by the synchrotron model with only one break at $E_m \sim 44$ keV, a cooling frequency constrained to be below 0.5 keV and a single power–law up to the LLE energy band (see the green SED in Fig. 6.3 and Table 6.1). Since the the synchrotron injection frequency $\nu_{\rm inj} \propto t^{-3/2}$ both in the homogeneous and wind–like medium cases (see Panaitescu and Kumar 2000), it cannot have crossed the LAT energy band and produce the observed peak in the LAT lightcurve at 78 s. The other synchrotron frequency that could pass through the LAT band is the cooling frequency $\nu_{\rm cool}$. While in the homogeneous case it goes like $t^{-1/2}$, and therefore the same argument applied before to $\nu_{\rm inj}$ is still valid, in the wind–like medium case it is proportional to $t^{1/2}$. Also in this case, however, the frequency is too far from the LAT energy band to be able to produce the peak in the LAT

lightcurve at the observed time. Moreover, we observed a transition of the photon index of the LAT spectrum from steep ($\sim$-4) to flat ($\sim$-2) values, and no spectral variations after the third time interval: this behaviour is inconsistent with the passage of a characteristic frequency, that instead would produce an evolution on the opposite direction, i.e. toward steeper values of the photon index of the spectrum once the frequency crossed the band. These reasons disfavour the interpretation of the peak of the LAT lightcurve as due to the passage of the characteristic synchrotron frequency inside the LAT energy band.

After 78 s, the LAT flux is a significant fraction of the total emission and characterised by a nearly flat spectrum in $EF(E)$. This implies that at this time the LAT flux can be considered a proxy of the bolometric flux. Ghisellini et al. (2010) and Ackermann et al. (2013) studied the theoretical temporal evolution of the observed bolometric flux emitted by a fireball expanding in a homogeneous interstellar medium. These authors found that the flux decays as $\sim t^{-1}$ in the adiabatic regime and as $\sim t^{-10/7}$ in the radiative regime.The flux decay slope we found (-2.2 ± 0.2) is steeper than both these theoretical predictions. When the temporal decay is fitted with a power–law, the *Fermi* Collaboration Catalog reported for this burst a flux decay of 1.88 ± 0.15 (Ajello et al., 2019), which is consistent at 1σ with our result and is also steeper than the theoretical predictions. However, the authors reported that the temporal decay is better fitted by a broken power–law, with a break around $\sim$ 230 s and the indices below and above the break corresponding to α_1=1.46$\pm$0.19 and α_2=3.20$\pm$0.56, respectively. While the first decay index is consistent with the radiative regime prediction, the second one is very steep: GRB 180720B is one of the only two GRBs in the LAT Catalog with the decay index that steepens after the break (Ajello et al., 2019). Fig. 6.4 shows the distribution of the late-time temporal decay index for 86 long GRBs light curves detected by LAT. As shown in the plot, the average temporal decay index is around -1, which supports the adiabatic regime scenario (represented by the leftmost solid vertical black line). Nevertheless, the radiative regime (rightmost solid vertical black line) is also allowed from the range of measured temporal indices. The steepest value in the plot is represented by the temporal index after the break of GRB 180720B, namely α_2=3.20. The other steep value corresponds to GRB 100116A, whose LAT lightcurve is fitted by a single power–law with temporal index α=2.7$\pm$0.2. The plot shows for comparison the 1-σ range for the temporal decay index of GRB 180720B found in this analysis, which is marked with a green rectangle. As shown in the plot, our result belongs to the tail of the distribution of temporal indices found for LAT-detected bursts, but it is not the steepest one. There could be the possibility of the presence a larger tail of steep decay indices populating the rightmost part of this plot, that could be not observed due to selection effects (e.g., those GRBs with a fast-decaying afterglow lightcurve could be difficult to be observed by LAT, because they quickly fade below the detection threshold).

Moreover, the afterglow of GRB 180720B does not satisfy the relations between the temporal decay index α and the spectral index β (the so-called *closure relation*) expected for synchrotron emission from the external shock model. Indeed, the spectrum and corresponding light curve from this process depend on the relative position of ν_m and ν_c and can be described as a series of broken power laws with the typical trend $F_\nu \propto t^{-\alpha}\nu^{-\beta}$ (Sari, Piran, and Narayan, 1998b; Granot and Sari, 2002). The set of standard closure relations depends on the combination of i) the cooling regime, ii) the electron spectral index p, and iii) the density profile of the surrounding medium. These relations have been derived both for the constant density medium and for wind-like medium (Sari, Piran, and Narayan, 1998b; Chevalier and Li, 2000; Gao et al., 2013). Given the fast cooling regime of the synchrotron spectrum with p>2 found from the fit of the third SED, the LAT emission should correspond to the part of the synchrotron spectrum above both ν_m and ν_c and the temporal index should be linked to the spectral index following the relation

$\alpha = (3\beta - 1)/2$, for both ISM and wind-like medium. Since the energy flux spectral index of the LAT spectrum found in the third SED is β=1.17$\pm$0.17, the corresponding temporal index should be $\alpha = 1.26 \pm 0.25$, which is not consistent with our result. Despite the fact that the standard closure relations do not always sufficiently explain the observed GRB GeV, X-ray and optical afterglows tested in literature (Willingale et al., 2007; Wang et al., 2015; Tak et al., 2019), the behaviour of the LAT temporal decay of GRB 180720B remains unusual and the origin of such fast decay does not have a straightforward interpretation.

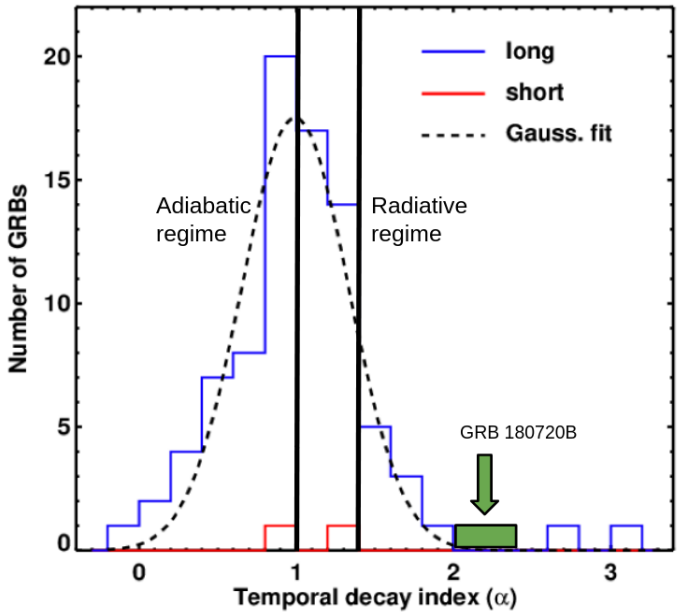

FIGURE 6.4: Distribution of the late-time temporal decay indices for 86 long (blue histogram) and 2 short (red histogram) bursts reported in the second *Fermi*/LAT Catalog (Ajello et al., 2019). The dashed black line represents the Gaussian fit of the lGRB indices, with mean 0.99 and standard deviation 0.80. The vertical solid lines represent the prediction for the temporal decay index of the bolometric flux, in the adiabatic (1) and radiative (10/7) regime. The green rectangle represents the 1σ range of the temporal decay index (2.2 ± 0.2) obtained from the analysis of the LAT lightcurve of GRB 180720B. Modified from Ajello et al. 2019.

6.2 GRB 190114C

This burst was the first to be detected at Very High Energies with high significance by a Cherenkov telescope: MAGIC was able to point the source 50 seconds after the *Swift* trigger, revealing the burst with a significance $> 20\sigma$ at energies >300 GeV (Mirzoyan, Noda, Moretti, et al., 2019). Thanks to the modeling of the multi–wavelength observations, the MAGIC Collaboration interpreted this emission as due to the SSC component of the afterglow of the burst (MAGIC Collaboration et al., 2019a). In light of this detection, it is interesting to study the temporal and spectral evolution of the emission detected at lower energies, e.g. in the GBM energy range. In fact, it is worth investigating if and when the component observed by MAGIC is also visible at lower energies, if and how it connects to the low energy spectrum. Moreover, it is important to study the emission at lower energies to characterize the other component, namely the prompt emission, and follow the transition from prompt to the afterglow, in an energy range where these two components compete with each other, both temporally and spectrally, as shown in the case of GRB 180720B (Sec.6.1).

In order to answer to these questions, triggered by the MAGIC detection, I analyzed the emission as detected by the GBM in the 10 keV – 40 MeV energy range, up to ∼60 seconds after the trigger. Data from BAT and XRT onboard *Swift* have been also considered in three time intervals. The fine time–resolved analysis led us to find the appearance and temporal evolution of a non-thermal power–law spectral component starting from 4 s after the trigger, which we interpret as the afterglow of the burst. The peak of the afterglow lightcurve allowed us to constraint the bulk Lorentz factor Γ of the jet during the coasting phase. The results presented in this Section have been published in Ravasio et al. 2019b.

6.2.1 Observational properties of GRB 190114C

On January 14 2019 at 20:57:03 UT GRB 190114C triggered both the *Fermi*/GBM and the *Swift*/BAT (Hamburg, Veres, Meegan, et al., 2019; Gropp et al., 2019), together with other several γ-ray satellites, e.g. INTEGRAL, AGILE, HXMT and Konus-Wind (Ursi et al., 2019; Xiao et al., 2019; Minaev and Pozanenko, 2019; Frederiks et al., 2019). The burst was also detected by LAT, remaining in its field of view until 150 s after the GBM trigger (Kocevski, Omodei, Axelsson, et al., 2019). The redshift was first measured by the Nordic Optical Telescope (NOT) (Selsing, Fynbo, Heintz, et al., 2019) and soon confirmed by the Gran Telescopio Canarias (GTC, Castro-Tirado, Hu, Fernandez-Garcia, et al. 2019), with $z = 0.4245 \pm 0.0005$.

In the time interval 0–38.59 s, the fluence (integrated in the 10–1000 keV energy range) measured by the GBM is $3.99 \times 10^{-4} \pm 8 \times 10^{-7}$ erg cm^{-2} and the peak energy is $E_{\rm peak}$= 998.6 ± 11.9 keV (Hamburg, Veres, Meegan, et al., 2019). As reported in Hamburg, Veres, Meegan, et al. 2019, the corresponding isotropic equivalent energy and luminosity are $E_{\rm iso} \sim 3 \times 10^{53}$ erg and $L_{\rm iso} \sim 1 \times 10^{53}$ erg s^{-1}, respectively. These values make this burst consistent with the $E_{\rm peak}$–$E_{\rm iso}$ (Amati et al., 2002) and $E_{\rm peak}$–$L_{\rm iso}$ (Yonetoku et al., 2004) correlations (Frederiks, Golenetskii, Aptekar, et al., 2019).

The prompt emission of GRB 190114C is characterized by a first (multi-peaked) pulse lasting ∼ 5.5 seconds, followed by a second weaker and softer pulse from 15 to 22 seconds after trigger (as shown in the top panel of Fig. 6.5), and then a weaker and long tail lasting up to hundreds of seconds (Hamburg, Veres, Meegan, et al., 2019; Minaev and Pozanenko, 2019).

6.2.2 Spectral analysis

In addition to the standard procedure described in Appendix A, I provide details of the analysis for *Fermi* and *Swift* data for this specific burst. Regarding *Fermi*/GBM, I analyzed the data of the three brightest NaI detectors with a viewing angle less than 60° (n3, n4, n7) and both the BGO detectors (b0 and b1). Since it is important to study in detail the possible emergence and evolution of the signature at lower energies of the component detected by MAGIC, I performed a fine time–resolved analysis of the emission of GRB 190114C by selecting TTE data and rebinning them with a time resolution of 0.3 s during the first emission episode of the burst. After the first emission episode, I rebinned the data in progressively larger time bins up to the second minor peak of the light curve (from $\sim$ 15 s to $\sim$ 23 s), that has been analyzed as a single bin. Finally, I analyzed the 23–61 s time interval as two consecutive time bins (23–47 s and 47–61 s). Regarding *Swift* data, we consider BAT data extracted for three time bins, namely 6–6.3 s, 47–61 s and 87–232 s, both as a way to better constrain the parameters of the fit obtained in the same time intervals from GBM data and as a way to extend our analysis to later times. For the XRT data, we excluded all the channels below 1.5 keV since an apparent low-energy excess has been reported in Beardmore 2019. We then re-binned the energy channels using the the *grppha* tool requiring at least 40 counts per bin. The intrinsic column density $7.7 \times 10^{22}\mathrm{cm}^{-2}$ is estimated by fitting the late-time X-ray spectrum ($5.6 \times 10^4 - 5.7 \times 10^5$ s).

In the time-resolved analysis, I fitted the spectra with a smoothly broken power–law (SBPL, see 2.15 for a description of the functional form). As in Ravasio et al. 2019a, the curvature parameter is kept fixed at $n = 2$. To check the possible presence of an extra power–law component (reported in Hamburg, Veres, Meegan, et al. 2019), that could represent the signature of the afterglow component rising in the GBM energy band, in the fitting procedure it was added an extra power–law, with two free parameters, namely the normalization N and the spectral index Γ_{PL}.

6.2.3 Results

Fig. 6.5 shows the results of the time resolved spectral analysis of GBM data. We find that all spectra belonging to the first emission episode (from 0 s to 4.8 s) are reasonably well fitted by a SBPL model without the need of an additional power–law component. The low and high energy spectral indices of the SBPL model are shown in panel (C) of Fig. 6.5 (red and black symbols respectively). Their values are consistent with the typical distributions obtained by the analysis of large samples of GBM bursts (Goldstein et al. 2012; Gruber et al. 2014; Nava et al. 2011b; Kaneko et al. 2006). The peak energy (panel D in Fig. 6.5) evolves tracking the flux of the light curve, with an average value of $E_{\mathrm{peak}} = 510 \pm 170\,\mathrm{keV}$.

The presence of the additional power–law component starts in the 4.8–5.4 s and 5.4–6.0 s time bins, where the superposition of a SBPL and a PL component is preferred over the SBPL component alone (an F-test yields a 6 and 7.5 σ preference for the SBPL+PL model in the first and second bin, respectively).

The power–law component reaches its peak in the time bin 6–6.3 s, with a flux of $1.7 \pm 0.2 \times 10^{-5}\,\mathrm{erg\,cm^{-2}\,s^{-1}}$, integrated in the energy range 10 keV–40 MeV. From 6.3 s onward, the spectrum is well fitted (p-value > 0.3 in all bins) by a single power–law component, with no increase in the goodness of fit when adding the SBPL component. Moreover, when we try to fit with the SBPL function, the peak energy E_{peak} is completely unconstrained, and the values found for the two spectral indices α and β are consistent with each other within the errors. The single power–law spectral slope is shown by the

blue symbols in panel (C) of Fig. 6.5. Its 10 keV – 40 MeV flux is shown by the blue symbols in panel (B).

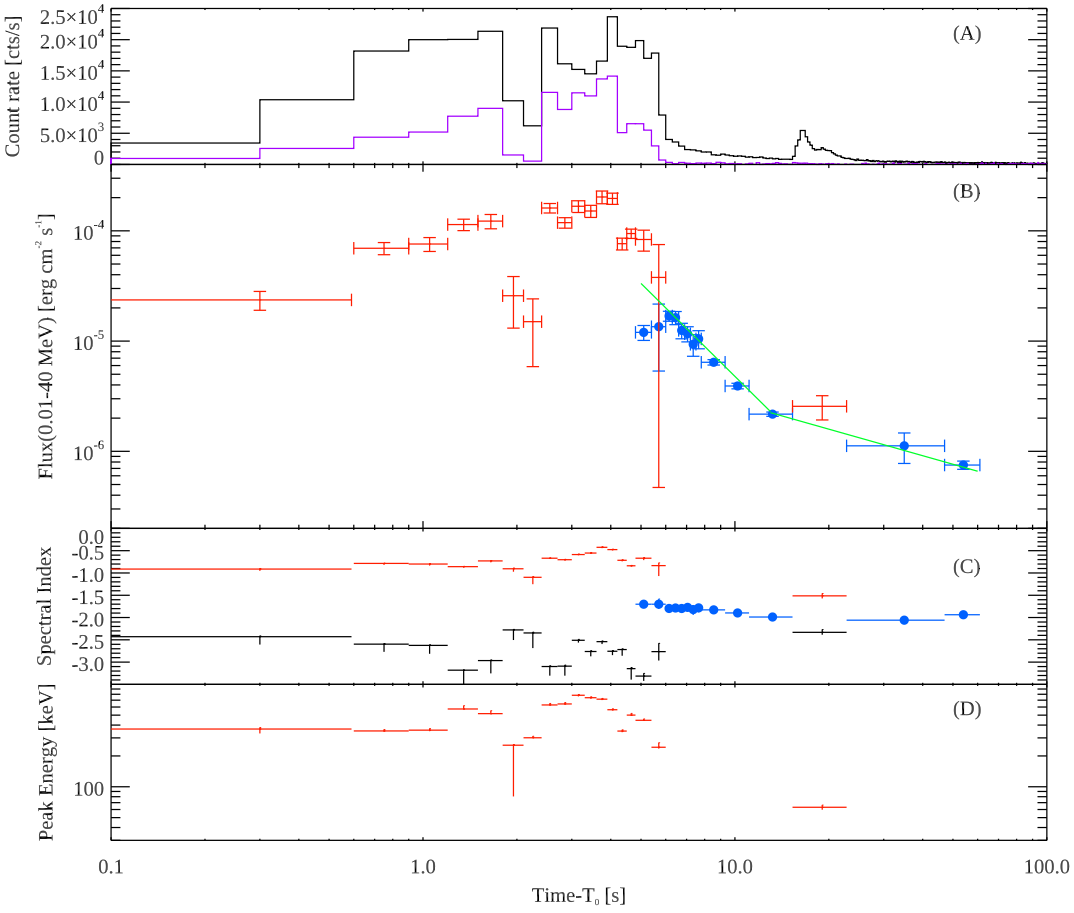

FIGURE 6.5: Spectral evolution of GRB 190114C. Two spectral components are shown: Smoothly broken power–law (SBPL - red symbols) and Power–law (PL - blue circles). 1σ errors are shown. Panel A: count rate light curve (black solid line for GBM NaI detector #3 and purple solid line for GBM BGO detector #0). Panel B: flux (integrated in the 10 keV – 40 MeV energy range) of the two spectral components. The green line is a power–law with slope –2.8 up to 15 seconds, with slope –1 when the decay of the flux is shallower. Panel C shows the temporal evolution of the spectral photon index of the SBPL (red and black symbols) and of the PL (blue symbols). Panel D shows the evolution of the peak energy (E_{peak}) of the SBPL model.

The average spectral slope of the PL component in the time interval 4.8–15.3 s is $\Gamma_{\rm PL} = -1.81 \pm 0.08$, similar to the spectral slope found in the LAT data (at >100 MeV, Kocevski, Omodei, Axelsson, et al. 2019) in the same time interval. After ∼10 seconds the slope of the power–law becomes constant and settles to the –2 value, again similar to the LAT index. The second emission episode is fitted by a SBPL, with $\alpha = -1.51 \pm 0.06$, $\beta = -2.33 \pm 0.06$ and $E_{\rm peak} = 63 \pm 3$ keV. The parameters of the additional power–law are not constrained and the fit does not improve with its inclusion. After 22.8 s, the spectrum is again well fitted by a power–law only, with index $\Gamma_{\rm PL} \sim -2$. The flux of the PL component (panel B of Fig. 6.5) decays steeply from the peak up to 15 seconds (a reference

green line $\propto t^{-2.8}$ is shown). From 15–50 seconds the flux temporal decay is consistent with $t^{-1.0}$.

We also added BAT data for the time intervals 6.0–6.3 s and 11–14 s. In both time bins, BAT+GBM data have been fitted together with a single PL, obtaining best fit parameters which are consistent with the analysis of GBM data only. We also verified that BAT data alone for the first time bin result in power–law parameters which are fully consistent with those derived from the fit of the GBM spectrum alone.

Fig. 6.6 shows the SED of the three time intervals (as labelled). Spectral data used in the fits are BAT+GBM for interval 6–6.3 s and 11–14 s, XRT+BAT+GBM spectra are shown for the last time bin (66–92 s). At the time of the analysis, we could only refer to the paper by Wang et al. (2019) for the analysis of the LAT spectrum of GRB 190114C, whose high energy data have been fitted with a power–law model. Therefore in Fig. 6.6 we show with butterfly symbols the LAT flux and spectral index (including the corresponding uncertainties) for the same time intervals, to be compared with our results.

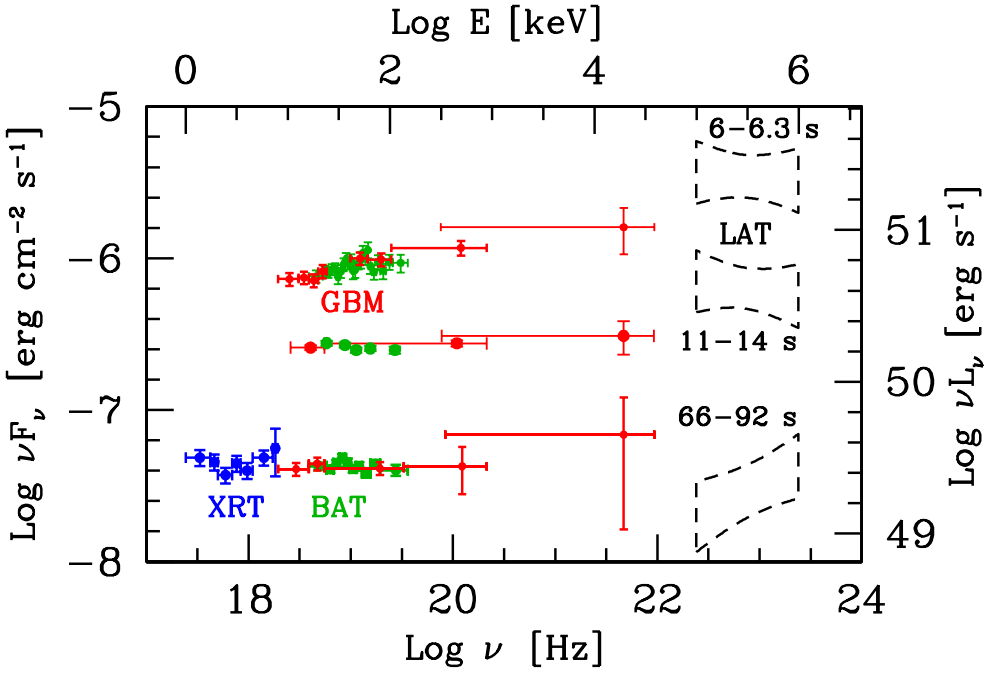

FIGURE 6.6: The X–ray to GeV SED of GRB 190114C at three specific times: at 6-6.3 s, when the power–law component has its peak in the GBM data (see panel (B) of Fig.6.5, blue symbols), at 11–14 s and at 66–92 s (as labelled). We show the GBM, BAT and XRT data (the latter de-absorbed as described in the text). Errors and upper limits on the data points represent 1σ. The LAT butterflies represent the range of fluxes and indices of the power–law reported in analysis of Wang et al. (2019).

Both GBM and BAT data appear to connect to the LAT emission as analyzed by Wang et al. (2019). Regarding the two time intervals, 6–6.3 s and 11–14 s, the photon indices of the LAT spectrum are $\Gamma_{\rm PL} = -2.06 \pm 0.30$ and $\Gamma_{\rm PL} = -2.10 \pm 0.31$ respectively, which are consistent with the values we obtained from our analysis. The LAT emission is slightly above the GBM extrapolation but compatible at less than 2σ. Moreover, we analyzed XRT+BAT+GBM data from 66 s to 92 s, to check again for consistency with the LAT flux and also to track the power–law evolution at later times. As shown in Fig. 6.6, the LAT flux is still consistent with extrapolation of the joint XRT+BAT+GBM data fit. From our analysis, the fit of XRT+BAT+GBM data from 66 s to 92 s with a PL function results in

a spectral slope $\Gamma_{\rm PL} = -2.01 \pm 0.05$, which is only marginally consistent with the LAT spectral slope ($\Gamma_{\rm PL} = -1.67 \pm 0.27$), that is characterized by a large uncertainty.

In summary, Fig. 6.6 shows that the keV-MeV and GeV emissions have similar time decay and similar slopes, suggesting that they belong to the same component. However, due to the uncertainties on the LAT spectral parameters, it cannot be excluded the possibility that the GeV and keV-MeV data belong to two different components.

6.2.4 Estimate of Γ

We followed the formula reported in Eq. 6.2 in the previous Section (derived in Nava et al. 2013) for the estimate of the bulk Lorentz factor of the jet during the coasting phase, using the afteglow onset time. Taking $E_{\rm iso} = 2.6 \times 10^{53}$ erg calculated from 0 to 6 s, $\eta = 0.2$, $t_{\rm p} = 6$ s, we estimate: $\Gamma \sim 700 \pm 26$ (resp. 520 ± 20) in the case of a homogeneous medium with density $n = 1$ cm^{-3} (resp. $n = 10$ cm^{-3}). For a wind medium with $\dot{M}_{\rm w} = 10^{-5} M_{\odot}$/yr and $v_{\rm w} = 10^3$ km/s (resp. $v_{\rm w} = 10^2$ km/s), following the relation $n_0 = \dot{M}_{\rm w}/4\pi v_{\rm w} m_p$, the initial bulk Lorentz factor is $\Gamma \sim 230 \pm 6$ (resp. 130 ± 3). The errors are only statistical and are calculated using the uncertainties on the observables $E_{\rm iso}$ and $t_{\rm p}$; the errors do not include the unknown uncertainties on the η and n_0 parameters.

The computed values are similar to those found for other GRBs detected by LAT which show a peak in the light curve in the LAT energy band (Ghirlanda et al., 2018).

6.2.5 Discussion and conclusion

Our results demonstrate the presence, in the GBM data, of a power–law component appearing at $\sim$ 4 s after trigger, peaking at 6 s, and then declining. This temporal behaviour matches that of the flux above 100 MeV, as seen by the analysis of the LAT data available at the time of the work. Fig. 6.3 shows that the emission in the two detectors (GBM and LAT) joins smoothly, with a consistent slope (within the errors). It is therefore compelling to interpret the two power–laws seen in LAT and GBM as belonging to a single emission component. We propose this non-thermal emission to be produced by the external shock driven by the jet into the circum-burst medium, with its peak marking the jet deceleration time, i.e. onset time of the afterglow. The reasons leading to this interpretation are: i) this component appears after the trigger of the prompt event, and peak when most of the prompt emission energy has already been radiated; ii) it lasts much longer than the prompt emission; iii) it is characterized by a spectral index ($\Gamma_{\rm PL} \sim -2$) typical of the known afterglows; iv) with the exception of the early, variable phase, its light curve is smoothly decaying with a temporal slope typical of the known afterglows. Therefore, thanks to the fine (0.3 s) time–resolved analysis of the keV-MeV data during the first $\sim$15 s of the bursts, we were able to follow the transition from the prompt to the afterglow phase.

A similar *Fermi-Swift* data joint spectral analysis has been performed by the *Fermi* and *Swift* Collaborations (Ajello et al., 2020). Analyzing the first $\sim$25 seconds of the emission detected by both instruments, they found the emergence of a power–law component, superimposed to the non-thermal component, fitted by Band, visible in the first $\sim$2 seconds after the trigger time. They interpreted the non-thermal and the power–law components as the prompt and the afterglow emissions of the burst, respectively, which is consistent with our results. Moreover, thanks to the addition of the LAT data up to $\sim$1 GeV in the first time intervals, they also found the presence of an exponential attenuation of the power–law component, modelled with a cutoff energy $E_{\rm cutoff}$ ranging between $\sim$

50 MeV and $\sim$ 140 MeV. This cutoff energy is observed to increase with time, until it disappear completely at $\sim$15 seconds. They attributed this spectral turnover to the opacity to electron-positron pair production within the source. Under the assumption that the cutoff energy is indeed the results of $\gamma\gamma$ annihilation, they derived the estimate of the bulk Lorentz factor $\Gamma \sim 210$. However, this estimate is based on an unusual assumption. In fact, the bulk Lorentz factor depends on the cutoff energy, on the variability timescale, on the luminosity and the power–law index of the spectrum, as shown by their Equation 1. The value of the variability timescale of $\sim$ 6 ms used in the formula is motivated by the assumption that the GBM and the LAT emissions are cospatial, implying that the afterglow component is cospatial with the prompt, which is not the standard scenario. Despite being derived with different methods and assumptions, their Γ value is consistent with the range of values derived from our analysis corresponding to the wind-like medium case ($\Gamma \sim$ 130-230). As highlighted both by the MAGIC and *Fermi* Collaborations (MAGIC Collaboration et al., 2019a; Ajello et al., 2020), a wind-like medium can explain the steepening observed in the X-ray lightcurve, which is instead not expected in a homogeneous medium. The MAGIC Collaboration reported a bulk Lorentz factor of about 140-160 at 100 s after trigger time.

We remark that this is not the first time that a power–law is necessary to model the hard X-rays, in addition to the spectral components usually seen during the prompt emission phase. In fact, such a component was well visible in GRB 090202B, another burst which was bright in the LAT band (Rao et al. 2013 and references above). What is new is the observation of the onset of the afterglow in the hard X-ray band, found to be simultaneous, within the uncertainties, to the peak of the LAT light-curve. Our results imply that emission in the energy range between 10 keV and 30 GeV is produced by a single mechanism, at least in the time interval analyzed (up to $\sim$90 s).

This is especially important in this burst, in light if the MAGIC detection. Indeed, the MAGIC flux and spectrum provided crucial information about the origin of the entire high energy spectrum of GRB 190114C. As shown in Fig. 3 in MAGIC Collaboration et al. 2019a (see Fig. 1.9 in Chapter 1), in the time interval 68–110 s the emission from the XRT up to the LAT energy range is dominated by a single component, consistent with the synchrotron emission, while at higher energies the MAGIC flux shows a spectral hardening, implying a separate spectral component. This component is consistent with the synchrotron self-Compton (SSC) emission. In the subsequent time interval, 110–180 s, the SSC component becomes more evident also in the LAT data. The afterglow parameters inferred from the synchrotron+SSC modelling reported in MAGIC Collaboration et al. 2019a are consistent with the ones typically inferred from broadband studies of GRB afterglow emission. This suggests that SSC emission in GRBs may be a relatively common process that does not require special conditions to be produced. In both time intervals, the powers of the synchrotron and SSC components are comparable, suggesting that a meaningful fraction of the total afterglow energy has been missed in GRBs studies so far.

6.3 GRB 190829A

Nearly 8 months after the first high-significance detection, another GRB has been observed at very high energies: GRB 190829A (de Naurois and H. E. S. S. Collaboration, 2019; HESS collaboration, Abdalla, et al., 2021). Besides the VHE detection, this burst shows other interesting peculiarities: it yields a small isotropic luminosity ($L_{\rm iso} \sim 10^{49}$ erg/s), demonstrating that also faint GRBs can produce VHE photons, and it is one of the closest GRB detected so far ($z = 0.0785$, ~ 370 Mpc). Its proximity offer us the unique opportunity to study in detail its radio emission, possibly allowing to measure the superluminal motion and/or the size of the radio image of the outflow. Moreover, the VHE detection has triggered an intensive multi-wavelength observational campaign, providing a rich dataset of observations covering all the electromagnetic spectrum and the time evolution of the emission components. This allows to test in detail the predictions of the GRB standard afterglow model, and to obtain insights into the physical properties of a TeV-emitting burst (e.g. the kinetic energy of the jet, its orientation, the progenitor environment, and the emission mechanisms).

We monitored the position of the radio counterpart of GRB 190829A, through very long baseline interferometry (VLBI) observations with the European VLBI Network (EVN) and the Very Long Baseline Array (VLBA), involving a total of 30 telescopes across four continents. After GRB 030329, this is the second long GRB for which high resolution radio images allow to partially resolve its size and track its superluminal evolution. These observations provided an independent constraint on the kinetic energy of the jet and the density of the ambient medium, which are key parameters for the interpretation of the origin of the very TeV emission. These measurements are in remarkable agreement with the detailed modeling of the multi-wavelength (from radio to TeV) afterglow emission with a forward plus reverse shock model, which includes the standard synchrotron emission and the SSC component (distinctly observed so far only in GRB 190114C). The wide coverage and high cadence of the observations allowed us to break many degeneracies that are inherent to afterglow model parameters, obtaining interesting constraints on shock micro-physics.

Within this work, I have analyzed the wealth of X-ray (0.3-10 keV) data collected by the instrument XRT. The results of my analysis was complemented including public optical and radio VLBI observations, with the aim of studying the spectral energy distribution of the source, especially at the times of the TeV observations. Moreover, I analyzed the γ–ray prompt emission detected by *Fermi*/GBM. Applying the compactness argument to the low-luminosity and low-peak energy spectrum, I constrained the angle from which we could have observed the GRB, setting a more stringent limit than the one derived from the radio observations of the source position.

In this Section I will describe the main results of our analysis. A more comprehensive description of the work, including the details of the radio data analysis and of the afterglow modeling, can be found in Salafia, Ravasio et al. 2021, submitted to Nature Astronomy.

6.3.1 Observational properties of GRB 190829A

GRB 190829A is a long GRB detected by *Fermi*/GBM on 2019 August 29 at 19:55:53 UT (Fermi GBM Team, 2019) and shortly thereafter by *Swift*/BAT (Dichiara et al., 2019). Compared to the other two previous GRBs detect at VHE (GRB 180720B, Abdalla et al. 2019 and GRB 190114C, MAGIC Collaboration et al. 2019b), it features an isotropic-equivalent energy three orders of magnitude smaller $E_{\rm iso} \sim 3 \times 10^{50}$ erg (Tsvetkova et al., 2019).

The redshift of the host galaxy (Valeev et al., 2019) $z = 0.0785$ (which corresponds to a distance of approximately 368 Mpc, adopting Planck cosmological parameters, Planck Collaboration 2016) makes this event one of the closest long GRBs known so far.

The afterglow emission of GRB 190829A has been monitored up to several months after the burst: after an initial peak and a fading phase, a re-brightening in the optical light curve at ∼5 days was attributed to the associated supernova emission (confirmed by the spectroscopic observations of the 10.4m Gran Telescopio Canarias (GTC) telescope Hu et al. 2020). Radio afterglow emission was first detected by the Australia Telescope Compact Array (ATCA) at 5.5 GHz (Laskar et al., 2019) and then by the Northern Extended Millimeter Array (NOEMA) at 90 GHz (de Ugarte Postigo et al., 2019), 20.2 hours and 29.48 hours after the burst, respectively. Subsequent high-cadence radio observations were performed with the Meer Karoo Array Telescope (MeerKAT) at 1.3 GHz and Arcminute Microkelvin Imager–Large Array (AMI-LA) at 15.5 GHz, reporting a fading radio source up to 143 days after the initial gamma-ray emission (Rhodes et al., 2020).

We constructed an extensive GRB 190829A afterglow dataset, shown in Fig. 6.7, combining publicly available data (marked with circles), the results of our VLBI flux density measurements (marked with stars).

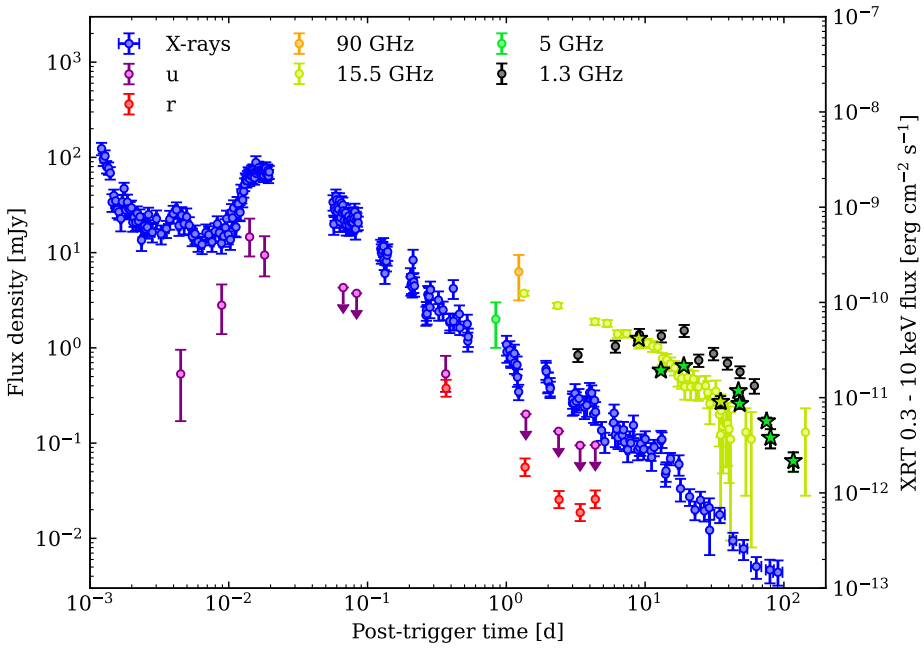

FIGURE 6.7: This plot shows the multi-wavelength afterglow lightcurve of GRB 190829A. Circles represent X-ray fluxes (blue, values shown on the right-hand axis) or flux densities (all other colours, values shown on the left-hand axis) measured at the position of GRB 190829A at different times after the GRB trigger in several bands (see the legend). Optical flux densities have been corrected for both the Milky Way and host galaxy extinction, and the contribution of the host galaxy has been subtracted. The host galaxy contribution (Rhodes et al., 2020) has also been subtracted from AMI-LA radio flux densities at 15.5 GHz. Stars mark the flux densities measured in our VLBI epochs.

In the following sections I describe the procedures and results of the analysis of the X–ray and γ–ray data (XRT and GBM respectively) which I have been in charge of within this collaboration work. I invite the reader to look to the paper on arXiv for details of the radio and optical data shown in Fig. 6.7, from our VLBI campaign and from public UVOT data.

6.3.1.1 *Swift*/XRT data analysis and results

In order to build the SEDs at the times of the H.E.S.S. observations, shown in Fig. 6.12, and check our model predictions, I retrieved the XRT spectral files from the *Swift*/XRT online archive [4] and analysed them with the public software XSPEC (v. 12.10.1f). The `tbabs` model for the Galactic absorption (using $N_{\rm H} = 0.056 \times 10^{22}$ cm^{-2}, Kalberla et al. 2005), and the `ztbabs` model for the host galaxy absorption, adopting the source redshift $z = 0.0785$, were used in the fitting procedure. The intrinsic $N_{\rm H}$ was fixed to the value obtained from the time resolved analysis of late XRT data. Indeed, in the 0.3–10 keV energy range, the fitted values of $N_{\rm H}$ and of the spectral index are closely correlated: a larger value of $N_{\rm H}$ allows for a softer spectrum, and *vice versa*, so that the net result of their combination is consistent with the observed spectrum. As a consequence, the intrinsic variations in the spectral index can be misinterpreted as variations of $N_{\rm H}$ when both these parameters are free to vary. Since no $N_{\rm H}$ variation is expected at the times analysed, I performed a time-resolved spectral analysis of the XRT data up to 10^7 s after the BAT trigger by leaving both the host $N_{\rm H}$ and the photon index free. I found that, at late times (from 2.8×10^4 s onward), the $N_{\rm H}$ parameter does not evolve and remains constant around $N_{\rm H} = 1.16 \times 10^{22}$ cm^{-2}. I therefore fitted the XRT spectra shown in Fig. 6.12 assuming the above mentioned value of the intrinsic $N_{\rm H}$ and leaving as free parameters the normalisation (at 1 keV) and the spectral index of the power law. The results of the spectral analysis of the XRT data are reported in Table 6.2. As shown in Fig. 6.12, in both intervals the XRT data are described by a quite flat power–law (photon index $\sim$-2). The results of this spectral analysis are consistent with those previously published in the literature for similar integration times (HESS collaboration, Abdalla, et al., 2021).

TABLE 6.2: Best fit parameters of the XRT data spectral analysis for the two SEDs epochs coincident with H.E.S.S. observations, as reported in Fig. 6.12.

Time interval (h)	Norm (10^{-2} ph/ s cm^2 keV)	Photon index	C-Stat/DOF
$[4.89 - 7.85]$	$1.60^{+0.11}_{-0.07}$	$-2.01^{+0.04}_{-0.05}$	398/420
$[29.02 - 29.16]$	$0.38^{+0.11}_{-0.09}$	$-2.10^{+0.23}_{-0.28}$	43.5/280

6.3.1.2 *Fermi*/GBM data analysis and results

The upper panel of Fig.6.8 shows the prompt emission lightcurve of GRB 190829A, characterized by the presence of two emission episodes (I refer hereafter to these as Episode I and Episode II, respectively), separated by $\sim$50 sec.

[4] https://www.swift.ac.uk/xrt_spectra

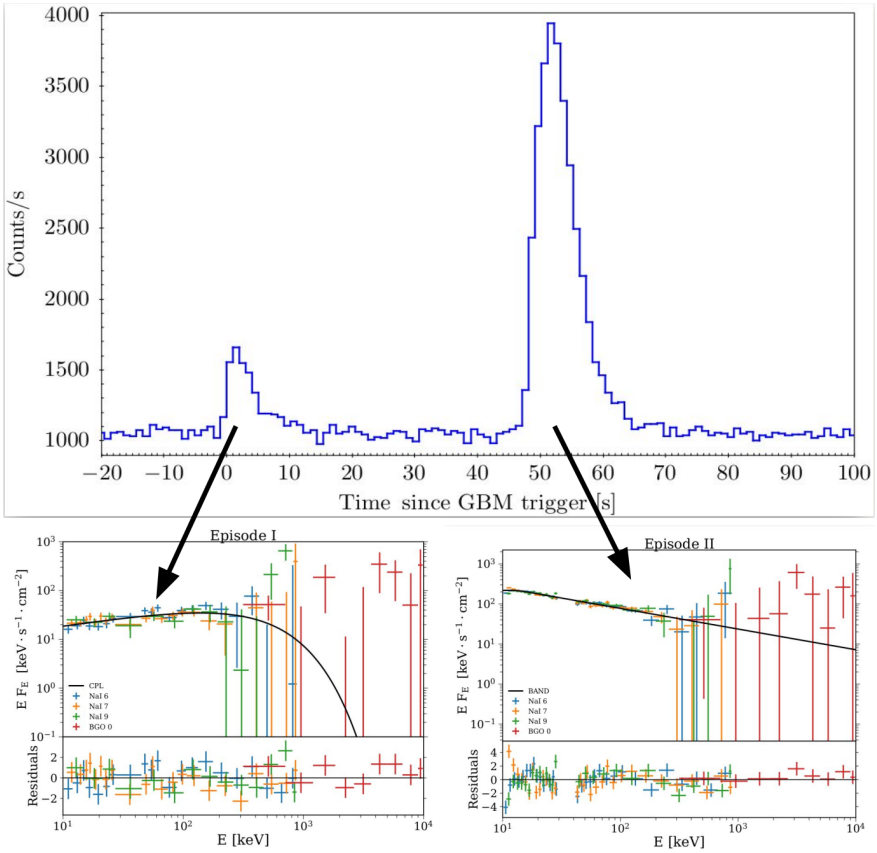

FIGURE 6.8: The top panel shows the prompt emission lightcurve of GRB 190829A detected in the energy range 10-900 keV (NaI detector #6, not background–subtracted), where the two emission episodes, Episode I and Episode II, are clearly visible. The bottom panel shows the data of the spectrum for each episode of the lightcurve in the νF_ν representation, together with the best–fitting model and the residuals. Data have been rebinned for graphical purposes.

I analyzed the spectra of the two prompt emission episodes detected by *Fermi*/GBM, using the data of the three most illuminated NaI detectors with a viewing angle smaller than 60° (n6, n7, and n9) and the most illuminated BGO detector (b1). Spectra were extracted using the public software GTBURST and analyzed with XSPEC (v. 12.10.1f). PG-Statistic, valid for Poisson data with a Gaussian background, is used in the fitting procedure.

For Episode I, I performed a time-integrated analysis from -1.79 to 10.5 seconds after GBM trigger and fitted the spectra with two models, namely the CPL and the Band function (defined in Chap. 1). I compared the models based on the AIC values (Akaike, 1974), finding that both fit the spectra equally well ($\Delta\text{AIC} \leq 3$), but the β parameter in the Band function fit has large uncertainties. I therefore considered the CPL as the best-fitting model of Episode I (see bottom panel in Fig. 6.8), with best-fitting parameters: $\alpha = -1.63^{+0.09}_{-0.08}$, $E_c = 380^{+318}_{-134}$ keV and $F = 1.98^{+0.07}_{-0.58} \times 10^{-7}\,\mathrm{erg\,cm^{-2}\,s^{-1}}$, where α is the low-energy spectral index and E_c is the scale energy of the spectral cutoff, and F is the flux integrated in the energy range 10 keV – 10 MeV. With this parameters, the peak of the νF_ν spectrum is at $E_{\mathrm{peak}} = 139.7^{+57.1}_{-21.3}$ keV and the isotropic equivalent energy is $E_{\mathrm{iso}} = 1.02^{+0.10}_{-0.12} \times 10^{49}$ erg.

For Episode II, I performed a time-integrated analysis in the interval 47.04 – 62.46 s

with the same approach. The best-fitting model in this case is the Band function (see bottom panel in Fig. 6.8) with $\alpha = -0.602^{+0.002}_{-0.358}$, $E_{\rm peak} = 11.30^{+0.39}_{-0.90}$ keV, $\beta = -2.52^{+0.01}_{-0.02}$ and $F = 7.56^{+0.12}_{-0.11} \times 10^{-7}$ erg cm^{-2} s^{-1}, where $E_{\rm p}$ is the peak photon energy of the $dF/dlog(E)$ spectrum, α and β are the low-energy and high-energy spectral indices, respectively. Despite the value of the peak energy is very close to the low-energy threshold of the GBM detectors (8 keV), the value of the low-energy photon index α is quite well constrained. This could be due to the fact that there is a correlation between the peak energy and the photon index α, that is visible in the combined posterior distribution of the two parameters: the larger is the peak energy, the harder is α. This reflects also in the error range of the α parameter: the negative error is much greater than the positive one. Indeed, α cannot assume too hard values, as it would imply larger values of the peak energy, which would be inconsistent with the data. Conversely, since the peak energy cannot be constrained to values below 8 keV, the photon index α cannot assume too soft values. Therefore, the constraints on the position of $E_{\rm peak}$ influences the value of the low-energy photon index parameter α. Taking the best-fit parameters obtained for the second Episode, the isotropic equivalent energy is $E_{\rm iso} = 2.81^{+0.17}_{-0.15} \times 10^{50}$ erg.

The results of the spectral analysis of the prompt emission are consistent with those previously published in literature (Lesage et al., 2019; Hu et al., 2020; Fraija et al., 2020; Chand et al., 2020).

6.3.2 Results of the radio observations

We carried out a total of 9 VLBI observations of GRB 190829A between 9 and 117 days after the GRB, with the Very Long Baseline Array (VLBA) at 5 and 15 GHz and the European VLBI Network (EVN) alongside the enhanced Multi-Element Remotely Linked Interferometer Network (e-MERLIN) at 5 GHz, reaching an overall excellent resolution.

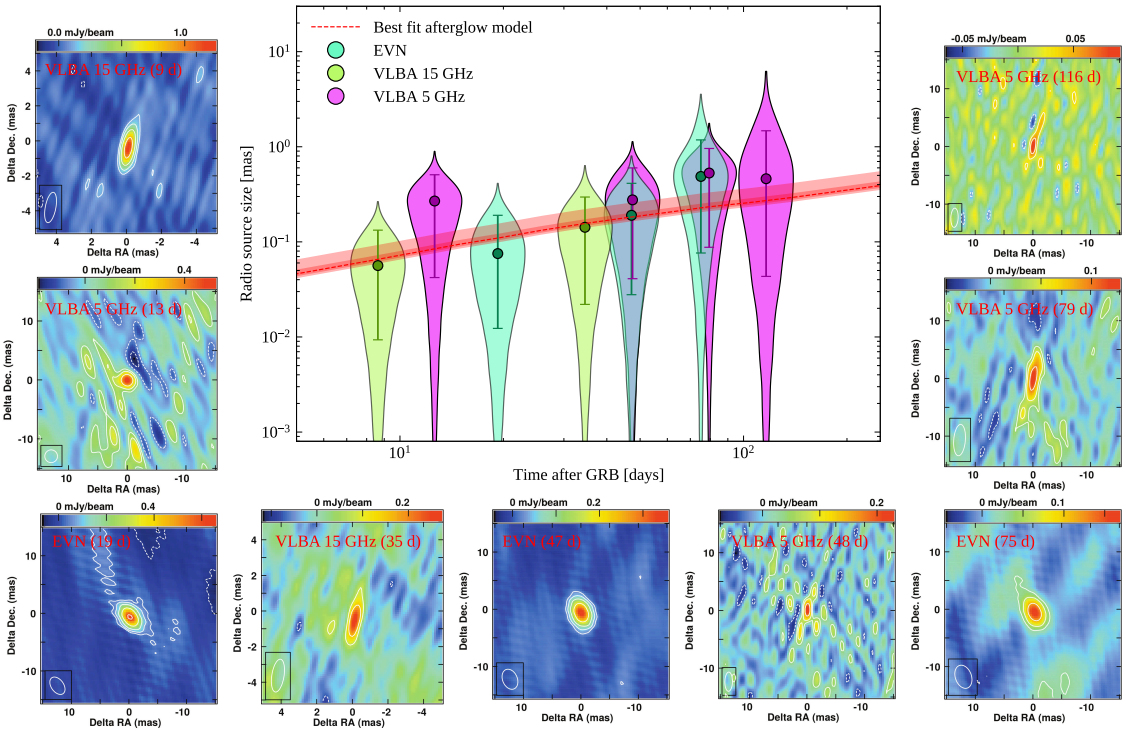

FIGURE 6.9: This plot shows the source size evolution and the comparison with the model. Central panel: circles with error bars show the measured size of the source at each epoch and its one-sigma uncertainty. For each epoch, the 'violin' shape shows the posterior probability density distribution of the logarithm of the source size. The red dashed line shows the source size evolution as predicted by our afterglow model with the best-fit parameters, while the shaded bands show the 50% and 90% confidence intervals. The remaining smaller panels show previews of the cleaned radio maps for each epoch (full-size maps are given in the Methods section).

By fitting a circular Gaussian source model to these data through a MCMC approach, we obtained the source size estimates shown in Figure 6.9. While the large uncertainties prevent us from making a statistically significant assessment of the superluminal expansion of the source, the data show a trend towards an increasing size, and the evolution is compatible with the $s \propto t^{5/8}$ scaling expected (Granot, Piran, and Sari, 1999) for the observed size s of a relativistic blastwave whose expansion is described by the self-similar Blandford-McKee solution (Blandford and McKee, 1976). Assuming this to be the case, we obtained an essentially model-independent estimate of the ratio between the blastwave energy E_k and the number density n of the surrounding ambient medium, for each epoch. In particular, the ratio E_k/n sets the fundamental length scale of the expansion, namely the Sedov length (Blandford and McKee, 1976) $\ell_S = (3E_k/4\pi n m_p c^2)^{1/3}$, where m_p is the proton mass and c is the speed of light. Since $s \propto \ell_S^{3/8} t^{5/8}$, we have that $E_k/n \propto \ell_S^3 \propto s^8 t^{-5}$. For each epoch of observation, we obtained posterior probability density of the ratio E_k/n, which are represented with the turquoise, green and fucsia lines in Fig. 6.10. After combining all measurements, we obtained a narrower posterior probability density which peaks at $\log[(E_k/n)/\mathrm{erg\,cm^3}] = 54.0^{+1.0}_{-1.4}$, represented by the red solid line in Fig. 6.10. The dashed blue line comes instead from the results of the afterglow modeling, which I described in the following section.

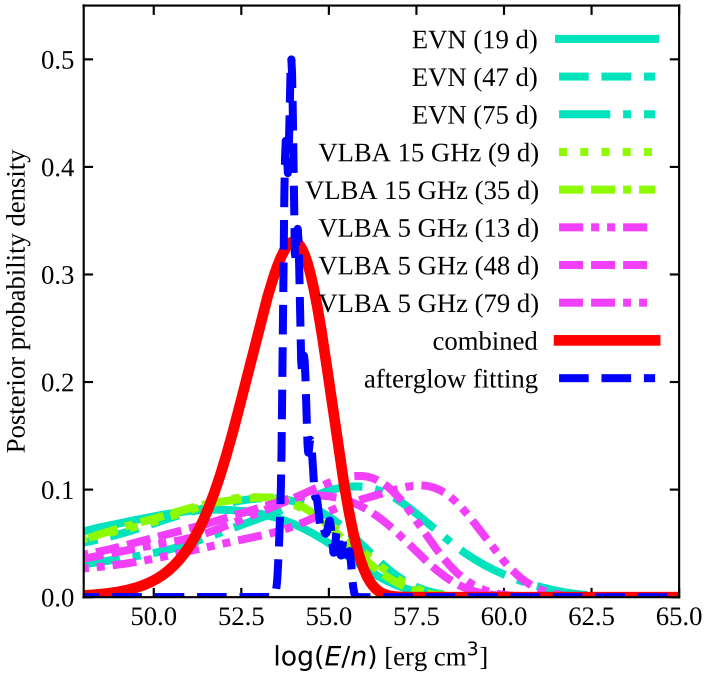

FIGURE 6.10: This plot shows the constraint on the energy-to-density ratio, derived from independent observations of GRB 190829A. Turquoise, green and fucsia lines show the posterior probability density distributions of $\log(E_k/n)$ obtained from the source size measurements in our VLBI imaging epochs assuming the source to be a relativistic shock in self-similar expansion (Blandford and McKee, 1976; Granot, Piran, and Sari, 1999). The red solid line is the combined posterior probability density. The blue dashed line shows the posterior probability density of the same quantity obtained from fitting our forward plus reverse shock afterglow emission model to the available multi-wavelength data.

6.3.3 Results of the multi-wavelength afterglow modeling

In order to test the result obtained from the radio observations and to get a deeper physical insight on this source, we performed a self-consistent modelling of all the available multi-wavelength observations of the afterglow. We included both the forward and reverse shock emission in our model, computing the shock dynamics self-consistently from deceleration down to the late side expansion phase. We computed the radiation in the shock downstream comoving frame including the effects of inverse Compton scattering on electron cooling (accounting for the Klein-Nishina suppression of the cross section above the relevant photon energy). We assumed a fixed fraction ϵ_e of the available energy density to be in relativistic electrons, which we assumed to be a fraction χ_e of the total electrons and to be injected with a power law energy distribution with index $p > 2$, and a fraction ϵ_B to be in the form of an effectively isotropic magnetic field. To compute the observed emission, we integrated over equal-arrival-time surfaces, accounting for relativistic beaming.

Figure 6.11 shows the GRB 190829A afterglow light curves in the X-ray, optical and radio bands combined with our modeling. Solid lines represent the predictions of our best-fit afterglow model, where the dashed lines show the contribution from the reverse

shock, while the solid lines also include the forward shock, which dominates the emission at all wavelengths from around one day onwards.

Figure 6.12 shows the predicted spectral energy distributions at 5 h (blue) and 30 h (red) after the GRB, which agree with the emission detected (de Naurois and H. E. S. S. Collaboration, 2019; HESS collaboration, Abdalla, et al., 2021) by H.E.S.S. (circles with error bars, corrected for extragalactic background light absorption (Domínguez et al., 2011), and 'butterflies' that show the one-sigma uncertainties when assuming a power law spectral shape). In our interpretation, therefore, the H.E.S.S. emission is synchrotron-Self Compton from the forward shock. Differently from the H.E.S.S. Collaboration (HESS collaboration, Abdalla, et al., 2021), we do not find significant photon-photon absorption, at least for our model parameters.

From this modelling, we obtain $\log[(E_{\rm k}/n)/{\rm erg\,cm^3}] = 53.9^{+0.4}_{-0.2}$ (see the blue dashed line in Fig. 6.10), in excellent agreement with the estimate from the VLBI size measurements. The good match can also be appreciated from Fig. 6.9, where the source size evolution entailed by the afterglow emission model (red dashed line) is compared with our source size measurements. We interpret this as a success of the standard GRB afterglow model, confirming our general understanding of these sources, but we stress that in order to obtain these results we had to include a number of often overlooked (even though widely agreed upon in most cases) elements in the model.

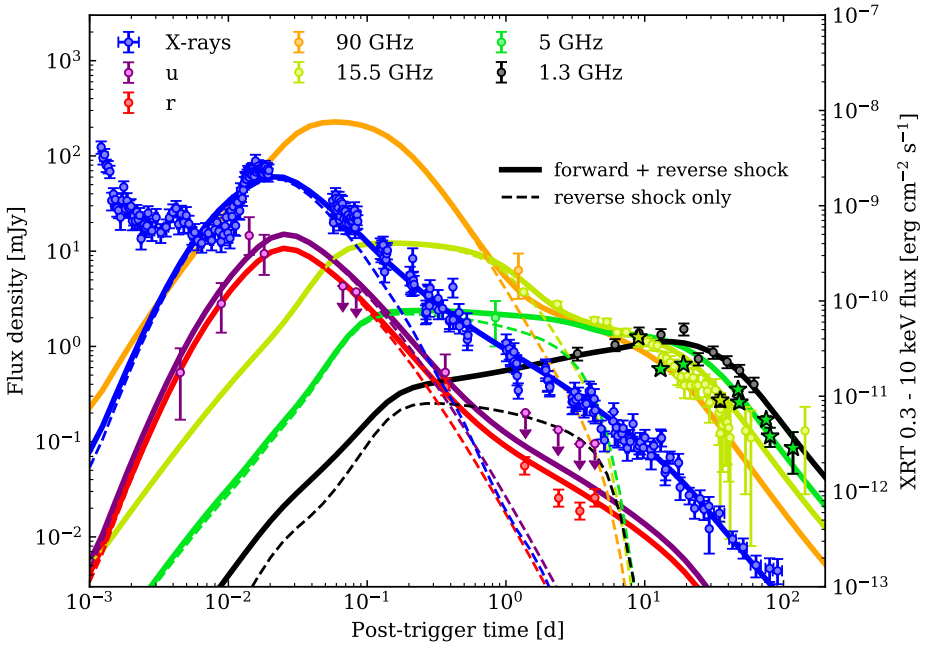

FIGURE 6.11: This plot shows the multi-wavelength afterglow lightcurve together with the emission model. Circles represent X-ray fluxes (blue, values shown on the right-hand axis) or flux densities (all other colours, values shown on the left-hand axis) measured at the position of GRB 190829A at different times after the GRB trigger in several bands (see the legend). Optical flux densities have been corrected for both the Milky Way and host galaxy extinction, and the contribution of the host galaxy has been subtracted. The host galaxy contribution (Rhodes et al., 2020) has also been subtracted from AMI-LA radio flux densities at 15.5 GHz. Stars mark the flux densities measured in our VLBI epochs. Solid lines of the corresponding colours show the predictions of our emission model including both the forward and reverse shocks. Dashed lines single out the contribution of the reverse shock emission. We interpret the initial plateau in the X-ray data as the superposition of the prompt emission tail and the rising reverse shock emission.

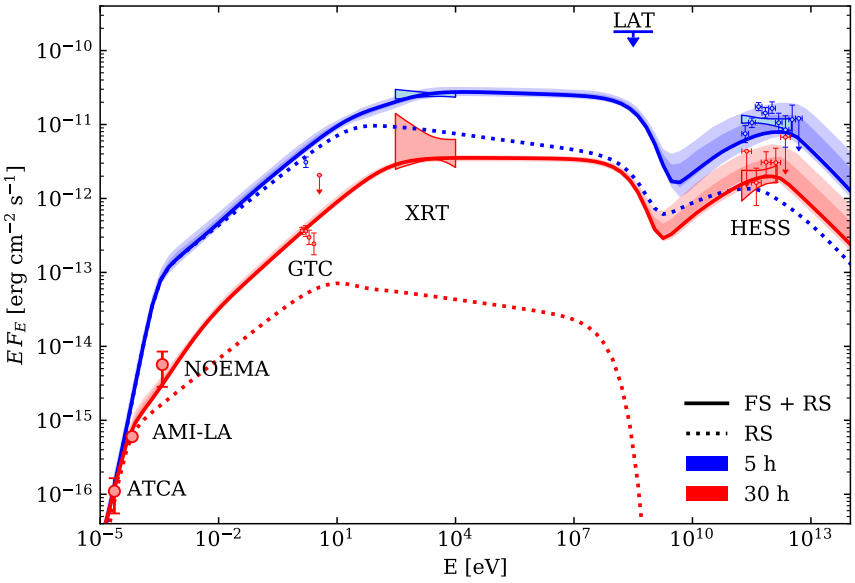

FIGURE 6.12: Spectral energy distributions at the times of the H.E.S.S. detections. We show with blue (resp. red) solid lines our model at 5 hours (resp. 30 hours) after the gamma-ray trigger, with 90% and 50% confidence bands in lighter shades. The H.E.S.S. datapoints HESS collaboration, Abdalla, et al. 2021 (corrected for extragalactic background light absorption, Domínguez et al. 2011) are shown by circles with error bars in the upper right of the plot, together with the corresponding 'butterflies' HESS collaboration, Abdalla, et al. 2021. We also show XRT butterflies at the corresponding times, plus GTC optical and NOEMA, ATCA and AMI-LA radio datapoints taken at observing times lying within 0.2 dex.

The results of our afterglow model fitting provided some rather unique insights on the physics of GRBs and of the forward and reverse shocks that form as the jet expands into the interstellar medium. Remarkably, we found that the usual simplifying assumption $\chi_e = 1$ in the forward shock is excluded: we were unable to find a statistically acceptable solution when assuming all electrons in the shock downstream to be accelerated to relativistic speeds, and we had $\chi_e < 0.05$ at 90% confidence when adopting a wide prior $-10 < \log(\chi_e) < 0$. On the other hand, with such a wide prior we found our uncertainty on the total (collimation-corrected, two-sided) jet kinetic energy to extend towards unrealistically large values $E_{\rm jet} \gtrsim 10^{53}$ erg, corresponding to very small fractions of accelerated electrons $\chi_e \lesssim 10^{-3}$. When adopting a tighter prior $-2 < \log(\chi_e) < 0$, motivated by particle-in-cell simulations of relativistic collisionless shocks (which typically find χ_e to be around a few per cent (Spitkovsky, 2008; Sironi and Spitkovsky, 2011)), we obtained the same best fit, but the unrealistic-energy tails were removed. In the following, we report the results for this latter prior choice (we report one-sigma confidence intervals unless otherwise stated). The jet isotropic-equivalent kinetic energy at the onset of the afterglow is $E_{\rm k} = 2.2^{+2.4}_{-1.1} \times 10^{53}$ erg and the jet half-opening angle is $\theta_{\rm jet} = 15 \pm 2$ degrees, implying a total jet energy $E_{\rm jet} = 7.6^{+0.9}_{-0.4} \times 10^{51}$ erg, which is about one half of the energy in the associated supernova (Hu et al., 2020). Given the observed gamma-ray isotropic equivalent energy $E_{\rm iso} = (2.91 \pm 0.18) \times 10^{50}$ erg, the implied gamma-ray efficiency is $\eta_\gamma = E_{\rm iso}/(E_{\rm iso} + E_{\rm k}) = 1.3^{+1.5}_{-0.7} \times 10^{-3}$. This efficiency is much lower than typical estimates for other GRBs in the literature (Fan and Piran, 2006; Zhang et al., 2007;

Wygoda et al., 2016; Beniamini, Nava, and Piran, 2016). We attribute this to the inclusion of the χ_e parameter and of Klein-Nishina effects in the treatment of electron cooling due to synchrotron self-Compton. The prompt emission efficiency we find is compatible with that expected in the case of internal shocks within the jet (Rees and Meszaros, 1994b) with a moderate Lorentz factor contrast (Kumar, 1999).

The jet bulk Lorentz factor before the onset of the deceleration is $\Gamma = 58 \pm 7$. Considering the isotropic-equivalent radiated energy $E_{\rm iso} \sim 3 \times 10^{50}$ erg, this is in agreement with the $\Gamma - E_{\rm iso}$ correlation found for long GRBs (Ghirlanda et al., 2018) (see Fig. 6.13).

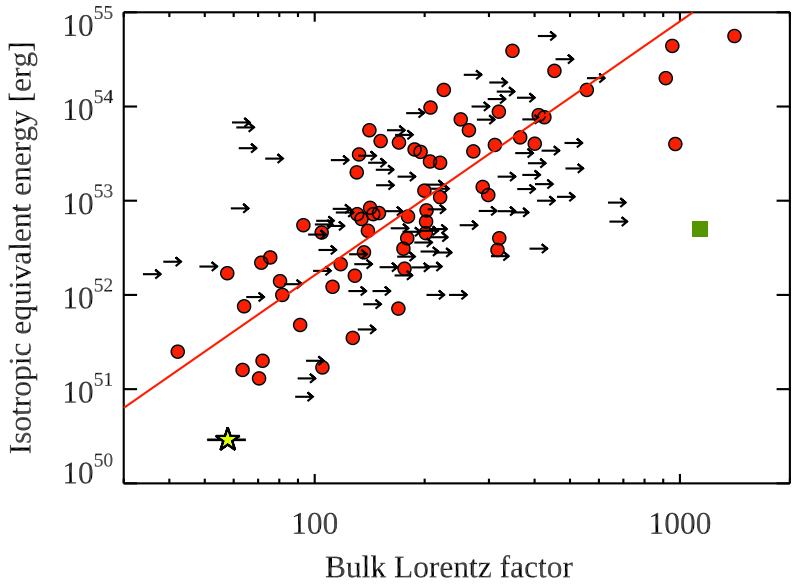

FIGURE 6.13: Correlation between the gamma-ray isotropic equivalent energy and the bulk Lorentz factor for 67 long GRBs (red symbols) and one short GRB (green square). GRB 190829A is shown by the yellow star symbol. Lower limits on Γ are also shown (black rightward arrows). Data are from Ghirlanda et al. 2018. The solid line shows the power law that best fits the red points.

The external medium number density (assumed constant) is relatively low $n = 1.7^{+3.5}_{-1.1} \times 10^{-1}\,{\rm cm}^{-3}$. This could be tentatively explained by the large offset of the GRB location with respect to the host galaxy centre. Indeed, using the GRB coordinates derived from our VLBI observations and the host galaxy centre position from the 2MASS catalogue (Skrutskie et al., 2006), we measure a separation of 9.6 arcseconds, corresponding to a physical projected separation of 14.7 kiloparsec. This is comparable to the largest previously measured offset in long GRBs (Blanchard, Berger, and Fong, 2016) (that of GRB 080928), placing it in the underdense outskirts of its host galaxy. On the other hand, even though the surrounding interstellar medium density may be low, the associated supernova indicates that the progenitor must have been a massive star, which should have polluted the environment with its stellar wind. By contrast, the steep increase in the flux density preceding the light curve peak as seen in the optical and X-rays is inconsistent with a wind-like external medium, which would result in a much shallower rise (Kobayashi and Zhang, 2003). This places stringent constraints on the properties of the pre-supernova stellar wind, whose termination shock radius (van Marle et al., 2006) must be smaller than the nominal deceleration radius in the progenitor wind

$R_{\rm dec,w} = E_{\rm k}/4\pi A m_{\rm p}\Gamma^2 c^2$, where $m_{\rm p}$ is the proton mass, c is the speed of light. The parameter A sets the stellar wind density, and can be expressed as a function of the wind mass loss rate $\dot{M}_{\rm w}$ and velocity $v_{\rm w}$ as $A = 3\times10^{35}\dot{M}_{\rm w,-5}v_{\rm w,3} \equiv 3\times10^{35}A_\star$, where $\dot{M}_{\rm w,-5} = \dot{M}_{\rm w}/10^{-5}{\rm M}_\odot$ and $v_{\rm w,3} = v_{\rm w}/1000\,{\rm km/s}$. Requiring the wind termination shock radius, which depends on the wind properties and also on the external interstellar medium density n_0 and on the progenitor lifetime $t_\star$, to be smaller than $R_{\rm dec,w}$, we obtain:

$$\dot{M}_{\rm w,-5} < 3\times10^{-4}E_{\rm k,52}^{10/13}\Gamma_2^{-20/13}v_{\rm w,3}^{9/13}n_{0,2}^{3/13}t_{\star,\rm Myr}^{-4/13} \tag{6.5}$$

where $E_{\rm k,52} = E_k/10^{52}$, $\Gamma_2 = \Gamma/100$, $n_{0,2} = n_0/100\,{\rm cm}^{-3}$ and $t_{\star,Myr} = t_\star/1\,{\rm Myr}$. Inserting our best-fit afterglow parameters, we obtain $\dot{M}_{\rm w,-5} < 7\times10^{-2}v_{\rm w,3}^{9/13}n_{0,2}^{3/13}t_{\star,\rm Myr}^{-4/13}$. An external interstellar medium density of $n_0 = 100\,{\rm cm}^{-3}$ could be achieved if, despite the large offset, the progenitor was embedded in a star forming region. For the fiducial wind speed $v_{\rm w}$, external medium density n_0 and progenitor lifetime parameters $t_{\star,Myr}$, this limits the wind mass loss rate to $\dot{M}_{\rm w} < 7\times10^{-7}\,{\rm M}_\odot\,{\rm yr}^{-1}$, which can be achieved only in the case of a very low metallicity, or a low Eddington ratio (Sander, Vink, and Hamann, 2020). Alternatively, the low wind mass loss rate could be explained as the result of wind anisotropy induced by the fast rotation of the progenitor star (Ignace, Cassinelli, and Bjorkman, 1996; Eldridge, 2007), which would reduce the wind mass loss rate along the stellar rotation axis.

For the forward shock, we found a relativistic electron power law slope $p_{\rm FS} = 2.010^{+0.002}_{-0.005}$, reminiscent of that expected for first-order Fermi acceleration in non-relativistic strong shocks (Bell, 1978), and slightly lower than $p \sim 2.2$ expected for relativistic shocks (Sironi and Spitkovsky, 2011). The 1–σ confidence interval on the fraction of accelerated electrons is $\chi_{\rm e,FS} = 2.2^{+2.2}_{-1.2}\times10^{-2}$. The electron energy density fraction is $\epsilon_{\rm e,FS} = 0.029^{+0.036}_{-0.016}$, slightly lower than, but comparable to, the expected $\epsilon_{\rm e} \sim 0.1$ for mildly relativistic, weakly magnetised shocks (Sironi and Spitkovsky, 2011). On the contrary, the magnetic field energy density fraction is $\epsilon_{\rm B,FS} = 5.4^{+4.5}_{-3.9}\times10^{-5}$, which implies inefficient small-scale magnetic field amplification by turbulence behind the shock, in line with previous studies of GRB afterglows (Barniol Duran, 2014; Wang et al., 2015). Interestingly, the best-fit values we found for the jet isotropic-equivalent energy $E_{\rm k}$, the interstellar medium number density n and the forward shock microphysical parameters $\epsilon_{\rm e,FS}$ and $\epsilon_{\rm B,FS}$ all closely resemble those found (MAGIC Collaboration et al., 2019a) for GRB 190114C, under the constant external density assumption.

For the reverse shock, we fixed $\chi_{\rm e,RS} = 1$ as usual to reduce the number of parameters, since we could not constrain it to be lower than this value. We found that, in order to be able to interpret the X-ray and optical peaks at $t \sim 10^{-2}$ days as reverse shock emission without overpredicting the later radio data, the magnetic field in the shock downstream must have decayed rapidly after the reverse shock crossed the jet. In particular, we found that the magnetic energy density must have decayed at least as fast as $B^2 \propto V^{-\eta_{\rm B}}$ with $\eta_{\rm B} \geq 6$, where V is the comoving volume of the shell (see Salafia et al. 2021 for a detailed description of the assumed dynamics before and after the shock crossing). This is different from the usual assumption (Kobayashi, 2000) that $\epsilon_{\rm B}$ remains constant before and after the shock crossing, but we consider this reasonable, as the magnetic field is most likely amplified by small-scale instabilities downstream of the shock, which are bound to decay (possibly exponentially) as soon as the shock disappears. For $\eta_{\rm B} \geq 6$ our results are independent of the exact value of $\eta_{\rm B}$, and we obtained $\epsilon_{\rm e,RS} = 0.27^{+0.32}_{-0.19}$ and $\epsilon_{\rm B,RS} = 1.7^{+3.6}_{-1.2}\times10^{-3}$, and the accelerated electron power law index $p_{\rm RS} = 2.15^{+0.01}_{-0.11}$.

The inference on the afterglow parameters described so far is based on the assumption of an on-axis viewing angle. On the other hand, a slightly off-axis viewing angle could explain the relatively low luminosity and low peak energy of the observed prompt emission (Sato et al., 2021). This would, however, imply some degree of proper motion in the VLBI images. To place a limit on the viewing angle based on that, we note that the apparent displacement δr of an off-axis jet is bound to be smaller, or at most equal to, the size increase δs of a spherical relativistic blastwave with the same $E_{\rm k}/n$ ratio (i.e., the same Sedov length) over the same time, since the jet can be thought of as a portion of that sphere. We therefore computed the largest displacement compatible at 1–σ with our astrometric measurements, considering the EVN 5 GHz and VLBA 15 GHz epochs only, as these were performed under sufficiently homogeneous observing strategies and shared same phase-reference source. Given the separation of $0.37^{+0.34}_{-0.36}$ mas between the first VLBA 15 GHz and the last EVN epoch, which are the two most widely separated in both time and centroid position, we cannot exclude a potential source centroid displacement of up to $\delta r_{\rm max} \sim 1.088$ parsecs (adopting Planck cosmological parameters, Planck Collaboration 2016) from $t_0 = 7.89$ to $t_1 = 69.5$ rest-frame days separating the two observations. To produce an expansion $\delta s \geq \delta r_{\rm max}$ over the same time range, a relativistic blastwave would need to have $\log[(E_{\rm k}/n)/{\rm erg\,cm^3}] \geq 59.3$, which is well beyond any conceivable value for a GRB (Granot, Piran, and Sari, 1999). This means that our astrometric measurements are not sufficiently precise as to exclude any viewing angle.

A relatively tight limit on the viewing angle can be obtained, on the other hand, by requiring the jet to be optically thin to the photons we observed during the prompt emission. In particular, we performed the calculation of the optical depth to γ-ray photons for an arbitrary viewing angle $\theta_{\rm view}$ and jet Lorentz factor Γ (Matsumoto, Nakar, and Piran, 2019b), given the observed spectrum. We focused on the brightest emission episode, namely Episode II, that provides the most stringent limit on the viewing angle. Photons of energy E must have been able to escape from the emitting region and not pair-annihilate with other photons of energy $\geq (\delta m_e c^2)^2/E$, where δ is the relativistic Doppler factor $\delta = [\Gamma(1-\beta cos\theta)]^{-1}$ (limit A); they must not have been scattered off by pairs produced by annihilation of other high energy photons (limit B); and they must not have been scattered off by the electrons associated with the baryons in the outflow (limit C). The first two sources of opacity depend on the observed spectrum, while the third one depends on the matter content of the jet, which we conservatively assumed to be the lowest compatible with the observed spectrum. Given the prompt emission spectrum observed in Episode II, we computed the optical depth as a function of the bulk Lorentz factor Γ and the viewing angle $\theta_{\rm view}$ for limits A, B and C following Matsumoto, Nakar, and Piran (2019b) and assumed an emission duration $\delta_t = 3s$, which corresponds to the brightest peak in the emission episode.

Figure 6.14 shows the regions on the Γ, $\theta_{\rm view} - \theta_{\rm jet}$ plane for which the optical depths are smaller than unity for the three limits. The solid black line corresponds to $\Gamma(\theta_{\rm view} - \theta_{\rm jet}) = 1$, therefore dividing the plot into on- and off-axis regions (inside or outside the relativistic beaming cone of material within the jet border). As shown in the plot, the value of Γ derived from our afterglow modelling (represented by the green star) is within the relatively small allowed region. The resulting upper limit on the viewing angle is $\theta_{\rm view} - \theta_{\rm jet} \lesssim 2^\circ$. Adopting the jet opening angle $\theta_{\rm jet} = 15^\circ$ obtained from the afterglow modelling, a viewing angle greater than 17° would not be compatible with the observed emission.

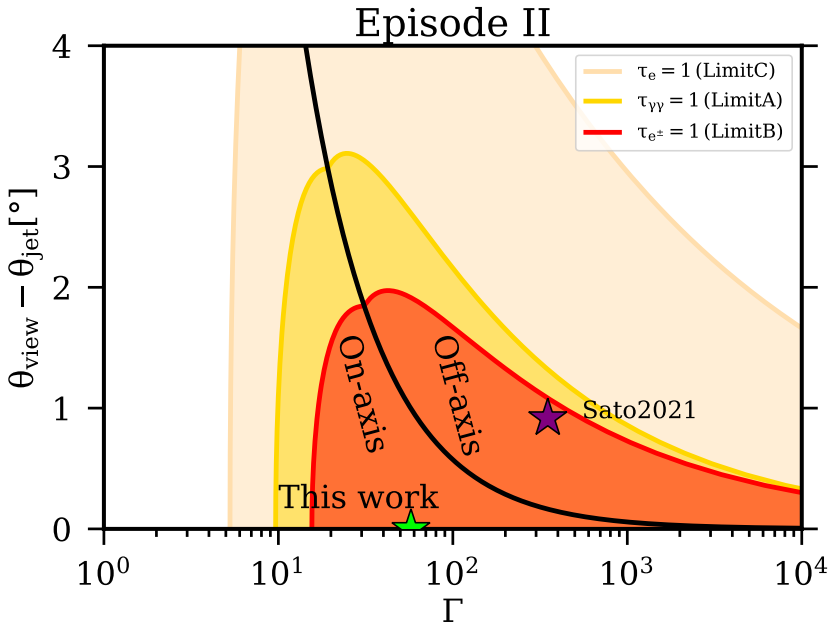

FIGURE 6.14: Limits on the viewing angle from compactness arguments on the prompt emission. Shaded areas show the allowed regions on the (Γ, $(\theta_{view} - \theta_{jet})$) plane, derived by the compactness limits A (photon-photon pair-production), B (scattering off $e^{\pm}$), and C (scattering off e^{-} associated to baryons). The solid black line ($\Gamma\theta = 1$) separates on-axis observers from off-axis ones. The green star marks the bulk Lorentz factor Γ value inferred from the afterglow lightcurve modelling, while the purple star marks the parameters used in Sato et al. (2021). Both solutions are in the allowed region that ensures the source to be transparent to the observed high-energy prompt emission photons.

Recently, a two-component jet model has been proposed by Sato et al. (2021) to explain the multi-wavelength observations of GRB 190829A. In particular, a narrow ($\theta_{jet} = 0.015\,\text{rad} = 0.86°$) and fast ($\Gamma = 350$) jet was used to reproduce the bumps observed in the optical and X-rays lightcurve at $t \sim 1.4 \times 10^3$ s from the trigger time, while a wide ($\theta_{jet} = 0.1\,\text{rad} = 5.73°$) and slow ($\Gamma = 20$) co-axial jet should explain the late ($t \gtrsim 10^5$ s) X-ray and radio emission. In this scenario, the observer is at an angle $\theta_{view} = 0.031\,\text{rad}\,(1.78°)$ with respect to the jet axis. Since the authors of that work point out that the narrow jet could be responsible for the prompt emission of both the Episodes I an II, we also applied the compactness argument to this solution for comparison. As shown in Figure 6.14, the parameters they assumed for the narrow jet are still inside the allowed region, although quite at its limit, and therefore the solution with an off-axis narrow jet as the source of the observed gamma-rays is not ruled out from the compactness argument.

6.3.4 Conclusion

In this Section I presented the results of our analysis combining VLBI observations and multi-wavelength afterglow emission of GRB 190829A, a remarkable GRB that was detected at TeV photon energies by the H.E.S.S. telescope. Our analysis provided evidence in support of the GRB 190829A afterglow being produced by a relativistic blastwave, at least at times $t \geq 9$ days. We found that a forward plus reverse shock afterglow model, assuming an on-axis viewing angle and a uniform external medium density, is

able to reproduce the observed light curves from the γ–rays down to the radio at 1.4 GHz, provided that only a relatively small fraction $\chi_e \lesssim$ few $\times 10^{-2}$ of the electrons are accelerated to relativistic speeds in the forward shock, and that the magnetic field in the reverse-shocked jet decays rapidly after the shock crossing. The required external medium density is relatively low, which points to a very weak progenitor stellar wind. The size evolution entailed by the model is in excellent agreement with our VLBI observations. Our analysis, on the other hand, cannot exclude a viewing angle slightly off the jet border, in which case our derived parameters (especially those related to the reverse shock) would possibly require some modification. The jet and forward shock parameters we obtain from our analysis are similar to those found by the MAGIC Collaboration (MAGIC Collaboration et al., 2019a) for GRB 190114C in the constant external density scenario.

Chapter 7

Discussion and conclusions

In the context of the GRB standard model, the knowledge of physical properties related to the prompt emission phase, e.g. the location of the emitting region, the strength of the magnetic field and the bulk velocity of the jet, as well as the physics underlying the particle acceleration, is still subject to large uncertainties. These information, though, can be extracted from a detailed study of prompt emission spectra, provided a good understanding of the emission mechanism of the observed radiation. This thesis shows that a broadband modeling of the whole spectral shape, when possible, can reveal deviations from the typical double power-law spectrum, both at low (∼keV) and high (∼MeV-GeV) energies, which can help in unveiling important features of the underlying physical processes. This thesis is focused on the interpretation of the features found in GRB prompt emission spectra and on their impact on the GRB standard model. Here I summarize and discuss the main results obtained during my PhD.

Motivated by the discovery of the break in the soft X-rays and its promising role in the interpretation of prompt emission spectra, I searched for its presence also at higher energies, using *Fermi*/GBM data (Chap. 3). My investigation started with the analysis of GRB 160625B, one of the brightest GRBs ever detected by *Fermi*/GBM (Sec. 3.1). The time-resolved spectral analysis of this burst with a more complex empirical function (2SBPL, see Sec. 2.3.1.1) allowed to find an additional break at low energies (around $\sim$ 100 keV) and two power-laws above and below this break, whose slopes are remarkably consistent with synchrotron predictions. Given the promising results obtained in GRB 160625B, I searched for the presence of a spectral break on an enlarged sample of 20 bright GRBs (Sec. 3.2). The sample consisted of 10 long and 10 short GRBs, thus extending for the first time the search of the break also to short GRBs. This study has confirmed the presence of the break in the $\sim$ 70% of the time–resolved spectra of bright long GRBs, located between $\sim$ 20 keV and 500 keV. For this sample of time–resolved spectra of long GRBs, the log–normal distributions of $E_{\rm break}$ and $E_{\rm peak}$ are centered around the mean values $\langle \log(E_{\rm break}/{\rm keV}) \rangle = 2.00 \pm 0.34$ and $\langle \log(E_{\rm peak}/{\rm keV}) \rangle = 3.00 \pm 0.26$. The photon indices of the power–laws below and above $E_{\rm break}$ are respectively $\langle \alpha_1 \rangle = -0.58 \pm 0.16$ and $\langle \alpha_2 \rangle = -1.52 \pm 0.20$. These are remarkably consistent with the predicted values for synchrotron emission in marginally fast cooling regime. These results confirm what already found in the X-rays, i.e. the presence of low–energy breaks in long GRBs spectra, and prove that the break energies can assume values as large as $\sim$ a few hundreds of keV. Contrary to long GRBs, no one of the short GRB spectra analyzed showed the presence of the additional spectral break, but the low–energy photon index is consistent with $-2/3$.

The spectral fits performed in the 10 brightest long GRBs with the standard fitting function confirmed the results present in the literature: the distribution of the low energy photon index is peaked at $\langle \alpha \rangle$= -1.02±0.19. The distribution of α lies in the middle of the two distributions of α_1 and α_2. This suggested that the value of $\alpha \sim -1$, commonly found in previous studies, can act as a weighted mean of two slopes, -2/3 and -3/2,

which characterize the spectrum below and above the spectral break. In Toffano et al. (2021), we investigated this hypothesis through spectral simulations (Sec. 3.3). We found that if the break energy is close to the peak energy or to the low-energy threshold of the instrument, the fit with Band results in a softer (if $E_{\rm break}$ departs from $E_{\rm peak}$) or harder (if $E_{\rm break}$ approaches $E_{\rm peak}$) low-energy index α. Intermediates values of $\alpha \sim -1$ are inferred when $E_{\rm break}$ is located between the low-energy threshold of the instrument and $E_{\rm peak}$ and in these cases the fit is still acceptable. Therefore, the value of the low-energy photon index of the Band function can be considered as a proxy of the break position with respect to $E_{\rm peak}$. Moreover, we showed that the fluence of the burst is a fundamental parameter to detect the spectral break, i.e. a burst with a typical fluence detected by *Fermi*/GBM can be adequately fitted by Band even though it has an additional break falling within the GBM energy range. Therefore, our analysis suggested that the identification of the break in the spectra of GRBs detected by *Fermi* or *Swift* could be hampered by either the separation of $E_{\rm break}$ from $E_{\rm peak}$ and the spectral signal-to-noise ratio of the spectrum. Taken together, these effects might explain why this fundamental spectral feature has not been previously identified.

The current distribution of known break energies (see Fig. 3.16) shows values in the soft X–rays ($\sim$ few keV) and in γ–ray ($\sim$ hundreds keV) energies. This is of course the result of a bias on the energy band of the instrument used to detect the break. It would be interesting to enlarge the number of detections of the spectral breaks and possibly sampling the distribution in the energy range between 10 and 100 keV, where a few values of $E_{\rm break}$ are found. As demonstrated by the spectral simulations showed in Sec. 3.3, the fluence plays a major role in the identification of the spectral break, thus considering bursts with lower fluence would not significantly enlarge the sample of break energies. Ideally, in order to enrich the sample of detected breaks in the range $\sim$few keV-100 keV, we would need an instrument with a large effective area and a wide energy range. In the work of Ghirlanda et al. (2021), we showed that instrumental designs such that conceived for the THESEUS space mission, extending from X-rays to several MeV and featuring a larger effective area with respect to *Fermi*/GBM, can reveal a larger fraction of GRBs with a spectral energy break, providing prompt emission spectra with high statistics from which $E_{\rm break}$ can be measured over a wider fluence range than what is now possible. A similar instrumental design has been also envisaged for the Franco-Chinese space mission SVOM (Cordier et al., 2015; Bernardini et al., 2017), expected to be launched at the end of 2021. Thanks to its large effective area (intermediate between *Fermi*/GBM and THESEUS/XGIS) and the wide coverage of the prompt emission spectrum through its two instruments ECLAIRs (4–150 keV) and GRM (15–5500 keV), SVOM will allow to enlarge the sample of bursts with a low-energy break measured for a wide fluence range.

Summarizing the results discussed so far, the analysis presented in this thesis supports the marginally fast cooling synchrotron scenario, whose identification in the spectrum has fundamental implications for the understanding of the physical parameters of the emitting region. As discussed in Chapter 5, the marginally fast cooling regime implies that the emitting particles do not cool completely, and this directly indicates a small value of the magnetic field strength in the emitting region, namely $B' \sim$1–40 G. These values are orders of magnitudes smaller than the values of $B' \sim 10^4 - 10^6$ G expected for a dissipation region located at $\sim 10^{13-14}$ cm from the central engine. At such small radii, given the above mentioned small B', the cooling of the particles should be dominated by the inverse Compton process, which is instead not observed in the $\sim$GeV energy range. Larger radii would accommodate weaker magnetic field values, but would be incompatible with the rapid variability of the lightcurve, of the order of $\sim$ a few tens of milliseconds

(e.g. Bhat et al. 1992; Golkhou and Butler 2014). Therefore, the physical parameters implied by these results represent a serious challenge for the GRB standard model. These results are consistent with those found by Oganesyan et al. (2019), who found acceptable fits of the broadband spectral shape with a physical synchrotron model. The ratio of $\gamma_{\rm min}/\gamma_{\rm cool} \sim 10$ found in their spectra led the author to derive a similar contrived parameter space of GRB emitting region.

A possible solution may come from the proton-synchrotron scenario, discussed in Chapter 5. Ascribing the emission to protons, which hold a much longer cooling timescale than electrons (Ghisellini et al., 2020), the observed cooling frequency can be explained assuming a standard magnetic field $B \sim 10^6$ G and maintaining the emission region at $R \sim 10^{13-14}$ cm. The proton-synchrotron scenario we proposed to explain the prompt emission calls now for more refined and extended calculations, aimed at investigating its consequences and criticalities. In particular, it has been recently suggested by Florou, Petropoulou, and Mastichiadis (2021) that marginally fast cooling protons are not a viable solution to explain the low-energy spectral break in the prompt GRB spectra. Two are the main difficulties raised by the authors. First, they found that the synchrotron emission of secondary pairs produced by $\gamma\gamma$ pair production should introduce a strong modification of the photon spectrum below the peak energy, which would be inconsistent with observations, unless the bulk Lorentz factor is very large ($\Gamma > 10^3$). However, a possible reason leading to such a high optical depth could be the large spectral peak energy $E_{\rm peak} \sim 10$ MeV used as a template in their calculation, that ensures the presence of a high fraction of the emitted photons above the pair-production threshold in the comoving frame. For a typical spectrum with peak energy $\sim 200 - 300$ keV, the pair-production should not be as important as to introduce such a modification in the spectrum. The second, and the most hardly reconcilable, issue is related to the high Poynting luminosities involved $L_{\rm poy} \sim 10^{57}$ erg/s, due to the strong magnetic fields ($10^6 - 10^7$ G) that are necessary for the incomplete proton cooling. The radius of the emitting region considered in their computation is $R \sim 10^{15}$ cm, which is not the one typically assumed in the standard model. Using a radius of $R \sim 10^{13}$ cm, it is possible to find a lower Poynting luminosity, of the order of $L_{\rm poy} \sim 10^{55}$ erg/s. Nevertheless, even though the value is not so extreme as the one reported Florou, Petropoulou, and Mastichiadis (2021), the energetic involved still represents an issue to be solved. While it is a promising way to explain the observed marginally fast cooling regime, the proton-synchrotron scenario seems to work in a reduced parameter space. Therefore, deeper investigations on its capability to explain all the observations are required.

The use of the *Fermi*/GBM data allowed me to investigate the presence of the spectral break also in the population of short GRBs, which was not possible in the works of Oganesyan et al. (2017) and Oganesyan et al. (2018) due to the requirement to have XRT observations simultaneous with the prompt emission. The analysis presented in Chapter 3 led me to find an interesting result: contrary to what found for long GRBs, no one of the short GRBs displayed an additional break at low energies, but their index α is $\sim$-2/3. In the context of the synchrotron interpretation, the consistency of the low-energy photon index with the synchrotron slope -2/3 indicates that the cooling frequency and the injection frequency are very close to each other. This however implies that the magnetic field in the emitting region is even weaker than what estimated for long GRBs, leading to a longer radiative cooling timescale. It would be worth to investigate what is the origin of this diversity in the spectrum of these two populations, as it might reveal interesting properties of the short GRBs. For example, one natural question that arises is whether this difference with long bursts is related to the different environment that the jet has to drill to emerge, either the massive star envelope (in the case of a long GRB) or the merger

ejecta of two compact objects (for short GRBs). In this case, the main difference might lie in the baryon loading and in the chemical composition of the jet. In the case of short GRBs the jet has to drill an ejecta typically dominated by neutrons and heavy elements and it could be more ion-polluted with respect to the jet emerging from a massive collapsing star. The heavier particles in the jet could be the responsible for a longer radiative cooling timescale, that prevent the cooling of the synchrotron frequency down to lower energies. This preliminary idea requires further investigations.

As discussed in Sec. 2.1 and Sec. 3.1, the inclusion of the break allows to model the deviations from a simple Band function observed at low-energies. These deviations have been alternatively modelled in the literature with the addition of a sub-dominant black body (BB) component, claimed to be present in several GRBs (Ryde et al., 2010; Guiriec et al., 2011; Guiriec et al., 2013; Guiriec et al., 2015; Guiriec et al., 2016; Guiriec et al., 2017). These two different approaches model in a very similar way the same data, especially in the X-rays and γ-rays. There is the possibility to distinguish which model is favoured by the data only in particular conditions, i.e. bright spectra and low-energy break far from the usual peak energy. Both these two conditions were satisfied in a few time–resolved spectra of GRB 160625B (Sec. 3.1), where the comparison of the fit probabilities firmly favored the 2SBPL as the best-fitting model, with respect to the SBPL+BB (e.g. in the spectrum accumulated at the peak of the lightcurve, $P_{\rm 2SBPL} = 0.15$ vs $P_{\rm 2SBPL} = 6 \times 10^{-4}$). However, in many GRB spectra it can be less obvious which one of the two different models is the correct one. The question is of paramount importance, since the two different descriptions of the spectra implies two different theoretical scenarios (related to the significance of the thermal component in the emission process and to the dominant energy reservoir of the jet). A possible way to distinguish between these two models is to extend the analysis at lower energies, where the models predict significantly different fluxes. In the work of Oganesyan et al. 2019 (see a similar approach also in Ghirlanda et al. 2007a), the authors included the optical data detected simultaneously to the X–rays and found that these data are consistent with the low-energy spectral slope -2/3 of the synchrotron model, and not with the extrapolation of the non-thermal+BB model.

The distributions of α_1 and α_2 found from my analysis are consistent, within 1σ, with the two predicted synchrotron slope, -2/3 and -3/2, respectively. However, they extend to values both softer and harder than the synchrotron predictions. While softer values may be more easily explained (e.g. as evolution of the spectrum), the presence of harder values in the observed distribution represents a major challenge for the synchrotron interpretation of the whole spectrum (e.g. see Preece et al. 1998). Both in GRB 160625B and in the 10 long bright GRBs analyzed, I performed a test in order to check the presence of the slope -2/3 in the spectrum. The test demonstrated that fixing the value of $\alpha_1 = -2/3$ for those GRBs with a harder α_1 value, the fit was still acceptable (see Section 3.1 and 3.2), and the other free parameters of the model assume values which are consistent, within their errors, with those obtained leaving α_1 free. This supports the hypothesis that the -2/3 slope is indeed present in the spectrum and indicates that the scatter of the values returned by the fit when α_1 is free to vary my be ascribed to the fitting process. Another indication of the reliability of the slopes obtained with empirical models comes from the successful synchrotron fit performed in GRB 180720B (see Sec. 3.4). In the energy range covered by GBM and LLE data, the synchrotron model well described a complex spectral shape that requires two break energies and three power–laws. In the fast cooling regime, the slopes of the two power–laws below $E_{\rm peak}$ are fixed and are not able to adapt to a different spectral shape (contrary to the fit with the empirical function, where the slopes were free to vary). This confirms the main results obtained with the empirical function

2SBPL, namely the presence of two frequencies and their relative ordering, as well as the consistency of the indices with the synchrotron predictions. Moreover, another aspect to investigate is the possible correlation between the spectral indices and the curvatures of the empirical models. The curvatures around the break and around the peak energies have been fixed throughout all the analysis presented in this thesis, to minimize the set of free parameters, and this could contribute to the observed scatter in the slopes distributions.

In light of the findings of this thesis, we can now reconsider the distribution of the low-energy photon index α typically found in literature (see Chapter 2). Speculating on the presence of the spectral break in each GRB, the marginally fast cooling regime can explain low-energy indices from -3/2 up to the asymptotic value of -2/3, depending on the relative position of the break inside the considered energy range. This is one of the most far-reaching results of this thesis, as it allows to safely reconcile the vast majority of the observed spectra with the synchrotron theory, without invoking other emission mechanisms.

There are still two main issues for the synchrotron interpretation of GRB spectra, though. The first one regards those spectra with α harder than -2/3 (the synchrotron line-of-death) at more than 1σ. However, as discussed above, in the fitting procedure fixing this value returns still acceptable fits of the spectral data. In addition, the spectral simulations described in Sec. 3.3 showed that, when fitting with the Band function a spectrum with $E_{\rm break}$ close to $E_{\rm peak}$, values harder than the input slope value of -2/3 were indeed found. This suggests that the use of an empirical function might introduce a bias in the estimates of the spectral slopes. While most of the inconsistencies between the observed hard low energy slopes and the predicted values could be reconcilable ascribing the discrepancies to the fitting function, there are still spectra that are much harder ($\alpha \sim 0$, see e.g. Yu, Dereli-Bégué, and Ryde 2019) than what could be explained by the synchrotron theory.

The second issue related to the synchrotron interpretation of the observations is related to the width of the spectrum, as anticipated in Chapter 2. Recently, Yu et al. (2015b) and Axelsson and Borgonovo (2015) showed that the observed spectra of most GRBs detected by the GBM are narrower than the spectra expected from an electron synchrotron model, calling for a new physical interpretation of the keV-MeV spectral component. However, it should be noted that the authors did not attempt to fit this theoretical model to the data, but they only compare the width parameter measurements obtained with empirical functions. The fit of the spectrum of GRB 180720B with the synchrotron model has demonstrated that the spectral data can be successfully fitted by synchrotron emission from a power-law distribution of electrons, without raising any issue related to the width of the spectrum. Moreover, direct fits of the synchrotron emission model to GRB prompt spectra have been performed by Zhang et al. (2016) and Burgess (2019), who showed that the line-of-death and spectral sharpness issues are likely artefacts due to the use of the Band function.

It is difficult to assess the fraction of these hard/narrow spectra in the *Fermi*/GBM bursts Catalog, as the different works that analyzed them followed different selection criteria and applied different fitting functions, making it challenging to make a homogeneous comparison and have a clear idea of the dimension of the sample over the total number of bursts detected. Nevertheless, even though they would represent a small fraction of the total, in those spectra neither the presence of the spectral break inside the energy band, nor curvature effects, or different fitting functions can help to mitigate the inconsistency with the synchrotron predictions. To explain these challenging spectra still in the context of the synchrotron theory, some modification on the assumptions of

the synchrotron theory applied to GRBs is required (e.g., as suggested in the past, considering anisotropic distribution of pitch angles as in Medvedev 2000). Other emission mechanisms, such as thermal components, or other effects not investigated here, e.g. pair production by high-energy γ-ray photons, may further produce an hardening of the low energy photon index α.

In addition to the studies of the low energies, I also focused on the analysis of the high energy extension of the prompt emission spectrum (Chapter 4). The joint analysis of GBM and LAT data for 22 time-integrated prompt GRB spectra revealed that in 10 burst the spectrum requires the presence of an exponential cutoff at high energies, between ∼14 and 300 MeV. For the other 12 bursts of the sample, a lower–limit on the cutoff energy has been derived. Interpreting the exponential cutoff as sign of opacity to pair-production, I estimated the values (and lower–limits) of the bulk Lorentz factor Γ of the jet during the prompt phase (Chapter 5). An alternative interpretation of the observed cutoff would invoke the maximum photon energy for synchrotron emission, which reflects the maximum energy $\gamma_{\rm max}$ of the particles distribution achieved during the acceleration. However, this limit is expected to be at higher energies both for the electrons ($E_{\rm e}^{\prime \rm max,syn} \sim 50$ MeV in the comoving frame) and for the protons ($E_{\rm p}^{\prime \rm max,syn} \sim 93$ GeV, see Chapter 5), therefore the interpretation of the cutoff as due to pair-production is more likely.

The distribution of the estimates of Γ inferred from the pair-production argument spans the range of values 100–400, which are compatible with the typical values assumed in the standard model. The inferred values are consistent with the estimates of Γ from the afterglow onset time (Ghirlanda et al., 2018) under the hypothesis of a constant density circum-burst medium. In the wind case, instead, the distribution of bulk Lorentz factors extends toward lower values of Γ. These would imply lower values of the cutoff energy, and then a fainter flux in the LAT range. Therefore the absence of such lower values in the Γ distribution of LAT-detected bursts could be due to a selection effect. The distribution of Γ may also extend towards higher values, as indeed suggested by the lower-limits on Γ values derived from the lower-limits on the cutoff energy $E_{\rm cutoff}$, which extends up to ∼750. An interesting next step of this work could be to explore the correlation between Γ and the isotropic energy of the burst $E_{\rm iso}$, the isotropic luminosity $L_{\rm iso}$, which have been tested in Ghirlanda et al. (2018) from the afterglow observations. A possible improvement of the analysis would also consist in considering finer temporal intervals, performing a time-resolved analysis. As the physical conditions in the emission region may vary with time, time-integrated spectra can easily smear out any signal. Instead, a time-resolved analysis, provided a sufficient signal-to-noise ratio to constrain the parameters of the fit, could reveal the evolution of the exponential cutoff. This could shed light on the evolution of the opacity in the emitting region, which has been also suggested as an explanation of the delayed onset of the GeV emission often observed in GRBs (e.g. Hascoët et al. 2012).

For the sake of simplicity, in the derivation of the Γ values described above I assumed for each GRB the same variability timescale $t_{\rm var} = 0.1$ s, which may not be appropriate for every burst. This implicitly implies an assumption on the distance R of the emitting region from the central engine. However, for those GRBs with Γ inferred from another independent method, it is possible to use such Γ value to derive the estimate of the distance R using the compactness argument. This method allows to bypass the problem of the measurement of the variability timescale of the prompt lightcurve, which is not always an easy task. I applied this method for the only two GRBs of the sample analyzed in this thesis with an independent estimate of Γ from the work of Ghirlanda et al. (2018). Depending on the assumptions on the homogeneous or wind medium cases, I found

values of $R > 10^{13} - 10^{15}$ cm, which are compatibles with the location of the prompt emission region predicted by the GRB standard model. This method provides a tool to restrict the acceptable range of values for the still uncertain parameter R. This is crucial in the framework of the synchrotron interpretation of the results obtained in Chapter 3. Building a distribution of the distances R would significantly help in constraining the parameter space of prompt emission models discussed above. This could be done, for example, by cross-matching the sample of GRBs with a detection of the afterglow onset present in the literature and the *Fermi* Catalog. The simple analysis of the *Fermi* spectrum would directly provide a value (or a lower-limit) of the distance R of the prompt emission region, given an estimate (or a lower–limit) of a cutoff energy. In addition, it would be interesting to derive the variability timescales corresponding to the estimates of R and Γ inferred with this method, and compared them with the prompt emission lightcurve. In principle, this method could help also to better explore the possible values of external medium densities and choose one between the homogeneous and wind-like cases, which are often difficult to distinguish from the afterglow observations.

In addition, the inclusion of the LLE and LAT data in the analysis allowed to constrain better the high–energy power–law slope β of the 22 observed spectra. I found a distribution of the slope β peaked at the median value $\langle\beta\rangle$ = -2.43$\pm$0.55, which is steeper than the value reported in the *Fermi*/GBM Catalog. This could suggest that the true slope of the GRBs prompt emission spectrum at high energies is softer than what is usually found limiting the analysis to the GBM energy range. The high–energy slope β is a key parameter to study the energy distribution of the emitting particles accelerated during the prompt emission. Assuming the emission as due to synchrotron, the slopes β of the spectrum allow to estimate the corresponding slopes p of the underlying distribution of non-thermal accelerated particles. The distribution of p is quite broad, centered around a median value of $p = 2.86$ with a tail reaching values $p \sim$ 5–7. The combination of such steep values of p and the large value of $\gamma_{\rm min}$ derived from the synchrotron modeling requires an efficient acceleration mechanism able to produce energetic particles, but with a narrow energy distribution. These results provide meaningful observational constraints to the theory of particle acceleration, which is still poorly understood in the case of mildly relativistic shocks or magnetic reconnection in magnetized plasma.

Besides the research on the prompt emission phase of GRBs, during my PhD I also focused on the study of the first three GRBs detected at VHE (GRB 180720B, GRB 190114C and GRB 190829A), presented in Chapter 6. My investigations were not focused on the VHE emission and its origin, but rather on the analysis and interpretation of their properties at lower frequencies.

Regarding GRB 180720B, the analysis of the *Fermi* data (GBM and LAT) and the *Swift* data (BAT and XRT) allowed to study the evolution of the afterglow component of the burst, which emerges when the prompt emission phase is still active and then it dominates at late times. In particular, the analysis of the emission detected by LAT revealed the rise and the fall of the afterglow component, pinpointing the peak of the lightcurve. Interpreting this peak as the sign of the deceleration of the jet led us to estimate the bulk Lorentz factor Γ of the jet before the deceleration phase. For typical values of the medium density, wind mass loss rate and velocity, we found the range $\Gamma = 220$–294 for the homogeneous medium case and $\Gamma = 80$–142 for the wind case. It is interesting to compare these estimates with the Γ values derived from the pair-production argument in Chapter 4. In fact, the analysis of the prompt spectrum of GRB 180720B with the empirical function 2SBPLCUTOFF revealed the presence of the exponential cutoff at $\sim$ 37 MeV, which implied a bulk Lorentz factor $\Gamma = 121^{+7}_{-14}$. Despite being derived with different methods and assumptions, this value of Γ is consistent with the range of values inferred from the

afterglow onset time assuming a wind-like medium.

Since for GRB 180720B we have all the required parameters, we can go beyond the comparison of the Γ values and instead apply the method suggested above, namely use the estimates of Γ inferred from the afterglow onset to derive the distance R, using the compactness argument (as done for only two GRBs so far). Using the range of Γ values inferred assuming a homogeneous medium, I obtain a distance of the prompt emission region of $R = 1.2\text{–}4.7 \times 10^{12}$ cm, while for the wind medium case, the distance is $R = 0.3\text{–}5.9 \times 10^{14}$ cm. The values of the distance derived for the homogeneous medium are smaller than what usually assumed. In particular, given the isotropic luminosity of the burst and assuming a typical prompt efficiency of η=0.2, they are below the value of photospheric radius $R_{\rm ph} \sim 2 - 5 \times 10^{12}$ cm, below which the emitting region is opaque (Daigne and Mochkovitch, 2002). On the contrary, the values derived for the wind–like case are compatible with the corresponding photospheric radius $R_{\rm ph}$. Both arguments expressed above support the case of a medium shaped by the wind of the progenitor.

In the VHE GRB 190114C, a fine time-resolved analysis of the *Fermi*/GBM data led me to sample the smooth transition from the prompt to the afterglow phase, revealing the presence of the afterglow component in the GBM energy range at very early times (see Sec. 6.2). This allowed to track the flux evolution of the afterglow from its beginning, revealing the peak at ∼6 s, thus enabling the estimate of Γ (found to be $\Gamma \sim$ 700-520 for the homogeneous case and $\Gamma \sim$ 130-230 for the wind case). The observation of the afterglow component at high energies is not new (see the case of GRB 180720B in this thesis, as many others in the literature), but finding the peak of the afterglow lightcurve in the GBM energy range is rare. This has been possible thanks to the combination of the presence of a fast jet, which allowed an early peak time of the afterglow lightcurve, and the fine time resolved analysis of the GBM data performed from the beginning of the emission. Indeed, following the evolution of the afterglow at high energies helps to measure the largest bulk Lorentz factors. GRBs with the detection of the peak of the afterglow lightcurve in the GeV energy range yield the highest value of Γ, compared to the ones with the peak in the early optical lightcurve (Ghirlanda et al., 2018). The peak time $t_{\rm p}$ of the afterglow lightcurve of GRB 190114C found in the GBM energy range is among the smallest values of peak times reported for long GRB afterglows in Ghirlanda et al. (2018), and it led to the estimate of a quite large bulk Lorentz factor. Considering the isotropic equivalent energy of the burst $E_{\rm iso} \sim 3 \times 10^{53}$ erg, the values of Γ derived are in agreement with the Γ–$E_{\rm iso}$ correlation found in Ghirlanda et al. (2018), with a slight preference for the values derived in the wind–like medium case.

Both studies showed that the temporal and spectral analysis of the solely high-energy emission allows to track the evolution not only of the prompt emission but also of the afterglow component, and possibly to pinpoint the deceleration time of afterglow (as observed in *Fermi*/LAT for GRB 180720B and in *Fermi*/GBM energy range for GRB 190114C), allowing to extract meaningful constraints on the physical parameters of the jet.

As shown in this thesis, combining the information gathered from the analysis of the prompt and the afterglow emission provides an efficient way to reduce the degeneracies in the parameter space. Also the case of GRB 190829A (see Sec. 6.3) serves as a good example. This burst has been detected at VHE but conversely to the previous burst, it yields a ∼3 orders of magnitude smaller isotropic equivalent energy, demonstrating that also fainter GRB can emit VHE photons. Moreover, it is one of the closest GRBs known to date ($z = 0.0785$) and this allowed us to apply the VLBI tecnique to observe its radio counterpart. VLBI observations of GRB afterglows can provide valuable information on the jet properties (e.g. the kinetic energy of the jet, its orientation and the progenitor environment), but have been rarely performed, due to the large distances involved. In only two cases, the on-axis long GRB 030329 ($z = 0.17$) and the off-axis short GRB 170817A

($z = 0.0097$), the VLBI tecnique allowed to directly observe the superluminal expansion (Taylor et al., 2004) and the superluminal proper motion (Mooley et al., 2018; Ghirlanda et al., 2019) of the source, providing solid evidence in support of the presence of an extremely fast jet of material.

Unfortunately, the astrometric measurements of our VLBI observations of GRB 190829A were not sufficiently tight as to significantly measure the superluminal motion of the source, and thus to provide any clue on the orientation of the jet with respect to the line of sight. However, a relatively tight constraint on the viewing angle $\theta_{\rm view}$ was instead derived from the analysis of the prompt emission of this burst. Applying the compactness argument to the low-luminosity ($\sim 10^{49}$ erg/s) and low-peak energy ($\sim$11 keV) spectrum and adopting the jet opening angle $\theta_{\rm jet} = 15^{\circ}$ obtained from the afterglow modelling (see below), I found that a viewing angle greater than $\theta_{\rm view} = 17^{\circ}$ would not be compatible with the observed emission.

In addition to the VLBI images obtained for the radio counterpart of GRB 190829A, the extremely rich dataset collected for the afterglow of this burst allowed us to perform a broadband detailed modeling of the multi–wavelength data, including also the VHE data detected by the H.E.S.S. Telescopes (HESS collaboration, Abdalla, et al., 2021). Modeling also the observations at TeV photon energies of GRB afterglows is fundamental as they help to constrain the physical processes underlying the observed emission (Zhang and Mészáros, 2001; Nava, 2018; MAGIC Collaboration et al., 2019a). Therefore, in order to build the SEDs of GRB 190829A, especially at the times of the TeV observations, I performed the analysis of the X-ray data detected by the instrument XRT. Our modeling, including both the standard synchrotron emission and the synchrotron self-Compton component, is able to satisfactorily explain the SEDs of GRB 190829A at the times of the H.E.S.S detection. The theoretical modeling of both the spectra and lightcurve afterglow emission of this burst agrees with the observations across almost 18 orders of magnitude in frequency and more than 4 orders of magnitude in time. The size evolution entailed by our model is in excellent agreement with our VLBI observations. Combining the afterglow modeling with the high-resolution VLBI images of the radio counterpart lead us to infer interesting constraints on the GRB micro-physical parameters. We found, in particular, that a relatively small fraction $\chi_{\rm e} \lesssim$ few $\times 10^{-2}$ of electrons should be accelerated by the forward shock (contrary to the whole population usually assumed for simplicity) and that the prompt emission radiates a very low fraction of the jet total energy (the efficiency is $\eta_\gamma = 1.3^{+1.5}_{-0.7} \times 10^{-3}$, compatible with the internal shocks theory, but at odds with typical estimates in the literature). Moreover, the required external medium density is relatively low, which points to a very weak progenitor stellar wind.

However, a different interpretation of the same SEDs has been proposed by the H.E.S.S. Collaboration (HESS collaboration, Abdalla, et al., 2021). Their alternative modeling explains the multi-wavelength spectrum, from X-rays to VHE γ–rays, as dominated by one single component, the synchrotron one. To do this, they need to abandon the theoretical limit on the maximum electron energy and extrapolate the synchrotron spectrum for more than three orders of magnitude beyond this limit. However, overcoming the synchrotron limit is challenging, as it requires a modification of the current understanding of particle acceleration in the shocks occurring during the afterglow phase. In particular, it would require to find an unknown acceleration mechanism able to efficiently accelerate PeV electrons or other *ad hoc* alterations of the distribution of the magnetic field strength in the medium (e.g. the clumpy environments model suggested by Khangulyan et al. 2021). Their modeling with synchrotron+SSC, taking into account the limit on the maximum synchrotron energy, has been reported to be inconsistent with the observation (see their Figure 4), as it predicts a steep spectral index in the VHE energy band. Conversely to the case of GRB 190114C, in this burst the upper limit provided by *Fermi*/LAT data does

not help in constraining the presence of the two separated spectral components. The necessity to go beyond the maximum electron energy limit seems to be not required by the VHE data detected so far, which can instead be satisfactorily fitted by a standard synchrotron+SSC model, as demonstrated by our work and also in the case of GRB 190114C by MAGIC Collaboration et al. (2019a). The jet and forward shock parameters we obtain from our analysis are similar to those found by the MAGIC Collaboration (MAGIC Collaboration et al., 2019a) for GRB 190114C in the constant external density scenario. In both GRB 190114C and GRB 190829A, the powers of the synchrotron and SSC components are comparable, suggesting that a meaningful fraction of the total afterglow energy may have been missed in GRBs studies so far. Further detections of GRBs at VHE will allow to study which ranges of the afterglow parameters are required to produce the SSC component and how common this component is.

Observations of GRBs at TeV energies are notoriously difficult, and only few detections have been reported so far (Atkins et al., 2000; MAGIC Collaboration et al., 2019b; HESS Collaboration et al., 2019; Blanch et al., 2020d; Blanch et al., 2020b; de Naurois and H. E. S. S. Collaboration, 2019; HESS collaboration, Abdalla, et al., 2021). All these detections occurred during the afterglow phase. Observations during the prompt are hard to perform, as IACTs require external alerts in order to point the source. However, the fast repointing capabilities of MAGIC already allowed to look at GRBs as soon as 24–100 seconds after the trigger: the detection of VHE radiation simultaneous with the prompt emission is thus certainly feasible and is one of the main goals of MAGIC. The next generation Cherenkov Telescope Array (CTA, Actis et al. 2011b) will have similar fast repointing capabilities (with a slewing time expected to be around 20 s). Moreover, CTA will cover the energy range from $\sim$ 20 GeV to 300 TeV, allowing to connect the prompt observations in the keV-MeV energy range to the GeV-TeV energies, with a much higher sensitivity than that of *Fermi*/LAT and current–generation IACTs. Thanks to these characteristics and a large effective area, CTA will be able to measure the variability and the spectra of GRBs at GeV-TeV energies with unprecedented photon statistics. Observations of the prompt emission at VHE energies, even resulting in a null detection, will improve our knowledge of the allowed parameter space for GRBs prompt emission phase (Bošnjak, Daigne, and Dubus, 2009; Daigne, 2012; Inoue et al., 2013; Beniamini and Piran, 2013; Vurm and Beloborodov, 2017).

Concluding, the work presented in this thesis can solve the issue of the inconsistency of observed spectra and synchrotron radiation for a large fraction of GRBs. From these results, we learned that the synchrotron process in marginally fast cooling regime provides a good modelling of GRB prompt emission spectra. At the same time, though, they open a new theoretical challenge within the GRB standard model. These results imply that the cooling of the particles is not complete, contrary to what has been assumed for years. The implied set of physical parameters makes it difficult to find a simple self consistent picture which explains all the observed properties of the prompt emission. In particular, we now know that any model proposed for the prompt emission mechanism must explain spectra with two breaks (which have been found in both X–rays and γ–rays for long GRBs), in addition to the already known properties, i.e. the fast variability of the prompt emission (of the order of $\sim$ tens of ms), the huge amount of energy radiated during the prompt ($\sim 10^{52-54}$ erg), and the absence of a strong SSC component in the $\sim$GeV energy range. To further constrain the allowed parameter space, it must be taken into account also the transparency to pair-production of the emitting region and the total energy of the jet (which may be problematic for the proton-synchrotron model). In any case, based on the results presented in this thesis, a revision of the so-called standard model of GRBs is required.

Appendix A

Data extraction and analysis

Here I report the common procedure followed for the extraction and analysis of the data of different instruments, which has been used for the different works presented in this thesis.

When a joint-analysis between different instruments data has been performed, multiplicative factors in the fitting models were introduced, in order to account for inter-calibration uncertainties between the different instruments. These factors were left free to vary (typically within 30%) except for the detector with the highest count rates, whose factor has been frozen to 1.

Fermi/GBM

The GBM is composed of 12 sodium iodide (NaI, 8 keV to 1 MeV) and two bismuth germanate (BGO, 200 keV to 40 MeV) scintillation detectors. For the analysis, I adopted the procedure explained in the Data Analysis Threads and Caveats[1]. Data from up to three NaI with the highest count rates and from one BGO detectors have been selected and retrieved from the online GBM GRB Catalogue. Spectral analysis has been performed using the public software RMFIT (v. 4.3.2). In particular, I selected energy channels in the range 8–900 keV for NaI detectors, and 0.3–40 MeV for BGO detectors, and excluded channels in the range 30–40 keV due to the presence of the Iodine K-edge at 33.17 keV. A free inter-calibration constant factor between the NaI and BGO detectors has been included. I selected background spectra in time intervals far from the burst and I fitted them with a polynomial function up to the fourth-order, according to the burst's background properties. The most updated spectral data files and the corresponding response matrix files (rsp2) were obtained from the online GBM GRB Catalog. The CSPEC data provide a time resolution of 1.024 s while the Time Tagged Event (TTE) data have a shorter time binning (64 ms). Both data have high spectral resolution, comprising 128 logarithmically spaced energy channels. Unless otherwise stated, we made use of CSPEC data.

Fermi/LAT

Data extraction from the online catalog[2] and analysis of Fermi/LAT data were performed with `gtburst`, following the procedure described in the online official Fermi guide [3]. The LAT data were filtered selecting photons within a region of interest (ROI) of 12° centred on the burst position and applyinh a maximum zenith angle cut of 100° to reduce contamination of gamma-rays from the Earth limb. An unbinned likelihood analysis was performed using `gtburst`, assuming a power-law model for the source photon spectrum.

[1] https://fermi.gsfc.nasa.gov/ssc/data/
[2] https://heasarc.gsfc.nasa.gov/W3Browse/all/fermilgrb.html
[3] https://fermi.gsfc.nasa.gov/ssc/data/analysis/scitools/gtburst.html

In the analysis it was assumed a `P8R3_TRANSIENT020E_2` instrument response function, a Galactic model template, and an isotropic template for particle background to take into account the background emission from the Milky Way, extra-galactic diffuse gamma rays, unresolved extragalactic sources, residual (misclassified) cosmic-ray emission, and other extragalactic sources[4].

LAT/LLE data have been extracted from the Fermi LLE Catalog[5]. The LLE spectra analysed cover the energy range 30-100 MeV (e.g. Ajello et al., 2019).

Swift/BAT

The BAT on board *Swift* (Gehrels et al., 2004) is a coded aperture mask which triggers GRBs by imaging photons in the energy range 15–350 keV. BAT event files were downloaded from the *Swift* archive[6]. To extract BAT spectra, we used the latest version of the HEASOFT package (v6.25). The BAT spectra were extracted with the `batbinevt` task and corrected for systematic errors (with the `batupdatephakw` and `batphasyserr` tasks). We generate response files with the `batdrmgen` tool. We adopt the latest calibration files (CALDB release 2017–10–16).

Swift/XRT

The XRT focusses photons in the 0.3–10 keV energy range (Wells et al., 2004). XRT event files were downloaded from *Swift*/XRT archive[7]. The source and background XRT spectra were extracted with `xselect` tool and standard procedures (Romano et al., 2006) were adopted to correct for the pile-up of X–ray photons. The corresponding ancillary response files were generated by the `xrtmkarf` task. The energy channels of XRT below 0.5 keV and above 10 keV have been excluded. In the fit procedure, we used the multiplicative XSPEC models `tbabs` and `ztbabs` to account for Galactic and intrinsic absorption of the X-ray spectrum by neutral hydrogen (Wilms, Allen, and McCray, 2000). The value of Galactic neutral hydrogen column density in the direction of each GRB is found from Kalberla et al. 2005.

[4] https://fermi.gsfc.nasa.gov/ssc/data/analysis/documentation/Cicerone/Cicerone.pdf
[5] https://heasarc.gsfc.nasa.gov/W3Browse/fermi/fermille.html
[6] http://heasarc.gsfc.nasa.gov/cgi-bin/W3Browse/swift.pl
[7] http://www.swift.ac.uk/archive/

Bibliography

Aartsen, M. G. et al. (June 2016). "An All-sky Search for Three Flavors of Neutrinos from Gamma-ray Bursts with the IceCube Neutrino Observatory". In: *ApJ* 824.2, 115, p. 115. DOI: 10.3847/0004-637X/824/2/115. arXiv: 1601.06484 [astro-ph.HE].

Aartsen, M. G. et al. (July 2017). "Extending the Search for Muon Neutrinos Coincident with Gamma-Ray Bursts in IceCube Data". In: *ApJ* 843.2, 112, p. 112. DOI: 10.3847/1538-4357/aa7569. arXiv: 1702.06868 [astro-ph.HE].

Abbott, B. P. et al. (Nov. 2017). "A gravitational-wave standard siren measurement of the Hubble constant". In: *Nature* 551.7678, pp. 85–88. DOI: 10.1038/nature24471. arXiv: 1710.05835 [astro-ph.CO].

Abbott, B. P. et al. (2017). "GW170817: Observation of Gravitational Waves from a Binary Neutron Star Inspiral". In: *Phys. Rev. Lett.* 119 (16), p. 161101. DOI: 10.1103/PhysRevLett.119.161101. URL: https://link.aps.org/doi/10.1103/PhysRevLett.119.161101.

Abdalla, H. et al. (Nov. 2019). "A very-high-energy component deep in the γ-ray burst afterglow". In: *Nature* 575.7783, pp. 464–467. DOI: 10.1038/s41586-019-1743-9. arXiv: 1911.08961 [astro-ph.HE].

Abdo, A. A. et al. (Nov. 2009a). "Fermi Observations of GRB 090902B: A Distinct Spectral Component in the Prompt and Delayed Emission". In: *ApJL* 706, pp. L138–L144. DOI: 10.1088/0004-637X/706/1/L138. arXiv: 0909.2470 [astro-ph.HE].

Abdo, A. A. et al. (Mar. 2009b). "Fermi Observations of High-Energy Gamma-Ray Emission from GRB 080916C". In: *Science* 323.5922, p. 1688. DOI: 10.1126/science.1169101.

Acciari, V. A. et al. (Dec. 2011). "VERITAS Observations of Gamma-Ray Bursts Detected by Swift". In: *ApJ* 743.1, 62, p. 62. DOI: 10.1088/0004-637X/743/1/62. arXiv: 1109.0050 [astro-ph.HE].

Acharya, B. S. et al. (Mar. 2013). "Introducing the CTA concept". In: *Astroparticle Physics* 43, pp. 3–18. DOI: 10.1016/j.astropartphys.2013.01.007.

Achterberg, Abraham et al. (Dec. 2001). "Particle acceleration by ultrarelativistic shocks: theory and simulations". In: *MNRAS* 328.2, pp. 393–408. DOI: 10.1046/j.1365-8711.2001.04851.x. arXiv: astro-ph/0107530 [astro-ph].

Ackermann, M. et al. (June 2010). "Fermi Observations of GRB 090510: A Short-Hard Gamma-ray Burst with an Additional, Hard Power-law Component from 10 keV TO GeV Energies". In: *ApJ* 716, pp. 1178–1190. DOI: 10.1088/0004-637X/716/2/1178. arXiv: 1005.2141 [astro-ph.HE].

Ackermann, M. et al. (Mar. 2011). "Detection of a Spectral Break in the Extra Hard Component of GRB 090926A". In: *ApJ* 729.2, 114, p. 114. DOI: 10.1088/0004-637X/729/2/114. arXiv: 1101.2082 [astro-ph.HE].

Ackermann, M. et al. (2013). "The First Fermi-LAT Gamma-Ray Burst Catalog". In: *ApJS* 209.1, 11, p. 11. DOI: 10.1088/0067-0049/209/1/11. arXiv: 1303.2908 [astro-ph.HE].

Ackermann, M. et al. (Jan. 2014). "Fermi-LAT Observations of the Gamma-Ray Burst GRB 130427A". In: *Science* 343, pp. 42–47. DOI: 10.1126/science.1242353. arXiv: 1311.5623 [astro-ph.HE].

Actis, M. et al. (Dec. 2011a). "Design concepts for the Cherenkov Telescope Array CTA: an advanced facility for ground-based high-energy gamma-ray astronomy". In: *Experimental Astronomy* 32.3, pp. 193–316. DOI: 10.1007/s10686-011-9247-0. arXiv: 1008.3703 [astro-ph.IM].

— (Dec. 2011b). "Design concepts for the Cherenkov Telescope Array CTA: an advanced facility for ground-based high-energy gamma-ray astronomy". In: *Experimental Astronomy* 32.3, pp. 193–316. DOI: 10.1007/s10686-011-9247-0. arXiv: 1008.3703 [astro-ph.IM].

Acuner, Zeynep and Felix Ryde (Dec. 2017). "Clustering of gamma-ray burst types in the Fermi GBM catalogue: indications of photosphere and synchrotron emissions during the prompt phase". In: *Monthly Notices of the Royal Astronomical Society* 475.2, pp. 1708–1724. ISSN: 0035-8711. DOI: 10.1093/mnras/stx3106. eprint: https://academic.oup.com/mnras/article-pdf/475/2/1708/23630073/stx3106.pdf. URL: https://doi.org/10.1093/mnras/stx3106.

Adrián-Martínez, S. et al. (Nov. 2013). "Search for muon neutrinos from gamma-ray bursts with the ANTARES neutrino telescope using 2008 to 2011 data". In: *A&A* 559, A9, A9. DOI: 10.1051/0004-6361/201322169. arXiv: 1307.0304 [astro-ph.HE].

Adrián-Martínez, S. et al. (Aug. 2016). "Letter of intent for KM3NeT 2.0". In: *Journal of Physics G Nuclear Physics* 43.8, 084001, p. 084001. DOI: 10.1088/0954-3899/43/8/084001. arXiv: 1601.07459 [astro-ph.IM].

Ajello, M. et al. (June 2019). "A Decade of Gamma-Ray Bursts Observed by Fermi-LAT: The Second GRB Catalog". In: *ApJ* 878.1, 52, p. 52. DOI: 10.3847/1538-4357/ab1d4e. arXiv: 1906.11403 [astro-ph.HE].

Ajello, M. et al. (Feb. 2020). "Fermi and Swift Observations of GRB 190114C: Tracing the Evolution of High-energy Emission from Prompt to Afterglow". In: *ApJ* 890.1, 9, p. 9. DOI: 10.3847/1538-4357/ab5b05. arXiv: 1909.10605 [astro-ph.HE].

Akaike, H. (1974). "A new look at the statistical model identification". In: *IEEE Transactions on Automatic Control* 19.6, pp. 716–723.

Alexander, K. D. et al. (Oct. 2017a). "A Reverse Shock and Unusual Radio Properties in GRB 160625B". In: *ApJ* 848, 69, p. 69. DOI: 10.3847/1538-4357/aa8a76. arXiv: 1705.08455 [astro-ph.HE].

Alexander, K. D. et al. (Oct. 2017b). "The Electromagnetic Counterpart of the Binary Neutron Star Merger LIGO/Virgo GW170817. VI. Radio Constraints on a Relativistic Jet and Predictions for Late-time Emission from the Kilonova Ejecta". In: *ApJL* 848.2, L21, p. L21. DOI: 10.3847/2041-8213/aa905d. arXiv: 1710.05457 [astro-ph.HE].

Alexander, K. D. et al. (Aug. 2018). "A Decline in the X-Ray through Radio Emission from GW170817 Continues to Support an Off-axis Structured Jet". In: *ApJL* 863.2, L18, p. L18. DOI: 10.3847/2041-8213/aad637. arXiv: 1805.02870 [astro-ph.HE].

Amati, L. et al. (July 2002). "Intrinsic spectra and energetics of BeppoSAX Gamma-Ray Bursts with known redshifts". In: *A&A* 390, pp. 81–89. DOI: 10.1051/0004-6361:20020722. arXiv: astro-ph/0205230 [astro-ph].

Andersson, Nils et al. (Oct. 2013). "The transient gravitational-wave sky". In: *Classical and Quantum Gravity* 30.19, 193002, p. 193002. DOI: 10.1088/0264-9381/30/19/193002. arXiv: 1305.0816 [gr-qc].

Asano, Katsuaki and Toshio Terasawa (Nov. 2009). "Slow Heating Model of Gamma-ray Burst: Photon Spectrum and Delayed Emission". In: *ApJ* 705.2, pp. 1714–1720. DOI: 10.1088/0004-637X/705/2/1714. arXiv: 0905.1392 [astro-ph.HE].

Atkins, R. et al. (Apr. 2000). "Evidence for TEV Emission from GRB 970417A". In: *ApJL* 533.2, pp. L119–L122. DOI: 10.1086/312629.

Atwood, W. B. et al. (June 2009). "The Large Area Telescope on the Fermi Gamma-Ray Space Telescope Mission". In: *ApJ* 697, pp. 1071–1102. DOI: 10.1088/0004-637X/697/2/1071. arXiv: 0902.1089 [astro-ph.IM].

Axelsson, M. et al. (Oct. 2012). "GRB110721A: An Extreme Peak Energy and Signatures of the Photosphere". In: *ApJL* 757.2, L31, p. L31. DOI: 10.1088/2041-8205/757/2/L31. arXiv: 1207.6109 [astro-ph.HE].

Axelsson, Magnus and Luis Borgonovo (Mar. 2015). "The width of gamma-ray burst spectra". In: *MNRAS* 447.4, pp. 3150–3154. DOI: 10.1093/mnras/stu2675. arXiv: 1412.5692 [astro-ph.HE].

Band, D. et al. (Aug. 1993). "BATSE observations of gamma-ray burst spectra. I - Spectral diversity". In: *ApJ* 413, pp. 281–292. DOI: 10.1086/172995.

Baring, Matthew G. (May 2009). "Probes of Diffusive Shock Acceleration using Gamma-Ray Burst Prompt Emission". In: *Gamma-ray Burst: Sixth Huntsville Symposium*. Ed. by Charles Meegan, Chryssa Kouveliotou, and Neil Gehrels. Vol. 1133. American Institute of Physics Conference Series, pp. 294–299. DOI: 10.1063/1.3155905. arXiv: 0901.2535 [astro-ph.HE].

Barniol Duran, R. (Aug. 2014). "Constraining the magnetic field in GRB relativistic collisionless shocks using radio data". In: *MNRAS* 442.4, pp. 3147–3154. DOI: 10.1093/mnras/stu1070. arXiv: 1311.1216 [astro-ph.HE].

Bartos, I., P. Brady, and S. Márka (June 2013). "How gravitational-wave observations can shape the gamma-ray burst paradigm". In: *Classical and Quantum Gravity* 30.12, 123001, p. 123001. DOI: 10.1088/0264-9381/30/12/123001. arXiv: 1212.2289 [astro-ph.CO].

Beardmore, A. P. (2019). "The Swift-XRT WT mode spectrum of GRB190114C". In: *GRB Coordinates Network, Circular Service, No. 23736, #1 (2019)* 23736.

Bednarz, J. and M. Ostrowski (May 1998). "Energy Spectra of Cosmic Rays Accelerated at Ultrarelativistic Shock Waves". In: *Physical Review Letters* 80.18, pp. 3911–3914. DOI: 10.1103/PhysRevLett.80.3911. arXiv: astro-ph/9806181 [astro-ph].

Bell, A. R. (Jan. 1978). "The acceleration of cosmic rays in shock fronts - I." In: *MNRAS* 182, pp. 147–156. DOI: 10.1093/mnras/182.2.147.

Beniamini, P., R. Barniol Duran, and D. Giannios (Jan. 2018). "Marginally fast cooling synchrotron models for prompt GRBs". In: *ArXiv e-prints*. arXiv: 1801.04944 [astro-ph.HE].

Beniamini, P. and T. Piran (May 2013). "Constraints on the Synchrotron Emission Mechanism in Gamma-Ray Bursts". In: *ApJ* 769, 69, p. 69. DOI: 10.1088/0004-637X/769/1/69. arXiv: 1301.5575 [astro-ph.HE].

Beniamini, Paz, Lara Nava, and Tsvi Piran (Sept. 2016). "A revised analysis of gamma-ray bursts' prompt efficiencies". In: *MNRAS* 461.1, pp. 51–59. DOI: 10.1093/mnras/stw1331. arXiv: 1606.00311 [astro-ph.HE].

Berger, E. (Aug. 2014). "Short-Duration Gamma-Ray Bursts". In: *Annual Review of Astronomy and Astrophysics* 52, pp. 43–105. DOI: 10.1146/annurev-astro-081913-035926. arXiv: 1311.2603 [astro-ph.HE].

Berger, E. et al. (Dec. 2011). "The Spectroscopic Classification and Explosion Properties of SN 2009nz Associated with GRB 091127 at z = 0.490". In: *ApJ* 743, 204, p. 204. DOI: 10.1088/0004-637X/743/2/204. arXiv: 1106.3073 [astro-ph.HE].

Bernardini, M. G. et al. (Oct. 2017). "Scientific prospects for spectroscopy of the gamma-ray burst prompt emission with SVOM". In: *Experimental Astronomy* 44.1, pp. 113–127. DOI: 10.1007/s10686-017-9551-4.

Berti, A. et al. (July 2019). "Searching for GRBs at VHE with MAGIC: the status before CTA". In: *36th International Cosmic Ray Conference (ICRC2019)*. Vol. 36. International Cosmic Ray Conference, p. 634. arXiv: 1909.02802 [astro-ph.HE].

Bethe, H. A. (Oct. 1990). "Supernova mechanisms". In: *Reviews of Modern Physics* 62.4, pp. 801–866. DOI: 10.1103/RevModPhys.62.801.

Bhat, P. N. et al. (Sept. 1992). "Evidence for sub-millisecond structure in a γ-ray burst". In: *Nature* 359.6392, pp. 217–218. DOI: 10.1038/359217a0.

Bissaldi, E. and J. L. Racusin (2018a). "GRB 180720B : Fermi-LAT detection." In: *GRB Coordinates Network* 22980, p. 1.

— (2018b). "GRB 180720B : Fermi-LAT detection." In: *GRB Coordinates Network* 22980, p. 1.

Blanch, O. et al. (Dec. 2020a). "GRB 201216C: MAGIC detection in very high energy gamma rays". In: *GRB Coordinates Network* 29075, p. 1.

— (Dec. 2020b). "GRB 201216C: MAGIC detection in very high energy gamma rays". In: *GRB Coordinates Network* 29075, p. 1.

Blanch, O. et al. (Oct. 2020c). "MAGIC observations of GRB 201015A: hint of very high energy gamma-ray signal". In: *GRB Coordinates Network* 28659, p. 1.

— (Oct. 2020d). "MAGIC observations of GRB 201015A: hint of very high energy gamma-ray signal". In: *GRB Coordinates Network* 28659, p. 1.

Blanchard, Peter K., Edo Berger, and Wen-fai Fong (Feb. 2016). "The Offset and Host Light Distributions of Long Gamma-Ray Bursts: A New View From HST Observations of Swift Bursts". In: *ApJ* 817.2, 144, p. 144. DOI: 10.3847/0004-637X/817/2/144. arXiv: 1509.07866 [astro-ph.HE].

Blandford, R. D. and C. F. McKee (Aug. 1976). "Fluid dynamics of relativistic blast waves". In: *Physics of Fluids* 19, pp. 1130–1138. DOI: 10.1063/1.861619.

Blandford, R. D. and R. L. Znajek (May 1977). "Electromagnetic extraction of energy from Kerr black holes". In: *MNRAS* 179, pp. 433–456. DOI: 10.1093/mnras/179.3.433.

Blinnikov, S. I., A. V. Kozyreva, and I. E. Panchenko (Nov. 1999). "Gamma-ray bursts: When does a blackbody spectrum look non-thermal?" In: *Astronomy Reports* 43.11, pp. 739–747. arXiv: astro-ph/9902378 [astro-ph].

Bošnjak, Ž., F. Daigne, and G. Dubus (May 2009). "Prompt high-energy emission from gamma-ray bursts in the internal shock model". In: *A&A* 498, pp. 677–703. DOI: 10.1051/0004-6361/200811375. arXiv: 0811.2956.

Briggs, M. S. et al. (Oct. 1999). "Observations of GRB 990123 by the Compton Gamma Ray Observatory". In: *ApJ* 524, pp. 82–91. DOI: 10.1086/307808. eprint: astro-ph/9903247.

Burgess, J. M. (Sept. 2019). "Is spectral width a reliable measure of GRB emission physics?" In: *A&A* 629, A69, A69. DOI: 10.1051/0004-6361/201935140.

Burgess, J. Michael, Felix Ryde, and Hoi-Fung Yu (Aug. 2015). "Taking the band function too far: a tale of two α's". In: *MNRAS* 451.2, pp. 1511–1521. DOI: 10.1093/mnras/stv775. arXiv: 1410.7647 [astro-ph.HE].

Burgess, J. Michael et al. (Feb. 2020). "Gamma-ray bursts as cool synchrotron sources". In: *Nature Astronomy* 4, pp. 174–179. DOI: 10.1038/s41550-019-0911-z. arXiv: 1810.06965 [astro-ph.HE].

Burnham, Kenneth P. and David R. Anderson (2004). "Multimodel Inference: Understanding AIC and BIC in Model Selection". In: *Sociological Methods & Research* 33.2, pp. 261–304. DOI: 10.1177/0049124104268644. eprint: https://doi.org/10.1177/0049124104268644. URL: https://doi.org/10.1177/0049124104268644.

Burrows, D. N. et al. (2005). "Swift X-Ray Telescope and Very Large Telescope Observations of the Afterglow of GRB 041223". In: *ApJL* 622.2, pp. L85–L88. DOI: 10.1086/429666. arXiv: astro-ph/0502326 [astro-ph].

Burrows, David N. et al. (Dec. 2006). "Jet Breaks in Short Gamma-Ray Bursts. II. The Collimated Afterglow of GRB 051221A". In: *ApJ* 653.1, pp. 468–473. DOI: 10.1086/508740. arXiv: astro-ph/0604320 [astro-ph].

Cano, Z. et al. (Sept. 2017). "GRB 161219B/SN 2016jca: A low-redshift gamma-ray burst supernova powered by radioactive heating". In: *A&A* 605, A107, A107. DOI: 10.1051/0004-6361/201731005. arXiv: 1704.05401 [astro-ph.HE].

Carilli, C. L. and S. Rawlings (Dec. 2004). "Motivation, key science projects, standards and assumptions". In: *New Astronomy Reviews* 48.11-12, pp. 979–984. DOI: 10.1016/j.newar.2004.09.001. arXiv: astro-ph/0409274 [astro-ph].

Castro-Tirado, A. J., Y. Hu, E. Fernandez-Garcia, et al. (2019). "GRB 190114C: refined redshift by the 10.4m GTC". In: *GRB Coordinates Network, Circular Service, No. 23708, #1 (2019)* 23708.

Cenko, S. B. et al. (Mar. 2010). "The Collimation and Energetics of the Brightest Swift Gamma-ray Bursts". In: *ApJ* 711.2, pp. 641–654. DOI: 10.1088/0004-637X/711/2/641. arXiv: 0905.0690 [astro-ph.HE].

Chand, Vikas et al. (July 2018). "AstroSat-CZTI detection of variable prompt emission polarization in GRB 171010A". In: *arXiv e-prints*, arXiv:1807.01737, arXiv:1807.01737. arXiv: 1807.01737 [astro-ph.HE].

Chand, Vikas et al. (July 2020). "Peculiar Prompt Emission and Afterglow in the H.E.S.S.-detected GRB 190829A". In: *ApJ* 898.1, 42, p. 42. DOI: 10.3847/1538-4357/ab9606. arXiv: 2001.00648 [astro-ph.HE].

Chevalier, Roger A. and Zhi-Yun Li (June 2000). "Wind Interaction Models for Gamma-Ray Burst Afterglows: The Case for Two Types of Progenitors". In: *ApJ* 536, pp. 195–212. DOI: 10.1086/308914. arXiv: astro-ph/9908272 [astro-ph].

Chornock, R. et al. (Oct. 2017). "The Electromagnetic Counterpart of the Binary Neutron Star Merger LIGO/Virgo GW170817. IV. Detection of Near-infrared Signatures of r-process Nucleosynthesis with Gemini-South". In: *ApJL* 848.2, L19, p. L19. DOI: 10.3847/2041-8213/aa905c. arXiv: 1710.05454 [astro-ph.HE].

Cordier, B. et al. (Dec. 2015). "The SVOM gamma-ray burst mission". In: *arXiv e-prints*, arXiv:1512.03323, arXiv:1512.03323. arXiv: 1512.03323 [astro-ph.IM].

Costa, E. et al. (June 1997). "Discovery of an X-ray afterglow associated with the γ-ray burst of 28 February 1997". In: *Nature* 387.6635, pp. 783–785. DOI: 10.1038/42885. arXiv: astro-ph/9706065 [astro-ph].

Coulter, D. A. et al. (Dec. 2017). "Swope Supernova Survey 2017a (SSS17a), the optical counterpart to a gravitational wave source". In: *Science* 358.6370, pp. 1556–1558. DOI: 10.1126/science.aap9811. arXiv: 1710.05452 [astro-ph.HE].

Covino, S. and D. Fugazza (2018). "GRB 180720B: REM photometry." In: *GRB Coordinates Network* 23021, p. 1.

Crouzet, N. and D. B. Malesani (2018). "GRB 180720B: LCO optical afterglow observations." In: *GRB Coordinates Network* 22988, p. 1.

Cucchiara, A. et al. (July 2011). "A Photometric Redshift of z ~ 9.4 for GRB 090429B". In: *ApJ* 736, 7, p. 7. DOI: 10.1088/0004-637X/736/1/7. arXiv: 1105.4915.

Daigne, F. (2012). "High-Energy Emission from Gamma-Ray Bursts". In: *International Journal of Modern Physics Conference Series*. Vol. 8. International Journal of Modern Physics Conference Series, pp. 196–208. DOI: 10.1142/S2010194512004606.

Daigne, F., Ž. Bošnjak, and G. Dubus (2011). "Reconciling observed gamma-ray burst prompt spectra with synchrotron radiation?" In: *A&A* 526, A110, A110. DOI: 10.1051/0004-6361/201015457. arXiv: 1009.2636 [astro-ph.HE].

Daigne, F. and R. Mochkovitch (May 1998). "Gamma-ray bursts from internal shocks in a relativistic wind: temporal and spectral properties". In: *MNRAS* 296.2, pp. 275–286. DOI: 10.1046/j.1365-8711.1998.01305.x. arXiv: astro-ph/9801245 [astro-ph].

Daigne, Frédéric and Robert Mochkovitch (Nov. 2002). "The expected thermal precursors of gamma-ray bursts in the internal shock model". In: *MNRAS* 336.4, pp. 1271–1280. DOI: 10.1046/j.1365-8711.2002.05875.x. arXiv: astro-ph/0207456 [astro-ph].

D'Avanzo, P. et al. (May 2018). "The evolution of the X-ray afterglow emission of GW 170817/ GRB 170817A in XMM-Newton observations". In: *A&A* 613, L1, p. L1. DOI: 10.1051/0004-6361/201832664. arXiv: 1801.06164 [astro-ph.HE].

de Naurois, M. and H. E. S. S. Collaboration (Aug. 2019). "GRB190829A: Detection of VHE gamma-ray emission with H.E.S.S." In: *GRB Coordinates Network* 25566, p. 1.

de Ugarte Postigo, A. et al. (Aug. 2019). "GRB 190829A: NOEMA detection of the mm afterglow". In: *GRB Coordinates Network* 25589, p. 1.

D'Elia, V. et al. (May 2015). "SN 2013dx associated with GRB 130702A: a detailed photometric and spectroscopic monitoring and a study of the environment". In: *A&A* 577, A116, A116. DOI: 10.1051/0004-6361/201425381. arXiv: 1502.04883 [astro-ph.HE].

Denton, Peter B. and Irene Tamborra (Apr. 2018). "The bright and choked gamma-ray burst contribution to the IceCube and ANTARES low-energy excess". In: *Journal of Cosmology and Astroparticle Physics* 2018.4, 058, p. 058. DOI: 10.1088/1475-7516/2018/04/058. arXiv: 1802.10098 [astro-ph.HE].

Dereli-Bégué, Hüsne, Asaf Pe'er, and Felix Ryde (July 2020). "Classification of Photospheric Emission in Short GRBs". In: *ApJ* 897.2, 145, p. 145. DOI: 10.3847/1538-4357/ab9a2d. arXiv: 2002.06408 [astro-ph.HE].

Derishev, E. V., V. V. Kocharovsky, and V. V. Kocharovsky (June 2001). "Physical parameters and emission mechanism in gamma-ray bursts". In: *A&A* 372, pp. 1071–1077. DOI: 10.1051/0004-6361:20010586. eprint: astro-ph/0006239.

Derishev, Evgeny V. (June 2007). "Synchrotron emission in the fast cooling regime: which spectra can be explained?" In: *Astrophysics and Space Science* 309.1-4, pp. 157–161. DOI: 10.1007/s10509-007-9421-z. arXiv: astro-ph/0611260 [astro-ph].

Dichiara, S. et al. (Aug. 2019). "GRB 190829A: Swift detection of a burst consistent with a galaxy at z=0.08". In: *GRB Coordinates Network* 25552, p. 1.

Domínguez, A. et al. (Feb. 2011). "Extragalactic background light inferred from AEGIS galaxy-SED-type fractions". In: *MNRAS* 410.4, pp. 2556–2578. DOI: 10.1111/j.1365-2966.2010.17631.x. arXiv: 1007.1459 [astro-ph.CO].

Drenkhahn, G. and H. C. Spruit (2002). "Efficient acceleration and radiation in Poynting flux powered GRB outflows". In: *A&A* 391, pp. 1141–1153. DOI: 10.1051/0004-6361:20020839. arXiv: astro-ph/0202387 [astro-ph].

Drout, M. R. et al. (Dec. 2017). "Light curves of the neutron star merger GW170817/SSS17a: Implications for r-process nucleosynthesis". In: *Science* 358.6370, pp. 1570–1574. DOI: 10.1126/science.aaq0049. arXiv: 1710.05443 [astro-ph.HE].

Eichler, David et al. (July 1989). "Nucleosynthesis, neutrino bursts and γ-rays from coalescing neutron stars". In: *Nature* 340.6229, pp. 126–128. DOI: 10.1038/340126a0.

Eldridge, John J. (May 2007). "The circumstellar environment of rotating Wolf Rayet Stars and the implications for GRB afterglows". In: *Philosophical Transactions of the Royal Society of London Series A* 365.1854, pp. 1255–1256. DOI: 10.1098/rsta.2006.1973. arXiv: astro-ph/0610413 [astro-ph].

Fan, Yizhong and Tsvi Piran (June 2006). "Gamma-ray burst efficiency and possible physical processes shaping the early afterglow". In: *MNRAS* 369.1, pp. 197–206. DOI: 10.1111/j.1365-2966.2006.10280.x. arXiv: astro-ph/0601054 [astro-ph].

Fermi GBM Team (Aug. 2019). "GRB 190829A: Fermi GBM Final Real-time Localization". In: *GRB Coordinates Network* 25551, p. 1.

Fermi Large Area Telescope Team et al. (Aug. 2012). "Constraining the High-energy Emission from Gamma-Ray Bursts with Fermi". In: *ApJ* 754.2, 121, p. 121. DOI: 10.1088/0004-637X/754/2/121. arXiv: 1201.3948 [astro-ph.HE].

Flanagan, Éanna É. and Scott A. Hughes (Apr. 1998). "Measuring gravitational waves from binary black hole coalescences. I. Signal to noise for inspiral, merger, and ringdown". In: *Physical Review D* 57.8, pp. 4535–4565. DOI: 10.1103/PhysRevD.57.4535. arXiv: gr-qc/9701039 [gr-qc].

Florou, Ioulia, Maria Petropoulou, and Apostolos Mastichiadis (July 2021). "A marginally fast-cooling proton-synchrotron model for prompt GRBs". In: *MNRAS* 505.1, pp. 1367–1381. DOI: 10.1093/mnras/stab1285. arXiv: 2102.02501 [astro-ph.HE].

Fong, W., E. Berger, and D. B. Fox (Jan. 2010). "Hubble Space Telescope Observations of Short Gamma-Ray Burst Host Galaxies: Morphologies, Offsets, and Local Environments". In: *ApJ* 708.1, pp. 9–25. DOI: 10.1088/0004-637X/708/1/9. arXiv: 0909.1804 [astro-ph.HE].

Fraija, N. et al. (Mar. 2020). "On the origin of the multi-GeV photons from the closest burst with intermediate luminosity: GRB 190829A". In: *arXiv e-prints*, arXiv:2003.11252, arXiv:2003.11252. arXiv: 2003.11252 [astro-ph.HE].

Frederiks, D., S. Golenetskii, R. Aptekar, et al. (2019). "Konus-Wind observation of GRB 190114C". In: *GRB Coordinates Network, Circular Service, No. 23737, #1 (2019)* 23737.

Frederiks, D. et al. (2018). "Konus-Wind observation of GRB 180720B." In: *GRB Coordinates Network* 23011, p. 1.

— (Jan. 2019). "Konus-Wind observation of GRB 190114C." In: *GRB Coordinates Network* 23737, p. 1.

Frontera, F. et al. (Mar. 2000). "Prompt and Delayed Emission Properties of Gamma-Ray Bursts Observed with BeppoSAX". In: *ApJS* 127, pp. 59–78. DOI: 10.1086/313316. eprint: astro-ph/9911228.

Frontera, F. et al. (Mar. 2000). "Prompt and Delayed Emission Properties of Gamma-Ray Bursts Observed with BeppoSAX". In: *ApJS* 127.1, pp. 59–78. DOI: 10.1086/313316. arXiv: astro-ph/9911228 [astro-ph].

Fruchter, A. S. et al. (May 2006). "Long γ-ray bursts and core-collapse supernovae have different environments". In: *Nature* 441.7092, pp. 463–468. DOI: 10.1038/nature04787. arXiv: astro-ph/0603537 [astro-ph].

Galama, T. J. et al. (Oct. 1998). "An unusual supernova in the error box of the γ-ray burst of 25 April 1998". In: *Nature* 395, pp. 670–672. DOI: 10.1038/27150. eprint: astro-ph/9806175.

Gao, He and Peter Mészáros (Jan. 2015). "Reverse Shock Emission in Gamma-Ray Bursts Revisited". In: *Advances in Astronomy* 2015, 192383, p. 192383. DOI: 10.1155/2015/192383. arXiv: 1507.01984 [astro-ph.HE].

Gao, He et al. (Dec. 2013). "A complete reference of the analytical synchrotron external shock models of gamma-ray bursts". In: *New Astronomy Reviews* 57.6, pp. 141–190. DOI: 10.1016/j.newar.2013.10.001. arXiv: 1310.2181 [astro-ph.HE].

Gehrels, N., E. Ramirez-Ruiz, and D. B. Fox (Sept. 2009). "Gamma-Ray Bursts in the Swift Era". In: *Annual Review of Astronomy and Astrophysics* 47.1, pp. 567–617. DOI: 10.1146/annurev.astro.46.060407.145147. arXiv: 0909.1531 [astro-ph.HE].

Gehrels, N. et al. (2004). "The Swift Gamma-Ray Burst Mission". In: *ApJ* 611.2, pp. 1005–1020. DOI: 10.1086/422091. arXiv: astro-ph/0405233 [astro-ph].

Ghirlanda, G., A. Celotti, and G. Ghisellini (Oct. 2002). "Time resolved spectral analysis of bright gamma ray bursts". In: *A&A* 393, pp. 409–423. DOI: 10.1051/0004-6361:20021038. eprint: astro-ph/0206377.

— (Aug. 2003). "Extremely hard GRB spectra prune down the forest of emission models". In: *A&A* 406, pp. 879–892. DOI: 10.1051/0004-6361:20030803. eprint: astro-ph/0210693.

Ghirlanda, G., G. Ghisellini, and A. Celotti (July 2004). "The spectra of short gamma-ray bursts". In: *A&A* 422, pp. L55–L58. DOI: 10.1051/0004-6361:20048008. arXiv: astro-ph/0310861 [astro-ph].

Ghirlanda, G., G. Ghisellini, and L. Nava (2010). "The onset of the GeV afterglow of GRB 090510". In: *A&A* 510, L7, p. L7. DOI: 10.1051/0004-6361/200913980. arXiv: 0909.0016 [astro-ph.HE].

Ghirlanda, G. et al. (July 2007a). "Blackbody components in gamma-ray bursts spectra?" In: *MNRAS* 379.1, pp. 73–85. DOI: 10.1111/j.1365-2966.2007.11890.x. arXiv: 0704.3438 [astro-ph].

Ghirlanda, G. et al. (Apr. 2007b). "Confirming the γ-ray burst spectral-energy correlations in the era of multiple time breaks". In: *A&A* 466.1, pp. 127–136. DOI: 10.1051/0004-6361:20077119. arXiv: astro-ph/0702352 [astro-ph].

Ghirlanda, G. et al. (Mar. 2009). "Short versus long gamma-ray bursts: spectra, energetics, and luminosities". In: *A&A* 496, pp. 585–595. DOI: 10.1051/0004-6361/200811209. arXiv: 0902.0983 [astro-ph.HE].

Ghirlanda, G. et al. (Feb. 2012). "Gamma-ray bursts in the comoving frame". In: *MNRAS* 420, pp. 483–494. DOI: 10.1111/j.1365-2966.2011.20053.x. arXiv: 1107.4096 [astro-ph.HE].

Ghirlanda, G. et al. (2018). "Bulk Lorentz factors of gamma-ray bursts". In: *A&A* 609, A112, A112. DOI: 10.1051/0004-6361/201731598. arXiv: 1711.06257 [astro-ph.HE].

Ghirlanda, G. et al. (Mar. 2019). "Compact radio emission indicates a structured jet was produced by a binary neutron star merger". In: *Science* 363.6430, pp. 968–971. DOI: 10.1126/science.aau8815. arXiv: 1808.00469 [astro-ph.HE].

Ghirlanda, G. et al. (Apr. 2021). "Gamma Ray Burst studies with THESEUS". In: *arXiv e-prints*, arXiv:2104.10448, arXiv:2104.10448. arXiv: 2104.10448 [astro-ph.IM].

Ghisellini, G. and A. Celotti (Feb. 1999). "Quasi-thermal Comptonization and Gamma-Ray Bursts". In: *ApJL* 511.2, pp. L93–L96. DOI: 10.1086/311845. arXiv: astro-ph/9812079 [astro-ph].

Ghisellini, G., A. Celotti, and D. Lazzati (Mar. 2000). "Constraints on the emission mechanisms of gamma-ray bursts". In: *MNRAS* 313, pp. L1–L5. DOI: 10.1046/j.1365-8711.2000.03354.x. eprint: astro-ph/9912461.

Ghisellini, G. et al. (2010). "GeV emission from gamma-ray bursts: a radiative fireball?" In: *MNRAS* 403.2, pp. 926–937. DOI: 10.1111/j.1365-2966.2009.16171.x. arXiv: 0910.2459 [astro-ph.HE].

Ghisellini, G. et al. (July 2017). "The Fermi blazar sequence". In: *MNRAS* 469.1, pp. 255–266. DOI: 10.1093/mnras/stx806. arXiv: 1702.02571 [astro-ph.HE].

Ghisellini, G. et al. (Apr. 2020). "Proton-synchrotron as the radiation mechanism of the prompt emission of gamma-ray bursts?" In: *A&A* 636, A82, A82. DOI: 10.1051/0004-6361/201937244. arXiv: 1912.02185 [astro-ph.HE].

Ghisellini, Gabriele (2013). *Radiative Processes in High Energy Astrophysics*. Vol. 873. DOI: 10.1007/978-3-319-00612-3.

Gill, Ramandeep and Christopher Thompson (Dec. 2014). "Non-thermal Gamma-Ray Emission from Delayed Pair Breakdown in a Magnetized and Photon-rich Outflow". In: *ApJ* 796.2, 81, p. 81. DOI: 10.1088/0004-637X/796/2/81. arXiv: 1406.4774 [astro-ph.HE].

Gilmozzi, R. and J. Spyromilio (Mar. 2007). "The European Extremely Large Telescope (E-ELT)". In: *The Messenger* 127, p. 11.

Goldstein, A. et al. (Mar. 2012). "The Fermi GBM Gamma-Ray Burst Spectral Catalog: The First Two Years". In: *ApJS* 199, 19, p. 19. DOI: 10.1088/0067-0049/199/1/19. arXiv: 1201.2981 [astro-ph.HE].

Golkhou, V. Zach, Nathaniel R. Butler, and Owen M. Littlejohns (Oct. 2015). "The Energy Dependence of GRB Minimum Variability Timescales". In: *ApJ* 811.2, 93, p. 93. DOI: 10.1088/0004-637X/811/2/93. arXiv: 1501.05948 [astro-ph.HE].

Golkhou, Vahid Z. and Nathaniel R. Butler (May 2014). "Uncovering the Intrinsic Variability of Gamma-Ray Bursts". In: *ApJ* 787.1, 90, p. 90. DOI: 10.1088/0004-637X/787/1/90. arXiv: 1403.4254 [astro-ph.HE].

Goodman, J. (Sept. 1986). "Are gamma-ray bursts optically thick?" In: *ApJL* 308, p. L47. DOI: 10.1086/184741.

Granot, Jonathan, Johann Cohen-Tanugi, and Eduardo do Couto e. Silva (Apr. 2008). "Opacity Buildup in Impulsive Relativistic Sources". In: *ApJ* 677.1, pp. 92–126. DOI: 10.1086/526414. arXiv: 0708.4228 [astro-ph].

Granot, Jonathan, Tsvi Piran, and Re'em Sari (Mar. 1999). "Images and Spectra from the Interior of a Relativistic Fireball". In: *ApJ* 513.2, pp. 679–689. DOI: 10.1086/306884. arXiv: astro-ph/9806192 [astro-ph].

Granot, Jonathan and Re'em Sari (Apr. 2002). "The Shape of Spectral Breaks in Gamma-Ray Burst Afterglows". In: *ApJ* 568.2, pp. 820–829. DOI: 10.1086/338966. arXiv: astro-ph/0108027 [astro-ph].

Gropp, J.D. et al. (2019). "GRB 190114C: Swift detection of a very bright burst with a bright optical counterpart". In: *GRB Coordinates Network, Circular Service, No. 23688, #1 (2019)* 23688.

Gruber, D. et al. (Mar. 2014). "The Fermi GBM Gamma-Ray Burst Spectral Catalog: Four Years of Data". In: *ApJS* 211, 12, p. 12. DOI: 10.1088/0067-0049/211/1/12. arXiv: 1401.5069 [astro-ph.HE].

Guilbert, P. W., A. C. Fabian, and M. J. Rees (1983). "Spectral and variability constraints on compact sources". In: *MNRAS* 205, pp. 593–603. DOI: 10.1093/mnras/205.3.593.

Guiriec, S. et al. (Feb. 2011). "Detection of a Thermal Spectral Component in the Prompt Emission of GRB 100724B". In: *ApJL* 727, L33, p. L33. DOI: 10.1088/2041-8205/727/2/L33. arXiv: 1010.4601 [astro-ph.HE].

Guiriec, S. et al. (June 2013). "Evidence for a Photospheric Component in the Prompt Emission of the Short GRB 120323A and Its Effects on the GRB Hardness-Luminosity Relation". In: *ApJ* 770, 32, p. 32. DOI: 10.1088/0004-637X/770/1/32. arXiv: 1210.7252 [astro-ph.HE].

Guiriec, S. et al. (Nov. 2015). "GRB 131014A: A Laboratory for Studying the Thermal-like and Non-thermal Emissions in Gamma-Ray Bursts, and the New $L^{nTh}{}_i$-$E^{nTh,rest}{}_{peak,i}$ Relation". In: *ApJ* 814, 10, p. 10. DOI: 10.1088/0004-637X/814/1/10. arXiv: 1507.06976 [astro-ph.HE].

Guiriec, S. et al. (Nov. 2016). "A Unified Model for GRB Prompt Emission from Optical to γ-Rays: Exploring GRBs as Standard Candles". In: *ApJL* 831, L8, p. L8. DOI: 10.3847/2041-8205/831/1/L8. arXiv: 1606.07193 [astro-ph.HE].

Guiriec, S. et al. (Sept. 2017). "Photospheric Emission in the Joint GBM and Konus Prompt Spectra of GRB 120323A". In: *ApJ* 846, 138, p. 138. DOI: 10.3847/1538-4357/aa81c2. arXiv: 1703.07846 [astro-ph.HE].

Gupta, Nayantara and Bing Zhang (Sept. 2007). "Prompt emission of high-energy photons from gamma ray bursts". In: *MNRAS* 380.1, pp. 78–92. DOI: 10.1111/j.1365-2966.2007.12051.x. arXiv: 0704.1329 [astro-ph].

Haggard, Daryl et al. (Oct. 2017). "A Deep Chandra X-Ray Study of Neutron Star Coalescence GW170817". In: *ApJL* 848.2, L25, p. L25. DOI: 10.3847/2041-8213/aa8ede. arXiv: 1710.05852 [astro-ph.HE].

Hajela, A. et al. (Nov. 2019). "Two Years of Nonthermal Emission from the Binary Neutron Star Merger GW170817: Rapid Fading of the Jet Afterglow and First Constraints on

the Kilonova Fastest Ejecta". In: *ApJL* 886.1, L17, p. L17. DOI: 10.3847/2041-8213/ab5226. arXiv: 1909.06393 [astro-ph.HE].

Hamburg, R., P. Veres, C. Meegan, et al. (2019). "GRB 190114C: Fermi GBM detection". In: *GRB Coordinates Network, Circular Service, No. 23707, #1 (2019)* 23707.

Harrison, F. A. et al. (Oct. 1999). "Optical and Radio Observations of the Afterglow from GRB 990510: Evidence for a Jet". In: *ApJL* 523.2, pp. L121–L124. DOI: 10.1086/312282. arXiv: astro-ph/9905306 [astro-ph].

Hascoët, R. et al. (Mar. 2012). "Do Fermi Large Area Telescope observations imply very large Lorentz factors in gamma-ray burst outflows?" In: *MNRAS* 421.1, pp. 525–545. DOI: 10.1111/j.1365-2966.2011.20332.x. arXiv: 1107.5737 [astro-ph.HE].

HESS collaboration, H. Abdalla, et al. (2021). "Revealing x-ray and gamma ray temporal and spectral similarities in the GRB 190829A afterglow". In: *Science* 372.6546, pp. 1081–1085. ISSN: 0036-8075. DOI: 10.1126/science.abe8560. eprint: https://science.sciencemag.org/content/372/6546/1081.full.pdf. URL: https://science.sciencemag.org/content/372/6546/1081.

HESS Collaboration et al. (Nov. 2019). "A very-high-energy component deep in the γ-ray burst afterglow". In: *Nature* 575.7783, pp. 464–467. DOI: 10.1038/s41586-019-1743-9. arXiv: 1911.08961 [astro-ph.HE].

Horiuchi, T. et al. (2018). "GRB 180720B: MITSuME Ishigaki optical observations." In: *GRB Coordinates Network* 23004, p. 1.

Hu, Y. D. et al. (Sept. 2020). "10.4m GTC observations of the nearby VHE-detected GRB 190829A/SN 2019oyw". In: *arXiv e-prints*, arXiv:2009.04021, arXiv:2009.04021. arXiv: 2009.04021 [astro-ph.HE].

Ignace, R., J. P. Cassinelli, and J. E. Bjorkman (Mar. 1996). "Equatorial Wind Compression Effects across the H-R Diagram". In: *ApJ* 459, p. 671. DOI: 10.1086/176932.

Inoue, Susumu et al. (Mar. 2013). "Gamma-ray burst science in the era of the Cherenkov Telescope Array". In: *Astroparticle Physics* 43, pp. 252–275. DOI: 10.1016/j.astropartphys.2013.01.004. arXiv: 1301.3014 [astro-ph.HE].

Itoh, R. et al. (2018). "GRB 180720B: MITSuME Akeno optical observations." In: *GRB Coordinates Network* 22983, p. 1.

Ivezić, Željko et al. (Mar. 2019). "LSST: From Science Drivers to Reference Design and Anticipated Data Products". In: *ApJ* 873.2, 111, p. 111. DOI: 10.3847/1538-4357/ab042c. arXiv: 0805.2366 [astro-ph].

Izzo, L. et al. (2018). "GRB 180720B: OAJ optical observations." In: *GRB Coordinates Network* 23040, p. 1.

Jelinek, M. et al. (2018). "GRB 180720B: D50 optical observations." In: *GRB Coordinates Network* 23024, p. 1.

Kalberla, P. M. W. et al. (Sept. 2005). "The Leiden/Argentine/Bonn (LAB) Survey of Galactic HI. Final data release of the combined LDS and IAR surveys with improved stray-radiation corrections". In: *A&A* 440.2, pp. 775–782. DOI: 10.1051/0004-6361:20041864. arXiv: astro-ph/0504140 [astro-ph].

Kaneko, Y. et al. (2006). "The Complete Spectral Catalog of Bright BATSE Gamma-Ray Bursts". In: *The Astrophysical Journal Supplement Series* 166.1, pp. 298–340. DOI: 10.1086/505911. URL: https://doi.org/10.1086\%2F505911.

Kaneko, Y. et al. (Sept. 2006). "The Complete Spectral Catalog of Bright BATSE Gamma-Ray Bursts". In: *ApJS* 166, pp. 298–340. DOI: 10.1086/505911. eprint: astro-ph/0601188.

Kann, D. A., L. Izzo, and V. Casanova (2018). "GRB 180720B: OSN detection, fading." In: *GRB Coordinates Network* 22985, p. 1.

Kann, D. A. et al. (Sept. 2010). "The Afterglows of Swift-era Gamma-ray Bursts. I. Comparing pre-Swift and Swift-era Long/Soft (Type II) GRB Optical Afterglows". In: *ApJ*

720.2, pp. 1513–1558. DOI: 10.1088/0004-637X/720/2/1513. arXiv: 0712.2186 [astro-ph].

Katz, J. I. (Sept. 1994). "Low-frequency spectra of gamma-ray bursts". In: *ApJL* 432, pp. L107–L109. DOI: 10.1086/187523. eprint: astro-ph/9312034.

Khangulyan, Dmitry et al. (June 2021). "Extension of the Synchrotron Radiation of Electrons to Very High Energies in Clumpy Environments". In: *ApJ* 914.2, 76, p. 76. DOI: 10.3847/1538-4357/abfcbf. arXiv: 2003.00927 [astro-ph.HE].

Klebesadel, Ray W., Ian B. Strong, and Roy A. Olson (June 1973). "Observations of Gamma-Ray Bursts of Cosmic Origin". In: *ApJL* 182, p. L85. DOI: 10.1086/181225.

Kobayashi, Shiho (Dec. 2000). "Light Curves of Gamma-Ray Burst Optical Flashes". In: *ApJ* 545.2, pp. 807–812. DOI: 10.1086/317869. arXiv: astro-ph/0009319 [astro-ph].

Kobayashi, Shiho, Tsvi Piran, and Re'em Sari (Nov. 1997). "Can Internal Shocks Produce the Variability in Gamma-Ray Bursts?" In: *ApJ* 490, p. 92. DOI: 10.1086/512791. arXiv: astro-ph/9705013 [astro-ph].

Kobayashi, Shiho and Bing Zhang (Nov. 2003). "Early Optical Afterglows from Wind-Type Gamma-Ray Bursts". In: *ApJ* 597.1, pp. 455–458. DOI: 10.1086/378283. arXiv: astro-ph/0304086 [astro-ph].

Kocevski, D., N. Omodei, M. Axelsson, et al. (2019). "GRB 190114C: Fermi-LAT detection". In: *GRB Coordinates Network, Circular Service, No. 23709, #1 (2019)* 23709.

Kouveliotou, C. et al. (Aug. 1993). "Identification of two classes of gamma-ray bursts". In: *ApJL* 413, pp. L101–L104. DOI: 10.1086/186969.

Kulkarni, S. R. et al. (Oct. 1998). "Radio emission from the unusual supernova 1998bw and its association with the γ-ray burst of 25 April 1998". In: *Nature* 395, pp. 663–669. DOI: 10.1038/27139.

Kumar, P. and E. McMahon (Feb. 2008a). "A general scheme for modelling γ-ray burst prompt emission". In: *MNRAS* 384, pp. 33–63. DOI: 10.1111/j.1365-2966.2007.12621.x. arXiv: 0802.2704.

Kumar, P. and B. Zhang (Feb. 2015). "The physics of gamma-ray bursts & relativistic jets". In: *Physics Reports* 561, pp. 1–109. DOI: 10.1016/j.physrep.2014.09.008. arXiv: 1410.0679 [astro-ph.HE].

Kumar, P. et al. (Nov. 2012). "Maximum synchrotron frequency for shock-accelerated particles". In: *MNRAS* 427, pp. L40–L44. DOI: 10.1111/j.1745-3933.2012.01341.x. arXiv: 1210.6033 [astro-ph.HE].

Kumar, Pawan (Oct. 1999). "Gamma-Ray Burst Energetics". In: *ApJL* 523.2, pp. L113–L116. DOI: 10.1086/312265. arXiv: astro-ph/9907096 [astro-ph].

Kumar, Pawan and Erin McMahon (2008b). "A general scheme for modelling γ-ray burst prompt emission". In: *MNRAS* 384.1, pp. 33–63. DOI: 10.1111/j.1365-2966.2007.12621.x. arXiv: 0802.2704 [astro-ph].

Laskar, T. et al. (Sept. 2019). "GRB 190829A: ATCA cm-band detection". In: *GRB Coordinates Network* 25676, p. 1.

Lazzati, Davide et al. (Jan. 2000). "Compton-dragged Gamma-Ray Bursts Associated with Supernovae". In: *ApJL* 529.1, pp. L17–L20. DOI: 10.1086/312452. arXiv: astro-ph/9910191 [astro-ph].

Lemoine, Martin and Guy Pelletier (June 2003). "Particle Transport in Tangled Magnetic Fields and Fermi Acceleration at Relativistic Shocks". In: *ApJL* 589.2, pp. L73–L76. DOI: 10.1086/376353. arXiv: astro-ph/0304058 [astro-ph].

Lesage, S. et al. (Aug. 2019). "GRB 190829A: Fermi GBM detection". In: *GRB Coordinates Network* 25575, p. 1.

Liang, Edison P. (Dec. 1997). "Saturated Compton Cooling Model of Cosmological Gamma-Ray Bursts". In: *ApJL* 491.1, pp. L15–L18. DOI: 10.1086/311046.

Lien, A. et al. (Sept. 2016a). "The Third Swift Burst Alert Telescope Gamma-Ray Burst Catalog". In: *ApJ* 829, 7, p. 7. DOI: 10.3847/0004-637X/829/1/7. arXiv: 1606.01956 [astro-ph.HE].

Lien, A. et al. (Sept. 2016b). "The Third Swift Burst Alert Telescope Gamma-Ray Burst Catalog". In: *ApJ* 829.1, 7, p. 7. DOI: 10.3847/0004-637X/829/1/7. arXiv: 1606.01956 [astro-ph.HE].

Ligorini, Arianna et al. (Apr. 2021). "Mildly relativistic magnetized shocks in electron-ion plasmas - II. Particle acceleration and heating". In: *MNRAS* 502.4, pp. 5065–5074. DOI: 10.1093/mnras/stab220. arXiv: 2101.09256 [astro-ph.HE].

Lipunov, V. et al. (2018). "GRB 180720B: MASTER Global Net OT observations." In: *GRB Coordinates Network* 23023, p. 1.

Lithwick, Y. and R. Sari (July 2001). "Lower Limits on Lorentz Factors in Gamma-Ray Bursts". In: *ApJ* 555, pp. 540–545. DOI: 10.1086/321455. eprint: astro-ph/0011508.

Lloyd, N. M. and V. Petrosian (Nov. 2000). "Synchrotron Radiation as the Source of Gamma-Ray Burst Spectra". In: *ApJ* 543, pp. 722–732. DOI: 10.1086/317125. eprint: astro-ph/0007061.

Logue, J. et al. (Aug. 2012). "Inferring core-collapse supernova physics with gravitational waves". In: *Physical Review D* 86.4, 044023, p. 044023. DOI: 10.1103/PhysRevD.86.044023. arXiv: 1202.3256 [gr-qc].

Lü, H.-J. et al. (Feb. 2017). "Extremely bright GRB 160625B with multi-episodes emission: Evidences for long-term ejecta evolution". In: *ArXiv e-prints*. arXiv: 1702.01382 [astro-ph.HE].

Lyutikov, M., V. I. Pariev, and R. D. Blandford (Nov. 2003). "Polarization of Prompt Gamma-Ray Burst Emission: Evidence for Electromagnetically Dominated Outflow". In: *ApJ* 597.2, pp. 998–1009. DOI: 10.1086/378497. arXiv: astro-ph/0305410 [astro-ph].

Lyutikov, Maxim and Roger Blandford (Dec. 2003). "Gamma Ray Bursts as Electromagnetic Outflows". In: *arXiv e-prints*, astro-ph/0312347, astro–ph/0312347. arXiv: astro-ph/0312347 [astro-ph].

MacLachlan, G. A. et al. (June 2013). "Minimum variability time-scales of long and short GRBs". In: *MNRAS* 432.2, pp. 857–865. DOI: 10.1093/mnras/stt241. arXiv: 1201.4431 [astro-ph.HE].

Maggiore, Michele et al. (Mar. 2020). "Science case for the Einstein telescope". In: *Journal of Cosmology and Astroparticle Physics* 2020.3, 050, p. 050. DOI: 10.1088/1475-7516/2020/03/050. arXiv: 1912.02622 [astro-ph.CO].

MAGIC Collaboration et al. (Nov. 2019a). "Observation of inverse Compton emission from a long γ-ray burst". In: *Nature* 575.7783, pp. 459–463. DOI: 10.1038/s41586-019-1754-6. arXiv: 2006.07251 [astro-ph.HE].

MAGIC Collaboration et al. (Nov. 2019b). "Teraelectronvolt emission from the γ-ray burst GRB 190114C". In: *Nature* 575.7783, pp. 455–458. DOI: 10.1038/s41586-019-1750-x. arXiv: 2006.07249 [astro-ph.HE].

Matsumoto, Tatsuya, Ehud Nakar, and Tsvi Piran (Feb. 2019a). "Constraints on the emitting region of the gamma-rays observed in GW170817". In: *MNRAS* 483.1, pp. 1247–1255. DOI: 10.1093/mnras/sty3200. arXiv: 1807.04756 [astro-ph.HE].

— (June 2019b). "Generalized compactness limit from an arbitrary viewing angle". In: *MNRAS* 486.2, pp. 1563–1573. DOI: 10.1093/mnras/stz923. arXiv: 1903.06712 [astro-ph.HE].

Mazzali, P. A. et al. (Dec. 2003). "The Type Ic Hypernova SN 2003dh/GRB 030329". In: *ApJL* 599, pp. L95–L98. DOI: 10.1086/381259. eprint: astro-ph/0309555.

Medvedev, M. V. (Sept. 2000). "Theory of "Jitter" Radiation from Small-Scale Random Magnetic Fields and Prompt Emission from Gamma-Ray Burst Shocks". In: *ApJ* 540, pp. 704–714. DOI: 10.1086/309374. eprint: astro-ph/0001314.

Meegan, C. et al. (Sept. 2009). "The Fermi Gamma-ray Burst Monitor". In: *ApJ* 702, 791-804, pp. 791–804. DOI: 10.1088/0004-637X/702/1/791. arXiv: 0908.0450 [astro-ph.IM].

Mészáros, P. and M. J. Rees (Feb. 1997). "Optical and Long-Wavelength Afterglow from Gamma-Ray Bursts". In: *ApJ* 476.1, pp. 232–237. DOI: 10.1086/303625. arXiv: astro-ph/9606043 [astro-ph].

— (Feb. 2000). "Steep Slopes and Preferred Breaks in Gamma-Ray Burst Spectra: The Role of Photospheres and Comptonization". In: *ApJ* 530.1, pp. 292–298. DOI: 10.1086/308371. arXiv: astro-ph/9908126 [astro-ph].

Meszaros, P., M. J. Rees, and H. Papathanassiou (1994). "Spectral Properties of Blast-Wave Models of Gamma-Ray Burst Sources". In: *ApJ* 432, p. 181. DOI: 10.1086/174559. arXiv: astro-ph/9311071 [astro-ph].

Minaev, P. and A. Pozanenko (Jan. 2019). "GRB 190114C: SPI-ACS/INTEGRAL extended emission detection." In: *GRB Coordinates Network* 23714, p. 1.

Minaev, P. and A. Pozanenko (2019). "GRB 190114C: SPI-ACS/INTEGRAL extended emission detection". In: *GRB Coordinates Network, Circular Service, No. 23714, #1 (2019)* 23714.

Mirzoyan, R., K. Noda, E. Moretti, et al. (2019). "MAGIC detects the GRB 190114C in the TeV energy domain". In: *GRB Coordinates Network, Circular Service, No. 23701, #1 (2019)* 23701.

Mochkovitch, R., V. Maitia, and R. Marques (Sept. 1995). "Internal Shocks in a Relativistic Wind as a Source for Gamma-Ray Bursts?" In: *Astrophysics and Space Science* 231.1-2, pp. 441–444. DOI: 10.1007/BF00658666.

Molinari, E. et al. (July 2007). "REM observations of GRB 060418 and GRB 060607A: the onset of the afterglow and the initial fireball Lorentz factor determination". In: *A&A* 469, pp. L13–L16. DOI: 10.1051/0004-6361:20077388. eprint: astro-ph/0612607.

Mooley, K. P. et al. (Sept. 2018). "Superluminal motion of a relativistic jet in the neutron-star merger GW170817". In: *Nature* 561.7723, pp. 355–359. DOI: 10.1038/s41586-018-0486-3. arXiv: 1806.09693 [astro-ph.HE].

Murase, Kohta et al. (Nov. 2006). "High-Energy Neutrinos and Cosmic Rays from Low-Luminosity Gamma-Ray Bursts?" In: *ApJL* 651.1, pp. L5–L8. DOI: 10.1086/509323. arXiv: astro-ph/0607104 [astro-ph].

Murase, Kohta et al. (Feb. 2012). "The Role of Stochastic Acceleration in the Prompt Emission of Gamma-Ray Bursts: Application to Hadronic Injection". In: *ApJ* 746.2, 164, p. 164. DOI: 10.1088/0004-637X/746/2/164. arXiv: 1107.5575 [astro-ph.HE].

Nakar, E., S. Ando, and R. Sari (Sept. 2009). "Klein-Nishina Effects on Optically Thin Synchrotron and Synchrotron Self-Compton Spectrum". In: *ApJ* 703, pp. 675–691. DOI: 10.1088/0004-637X/703/1/675. arXiv: 0903.2557 [astro-ph.HE].

Nakar, Ehud and Tsvi Piran (Sept. 2004). "Early afterglow emission from a reverse shock as a diagnostic tool for gamma-ray burst outflows". In: *MNRAS* 353.2, pp. 647–653. DOI: 10.1111/j.1365-2966.2004.08099.x. arXiv: astro-ph/0403461 [astro-ph].

Nava, L. et al. (Aug. 2011a). "Fermi/GBM and BATSE gamma-ray bursts: comparison of the spectral properties". In: *MNRAS* 415, pp. 3153–3162. DOI: 10.1111/j.1365-2966.2011.18928.x. arXiv: 1012.3968 [astro-ph.HE].

— (June 2011b). "Spectral properties of 438 GRBs detected by Fermi/GBM". In: *A&A* 530, A21, A21. DOI: 10.1051/0004-6361/201016270. arXiv: 1012.2863 [astro-ph.HE].

Nava, L. et al. (2013). "Afterglow emission in gamma-ray bursts - I. Pair-enriched ambient medium and radiative blast waves". In: *MNRAS* 433.3, pp. 2107–2121. DOI: 10.1093/mnras/stt872. arXiv: 1211.2806 [astro-ph.HE].

Nava, L. et al. (Feb. 2017). "Constraints on the bulk Lorentz factor of gamma-ray burst jets from Fermi /LAT upper limits". In: *MNRAS* 465, pp. 811–819. DOI: 10.1093/mnras/stw2771. arXiv: 1610.08056 [astro-ph.HE].

Nava, Lara (2018). "High-energy emission from gamma-ray bursts". In: *International Journal of Modern Physics D* 27.13, 1842003, p. 1842003. DOI: 10.1142/S0218271818420038. arXiv: 1804.01524 [astro-ph.HE].

Oganesyan, G. et al. (2018). "Characterization of gamma-ray burst prompt emission spectra down to soft X-rays". In: *A&A* 616, A138, A138. DOI: 10.1051/0004-6361/201732172. arXiv: 1710.09383 [astro-ph.HE].

Oganesyan, G. et al. (2019). "Prompt optical emission as a signature of synchrotron radiation in gamma-ray bursts". In: *A&A* 628, A59, A59. DOI: 10.1051/0004-6361/201935766. arXiv: 1904.11086 [astro-ph.HE].

Oganesyan, Gor et al. (2017). "Detection of Low-energy Breaks in Gamma-Ray Burst Prompt Emission Spectra". In: *ApJ* 846.2, 137, p. 137. DOI: 10.3847/1538-4357/aa831e. arXiv: 1709.04689 [astro-ph.HE].

Paczynski, B. (Sept. 1986). "Gamma-ray bursters at cosmological distances". In: *ApJL* 308, pp. L43–L46. DOI: 10.1086/184740.

Paczynski, B. and J. E. Rhoads (Nov. 1993). "Radio Transients from Gamma-Ray Bursters". In: *ApJL* 418, p. L5. DOI: 10.1086/187102. eprint: astro-ph/9307024.

Panaitescu, A. and P. Kumar (Nov. 2000). "Analytic Light Curves of Gamma-Ray Burst Afterglows: Homogeneous versus Wind External Media". In: *ApJ* 543.1, pp. 66–76. DOI: 10.1086/317090. arXiv: astro-ph/0003246 [astro-ph].

— (June 2002). "Properties of Relativistic Jets in Gamma-Ray Burst Afterglows". In: *ApJ* 571, pp. 779–789. DOI: 10.1086/340094.

Paschalidis, Vasileios, Milton Ruiz, and Stuart L. Shapiro (June 2015). "Relativistic Simulations of Black Hole-Neutron Star Coalescence: The Jet Emerges". In: *ApJL* 806.1, L14, p. L14. DOI: 10.1088/2041-8205/806/1/L14. arXiv: 1410.7392 [astro-ph.HE].

Pe'er, A. and B. Zhang (Dec. 2006). "Synchrotron Emission in Small-Scale Magnetic Fields as a Possible Explanation for Prompt Emission Spectra of Gamma-Ray Bursts". In: *ApJ* 653, pp. 454–461. DOI: 10.1086/508681. eprint: astro-ph/0605641.

Pe'er, A. et al. (Feb. 2012). "The connection between thermal and non-thermal emission in gamma-ray bursts: general considerations and GRB 090902B as a case study". In: *MNRAS* 420, pp. 468–482. DOI: 10.1111/j.1365-2966.2011.20052.x. arXiv: 1007.2228 [astro-ph.HE].

Pe'er, Asaf, Peter Mészáros, and Martin J. Rees (May 2006). "The Observable Effects of a Photospheric Component on GRB and XRF Prompt Emission Spectrum". In: *ApJ* 642.2, pp. 995–1003. DOI: 10.1086/501424. arXiv: astro-ph/0510114 [astro-ph].

Pe'er, Asaf and Felix Ryde (May 2011). "A Theory of Multicolor Blackbody Emission from Relativistically Expanding Plasmas". In: *ApJ* 732.1, 49, p. 49. DOI: 10.1088/0004-637X/732/1/49. arXiv: 1008.4590 [astro-ph.HE].

— (Jan. 2017). "Photospheric emission in gamma-ray bursts". In: *International Journal of Modern Physics D* 26.10, 1730018-296, pp. 1730018–296. DOI: 10.1142/S021827181730018X. arXiv: 1603.05058 [astro-ph.HE].

Pelassa, V. et al. (2010). "The LAT Low-Energy technique for Fermi Gamma-Ray Bursts spectral analysis". In: *arXiv e-prints*, arXiv:1002.2617, arXiv:1002.2617. arXiv: 1002.2617 [astro-ph.HE].

Perley, D. A. et al. (Jan. 2014). "The Afterglow of GRB 130427A from 1 to 10^{16} GHz". In: *ApJ* 781.1, 37, p. 37. DOI: 10.1088/0004-637X/781/1/37. arXiv: 1307.4401 [astro-ph.HE].

Petropoulou, Maria et al. (2019). "Relativistic Magnetic Reconnection in Electron–Positron–Proton Plasmas: Implications for Jets of Active Galactic Nuclei". In: *ApJ* 880.1, 37, p. 37. DOI: 10.3847/1538-4357/ab287a. arXiv: 1906.03297 [astro-ph.HE].

Pian, E. et al. (Nov. 2017). "Spectroscopic identification of r-process nucleosynthesis in a double neutron-star merger". In: *Nature* 551.7678, pp. 67–70. DOI: 10.1038/nature24298. arXiv: 1710.05858 [astro-ph.HE].

Piel, Q. et al. (July 2019). "Gamma-Ray Burst observation at Very High Energy with H.E.S.S." In: *36th International Cosmic Ray Conference (ICRC2019)*. Vol. 36. International Cosmic Ray Conference, p. 761.

Piran, T., A. Shemi, and R. Narayan (Aug. 1993). "Hydrodynamics of Relativistic Fireballs". In: *MNRAS* 263, p. 861. DOI: 10.1093/mnras/263.4.861. arXiv: astro-ph/9301004 [astro-ph].

Piran, Tsvi (July 1995). "Towards Understanding Gamma-Ray Bursts". In: *arXiv e-prints*, astro-ph/9507114, astro–ph/9507114. arXiv: astro-ph/9507114 [astro-ph].

— (Sept. 2005). "Magnetic Fields in Gamma-Ray Bursts: A Short Overview". In: *Magnetic Fields in the Universe: From Laboratory and Stars to Primordial Structures.* Ed. by Elisabete M. de Gouveia dal Pino, Germán Lugones, and Alexander Lazarian. Vol. 784. American Institute of Physics Conference Series, pp. 164–174. DOI: 10.1063/1.2077181. arXiv: astro-ph/0503060 [astro-ph].

Piran, Tsvi and Ehud Nakar (Aug. 2010). "On the External Shock Synchrotron Model for Gamma-ray Bursts' GeV Emission". In: *ApJL* 718.2, pp. L63–L67. DOI: 10.1088/2041-8205/718/2/L63. arXiv: 1003.5919 [astro-ph.HE].

Planck Collaboration (Sept. 2016). "Planck 2015 results. XIII. Cosmological parameters". In: *A&A* 594, A13, A13. DOI: 10.1051/0004-6361/201525830. arXiv: 1502.01589 [astro-ph.CO].

Powell, Jade et al. (Dec. 2016). "Inferring the core-collapse supernova explosion mechanism with gravitational waves". In: *Physical Review D* 94.12, 123012, p. 123012. DOI: 10.1103/PhysRevD.94.123012. arXiv: 1610.05573 [astro-ph.HE].

Preece, R. et al. (Jan. 2014). "The First Pulse of the Extremely Bright GRB 130427A: A Test Lab for Synchrotron Shocks". In: *Science* 343, pp. 51–54. DOI: 10.1126/science.1242302. arXiv: 1311.5581 [astro-ph.HE].

Preece, R. D. et al. (Oct. 1998). "The Synchrotron Shock Model Confronts a "Line of Death" in the BATSE Gamma-Ray Burst Data". In: *ApJL* 506, pp. L23–L26. DOI: 10.1086/311644. eprint: astro-ph/9808184.

— (Jan. 2000). "The BATSE Gamma-Ray Burst Spectral Catalog. I. High Time Resolution Spectroscopy of Bright Bursts Using High Energy Resolution Data". In: *ApJS* 126.1, pp. 19–36. DOI: 10.1086/313289. arXiv: astro-ph/9908119 [astro-ph].

Price, P. A. et al. (Mar. 2001). "Multicolor Observations of the GRB 000926 Afterglow". In: *ApJL* 549.1, pp. L7–L10. DOI: 10.1086/319152. arXiv: astro-ph/0012303 [astro-ph].

Protassov, R. et al. (May 2002). "Statistics, Handle with Care: Detecting Multiple Model Components with the Likelihood Ratio Test". In: *ApJ* 571, pp. 545–559. DOI: 10.1086/339856. eprint: astro-ph/0201547.

Punturo, M. et al. (Apr. 2010). "The third generation of gravitational wave observatories and their science reach". In: *Classical and Quantum Gravity* 27.8, 084007, p. 084007. DOI: 10.1088/0264-9381/27/8/084007.

Rao, A et al. (Dec. 2013). "Time-resolved spectral analysis of prompt emission from long gamma-ray bursts with GeV emission". In: *Research in Astronomy and Astrophysics* 14. DOI: 10.1088/1674-4527/14/1/003.

Ravasio, M. E. et al. (May 2018). "Consistency with synchrotron emission in the bright GRB 160625B observed by Fermi". In: *A&A* 613, A16, A16. DOI: 10.1051/0004-6361/201732245. arXiv: 1711.03106 [astro-ph.HE].

Ravasio, M. E. et al. (May 2019a). "Evidence of two spectral breaks in the prompt emission of gamma-ray bursts". In: *A&A* 625, A60, A60. DOI: 10.1051/0004-6361/201834987. arXiv: 1903.02555 [astro-ph.HE].

Ravasio, M. E. et al. (June 2019b). "GRB 190114C: from prompt to afterglow?" In: *A&A* 626, A12, A12. DOI: 10.1051/0004-6361/201935214. arXiv: 1902.01861 [astro-ph.HE].

Rees, M. J. and P. Meszaros (Sept. 1992). "Relativistic fireballs - Energy conversion and time-scales". In: *MNRAS* 258, 41P–43P. DOI: 10.1093/mnras/258.1.41P.

— (Aug. 1994a). "Unsteady outflow models for cosmological gamma-ray bursts". In: *ApJL* 430, pp. L93–L96. DOI: 10.1086/187446. eprint: astro-ph/9404038.

— (1994b). "Unsteady Outflow Models for Cosmological Gamma-Ray Bursts". In: *ApJL* 430, p. L93. DOI: 10.1086/187446. arXiv: astro-ph/9404038 [astro-ph].

Reichart, D. E. (Mar. 1998). "The Redshift of GRB 970508". In: *ApJL* 495, pp. L99–L101. DOI: 10.1086/311222. eprint: astro-ph/9712100.

Reva, I. et al. (2018). "GRB 180720B : TSHAO optical observations." In: *GRB Coordinates Network* 22979, p. 1.

Rhoads, James E. (Sept. 1997). "How to Tell a Jet from a Balloon: A Proposed Test for Beaming in Gamma-Ray Bursts". In: *ApJL* 487.1, pp. L1–L4. DOI: 10.1086/310876. arXiv: astro-ph/9705163 [astro-ph].

Rhodes, L. et al. (June 2020). "Radio afterglows of very high-energy gamma-ray bursts 190829A and 180720B". In: *MNRAS* 496.3, pp. 3326–3335. DOI: 10.1093/mnras/staa1715. arXiv: 2004.01538 [astro-ph.HE].

Roberts, O. J. and C. Meegan (2018). "GRB 180720B: Fermi GBM observation." In: *GRB Coordinates Network* 22981, p. 1.

Romano, P. et al. (Sept. 2006). "Panchromatic study of GRB 060124: from precursor to afterglow". In: *A&A* 456, pp. 917–927. DOI: 10.1051/0004-6361:20065071. eprint: astro-ph/0602497.

Ronchi, M. et al. (Apr. 2020). "Rise and fall of the high-energy afterglow emission of GRB 180720B". In: *A&A* 636, A55, A55. DOI: 10.1051/0004-6361/201936765. arXiv: 1909.10531 [astro-ph.HE].

Ruderman, M. (Oct. 1975). "Theories of gamma -ray bursts." In: *Seventh Texas Symposium on Relativistic Astrophysics*. Ed. by P. G. Bergman, E. J. Fenyves, and L. Motz. Vol. 262, pp. 164–180. DOI: 10.1111/j.1749-6632.1975.tb31430.x.

Ruiz, Milton, Stuart L. Shapiro, and Antonios Tsokaros (Dec. 2018). "Jet launching from binary black hole-neutron star mergers: Dependence on black hole spin, binary mass ratio, and magnetic field orientation". In: *Physical Review D* 98.12, 123017, p. 123017. DOI: 10.1103/PhysRevD.98.123017. arXiv: 1810.08618 [astro-ph.HE].

Ruiz-Velasco, E. L. (2019). In: *1st International Cherenkov Telescope Array Symposium - Exploring the High-Energy Universe with CTA, Bologna, 6-9 May 2019*.

Rybicki, George B. and Alan P. Lightman (1986). *Radiative Processes in Astrophysics*.

Ryde, F. et al. (Feb. 2010). "Identification and Properties of the Photospheric Emission in GRB090902B". In: *ApJL* 709, pp. L172–L177. DOI: 10.1088/2041-8205/709/2/L172. arXiv: 0911.2025 [astro-ph.HE].

Sakamoto, T. et al. (July 2011a). "The Second Swift Burst Alert Telescope Gamma-Ray Burst Catalog". In: *ApJS* 195, 2, p. 2. DOI: 10.1088/0067-0049/195/1/2. arXiv: 1104.4689 [astro-ph.HE].

Sakamoto, T. et al. (June 2011b). "The Second Swift Burst Alert Telescope Gamma-Ray Burst Catalog". In: *The Astrophysical Journal Supplement Series* 195, p. 2. DOI: 10.1088/0067-0049/195/1/2.

Salafia, O. S. et al. (June 2021). "Multi-wavelength view of the close-by GRB$_\sim$190829A sheds light on gamma-ray burst physics". In: *arXiv e-prints*, arXiv:2106.07169, arXiv:2106.07169. arXiv: 2106.07169 [astro-ph.HE].

Sander, Andreas A. C., J. S. Vink, and W. R. Hamann (Jan. 2020). "Driving classical Wolf-Rayet winds: a Γ- and Z-dependent mass-loss". In: *MNRAS* 491.3, pp. 4406–4425. DOI: 10.1093/mnras/stz3064. arXiv: 1910.12886 [astro-ph.SR].

Sari, R., R. Narayan, and T. Piran (Dec. 1996). "Cooling Timescales and Temporal Structure of Gamma-Ray Bursts". In: *ApJ* 473, p. 204. DOI: 10.1086/178136. eprint: astro-ph/9605005.

Sari, R. and T. Piran (1999). "The early afterglow". In: *Astronomy and Astrophysics Supplement* 138, pp. 537–538. DOI: 10.1051/aas:1999342. arXiv: astro-ph/9901105 [astro-ph].

Sari, R., T. Piran, and R. Narayan (Apr. 1998a). "Spectra and Light Curves of Gamma-Ray Burst Afterglows". In: *ApJL* 497, pp. L17–L20. DOI: 10.1086/311269. eprint: astro-ph/9712005.

Sari, Re'em and Ann A. Esin (Feb. 2001). "On the Synchrotron Self-Compton Emission from Relativistic Shocks and Its Implications for Gamma-Ray Burst Afterglows". In: *ApJ* 548.2, pp. 787–799. DOI: 10.1086/319003. arXiv: astro-ph/0005253 [astro-ph].

Sari, Re'em, Tsvi Piran, and Ramesh Narayan (Apr. 1998b). "Spectra and Light Curves of Gamma-Ray Burst Afterglows". In: *ApJL* 497.1, pp. L17–L20. DOI: 10.1086/311269. arXiv: astro-ph/9712005 [astro-ph].

Sasada, M. et al. (2018). "GRB 180720B: Kanata 1.5m optical/NIR observation." In: *GRB Coordinates Network* 22977, p. 1.

Sato, Yuri et al. (July 2021). "Off-axis jet scenario for early afterglow emission of low-luminosity gamma-ray burst GRB 190829A". In: *MNRAS* 504.4, pp. 5647–5655. DOI: 10.1093/mnras/stab1273. arXiv: 2101.10581 [astro-ph.HE].

Schmalz, S. et al. (2018). "GRB 180720B: ISON-Castelgrande optical observations." In: *GRB Coordinates Network* 23020, p. 1.

Schmidt, W. K. H. (Feb. 1978). "Distance limit for a class of model γ-ray burst sources". In: *Nature* 271.5645, pp. 525–527. DOI: 10.1038/271525a0.

Selsing, J., J. P. U. Fynbo, K. E. Heintz, et al. (2019). "GRB 190114C: NOT optical counterpart and redshift". In: *GRB Coordinates Network, Circular Service, No. 23695, #1 (2019)* 23695.

Shappee, B. J. et al. (Dec. 2017). "Early spectra of the gravitational wave source GW170817: Evolution of a neutron star merger". In: *Science* 358.6370, pp. 1574–1578. DOI: 10.1126/science.aaq0186. arXiv: 1710.05432 [astro-ph.HE].

Shemi, Amotz and Tsvi Piran (Dec. 1990). "The Appearance of Cosmic Fireballs". In: *ApJL* 365, p. L55. DOI: 10.1086/185887.

Shen, Rongfeng, Pawan Kumar, and Edward L. Robinson (Sept. 2006). "No universality for the electron power-law index (p) in gamma-ray bursts and other relativistic sources". In: *MNRAS* 371.3, pp. 1441–1447. DOI: 10.1111/j.1365-2966.2006.10768.x. arXiv: astro-ph/0512489 [astro-ph].

Siegel, M. H. et al. (2018). "GRB 180720A: Swift detection of a burst." In: *GRB Coordinates Network* 22973, p. 1.

Sironi, L., U. Keshet, and M. Lemoine (2015). "Relativistic Shocks: Particle Acceleration and Magnetization". In: *Space Science Reviews* 191.1-4, pp. 519–544. DOI: 10.1007/s11214-015-0181-8. arXiv: 1506.02034 [astro-ph.HE].

Sironi, Lorenzo, Maria Petropoulou, and Dimitrios Giannios (2015). "Relativistic jets shine through shocks or magnetic reconnection?" In: *MNRAS* 450.1, pp. 183–191. DOI: 10.1093/mnras/stv641. arXiv: 1502.01021 [astro-ph.HE].

Sironi, Lorenzo and Anatoly Spitkovsky (2011). "Particle Acceleration in Relativistic Magnetized Collisionless Electron-Ion Shocks". In: *ApJ* 726.2, 75, p. 75. DOI: 10.1088/0004-637X/726/2/75. arXiv: 1009.0024 [astro-ph.HE].

— (2014). "Relativistic Reconnection: An Efficient Source of Non-thermal Particles". In: *ApJL* 783.1, L21, p. L21. DOI: 10.1088/2041-8205/783/1/L21. arXiv: 1401.5471 [astro-ph.HE].

Skrutskie, M. F. et al. (Feb. 2006). "The Two Micron All Sky Survey (2MASS)". In: *The Astronomical Journal* 131.2, pp. 1163–1183. DOI: 10.1086/498708.

Smartt, S. J. et al. (Nov. 2017). "A kilonova as the electromagnetic counterpart to a gravitational-wave source". In: *Nature* 551.7678, pp. 75–79. DOI: 10.1038/nature24303. arXiv: 1710.05841 [astro-ph.HE].

Sollerman, J. et al. (Aug. 2006). "Supernova 2006aj and the associated X-Ray Flash 060218". In: *A&A* 454, pp. 503–509. DOI: 10.1051/0004-6361:20065226. eprint: astro-ph/0603495.

Sparre, M. et al. (July 2011). "Spectroscopic Evidence for SN 2010ma Associated with GRB 101219B". In: *ApJL* 735, L24, p. L24. DOI: 10.1088/2041-8205/735/1/L24. arXiv: 1105.0422 [astro-ph.CO].

Spitkovsky, Anatoly (July 2008). "Particle Acceleration in Relativistic Collisionless Shocks: Fermi Process at Last?" In: *ApJL* 682.1, p. L5. DOI: 10.1086/590248. arXiv: 0802.3216 [astro-ph].

Spruit, H. C., F. Daigne, and G. Drenkhahn (2001). "Large scale magnetic fields and their dissipation in GRB fireballs". In: *A&A* 369, pp. 694–705. DOI: 10.1051/0004-6361:20010131. arXiv: astro-ph/0004274 [astro-ph].

Stern, Boris E. and Juri Poutanen (Aug. 2004). "Gamma-ray bursts from synchrotron self-Compton emission". In: *MNRAS* 352.3, pp. L35–L39. DOI: 10.1111/j.1365-2966.2004.08163.x. arXiv: astro-ph/0405488 [astro-ph].

Svensson, Roland (July 1987). "Non-thermal pair production in compact X-ray sources : first-order Compton cascades in soft radiation fields." In: *MNRAS* 227, pp. 403–451. DOI: 10.1093/mnras/227.2.403.

Tak, Donggeun et al. (Oct. 2019). "Closure Relations of Gamma-Ray Bursts in High Energy Emission". In: *ApJ* 883.2, 134, p. 134. DOI: 10.3847/1538-4357/ab3982. arXiv: 1910.05418 [astro-ph.HE].

Tang, Qing-Wen et al. (June 2015). "Measuring the Bulk Lorentz Factors of Gamma-ray Bursts with Fermi". In: *ApJ* 806.2, 194, p. 194. DOI: 10.1088/0004-637X/806/2/194. arXiv: 1412.3342 [astro-ph.HE].

Tavani, M. (Aug. 1996). "A Shock Emission Model for Gamma-Ray Bursts. II. Spectral Properties". In: *ApJ* 466, p. 768. DOI: 10.1086/177551.

Taylor, G. B. et al. (July 2004). "The Angular Size and Proper Motion of the Afterglow of GRB 030329". In: *ApJL* 609.1, pp. L1–L4. DOI: 10.1086/422554. arXiv: astro-ph/0405300 [astro-ph].

Thompson, C. (Oct. 1994). "A model of gamma-ray bursts." In: *MNRAS* 270, pp. 480–498. DOI: 10.1093/mnras/270.3.480.

Tierney, D. et al. (Feb. 2013). "Anomalies in low-energy gamma-ray burst spectra with the Fermi Gamma-ray Burst Monitor". In: *A&A* 550, A102, A102. DOI: 10.1051/0004-6361/201220710. arXiv: 1301.4859 [astro-ph.HE].

Toffano, M. et al. (Aug. 2021). "The slope of the low-energy spectrum of prompt gamma-ray burst emission". In: *A&A* 652, A123, A123. DOI: 10.1051/0004-6361/202141032.

Toy, V. L. et al. (Feb. 2016). "Optical and Near-infrared Observations of SN 2013dx Associated with GRB 130702A". In: *ApJ* 818.1, 79, p. 79. DOI: 10.3847/0004-637X/818/1/79. arXiv: 1508.00575 [astro-ph.HE].

Troja, E. et al. (Aug. 2016). "An Achromatic Break in the Afterglow of the Short GRB 140903A: Evidence for a Narrow Jet". In: *ApJ* 827.2, 102, p. 102. DOI: 10.3847/0004-637X/827/2/102. arXiv: 1605.03573 [astro-ph.HE].

Troja, E. et al. (2017). "Significant and variable linear polarization during the prompt optical flash of GRB 160625B". In: *Nature* 547.7664. Letter, pp. 425–427. ISSN: 0028-0836. URL: http://dx.doi.org/10.1038/nature23289.

Troja, E. et al. (Nov. 2017). "The X-ray counterpart to the gravitational-wave event GW170817". In: *Nature* 551.7678, pp. 71–74. DOI: 10.1038/nature24290. arXiv: 1710.05433 [astro-ph.HE].

Troja, E. et al. (Nov. 2020). "A thousand days after the merger: Continued X-ray emission from GW170817". In: *MNRAS* 498.4, pp. 5643–5651. DOI: 10.1093/mnras/staa2626. arXiv: 2006.01150 [astro-ph.HE].

Tsvetkova, A. et al. (Sept. 2019). "Konus-Wind observation of GRB 190829A". In: *GRB Coordinates Network* 25660, p. 1.

Uhm, Z. L. and B. Zhang (May 2014). "Fast-cooling synchrotron radiation in a decaying magnetic field and γ-ray burst emission mechanism". In: *Nature Physics* 10, pp. 351–356. DOI: 10.1038/nphys2932. arXiv: 1303.2704 [astro-ph.HE].

Ursi, A. et al. (Jan. 2019). "GRB 190114C: AGILE/MCAL detection." In: *GRB Coordinates Network* 23712, p. 1.

Valeev, A. F. et al. (Aug. 2019). "GRB 190829A: 10.4m GTC spectroscopy". In: *GRB Coordinates Network* 25565, p. 1.

van Marle, A. J. et al. (Dec. 2006). "Forming a constant density medium close to long gamma-ray bursts". In: *A&A* 460.1, pp. 105–116. DOI: 10.1051/0004-6361:20065709. arXiv: astro-ph/0605698 [astro-ph].

Vianello, G. et al. (Sept. 2018). "The Bright and the Slow—GRBs 100724B and 160509A with High-energy Cutoffs at $\lesssim$100 MeV". In: *ApJ* 864.2, 163, p. 163. DOI: 10.3847/1538-4357/aad6ea. arXiv: 1706.01481 [astro-ph.HE].

von Kienlin, A. et al. (Apr. 2020). "The Fourth Fermi-GBM Gamma-Ray Burst Catalog: A Decade of Data". In: *ApJ* 893.1, 46, p. 46. DOI: 10.3847/1538-4357/ab7a18. arXiv: 2002.11460 [astro-ph.HE].

Vreeswijk, P. M. et al. (2018). "GRB 180720B: VLT/X-shooter redshift." In: *GRB Coordinates Network* 22996, p. 1.

Vurm, Indrek and Andrei M. Beloborodov (Sept. 2017). "On the Prospects of Gamma-Ray Burst Detection in the TeV Band". In: *ApJ* 846.2, 152, p. 152. DOI: 10.3847/1538-4357/aa7ddb. arXiv: 1611.05027 [astro-ph.HE].

Walker, Katharine C., Bradley E. Schaefer, and E. E. Fenimore (July 2000). "Gamma-Ray Bursts Have Millisecond Variability". In: *ApJ* 537.1, pp. 264–269. DOI: 10.1086/308995.

Wang, Xiang-Gao et al. (July 2015). "How Bad or Good Are the External Forward Shock Afterglow Models of Gamma-Ray Bursts?" In: *ApJS* 219.1, 9, p. 9. DOI: 10.1088/0067-0049/219/1/9. arXiv: 1503.03193 [astro-ph.HE].

Wang, Xiang-Yu et al. (Oct. 2019). "Synchrotron Self-Compton Emission from External Shocks as the Origin of the Sub-TeV Emission in GRB 180720B and GRB 190114C". In: *ApJ* 884.2, 117, p. 117. DOI: 10.3847/1538-4357/ab426c. arXiv: 1905.11312 [astro-ph.HE].

Wang, Y.-Z. et al. (Feb. 2017). "Evaluating the Bulk Lorentz Factors of Outflow Material: Lessons Learned from the Extremely Energetic Outburst GRB 160625B". In: *ApJ* 836, 81, p. 81. DOI: 10.3847/1538-4357/aa56c6. arXiv: 1611.04879 [astro-ph.HE].

Watson, A. M. et al. (2018). "GRB 180720B: COATLI Optical Detection." In: *GRB Coordinates Network* 23017, p. 1.

Waxman, E. (Aug. 1997). "Gamma-Ray–Burst Afterglow: Supporting the Cosmological Fireball Model, Constraining Parameters, and Making Predictions". In: *ApJL* 485, pp. L5–L8. DOI: 10.1086/310809. eprint: astro-ph/9704116.

Wei, D. M. and T. Lu (Sept. 1998). "Diverse Temporal Properties of Gamma-Ray Burst Afterglows". In: *ApJ* 505, pp. 252–254. DOI: 10.1086/306147. eprint: astro-ph/9712350.

Wells, A. et al. (2004). "The X-ray Telescope for the SWIFT Gamma-Ray Burst Mission". In: *Gamma-Ray Bursts: 30 Years of Discovery*. Ed. by E. Fenimore and M. Galassi. Vol. 727. American Institute of Physics Conference Series, pp. 642–646. DOI: 10.1063/1.1810925.

Willingale, R. et al. (June 2007). "Testing the Standard Fireball Model of Gamma-Ray Bursts Using Late X-Ray Afterglows Measured by Swift". In: *ApJ* 662.2, pp. 1093–1110. DOI: 10.1086/517989. arXiv: astro-ph/0612031 [astro-ph].

Wilms, J., A. Allen, and R. McCray (Oct. 2000). "On the Absorption of X-Rays in the Interstellar Medium". In: *ApJ* 542, pp. 914–924. DOI: 10.1086/317016. eprint: astro-ph/0008425.

Woosley, S. E. (Mar. 1993). "Gamma-Ray Bursts from Stellar Mass Accretion Disks around Black Holes". In: *ApJ* 405, p. 273. DOI: 10.1086/172359.

Wygoda, N. et al. (June 2016). "The Energy Budget of GRBs Based on a Large Sample of Prompt and Afterglow Observations". In: *ApJ* 824.2, 127, p. 127. DOI: 10.3847/0004-637X/824/2/127. arXiv: 1504.01056 [astro-ph.HE].

Xiao, S. et al. (Jan. 2019). "GRB 190114C:Insight-HXMT/HE detection." In: *GRB Coordinates Network* 23716, p. 1.

Xu, D. et al. (2016). "GRB 160625B: VLT/X-shooter redshift." In: *GRB Coordinates Network, Circular Service, No. 19600, #1 (2016)* 9600.

Yassine, M. et al. (Oct. 2017). "Time evolution of the spectral break in the high-energy extra component of GRB 090926A". In: *A&A* 606, A93, A93. DOI: 10.1051/0004-6361/201630353. arXiv: 1705.03384 [astro-ph.HE].

Yonetoku, D. et al. (July 2004). "Gamma-Ray Burst Formation Rate Inferred from the Spectral Peak Energy-Peak Luminosity Relation". In: *ApJ* 609, pp. 935–951. DOI: 10.1086/421285. arXiv: astro-ph/0309217 [astro-ph].

Yu, H.-F. et al. (Jan. 2015a). "Synchrotron cooling in energetic gamma-ray bursts observed by the Fermi Gamma-Ray Burst Monitor". In: *A&A* 573, A81, A81. DOI: 10.1051/0004-6361/201424858. arXiv: 1410.7602 [astro-ph.HE].

Yu, H-F. et al. (Apr. 2016). "The Fermi GBM gamma-ray burst time-resolved spectral catalog: brightest bursts in the first four years". In: *A&A* 588, A135, A135. DOI: 10.1051/0004-6361/201527509. arXiv: 1601.05206 [astro-ph.HE].

Yu, Hoi-Fung, Hüsne Dereli-Bégué, and Felix Ryde (Nov. 2019). "Bayesian Time-resolved Spectroscopy of GRB Pulses". In: *ApJ* 886.1, 20, p. 20. DOI: 10.3847/1538-4357/ab488a. arXiv: 1810.07313 [astro-ph.HE].

Yu, Hoi-Fung et al. (Nov. 2015b). "The sharpness of gamma-ray burst prompt emission spectra". In: *A&A* 583, A129, A129. DOI: 10.1051/0004-6361/201527015. arXiv: 1507.05589 [astro-ph.HE].

Zhang, B.-B. et al. (Apr. 2011). "A Comprehensive Analysis of Fermi Gamma-ray Burst Data. I. Spectral Components and the Possible Physical Origins of LAT/GBM GRBs". In: *ApJ* 730, 141, p. 141. DOI: 10.1088/0004-637X/730/2/141. arXiv: 1009.3338 [astro-ph.HE].

Zhang, B.-B. et al. (Dec. 2016). "Transition from Fireball to Poynting-flux-dominated Outflow in Three-Episode GRB 160625B". In: *ArXiv e-prints*. arXiv: 1612.03089 [astro-ph.HE].

Zhang, Bing and Peter Mészáros (Sept. 2001). "High-Energy Spectral Components in Gamma-Ray Burst Afterglows". In: *ApJ* 559.1, pp. 110–122. DOI: 10.1086/322400. arXiv: astro-ph/0103229 [astro-ph].

Zhang, Bing et al. (2006). "Physical Processes Shaping Gamma-Ray Burst X-Ray Afterglow Light Curves: Theoretical Implications from the Swift X-Ray Telescope Observations". In: *ApJ* 642.1, pp. 354–370. DOI: 10.1086/500723. arXiv: astro-ph/0508321 [astro-ph].

Zhang, Bing et al. (Feb. 2007). "GRB Radiative Efficiencies Derived from the Swift Data: GRBs versus XRFs, Long versus Short". In: *ApJ* 655.2, pp. 989–1001. DOI: 10.1086/510110. arXiv: astro-ph/0610177 [astro-ph].

Zheng, W. and A. V. Filippenko (2018). "GRB 180720B: KAIT Optical Observations." In: *GRB Coordinates Network* 23033, p. 1.

Zheng, W. et al. (2012). "Panchromatic Observations of the Textbook GRB 110205A: Constraining Physical Mechanisms of Prompt Emission and Afterglow". In: *ApJ* 751.2, 90, p. 90. DOI: 10.1088/0004-637X/751/2/90. arXiv: 1111.0283 [astro-ph.HE].

Zou, Yuan-Chuan, Yi-Zhong Fan, and Tsvi Piran (Jan. 2011). "A Revised Limit of the Lorentz Factors of Gamma-ray Bursts with Two Emitting Regions". In: *ApJL* 726.1, L2, p. L2. DOI: 10.1088/2041-8205/726/1/L2. arXiv: 1008.2253 [astro-ph.HE].